# **Springer Theses**Recognizing Outstanding Ph.D. Research

Claudia Fasolato

# Surface Enhanced Raman Spectroscopy for Biophysical Applications

Using Plasmonic Nanoparticle Assemblies



## **Springer Theses**

Recognizing Outstanding Ph.D. Research

## **Aims and Scope**

The series "Springer Theses" brings together a selection of the very best Ph.D. theses from around the world and across the physical sciences. Nominated and endorsed by two recognized specialists, each published volume has been selected for its scientific excellence and the high impact of its contents for the pertinent field of research. For greater accessibility to non-specialists, the published versions include an extended introduction, as well as a foreword by the student's supervisor explaining the special relevance of the work for the field. As a whole, the series will provide a valuable resource both for newcomers to the research fields described, and for other scientists seeking detailed background information on special questions. Finally, it provides an accredited documentation of the valuable contributions made by today's younger generation of scientists.

## Theses are accepted into the series by invited nomination only and must fulfill all of the following criteria

- They must be written in good English.
- The topic should fall within the confines of Chemistry, Physics, Earth Sciences, Engineering and related interdisciplinary fields such as Materials, Nanoscience, Chemical Engineering, Complex Systems and Biophysics.
- The work reported in the thesis must represent a significant scientific advance.
- If the thesis includes previously published material, permission to reproduce this must be gained from the respective copyright holder.
- They must have been examined and passed during the 12 months prior to nomination.
- Each thesis should include a foreword by the supervisor outlining the significance of its content.
- The theses should have a clearly defined structure including an introduction accessible to scientists not expert in that particular field.

More information about this series at http://www.springer.com/series/8790

## Claudia Fasolato

## Surface Enhanced Raman Spectroscopy for Biophysical Applications

Using Plasmonic Nanoparticle Assemblies

Doctoral Thesis accepted by the Sapienza University of Rome, Rome, Italy



Author Dr. Claudia Fasolato Dipartimento di Fisica e Geologia Università degli Studi di Perugia Perugia, Italy Supervisor Prof. Dr. Paolo Postorino Department of Physics Sapienza University Rome, Italy

ISSN 2190-5053 ISSN 2190-5061 (electronic) Springer Theses ISBN 978-3-030-03555-6 ISBN 978-3-030-03556-3 (eBook) https://doi.org/10.1007/978-3-030-03556-3

Library of Congress Control Number: 2018960211

#### © Springer Nature Switzerland AG 2018

This work is subject to copyright. All rights are reserved by the Publisher, whether the whole or part of the material is concerned, specifically the rights of translation, reprinting, reuse of illustrations, recitation, broadcasting, reproduction on microfilms or in any other physical way, and transmission or information storage and retrieval, electronic adaptation, computer software, or by similar or dissimilar methodology now known or hereafter developed.

The use of general descriptive names, registered names, trademarks, service marks, etc. in this publication does not imply, even in the absence of a specific statement, that such names are exempt from the relevant protective laws and regulations and therefore free for general use.

The publisher, the authors and the editors are safe to assume that the advice and information in this book are believed to be true and accurate at the date of publication. Neither the publisher nor the authors or the editors give a warranty, express or implied, with respect to the material contained herein or for any errors or omissions that may have been made. The publisher remains neutral with regard to jurisdictional claims in published maps and institutional affiliations.

This Springer imprint is published by the registered company Springer Nature Switzerland AG The registered company address is: Gewerbestrasse 11, 6330 Cham, Switzerland

In the clearing stands a boxer
And a fighter by his trade
And he carries the reminders
Of ev'ry glove that laid him down
And cut him till he cried out
In his anger and his shame
I am leaving I am leaving
But the fighter still remains.
Simon and Garfunkel—The Boxer

To the ones who have taught me something. A bit to everyone of them. (A quelli che mi hanno insegnato qualcosa. Un po' a ciascuno).

## **Supervisor's Foreword**

Surface-enhanced Raman scattering (SERS) has attracted a growing interest over the last few decades mainly owing to its huge applicative potential. Indeed, combining the molecular fingerprint specificity of Raman spectroscopy with an ultrasensitive detection capability, this technique can bring the limits of the spectroscopic investigation down to the single-molecule level. Metallic nanostructures illuminated by radiation at frequencies close to the plasmon resonance can act as nanoantennas, focusing strong electromagnetic fields in small volumes, well beyond the diffraction limit, thus enabling the spectroscopic analysis of the molecular environment in close proximity to the metallic surface.

Possibly, the most promising applications of SERS spectroscopy can be found in the field of biophysics, where it is often necessary to unravel the complex interplay of multiple factors activating biological processes. To this aim, SERS can represent a powerful tool to reveal specific molecular binding events or structural modifications, *e.g.* changes in the functional groups of a ligand triggered by external stimuli, like prolonged irradiation or changes in the pH or temperature of the environment. The high intensity of SERS signals also allows to efficiently trace SERS-active nanostructures interacting with biosystems, paving the way to their application as biotags for optical experiments in alternative to fluorescent dyes.

With her doctoral dissertation, Claudia Fasolato has proved the high potentialities of SERS in approaching different biophysical problems. Particularly, she focused on molecular sensing and cellular screening for biomedical purposes. Molecular sensing is the topic of the first part of the thesis. Following the basic idea to exploit the huge signal enhancement achieved upon nanoparticle aggregation, she has functionalized gold and silver nanocolloids and monitored the effect on the SERS response of their self-assembled aggregation in mesoscopic structures. A correlation between the aggregate morphologies and the enhancement efficiency clearly emerged from the first attempts. SERS-active substrates were then designed and realized by EBL-driven self-assembly of nanoparticles into regular arrays of mesoscopic aggregates, organized on a solid flat surface. Careful experimental investigations demonstrated the high performances in signal enhancement and the good signal reproducibility of this peculiar kind SERS-active substrates. The

simplicity of the realization protocol and the intrinsic tunability of these structures make them very promising for molecular sensing applications.

The second part of the thesis approaches the problem of a reliable of cellular screening for cancer diagnostics. Claudia has proved the diagnostic capabilities of a folate-based SERS-active nanovector in screening single cells and identifying the cancer ones. It is well known that folic acid is an essential molecule for cell reproduction, and quickly replicating cancer cells show an overexpression of folate-binding proteins on their membrane. Properly functionalized folate nanoparticles can thus be exploited for an efficient selective targeting of cancer cells which bind much more nanoparticles than healthy cells. A single-cell Raman imaging protocol was applied to statistically relevant cell populations from three cell lines used as a test. The analysis of the spectroscopic data enabled not only to discriminate between cancer and normal cells, but also to quantify the nanovector binding efficiency. This was found to be proportional to the level of expression of folate receptors in the different cell lines. The cell/nanovector biorecognition strategy used in the case of folate was then extended to a class of molecules known as antifolates, as aminopterin and methotrexate, which exhibit a strong cytotoxic action, blocking folate metabolism and leading the cell to death. This cytotoxicity was exploited in the design of a theranostic SERS-active nanovector, in principle capable of combining the high selectivity of the folate nanovector with a therapeutic action against the targeted cancer cells.

The experimental studies presented in this thesis aim at a thorough comprehension of the mechanisms affecting the spectroscopic response of SERS-active systems, in order to design effective applications. Claudia has suggested novel paths for systematizing the design of SERS nanosystems and of the experimental protocols adopted: optimizing the sensitivity and reproducibility of SERS spectroscopy is of crucial importance in biophysical and biomedical investigations.

For the combined approach, both fundamental and applied, and for the thorough analysis of the state of the art, this thesis can represent a relevant overview for both students approaching SERS spectroscopy and experts of the field.

Rome, Italy September 2018 Prof. Dr. Paolo Postorino

## **Abstract**

The thesis *Surface Enhanced Raman Spectroscopy for Biophysical Applications* explores the phenomenon of surface-enhanced Raman scattering (SERS), the huge amplification of Raman signal coming from molecules in proximity of a metallic nanostructured surface. SERS spectroscopy is an ultrasensitive analytical technique with a strong potential for applications in the fields of biophysics and nanomedicine. As a title of example, we discuss the design of nanocolloid-based SERS-active substrates for molecular sensing and of a folate-based SERS-active nanosensor capable of selectively interacting with cancer cells, enabling cancer diagnostics and therapy at single-cell level.

### Parts of this thesis have been published in the following articles

Some of the sections and chapters of this thesis are adaptations and/or extensions of the following publications and manuscripts:

- C. Fasolato, F. Domenici, S. Sennato, F. Mura, L. De Angelis, F. Luongo, F. Costantini, F. Bordi, and P. Postorino: Dimensional scale effects on surface enhanced Raman scattering efficiency of self-assembled silver nanoparticle clusters, *Applied Physics Letters* 105.7 (2014):073105.
- F. Domenici, C. Fasolato, E. Mazzi, L. De Angelis, F. Brasili, F. Mura,
   P. Postorino, F. Bordi: Engineering microscale two-dimensional gold nanoparticle cluster arrays for advanced Raman sensing: An AFM study,
   Colloids and surfaces A: Physicochemical and engineering aspects 498 (2016):168–175.
- C. Fasolato, S. Giantulli, I. Silvestri, F. Mazzarda, Y. Toumia, F. Ripanti,
   F. Mura, F. Luongo, F. Costantini, F. Bordi, P. Postorino, F. Domenici:
   Folate-based single cell screening using surface enhanced Raman microimaging,
   Nanoscale 8.39 (2016):17304–17313.
- I. Serafini, L. Lombardi, C. Fasolato, M. Sergi, F. Di Ottavio, F. Sciubba, C. Montesano, M. Guiso, R. Costanza, L. Nucci, R. Curini, P. Postorino, M. Bruno, A. Bianco: A new multi analytical approach for the identification of synthetic and natural dyes mixtures. The case of orcein-mauveine mixture in a historical dress of a Sicilian noblewoman of nineteenth century, *Natural product research* (2017):1–12.

## Acknowledgements

Who knows me, knows as well that I cannot accomplish anything without mixing my efforts with trust, passion and a considerable load of emotions: therefore, here are my acknowledgements which are part of the road as much as the graphs and publications. I spent so many words in the Italian version of my acknowledgements that I think it would be hard to try and reproduce the completeness of that text hereby. So here is a summarized (but thorough) version of my thanksgiving.

I would like to start from the people who built this path together with me, because it is not straightforward to turn the right ingredients into a proper meal. So thanks to Paolo "PP" Postorino, my professor, because he shaped my scientific thinking. For being generous and, most importantly, truly trustworthy. Thanks to Fabio Domenici, a real biophysicist, because he provides essential scientific feedback (as well as motivation). He can be silly and genius in the same five minutes, and this is very appreciable. Thanks to Paolo Dore for being wise, careful and nice.

Thanks to my colleagues. Francesca Ripanti is a friend. She is the most precise, rigorous and wise, and she could keep a calm attitude even in the middle of a tempest. I am lucky she has been on my side. Thanks to Francesco Capitani, my lab buddy, because we grew up together and now we are probably adults (at least, he is). Because we stopped fighting and started complimenting each other. Support from people that know you well is the most important thing. Thanks to the funniest Simone Caramazza, to Angelo Sarra (a true experimentalist) and to Flavia Mazzarda (sweet girls can get angry sometimes, and this is wonderful!). Thanks to Camilla Dore, Lorenzo De Angelis and Francesco Brasili. Special thanks to Angela Capocefalo, for being brave enough to pick a scientific path that looks familiar to me and for helping me out in the revision of this manuscript. Thanks to Debora Caprara, Anna Celeste and all the other students of HPS Group: it is cool to work together with you guys! Thanks to my friends and colleagues Leonetta Baldassarre and Valeria Giliberti, because I know that sometimes we feel the same and it is nice and helpful to know that we are not alone. You are an inspiration in many ways.

xvi Acknowledgements

Thanks to Nico Pigato that is my first mentor, for slightly tilting the direction of my initial velocity, suggesting this path. All of this began with a friendly chat on a sunny afternoon in Sant'Andrea, Vicenza: I don't forget it. Also, thanks to all my wonderful teachers in high school, especially to my female role models, Giovanna Simonetto and Mary Pilastro. Imprinting is important!

Thanks to my parents, my safe harbour, for always being there for me, so much that one could almost take you for granted (but I don't). I am very lucky. Thanks to my grandparents Luigina and Leandro, that are my sponsors, for being so proud of me and for trusting me that much. Thanks to the Fasolato side of my family, because even if we live apart I feel them very close, for so many reasons. Blood ain't water! One though is also for my other grandparents, Bruna and Luigi ("study, so that you can speak up for yourself!"). I know they would be happy for me, today.

Thanks to my friends that are my roots and my wings, that help me see everything from a different perspective, all the times. To Noemi, my friend, my mirror, my favourite stormy sea: I know there will be many days, roads and perspectives to share. Thanks to Laura, that is like me even if we are so different (for that hug on the bridge at the very beginning, most of all). Thanks to Angelica, that is one of the finest intelligences I have ever met: I want to be a bit like you when I grow up! Thanks to Livia, Meri and Ross. Thanks to Davide for being my flatmate and my Ph.D.-mate. Because he was there to share the good, the bad and the food. Thanks to my scientist friends of *The Science Zone*. Because ours is a big crazy experiment that seems to work very well! Thanks to Squenqui that is the ideal partner in business, to Claudio, to Giammi, to Noemi (again), to Fabio, Riccardo Vest and finally to Cocco (with whom I also shared a house ... that luckily did not burn down!). Thanks to my friends "from Centocelle" for always making me laugh and for being a funny and nice human gathering. I love you guys.

In the end thanks to Marco, who has taught me so much about cynicism (without speaking), while always supporting me; for providing me with incredible loads of confidence and trust and for proving that yes, kind men exist. Because we are alike in few, important things and completely different in so many others, and this adds new perspectives to my world.

Since ten years now, on the background there is my city, Rome. I was not born here but I chose this place, and it gave me freedom and joy, and the time and space for being passionate. It is hard to explain, but it is the thing I am less doubtful about. Scenography is a big thing to be thankful for.

## **Contents**

1		erences			
2	Traditional Raman and SERS: Fundamentals and State				
		he Art			
	2.1	Optical Vibrational Spectroscopy of Molecules			
		2.1.1 Theory of Raman Scattering			
	2.2	Surface Enhanced Raman Scattering			
		2.2.1 Electromagnetic Mechanism			
		2.2.2 Chemical Mechanism			
	2.3	Current Trends in Surface Enhanced Raman Scattering 3			
		2.3.1 Nanoparticle-Based SERS Substrates			
		2.3.2 SERS Applications in Nanomedicine			
		2.3.3 Non Metallic Substrates: SERS from Semiconductor			
		Nanostructures			
	Refe	erences			
3	Investigation on Nanoparticles and Their Molecular				
	Fun	ctionalization			
	3.1	Model Functionalization with 4ATP Linker			
		3.1.1 Preparation and Control Characterization 5			
		3.1.2 SERS Versus Raman Spectrum 6			
	3.2	Further Conjugation: Folate and Antifolates			
		3.2.1 Nanovector Functionalization: The Case of Folate 6			
		3.2.2 SERS Signature of Folate/Antifolate Nanovectors			
	3.3	Experimental Details			
	Refe	erences			

xviii Contents

4	Nanoparticle-Based SERS Substrates for Molecular Sensing Applications					
	4.1	Self-assembled Mesoscopic Silver Nanoparticle Clusters	86			
	4.1	4.1.1 Coupled AFM and Raman Analysis	87			
		4.1.2 Dimensional Scale Effect on SERS Efficiency	89			
	4.2	FDTD Simulation: Theoretical Predictions	92			
	4.2	4.2.1 The FDTD Software	92			
		4.2.2 Results on Silver and Gold Np Multilayers	95			
	4.3	Electron Beam Lithography Driven Self-assembly	98			
	<b>T.</b> 3	4.3.1 Nanoparticle Cluster Array Preparation	100			
		4.3.2 Analysis of the Patterned Arrays	100			
		4.3.3 Analysis of the Ordered Nanoparticle Cluster Arrays	102			
		4.3.4 SERS Reproducibility	109			
	Dof	erences	110			
	KCIC	itelices	110			
5	SERS-Active Nanovectors for Single-Cell Cancer Screening					
	and Theranostics					
	5.1	Early Cancer Diagnostics and Theranostics	114			
	5.2	Folate-Based SERS Diagnostics	115			
		5.2.1 Idea of the Experiment	116			
		5.2.2 Cell Treatment and Viability Tests	119			
		5.2.3 Raman and SERS Imaging on Treated Cells	119			
		5.2.4 SEM Imaging on Treated Cells	122			
		5.2.5 SERS Screening and Results	124			
	5.3	From Selectivity to Theranostics: Antifolate Nanovectors	127			
		5.3.1 Preliminary Cytotoxicity Results	128			
		5.3.2 Enhanced Toxicity of Nanostructured Drugs	129			
	Refe	erences	132			
6	Con	clusions	137			
Aj	pend	lix A: SERS Application in Cultural Heritage	141			
C.	ırricı	ulum Vitaa	151			

## Chapter 1 Introduction



1

In recent years, the development of novel technological platforms for the study of biosystems has allowed for reaching extreme sensitivity and gaining deep insight in the physical mechanisms at the basis of biophysical processes. Interesting results have been obtained with imaging techniques [HD2005, Hua2009], as well as in the development of refined approaches for biosystem manipulation and control like microfluidic devices [Krü2002, SW2003], optical tweezers [Gri2003], etc.. Among these novel tools, innovative spectroscopic techniques enable probing specific biomolecules and investigating their composition, structural properties, location and interaction with other elements also in complex environments, as inside a cell [And2011, Gil2016]. This can allow to unravel the biological function of specific molecules in the metabolic processes or their role in the development of diseases: a very important example is the identification of biomarkers for cancer [Abe2010, Pep2001, WQ2015] or other degenerative diseases [Doe2012, ElA2006]. For approaching this kind of problems it is crucial to push the limits of our biophysical investigation down to the single cell and single molecule level [Den2008, WB2010, Gal2014].

In this framework, a wide interest has raised around surface enhanced spectroscopies, based on the plasmonic properties of metallic nanostructures [Bau2017, Sch2014, Rod2015]. In a metal nanoparticle (Np), the collective oscillation of the free electron gas, namely the surface plasmon, can be excited by electromagnetic radiation, tipically in the visible - near infrared spectral range [Sti2008]. The plasmonic excitation induces the Np to act as an electromagnetic nanoantenna. The electromagnetic scattering of light by the plasmonic nanostructure causes the localization of an extremely intense electromagnetic field close to the Np surface. This can be exploited for the spectroscopic investigation of the molecular environment surrounding the Np [Sti2008, NE1997]. In particular, Surface Enhanced Raman Scattering (SERS) consists of the increment of several orders of magnitude in the Raman intensity scattered by a molecule close to a metal nanostructured surface [Sch2014, Fas2014].

2 1 Introduction

Raman scattering is an inelastic light scattering process in which a solid/molecular system is excited by a photon to a so-called virtual electronic state, from which it relaxes almost instantaneously to the fundamental electronic state, but in a different vibrational level, with the creation/destruction of a quantum of vibrational energy that in solid systems is defined as a phonon [Col1975]. The vibrational energetic levels of a molecule depend on its atomic composition and on the chemical bonds that it contains. For this reason, the spectral distribution of the scattered photons - that is the number, position and relative intensity of peaks in the Raman spectrum - is a characteristic of a given molecule, being known as the spectroscopic molecular fingerprint [EG2006]. Raman scattering experiments allow identifying the molecular composition of unknown samples and gaining additional information about the molecular interaction, chemical environment and 3D-organization. Raman spectroscopy is a very powerful tool for the investigation of biomaterials, despite its considerably low intensity: Raman cross sections are typically  $10^9 - 10^{12}$  times lower than fluorescence ones, and even  $10^7 - 10^{10}$  times lower than typical infrared absorption [Sch1986, Sut1992, Etz1999]. Coupling the potentialities of Raman spectroscopy with the field enhancement provided by plasmonic Nps is therefore a promising strategy: SERS spectra display signal enhancements of 6-10 orders of magnitude for nonresonant molecular probes compared to their Raman counterparts [Sti2008, Fan20081.

From a quantitative point of view, the plasmonic excitation inside the metal nanostructure typically accounts for most of the SERS enhancement: this phenomenon is known as electromagnetic SERS mechanism [Sch2006, Yos2010]. Nevertheless, some changes in the features of SERS spectra with respect to conventional Raman, as well as a further signal enhancement, not predictable within the electromagnetic mechanism, need a thorough explanation [Osa1994, Are2000]. To this aim, the changes in the electronic polarizability of the molecule, due to its proximity to a metal surface, have to be considered [Lom1986]. Indeed, charge-transfer resonances and orbital hybridization between molecule and metal substrate can occur. Since the Raman cross section depends on the electronic polarizability of the scatterer, these phenomena affect both shape and intensity of the final SERS spectrum [LB2008]. This effect is usually referred to as chemical SERS mechanism.

The potentiality of SERS as an ultrasensitive spectroscopic technique has been confirmed by the impressive results obtained in SERS probing of even single- or few-molecules, avoiding ensemble measurements. In this regard, SERS represents a powerful tool for fundamental studies, aimed at exploring the vibrational dynamics of single nanoscaled objects. The observation of single molecule Raman scattering has been demonstrated in the late Nineties detecting dye molecules in solution [Kne1997] or proteins on solid plasmonic substrates [Xu1999] using statistical arguments on the SERS intensity detected as a function of time. More recently, the coexistence of persistent and blinking Raman bands in the temporal evolution of SERS spectra of a single organic molecule has been ascribed to the optomechanical coupling between the molecular vibrations and the sub-nanoscale sized plasmonic cavity in which it was immobilized [Ben2016]. These studies have been of pivotal importance for the

1 Introduction 3

field of single molecule spectroscopy [PA2008]. However, since the early era of SERS, it has been clear that its potentialities lie even more in the field of applied science and technology.

In the last decades, considerable efforts have been devoted to the development of SERS-based protocols and/or devices for large-scale applications, especially in the field of biomedicine [Qia2008, Sch2014]. Indeed, in principle, SERS-active systems could grant specific and ultrasensitive biomolecular detection [Dom2011], a great versatility in terms of size, shape and molecular functionalization [VoD2010], and the capability to selectively interact with cells for aims of diagnostics [Pal2015, Fas2016]. Therefore, it is possible not only to develop SERS-based sensors and biosensors, but also to design SERS-active nanosystems capable of tracking bacteria, cancer cells and other specific biomarkers, not only in vitro but also in bodily fluids [Kne2017]. Despite all these possibilities, though, SERS-based technologies often suffer from a lack in the control of the outcome response, which is affected by the somehow competing issues of combining high intensities (i.e. high sensitivity) and experimental reliability through signal reproducibility [Bau2017]. This causes a limitation of the translational impact of SERS-based technologies.

Frequently, reviews on SERS research point out that SERS effect is not easily predictable and reproducible because it is poorly understood [Mos2013]. Nevertheless, this interpretation is probably too cautious and does not identify the central problem in the field. Indeed, the physico-chemical mechanisms on which SERS enhancement relies are widely studied from both experimental and theoretical point of view [LB2008, Aus2012, Gra2017]. On the contrary, the issue is that SERS enhancement is produced and affected by a complex cooperation of different elements. These are the intrinsic properties of the molecule, the shape and composition of the metal substrate, but also their interplay, environment, and spatial organization at the subnanometer level [Gra2017]. In this respect, SERS technique can be considered a purely nanoscale effect, because it depends on local properties, as field enhancement and charge transfer processes, and can be employed for probing nanoscaled systems. For all these reasons, the simultaneous control of all the involved parameters is difficult to achieve.

The urgent need of studies addressing the comprehension and control of the response of SERS-active systems motivates this research. This Ph.D. Thesis addresses the problem of SERS application to biophysical issues. The *fil rouge* of this work is the attempt to gain a thorough comprehension of the mechanisms affecting the spectroscopic response for effective applications. Moreover, when possible, we have tried to suggest a path for the systematization of the nanostructure design and of the experimental protocol to follow in order to reach a high as possible gain in terms of sensitivity and reproducibility. This is essential when dealing with the problems of molecular sensing and cellular screening for early cancer detection and therapy [Str2007, Bau2017].

In the first part, we have focused on the issue of molecular sensing, i.e. detecting specific molecules at ultralow concentration exploiting their intense SERS signal. To this aim, we have developed and thoroughly characterized the plasmonic behaviour

4 1 Introduction

of SERS-active substrates based on metal Np self-assembly in micrometric-sized aggregates on a solid support, starting from their water dispersion. We have studied the SERS activity of self-assembled Np clusters, correlating maximum SERS intensity provided by these structures with the morphological characteristics of the aggregate. We have found a linear dependence of the SERS efficiency on the cluster area up to very large surfaces ( $\sim\!30~\mu\text{m}^2$ ) and a further contribution on the number of Np layers composing the aggregate. The results pointed out a cooperative effect of the whole mesoscopic cluster for generating the maximum SERS signal and of a specific influence of the morphology on the efficiency [Fas2014]. On these bases, we developed a template-guided self-assembly strategy for the preparation of a SERS active substrate [Fas2015]. Electron beam lithography was used to produce a two dimensional, ordered array of micrometric cavities in which the Np assembly was induced into designed shapes [Bra2015]. The accurate control on the Np aggregation resulted in a good combination of signal enhancement and reproducibility [Dom2016].

In the second part of the work, we have addressed a more refined clinical issue, that is early cancer detection through single-cell screening and diagnostics. To this aim, we have exploited the versatility of SERS-active gold Nps in terms of molecular functionalization for developing a folic acid conjugated nanovector [Fas2016]. We have chosen folate because of its key role in cellular metabolism and reproduction: for this reason, it is known that cancer cells overexpress folate binding proteins on their membrane. This feature allows targeting cancer cells with a high selectivity using a folate nanovector. In particular, we have developed a SERS based screening protocol that has allowed for discriminating three distinct cell lines for their different bioaffinity for folate, related to the density and type of folate receptors on the cell membrane [Par2005, Kel2006]. The sensitivity of this strategy in single cell cancer diagnostics suggested the possibility of implementing a therapeutic action of our nanovector [Fas2018]. This was performed through the substitution of folate with antifolate drugs, such as aminopterin and methotrexate. These nanovectors for theranostics (diagnostics and therapy) have shown an enhanced cytotoxicity with respect to the molecular drugs, due to the oriented binding of the molecules loaded on the Nps, favoring both the biorecognition and the toxic action inside the cell.

In the various Chapters, a thorough report of the research activity is provided. We start from the basics and describe in detail the experimental protocols employed and the optimization implemented experimentally along the way. We believe that the presented results well illustrate the state-of-the art in SERS application to biophysical investigations.

#### **Thesis Outline**

The content of this Thesis is organized as follows.

In Chap. 2, the theoretical bases of conventional and surface enhanced Raman scattering are presented, together with a review of the state of the art regarding SERS application in our field of investigation. After an introduction on optical spectroscopies, we have provided a semiclassical, intuitive description of conventional Raman scattering, and then derived a complete quantum mechanical expression for

1 Introduction 5

the cross section of the process. Then, the two main mechanisms of SERS signal enhancement are explained. In the case of electromagnetic enhancement, we have thoroughly described the plasmonic excitation in the simple, emblematic case of a single spherical Np. We have then qualitatively reviewed the interparticle near-and far-field coupling effects in Np assemblies. The state of the art of SERS studies relevant to this Thesis is reviewed in the final Section.

In Chap. 3, we focus on the characterization of functionalized noble metal Nps by means of SERS and complementary techniques. The aim of the presentation of these results is to discuss an experimental investigation on how SERS works in a very simple system, formed by a metal Np covered by a molecular monolayer acting as a SERS label. As SERS probe, we have chosen the well studied 4-aminothiophenol which can act as both a spectroscopic label and a molecular bridge between the Np and a biofunctional layer around the Np. The effect of molecular conjugation in the case of folate- and antifolate-functionalized systems is described with a quantitative SERS characterization. The experimental details and instrumental setups are also briefly described.

In Chap.4, the effect of electromagnetic amplification mechanism on SERS enhancement is studied in disordered, self-assembly nanoparticle aggregates. To begin, the correlation between morphology and SERS efficiency on functionalized silver Np aggregates is investigated. Then, the results of electromagnetic simulation on multilayer Np structures are presented. Finally the EBL-based template-guided strategy for controlling the Np self-assembly is presented, and two dimensional gold Np aggregate arrays are characterized by SERS and AFM measurements.

The first Section of Chap. 5 is focused on the application of folate based SERS active nanovectors to single cell cancer diagnostics. The SERS screening protocol we developed for monitoring the folate receptor density on the membrane of three types of cells is explained. The high sensitivity of this method allowed the implementation of additional therapeutic features, through the substitution of folic acid with antifolate drugs. In the second part of the chapter, the comparative cytotoxicity study on drugloaded nanovector and molecular drug is presented, together with the results on the antifolate nanovector selectivity.

The final remarks in the Conclusions summarize in detail the obtained results, and point out the open issues and the future perspectives of this work.

In Appendix A, we present some interesting results obtained in collaboration with Dr. L. Lombardi (Chemistry Dept., Sapienza University) in the application of SERS to cultural heritage and diagnostics. We describe a SERS-based characterization of the molecular components of madder lake, an ancient dye. These results were obtained by coupling the spectroscopic investigation with high performance thin layer chromatography. We also present results in the SERS identification of organic pigments, obtained by the direct application of silver nanocolloids on fibers. SERS was the first step of a multianalytical investigation on a historical dress that belonged to a Sicilian noblewoman in the 19th century.

6 1 Introduction

#### References

[Abe2010]	Abeel T, Helleputte T et al (2010) Robust biomarker identification for cancer diagno-
	sis with ensemble feature selection methods. Bioinformatics 26(3):392–398. ISSN:
	1460-2059

- [And2011] Ando J, Fujita K et al (2011) Dynamic SERS imaging of cellular transport pathways with endocytosed gold nanoparticles. Nano lett 11(12):5344–5348
- [Are2000] Arenas JF, Woolley MS et al (2000) Complete analysis of the surface-enhanced Raman scattering of pyrazine on the silver electrode on the basis of a resonant charge transfer mechanism involving three states. J Chem Phys 112(17):7669–7683
- [Aus2012] Ausman LK, Li S et al (2012) Structural effects in the electromagnetic enhancement mechanism of surface-enhanced Raman scattering: dipole reradiation and rectangular symmetry effects for nanoparticle arrays. J Phys Chem C 116(33):17318–17327
- [Bau2017] Baumberg J, Bell S et al (2017) SERS in biology/biomedical SERS: general discussion. Faraday Discuss 205:429–456
- [Ben2016] Benz F, Schmidt MK et al (2016) Single-molecule optomechanics in "picocavities". Science 354(6313):726–729
- [Bra2015] Brasili F, Mazzi E et al (2015) Gold nanoparticle cluster arrays for advanced optical sensing: an AFM study. In: 2015 IEEE 15th international conference on nanotechnology (IEEE-NANO). IEEE, pp 1023–1028
- [Col1975] Colthup N, Daly LH et al (1975) Introduction to infrared and Raman spectroscopy. Elsevier, Amsterdam
- [Den2008] Deniz AA, Mukhopadhyay S et al (2008) Single-molecule biophysics: at the interface of biology, physics and chemistry. J R Soc Interface 5(18):15–45. ISSN: 1742-5689
- [Doe2012] Doecke JD, Laws SM et al (2012) Blood-based protein biomarkers for diagnosis of alzheimer disease. Arch Neurol 69(10):1318. ISSN: 0003-9942
- [Dom2011] Domenici F, Bizzarri AR et al (2011) SERS-based nanobiosensing for ultrasensitive detection of the p53 tumor suppressor. Int J Nanomed 6:2033–2042
- [Dom2016] Domenici F, Fasolato C et al (2016) Engineering microscale two-dimensional gold nanoparticle cluster arrays for advanced Raman sensing: an AFM study. Colloids Surf A: Physicochem Eng Asp 498:168–175
- [EG2006] Ellis DI, Goodacre R (2006) Metabolic fingerprinting in disease diagnosis: biomedical applications of infrared and Raman spectroscopy. Analyst 131(8):875. ISSN: 0003-2654
- [ElA2006] El-Agnaf OMA, Salem SA et al (2006) Detection of oligomeric forms of a-synuclein protein in human plasma as a potential biomarker for Parkinson's disease. FASEB J 20(3):419–425. ISSN: 0892-6638
- [Etz1999] Etzkorn T, Klotz B et al (1999) Gas-phase absorption cross sections of 24 monocyclic aromatic hydrocarbons in the UV and IR spectral ranges. Atmos Environ 33(4):525–540
- [Fan2008] Fang Y, Seong N-H et al (2008) Measurement of the distribution of site enhancements in surface-enhanced Raman scattering. Science 321(5887):388–392
- [Fas2014] Fasolato C, Domenici F et al (2014) Dimensional scale effects on surface enhanced Raman scattering efficiency of self-assembled silver nanoparticle clusters. Appl Phys Lett 105(7):073105
- [Fas2015] Fasolato C, Domenici F et al (2015) Self-assembled nanoparticle aggregates: organizing disorder for high performance surface-enhanced spectroscopy. In: Nanoforum 2014, vol 1667. AIP Publishing, pp 020012
- [Fas2016] Fasolato C, Giantulli S et al (2016) Folate-based single cell screening using surface enhanced Raman microimaging. Nanoscale 8(39):17304–17313
- [Fas2018] Fasolato C, Giantulli S et al (2018) Antifolate functionalized nanovectors: SERS investigation motivates effective theranostics. In preparation

References 7

[Gal2014] Galler K, Bräutigam K et al (2014) Making a big thing of a small cell-recent advances in single cell analysis. Analyst 139(6):1237–1273

- [Gil2016] Giliberti V, Baldassarre L et al (2016) Protein clustering in chemically stressed HeLa cells studied by infrared nanospectroscopy. Nanoscale 8(40):17560–17567. ISSN: 2040-3364
- [Gra2017] Graham D, Goodacre R et al (2017) Theory of SERS enhancement: general discussion. Faraday Discuss 205:173–211
- [Gri2003] Grier DG (2003) A revolution in optical manipulation. Nature 424(6950):810–816. ISSN: 0028-0836
- [HD2005] Helmchen F, Denk W (2005) Deep tissue two-photon microscopy. Nat Methods 2(12):932–940. ISSN: 1548-7091
- [Hua2009] Huang B, Bates M et al (2009) Super-resolution fluorescence microscopy. Ann Rev. Biochem 78(1):993–1016. ISSN: 0066-4154
- [Kel2006] Kelemen LE (2006) The role of folate receptor a in cancer development, progression and treatment: cause, consequence or innocent bystander? Int J Cancer 119(2):243–250
- [Kne1997] Kneipp K, Wang Y et al (1997) Single molecule detection using surface-enhanced Raman scattering (SERS). Phys Rev Lett 78(9):1667
- [Kne2017] Kneipp J (2017) Interrogating cells, tissues, and live animals with new generations of surface-enhanced Raman scattering probes and labels. ACS Nano 11(2):1136–1141
- [Krü2002] Krüger J, Singh K et al (2002) Development of a microfluidic device for fluorescence activated cell sorting. J Micromech Microeng 12(4):486
- [LB2008] Lombardi JR, Birke RL (2008) A unified approach to surface-enhanced Raman spectroscopy. J Phys Chem C 112(14):5605–5617
- [Lom1986] Lombardi JR, Birke RL et al (1986) Charge-transfer theory of surface enhanced Raman spectroscopy: Herzberg-Teller contributions. J Chem Phys 84(8):4174–4180
- [Mos2013] Moskovits M (2013) Persistent misconceptions regarding SERS. Phys Chem Chem Phys 15(15):5301–5311
- [NE1997] Nie S, Emory SR (1997) Probing single molecules and single nanoparticles by surface-enhanced Raman scattering. Science 275(5303):1102–1106
- [Osa1994] Osawa M, Matsuda N et al (1994) Charge transfer resonance Raman process in surface-enhanced Raman scattering from p-aminothiophenol adsorbed on silver: Herzberg-Teller contribution. J Phys Chem 98(48):12702–12707
- [PA2008] Pieczonka NPW, Aroca RF (2008) Single molecule analysis by surface-enhanced Raman scattering. Chem Soc Rev 37(5):946–954
- [Pal2015] Pallaoro A, Hoonejani MR et al (2015) Rapid identification by surface-enhanced Raman spectroscopy of cancer cells at low concentrations flowing in a microfluidic channel. ACS Nano 9(4):4328–4336
- [Par2005] Parker N, Turk MJ et al (2005) Folate receptor expression in carcinomas and normal tissues determined by a quantitative radioligand binding assay. Anal Biochem 338(2):284–293
- [Pep2001] Pepe MS, Etzioni R et al (2001) Phases of biomarker development for early detection of cancer. J Natl Cancer Inst 93(14):1054–1061
- [Qia2008] Qian X, Peng X-H et al (2008) In vivo tumor targeting and spectroscopic detection with surface-enhanced Raman nanoparticle tags. Nat Biotechnol 26(1):83
- [Rod2015] Rodrigo D, Limaj O et al (2015) Mid-infrared plasmonic biosensing with graphene. Science 349(6244):165–168
- [Sch1986] Schomacker KT, Delaney JK et al (1986) Measurements of the absolute Raman cross sections of benzene. J Chem Phys 85(8):4240–4247
- [Sch2006] Schatz GC, Young MA et al (2006) Electromagnetic mechanism of SERS. Surfaceenhanced Raman scattering. Springer, pp 19–45
- [Sch2014] Schlücker S (2014) Surface-Enhanced raman spectroscopy: concepts and chemical applications. Angewandte Chemie International Edition 53(19):4756–4795

8 1 Introduction

[Sti2008] Stiles PL, Dieringer JA et al (2008) Surface-enhanced Raman spectroscopy. Ann Rev Anal Chem 1:601–626

- [Str2007] Strehle KR, Cialla D et al (2007) A reproducible surface-enhanced Raman spectroscopy approach. Online SERS measurements in a segmented microfluidic system. Anal Chem 79(4):1542–1547
- [Sut1992] Suto M, Wang X et al (1992) Quantitative photoabsorption and fluorescence spectroscopy of benzene, naphthalene, and some derivatives at 106–295 nm. J Quant Spectrosc Radiat Transf 48(1):79–89
- [SW2003] Sia SK, Whitesides GM (2003) Microfluidic devices fabricated in Poly(dimethylsiloxane) for biological studies. Electrophoresis 24(21):3563–3576. ISSN: 0173-0835
- [VoD2010] Vo-Dinh T, Wang H-N et al (2010) Plasmonic nanoprobes for SERS biosensing and bioimaging. J Biophotonics 3(1–2):89–102
- [WB2010] Wang D, Bodovitz S (2010) Single cell analysis: the new frontier in 'omics'. Trends Biotechnol 28(6):281–290. ISSN: 0167-7799
- [WQ2015] Wu L, Qu X (2015) Cancer biomarker detection: recent achievements and challenges. Chem Soc Rev 44(10):2963–2997. ISSN: 0306-0012
- [Xu1999] Xu H, Bjerneld EJ et al (1999) Spectroscopy of single hemoglobin molecules by surface enhanced Raman scattering. Phys Rev Lett 83(21):4357
- [Yos2010] K-i Yoshida, Itoh T et al (2010) Quantitative evaluation of electromagnetic enhancement in surface-enhanced resonance Raman scattering from plasmonic properties and morphologies of individual Ag nanostructures. Phys Rev B 81(11):115406

## Chapter 2 Traditional Raman and SERS: Fundamentals and State of the Art



An interesting approach to the study of matter is represented by spectroscopy. Indeed, as the direct observation of atoms and molecules is impossible, the best solution to gain information on the physical systems under investigation is to induce the interaction of the "target" matter with a controlled probe, as a beam of light, electrons, neutrons, etc. In this chapter, the basic physics of Raman and SERS processes will be discussed.

The spectroscopic approach to the study of molecules will be firstly introduced. In this framework, we will illustrate the advantages and the potential of Raman spectroscopy for the study of biosystems. It is well known that vibrational spectroscopy can allow the straightforward identification of the molecular species in the sample under investigation, through the recognition of chemical bonds from their characteristic vibrational energies. Beside chemical analysis, probing biomatter with visible radiation allows combining the "soft" effect of the probe (low-energy visible radiation) with the possibility to perform spectroscopic imaging. This means comparing the optical image of a sample, as for example a tissue or a single cell, with the map of the spectroscopic intensity of specific vibrational bands, therefore identifying the chemical composition of the object and the location of the different molecular components (e.g. proteins, lipids, nucleic acids) inside it.

Biophysics is usually interested in monitoring rare biochemical events (e.g. molecular binding, target-receptor interaction, etc.) occurring in precise locations, tipically inside a cell. To this aim, despite the advantages discussed above, Raman spectroscopy presents some intrinsic limitations. First of all, we need to consider the rather low signal intensity (Raman is a second order process in light matter interaction). Moreover, Raman-based spatial investigation is diffraction limited: the spatial resolution of Raman imaging depends on the exciting wavelength through Abbe's definition and is therefore limited to a few hundred nanometers, at best. This often hinders collecting information about interesting biophysical processes, e.g. the receptor distribution on the cell membrane, the formation of protein aggregates inside the

cell, etc. These limitations can be overcome by exploiting the local field enhancement arising at the surface of metallic nanostructures illuminated by light.

Surface Enhanced Raman Scattering (SERS) occurs when a molecule located close to a nano-curved metallic surface is impinged by electromagnetic radiation, tipically in the UV-visible or near infrared spectral ranges. The excitation of the collective electronic oscillation in the metal nanostructure (plasmon resonance) gives rise to the localization of extremely intense electromagnetic fields which can increment the Raman signal from the molecule of several orders of magnitude. Besides the amplification of Raman intensity, the light confinement caused by the nanostructures can be exploited as a local probe for the study of biosystems.

Some of the current trends in SERS research and applications in several fields of research will be reviewed in the final Section of the chapter. We will mainly focus on aspects that are relevant for the presentation of this work of thesis.

## 2.1 Optical Vibrational Spectroscopy of Molecules

In biophysical studies, a key role for the interpretation of the behavior of biosystems and the interaction of their components is played by the structural investigation of biomolecules. Probing the structural properties of macromolecules such as proteins or nucleic acids, as well as unraveling the organization of molecular aggregates on the nanometric scale is fundamental for understanding the biofunctionality of these systems.

The natural approach to this problem is the diffraction of coherent beams of X-rays and neutrons from ordered crystal of biomolecules [Fra1979, Sun1997]. Indeed, the structure of DNA was first disclosed through X-ray diffraction, leading Watson and Crick to the Nobel Prize for Medicine in 1962 [W1953]. Diffraction is based on the interference between beams reflected by different crystal planes in ordered systems. Unfortunately, the crystallization of complex biomacromolecules, such as proteins, is not trivial to obtain [McP1976]. Crystallization also implies a change in the molecular biochemical environment: biomolecules are necessarily investigated in a form that is very different from the native one, often preventing to understand their biofunctionality. Novel techniques, such as coherent diffraction imaging [Mia2008], allow the direct reconstruction of the image of single nanoscaled structures, but they require highly intense and coherent X-ray beam sources [Cha2011]. A significant boost to the application of diffraction has come from the availability of new brilliant sources such as neutron sources and third generation synchrotrons. Overall, diffraction is a demanding approach for the structural study of molecules, requiring a careful sample preparation, very difficult data analysis procedures and peculiar experimental setups, which are not currently available at laboratory level.

An indirect approach to the problem is represented by optical vibrational spectroscopies [Col1975]. When investigating molecular systems, the study of light-matter interaction can allow accessing different kind of information, from the identification of elemental composition and chemical species to the comprehension of the structural

organization of molecules. The analysis of Raman and IR spectra provides a direct and complete set of information about the molecular/lattice dynamics of the system and in particular about the vibrational dynamics. For this reason, these techniques can be also exploited to obtain information about the chemical composition of a sample. Indeed, the vibrational spectrum, that is the sequence of both frequencies and relative intensities of the spectral features (vibrational fingerprint), is molecule-specific but also basically bond-specific. Moreover, Raman and infrared (IR) spectroscopies can give insight into the structure of the system, through conformational spectroscopic markers [GP1977, Pet2003]. An important example is the spectroscopic signature of amide modes, which can be used to infer the secondary and tertiary structure of proteins [Man2012, Pic2012, Sig2016].

Summarizing, optical vibrational spectroscopies offer several advantages for the study of biomolecules and biosystems, and in particular:

- the low energies involved in the physical process make these techniques suitable for the study of delicate samples, as nanostructured systems or biomatter;
- optical vibrational experiments are easy to realize with laboratory table-top setups;
- as already mentioned, they can provide the direct chemical identification of species in the sample through the molecular vibrational fingerprint;
- they allow infering structural information about the system by observing spectroscopic conformational markers, which can be either specific peaks or other spectral characteristics as the peak width.

Raman Scattering and IR absorption differ for the mechanism of light-matter interaction they are based on. If a system is illuminated with electromagnetic radiation, different processes can take place: the incident photons can either be absorbed, or scattered, or they can be transmitted without interacting with the sample. In absorption processes, only one photon is involved: it is absorbed, indeed, if its energy is resonant with a proper excitation in the system. Typical vibrational energies match the energies of photons in the infrared spectral range. Therefore, IR photons will be absorbed and induce a vibrational transition in the system, as shown in the scheme in Fig. 2.1. Scattering processes involve two photons: the first is absorbed and excites the system to an intermediate state, the second is reemitted in the deexcitation. If the system relaxes to the initial level, which is usually the ground state, the emitted photon will have the same energy as the absorbed one: this is a Rayleigh elastic scattering process. Raman inelastic scattering takes place when the final state is different from the initial one. In this case, the energy difference between the incident and scattered photons provides the energy spacing of the vibrational levels of the system.

In the next Sect. 2.1.1, a thorough theoretical description of the Raman effect will be presented. We anticipate that the electromagnetic radiation couples with the induced dipole moment in IR absorption and polarizability in Raman scattering. Both these microscopic quantities are modulated by the interatomic vibrations (see for example Eq. (2.4)). For this reason, Raman and IR can be considered to some extent complementary techniques, as their selection rules are mutually exclusive

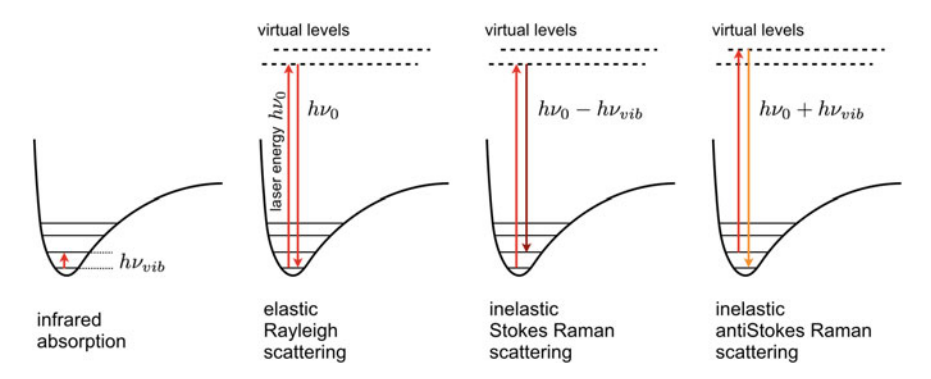


Fig. 2.1 Schematic representation of vibrational absorption and scattering processes

in centrosymmetric media, and generally lead to different kind of spectra. When comparing Raman and IR absorption techniques, the advantages of employing visible radiation for vibrational spectroscopy must be highlighted. Visible light enables indeed to collect Raman signal from a very small scattering volume, diffractionlimited to a few hundreds of nanometers, and allows spectroscopic imaging with submicrometric resolution. Moreover, Raman measurements can be performed in water solution, which is not possible using IR due to the superimposition of water absorption peaks with the molecular fingerprint of organic molecules. For the same reason, IR experiments often need to be performed in controlled atmosphere, as the absorption from water molecules in the air is likely to cause noise in the measurement. Finally, the availability of high performance instrumentation for working with visible light has to be considered: with visible radiation, lenses can be used instead of mirrors, lasers represent brilliant light sources with reasonable costs, and the availability of position sensitive photodetectors (like Peltier-cooled CCDs) allow to simultaneously acquire signal at different spectral components, without requiring a preliminar treatment of the signal as necessary in the case of Fourier transformed IR spectroscopy.

## 2.1.1 Theory of Raman Scattering

### **Semiclassical Description**

The semiclassical explanation of Raman spectroscopy is straightforward: when an electric field is applied to a molecule, a dipole moment  $\mu_{ind}$  is generated in the system, which depends on the incoming electric field. If this not too strong, a linear relationship between dipole and field can be assumed. Being  $\alpha$  defined as the polarizability of the system, we have:

$$\mu_{ind}(\omega) = \alpha \mathbf{E}_0 \cos(\omega t) \tag{2.1}$$

This oscillating dipole acts as a source of electromagnetic field, which, assuming  $\alpha$  as a constant, emits radiation at the frequency  $\omega$  (Rayleigh elastic scattered radiation). If we consider a molecule, the polarizability can be tuned by the internal degrees of freedom and energy transfer can occur from the external electromagnetic field and the molecule. For simplicity, let us consider a biatomic molecule which vibrates at  $\Omega$  frequency: the interatomic distance will vary in time with respect to the equilibrium distance  $R_0$ , causing therefore a change in the polarizability, which can be expanded in Taylor series:

$$\alpha(R) = \alpha(R_0) + \left. \frac{\partial \alpha}{\partial R} \right|_{R=R_0} (R - R_0) = \alpha_0 + \alpha'(R_0)(R - R_0)$$
 (2.2)

The deformation associated with this normal vibrational motion is  $R = R_0 + \rho cos(\Omega t)$  and therefore:

$$\alpha(t) = \alpha_0 + \alpha'(R_0)\rho\cos(\Omega t) = \alpha_0 + \alpha_1\cos(\Omega t) \tag{2.3}$$

From Eqs. (2.1), (2.3) we can derive:

$$\mu_{ind}(\omega) = \alpha_0 \mathbf{E}_0 \cos(\omega t) + \frac{\alpha_1 \mathbf{E}_0}{2} \left[ \cos((\omega + \Omega)t) + \cos((\omega - \Omega)t) \right]$$
 (2.4)

The effect of molecular vibration is the emission of radiation at a different frequency with respect to the exciting field, namely at  $\omega \pm \Omega$ . This inelastic scattering process is called Raman effect. Raman intensity is tipically much lower than Rayleigh scattering, as  $\alpha_1 \ll \alpha_0$ .

In the case of a solid system we can propose a treatment in which we explicitly include the dependence on the  $\mathbf{k}$  vector of the field. Let us consider a crystal impinged by a field  $\mathbf{E}(\mathbf{r},t) = \mathbf{E}(\mathbf{k},\omega)\cos(\mathbf{k}\cdot\mathbf{r}-\omega t)$ . One can derive the expression of the polarization induced in the material  $\mathbf{P}(\mathbf{r},t) = \mathbf{P}(\mathbf{k},\omega)\cos(\mathbf{k}\cdot\mathbf{r}-\omega t)$ . Once again, if the electric field is not too intense, we can assume its linear dependence on the external field. Therefore, including the dependence on the electric field wavevector  $\mathbf{k}$  and on the lattice displacement  $\mathbf{Q}$  in the expression of the polarizability  $\alpha$ , we obtain:

$$\mathbf{P}(\mathbf{k}, \omega)\cos(\mathbf{k} \cdot \mathbf{r} - \omega t) = \alpha(\mathbf{k}, \omega, \mathbf{Q})\mathbf{E}(\mathbf{k}, \omega)\cos(\mathbf{k} \cdot \mathbf{r} - \omega t)$$
(2.5)

and therefore

$$\mathbf{P}(\mathbf{k}, \omega) = \alpha(\mathbf{k}, \omega, \mathbf{Q})\mathbf{E}(\mathbf{k}, \omega) \tag{2.6}$$

The lattice displacement can be expressed as a function of the phonon frequency  $\Omega$  and wavevector  $\mathbf{q}$  as  $\mathbf{Q}(\mathbf{r},t) = \mathbf{Q}(\mathbf{q},\Omega)\cos(\mathbf{q}\cdot\mathbf{r}-\Omega t)$ . As explained in the molecular case, the polarizability of the system depends on the atomic positions, and we can therefore expand the polarizability as a Taylor series in  $\mathbf{Q}$ :

$$\alpha(\mathbf{k}, \omega, \mathbf{Q}) = \alpha_0(\mathbf{k}, \omega) + \left(\frac{\partial \alpha}{\partial \mathbf{Q}}\right)_0 \mathbf{Q}(\mathbf{r}, t) + \dots$$
 (2.7)

and we find the polarizability once again (see Eq. (2.2)) to be composed of a static and a dynamic part, which is here **q**-dependent. Using the same arguments presented for the molecular case, we find that the induced polarization contains terms causing the emission of radiation at different frequencies with respect to the exciting field, namely at  $\omega \pm \Omega$ , with an associated wavevector  $\mathbf{k} \pm \mathbf{q}$ :

$$\mathbf{P}(\mathbf{r}, t, \mathbf{Q}) = \alpha_0(\mathbf{k}, \omega)\mathbf{E}(\mathbf{k}, \omega)\cos(\mathbf{k} \cdot \mathbf{r} - \omega t) + \frac{1}{2} \left(\frac{\partial \alpha}{\partial Q}\right)_0 \mathbf{Q}(\mathbf{q}, \omega)\cos(\mathbf{q} \cdot \mathbf{r} - \omega t)\mathbf{E}(\mathbf{k}, \omega) \cdot \left\{\cos[(\mathbf{k} + \mathbf{q}) \cdot \mathbf{r} - (\omega + \Omega)] + \cos[(\mathbf{k} - \mathbf{q}) \cdot \mathbf{r} - (\omega - \Omega)]\right\}$$
(2.8)

This expression demonstrates that a simple semiclassical description allows to account for Raman effect, satisfying both the conservation of energy and the conservation of momentum.

#### **Quantum Description**

Even though the classical explanation allows for an intuitive comprehension of Raman effect, for a more rigorous description quantum mechanics is needed [CK2007].

The process can be schematized as a transition of the molecule from the fundamental state to a virtual energy level due to the absorption of a photon of energy  $h\nu$  (see Fig. 2.1). This intermediate virtual state can be considered a quantum state with a lifetime so small that it cannot be directly measured: consequently, due to Heisenberg principle, its energy indetermination is huge. For this reason, in the first transition, a violation of the conservation of energy is possible. In the second transition, the molecule relaxes to a stationary state. In the complete process, where the excitation is immediately followed by the disexcitation, the conservation of energy of course holds. If the final state of the molecule relaxation is an excited vibrational level, the emitted photon (Stokes photon) will have an evergy of  $h\nu_{St} = h(\nu - \nu_{vib})$  ( $h\nu_{vib}$  is the energy spacing between the initial and final vibrational states). If, at the beginning of the process, the molecule occupies an excited vibrational state, it can relax to the ground state emitting an Antistokes photon, with the energy of  $h\nu_{ASt} = h(\nu + \nu_{vib})$ .

It is possible to derive the expression of the quantum Raman cross section by considering the radiation-molecule interaction as a perturbation of the system composed by non-interacting molecule and electromagnetic field. Let us consider the radiation-matter interaction that can be obtained in the minimal coupling conditions, and assume that the system is unperturbed for  $t \to \pm \infty$ . For these values of t, we can write the Hamiltonian of the system as the sum of a molecular and a radiation term:

$$\hat{\mathcal{H}}_0 = \hat{\mathcal{H}}_{rad} + \hat{\mathcal{H}}_{mol} \tag{2.9}$$

$$\hat{\mathcal{H}}_{mol} = \sum_{i} \frac{\mathbf{p}_{i}^{2}}{2m_{i}} + \Phi(\{\mathbf{r}_{i}\}) \quad \hat{\mathcal{H}}_{rad} = \sum_{\mathbf{k},\lambda} \hbar \omega_{\mathbf{k},\lambda} \left( n_{\mathbf{k},\lambda} + \frac{1}{2} \right)$$
 (2.10)

where the radiative term is decomposed into a sum of plane waves:  $\mathbf{k}$  identifies the wavevector and  $\lambda$  is one of the two independent polarizations  $\hat{\varepsilon}_{\lambda}$  of a certain mode. The scattering process consists of the absorption of an incident photon with wavevector  $\mathbf{k}$ , polarization  $\hat{\varepsilon}$  and energy  $\hbar\omega = \hbar kc$  and in the emission of a scattered photon with wavevector  $\mathbf{k}'$ , polarization  $\hat{\varepsilon}'$  and energy  $\hbar\omega' = \hbar k'c$ .

The molecule-radiation interaction hamiltonian is

$$\hat{\mathcal{V}}_{int} = \hat{\mathcal{V}}_1 + \hat{\mathcal{V}}_2 \tag{2.11}$$

where

$$\hat{\mathcal{V}}_1 = \sum_i \frac{q_i}{m_i c} \, \mathbf{p}_i \cdot \mathbf{A}_i \quad \hat{\mathcal{V}}_2 = \sum_i \frac{q_i^2}{2m_i c^2} \, A_i^2 \tag{2.12}$$

with  $A_i$  vector potential operator:

$$\mathbf{A}_{i} = \sum_{\mathbf{k},\lambda} \sqrt{\frac{2\pi\hbar c^{2}}{V\omega_{\mathbf{k}}}} \left( a_{\mathbf{k},\lambda} e^{i\mathbf{k}\cdot\mathbf{r}} + a_{\mathbf{k},\lambda}^{+} e^{-i\mathbf{k}\cdot\mathbf{r}} \right)$$
(2.13)

 $a_{{\bf k},\lambda}^+$  and  $a_{{\bf k},\lambda}$  are the creation and distruction operators of photons with  ${\bf k}$  wavevector and  $\lambda$  polarization.

As said before, when  $t \to \pm \infty$  the system occupies stationary states, which are eigenstates of the unperturbed hamiltonian:

$$\hat{\mathcal{H}}_0|i\rangle = E_i|i\rangle \ \hat{\mathcal{H}}_0|f\rangle = E_f|f\rangle$$

As at these times, the molecule and the electromagnetic field do not interact,  $|i\rangle$  and  $|f\rangle$  can be obtained from the tensor product of the molecule and field eigenstates:

$$|i\rangle = |1_{\mathbf{k},\lambda}, 0_{\mathbf{k}',\lambda'}\rangle|A\rangle \quad |f\rangle = |0_{\mathbf{k},\lambda}, 1_{\mathbf{k}',\lambda'}\rangle|B\rangle$$

where

$$\begin{split} \hat{\mathcal{H}}_{mol} \big| A \big\rangle &= E_A \big| A \big\rangle \qquad \hat{\mathcal{H}}_{mol} \big| B \big\rangle = E_B \big| B \big\rangle \\ \hat{\mathcal{H}}_{rad} \big| \mathbf{1}_{\mathbf{k},\lambda}, \mathbf{0}_{\mathbf{k}',\lambda'} \big\rangle &= \hbar \omega \big| \mathbf{1}_{\mathbf{k},\lambda}, \mathbf{0}_{\mathbf{k}',\lambda'} \big\rangle \qquad \hat{\mathcal{H}}_{rad} \big| \mathbf{0}_{\mathbf{k},\lambda}, \mathbf{1}_{\mathbf{k}',\lambda'} \big\rangle = \hbar \omega' \big| \mathbf{0}_{\mathbf{k},\lambda}, \mathbf{1}_{\mathbf{k}',\lambda'} \big\rangle \end{split}$$

Therefore:

$$E_i = E_A + \hbar \omega \quad E_f = E_B + \hbar \omega'$$

The transition probability from  $|i\rangle$  to  $|f\rangle$  per unit time is given by Fermi's golden rule:

$$W_{fi} = \frac{2\pi}{\hbar} \left| \left\langle f \left| \hat{\mathcal{V}}_{int} \right| i \right\rangle \right|^2 \delta(E_f - E_i)$$
 (2.14)

where  $\langle f | \hat{\mathcal{V}}_{int} | i \rangle$  is an element of the transition matrix

$$\langle f | \hat{\mathcal{S}} | i \rangle = \delta_{fi} + \langle f | \hat{\mathcal{V}}_{int} | i \rangle + \sum_{l \neq i} \frac{\langle f | \hat{\mathcal{V}}_{int} | l \rangle \langle l | \hat{\mathcal{V}}_{int} | i \rangle}{E_i - E_l} + \dots$$
 (2.15)

at different perturbation orders.

The vector potential **A** depends linearly on  $a_{\mathbf{k},\lambda}$  and  $a_{\mathbf{k},\lambda}^+$ . When applied to an eigenstate of the field, it gives a linear combination of states, each one differing from the initial state for one unity of a single occupational number  $n_{\mathbf{k},\lambda}$ . The **A** matrix element for the scattering therefore vanishes, as the final state differs from the initial one for the value of two occupational numbers  $(n_{\mathbf{k},\lambda})$  and  $(n_{\mathbf{k}',\lambda'})$ . On the contrary, we have for  $A_i^2$  the following expression:

$$A_{i}^{2} = \frac{2\pi\hbar c^{2}}{V} \sum_{\mathbf{k},\lambda;\mathbf{k}',\lambda'} \frac{1}{\sqrt{\omega_{k}\omega_{k'}}} \left( a_{\mathbf{k}',\lambda'} a_{\mathbf{k},\lambda} e^{i(\mathbf{k}+\mathbf{k}')\cdot\mathbf{r}_{i}} + a_{\mathbf{k}',\lambda'}^{+} a_{\mathbf{k},\lambda}^{+} e^{-i(\mathbf{k}+\mathbf{k}')\cdot\mathbf{r}_{i}} + a_{\mathbf{k}',\lambda'}^{+} a_{\mathbf{k},\lambda}^{+} e^{i(\mathbf{k}-\mathbf{k}')\cdot\mathbf{r}_{i}} + a_{\mathbf{k}',\lambda'}^{+} a_{\mathbf{k},\lambda} e^{-i(\mathbf{k}-\mathbf{k}')\cdot\mathbf{r}_{i}} \right) \hat{\varepsilon}_{\mathbf{k}',\lambda'}^{*} \cdot \hat{\varepsilon}_{\mathbf{k},\lambda}$$
(2.16)

From this expression, non-zero terms arise in the transition matrix, and they are associated to the scattering process.

The transition matrix for the scattering processes is therefore given by the secondorder terms:

$$\langle f | \hat{S} | i \rangle = K^{(1)}(A_i^2) + K^{(2)}(\mathbf{A}_i)$$
 (2.17)

where

$$K^{(1)}(A_i^2) = \langle f | \sum_i \frac{q_i^2}{2m_i c^2} A_i^2 | i \rangle$$
 (2.18)

$$K^{(2)}(\mathbf{A}_{i}) = \sum_{l \neq i} \frac{\langle f \mid \sum_{i} \frac{q_{i}}{m_{i}c} \mathbf{p}_{i} \cdot \mathbf{A}_{i} \mid l \rangle \langle l \mid \sum_{i} \frac{q_{i}}{m_{i}c} \mathbf{p}_{i} \cdot \mathbf{A}_{i} \mid i \rangle}{E_{i} - E_{l}}$$
(2.19)

We therefore have  $K^{(1)}(A_i^2)$ , the second order of the interaction, and  $K^{(2)}(\mathbf{A}_i)$ , the first order in the interaction and second in the perturbation expansion.

If dipole approximation holds,  $e^{-i\mathbf{k}\cdot\mathbf{r}_i} \simeq 1$ , and we take into account the expression (2.16):

$$K^{(1)}(A_{i}^{2}) = \frac{\pi\hbar}{V} \frac{1}{\sqrt{\omega_{k}\omega_{k'}}} \hat{\varepsilon}_{\mathbf{k}',\lambda'}^{*} \cdot \hat{\varepsilon}_{\mathbf{k},\lambda} \times \times \sum_{i} \frac{q_{i}^{2}}{m_{i}} \langle B | \langle 0_{\mathbf{k},\lambda}, 1_{\mathbf{k}',\lambda'} | (a_{\mathbf{k},\lambda}a_{\mathbf{k}',\lambda'}^{+} + a_{\mathbf{k}',\lambda'}^{+} a_{\mathbf{k},\lambda}) e^{-i(\mathbf{k}-\mathbf{k}') \cdot \mathbf{r}_{i}} | 1_{\mathbf{k},\lambda}, 0_{\mathbf{k}',\lambda'} \rangle | A \rangle$$

$$= \frac{\pi\hbar}{V} \frac{1}{\sqrt{\omega_{k}\omega_{k'}}} \hat{\varepsilon}_{\mathbf{k}',\lambda'}^{*} \cdot \hat{\varepsilon}_{\mathbf{k},\lambda} \delta_{BA} \sum_{i} \frac{q_{i}^{2}}{2m_{i}}$$

$$(2.20)$$

The expression for  $K^{(1)}(A_i^2)$  is zero for transitions in which the molecular state changes,  $(|A\rangle \neq |B\rangle)$ , as in the case of Raman scattering.

In the calculation of  $K^{(2)}(\mathbf{A}_i)$ , it is necessary to take into account the two different possible intermediate states  $|l\rangle$  that will give rise to non-zero terms:

$$|l\rangle = |0_{\mathbf{k},\lambda}, 0_{\mathbf{k}',\lambda'}\rangle|I\rangle \quad |l\rangle = |1_{\mathbf{k},\lambda}, 1_{\mathbf{k}',\lambda'}\rangle|I\rangle$$

where  $|I\rangle$  is the intermediate state for the molecule. Therefore, we have:

$$K^{(2)}(\mathbf{A}_{i}) = \sum_{I} \frac{\langle B | \langle 0_{\mathbf{k},\lambda}, 1_{\mathbf{k}',\lambda'} | \hat{\mathcal{V}}_{1} | 0_{\mathbf{k},\lambda}, 0_{\mathbf{k}',\lambda'} \rangle | I \rangle \langle I | \langle 0_{\mathbf{k},\lambda}, 0_{\mathbf{k}',\lambda'} | \hat{\mathcal{V}}_{1} | 1_{\mathbf{k},\lambda}, 0_{\mathbf{k}',\lambda'} \rangle | A \rangle}{E_{A} + \hbar \omega - E_{I}} + \frac{\langle B | \langle 0_{\mathbf{k},\lambda}, 1_{\mathbf{k}',\lambda'} | \hat{\mathcal{V}}_{1} | 1_{\mathbf{k},\lambda}, 1_{\mathbf{k}',\lambda'} \rangle | I \rangle \langle I | \langle 1_{\mathbf{k},\lambda}, 1_{\mathbf{k}',\lambda'} | \hat{\mathcal{V}}_{1} | 1_{\mathbf{k},\lambda}, 0_{\mathbf{k}',\lambda'} \rangle | A \rangle}{E_{A} - E_{I} - \hbar \omega'}$$

$$(2.21)$$

Using for  $\hat{V}_1$  the expression (2.12), the (2.21) becomes:

$$K^{(2)}(\mathbf{A}_i) = \frac{2\pi\hbar\sqrt{\omega_k\omega_{k'}}}{V}\,\varepsilon_{\mathbf{k'},\lambda'}\cdot\mathbf{P}_{BA}\cdot\varepsilon_{\mathbf{k},\lambda} \tag{2.22}$$

where we have implicitly defined the expression for the polarizability tensor:

$$\mathbf{P}_{BA} = \sum_{I} \frac{\mu_{BI} \,\mu_{IA}}{E_A + \hbar\omega - E_I} + \frac{\mu_{IA} \,\mu_{BI}}{E_A - E_I - \hbar\omega'} \tag{2.23}$$

based on the dipole moment expression  $\mu = \sum_i q_i \mathbf{r}_i$ .

From (2.14) the transition probability per unit time can be derived:

$$W_{fi} = \frac{(2\pi)^3 \hbar}{V^2} \omega_k \omega_{k'} \left| \boldsymbol{\varepsilon}_{\mathbf{k'},\lambda'} \cdot \mathbf{P}_{BA} \cdot \boldsymbol{\varepsilon}_{\mathbf{k},\lambda} \right|^2 \delta(E_f - E_i)$$
 (2.24)

Introducing the final density of states for the photon:

$$\rho(\mathbf{k}')d\mathbf{k}' = \frac{V}{(2\pi)^3}k'^2dk'd\Omega$$
 (2.25)

and the incident flux of photons  $\Phi_{inc} = \frac{c}{V}$ , it is possible to write the expression of the scattering cross section for a photon with wavevector between  $\mathbf{k}'$  and  $\mathbf{k}' + \Delta \mathbf{k}'$ :

$$d\sigma = \frac{W_{fi} \rho(\mathbf{k}') d\mathbf{k}'}{\Phi_{inc}} = \hbar c k k'^3 \left| \varepsilon_{\mathbf{k}', \lambda'} \cdot \mathbf{P}_{BA} \cdot \varepsilon_{\mathbf{k}, \lambda} \right|^2 \delta(E_f - E_i) dk' d\Omega \qquad (2.26)$$

and the differential cross section:

$$\frac{\partial^2 \sigma}{\partial \Omega \partial E'} = k k'^3 \left| \boldsymbol{\varepsilon}_{\mathbf{k}', \lambda'} \cdot \mathbf{P}_{BA} \cdot \boldsymbol{\varepsilon}_{\mathbf{k}, \lambda} \right|^2 \delta(E_f - E_i)$$
 (2.27)

Eventually, we can sum all the possible molecular states satisfying the conservation of energy  $E_B - E_A = \hbar(\omega - \omega')$ , multiplying the initial states by their probability, given by Boltzmann distribution

$$P(A) = \frac{e^{-\frac{E_A}{k_B T}}}{\sum_{I} e^{-\frac{E_I}{k_B T}}}$$
(2.28)

In this way, we obtain the Raman scattering cross section, which is independent on the molecular states involved in the process:

$$\frac{\partial^2 \sigma}{\partial \Omega \partial E'} = kk'^3 \sum_A P(A) \sum_B \left| \boldsymbol{\varepsilon}_{\mathbf{k}',\lambda'} \cdot \mathbf{P}_{BA} \cdot \boldsymbol{\varepsilon}_{\mathbf{k},\lambda} \right|^2 \delta(E_A - E_B - \hbar \Delta \omega) \tag{2.29}$$

Notice in expression (2.29) the dependence on the forth power of the radiation frequency  $(k \simeq k')$  and  $\nu \propto k$  and on the system polarizability,  $\mathbf{P}_{BA}$ , also depending on light polarization. As this effect is a second order process, it will be obscured by the possible first order resonant processes, such as rotovibrational transitions (energies comparable with IR photons) or electronic transitions (typical energies comparable to UV photons). Taking these aspects into account, the more useful spectral region to perform Raman spectroscopy is the visible-near infrared range. Resonant Raman occurs when the denominator in expression (2.23) is close to zero: from a physical point of view, this means that the initial transition in the Raman process does not target a virtual state but an electronic excited state in the system. The theoretical description of this effect is rather complex, and will therefore be omitted here [Lon2002]. Similarly, if the exciting photon has an energy sufficient to induce an electronic transition in the system, a fluorescent disexcitation process can take place. This involves a non radiative transition to the ground vibrational level in the excited electronic state, which is followed by the relaxation to the fundamental electronic level with the emission of a photon. Fluorescence processes give rise to broad and intense spectral features superimposed to the Stokes region of the Raman spectrum.

We have discussed above the advantages of Raman spectroscopy, which presents as an ideal technique for studying biomolecules and investigating biosystems.

Unfortunately, the drawback of the intrinsically low signal intensity prevents the application of this technique in several real scientific problems. One important example is the case of biosensing, that is revealing the presence of specific biomolecules at low concentration in a solution or a mixture. The detection limit, that is the concentration threshold necessary to trace the presence of a molecule, depends on molecular weight and Raman activity, but is typically restricted to the micromolar range of concentration, far beyond the biologically relevant thresholds.

Moreover, in the study of biosystems a nanometric spatial resolution is desirable for probing specific processes occurring in precise locations, for example in a particular region of a cell or on its membrane. For this reason, the micrometric spatial resolution achievable in conventional Raman spectroscopy and imaging is not sufficient.

This limitation can be substantially overcome with Surface Enhanced Raman Scattering, which exploits plasmonic excitations for the nanoscale confinement of strong electromagnetic fields close to the surface of metallic nanostructures. On one hand, this enhances the intensity of both the incident and scattered fields, resulting in a remarkable increase of the Raman signal from molecules located close to the metal. On the other hand, as signal enhancement depends on the local fields (nanometer-close to the surface) the use of SERS necessarily boosts the spatial resolution of the spectroscopic investigation to the nanoscale.

Another indirect advantage of employing plasmonic nanostructures for molecular spectroscopy is the effect of fluorescence quenching, typically occurring to molecules due to their proximity to the metal surface [Kne2007]. Moreover, the intense surface enhanced Raman signal can easily overstep the fluorescent background typical of many biological environments.

## 2.2 Surface Enhanced Raman Scattering

The phenomenon of Surface Enhanced Raman Scattering (SERS) consists of a strong increment of Raman intensity from a molecule located close to a nano-curved metallic surface. This enhancement of the spectroscopic signal can reach 8-9 orders of magnitude per single molecule [Sti2008]. Since its first observation in 1974 [Fle1974], different possible explanations for SERS effect have been proposed, some of them focusing on the metallic nature of the substrate, some on the surface chemistry of the system [Jen2008]. Nowadays SERS enhancement is usually ascribed to two main mechanisms [Kne2006, Sti2008].

The first is the electromagnetic mechanism: this is related to the presence of the metal surface. When electromagnetic radiation, tipically in the ultraviolet-visible or near infrared spectral ranges, illuminates a metallic nanostructure, the collective oscillation of free electrons in the metal can be excited. This excitation, called surface plasmon, causes the localization of strong electromagnetic fields at the metal surface, impinging the molecules and thus incrementing their Raman signal. As Raman

scattering is proportional to the square of the induced dipole moment, which is in turn proportional to the magnitude of the incident electromagnetic field E, a g factor of 10 in the amplification of the local field intensity can reflect as  $g^4 = 10^4$  on the spectroscopic signal enhancement. This is the reason of the quantitative importance of electromagnetic SERS mechanism.

The second enhancement mechanism is the chemical effect, which deals with the changes in the polarizability of the molecule due to its proximity to the metal and to the possibility of chemical binding. This second effect is less important from a quantitative point of view, as it tipically contributes to the enhancement of intensity up to two orders of magnitude [Sti2008]. Nevertheless, the chance of exploiting the molecular hybridization with the substrate can lead to interesting applications. Among these, it is worth mentioning SERS from non-metallic substrates, semiconductors in particular [Wan2012], and the recently reported Photoinduced Enhanced Raman Spectroscopy (PIERS) [BP2016] (see Sect. 2.3.3).

A very important parameter to be introduced when dealing with SERS is the enhancement factor (EF), which can give a quantification of SERS efficiency in incrementing the spectroscopic signal of a given molecule. Enhancement factors can be differently calculed (for comprehensive discussion on the subject, see Ref. [Le 2007]), but we are here adopting the most common and straightforward definition, which is the following:

$$EF = \frac{I_{SERS}}{I_{Raman}} \frac{N_{Raman}}{N_{SERS}}$$
 (2.30)

that is, the ratio between SERS and Raman intensity per single molecule.

Since its discovery, the field of SERS has experienced dramatic growth, demonstrating its power as an analytical tool for the sensitive and selective detection of molecules adsorbed on noble metal nanostructures [Sti2008, Das2012]. Other interesting applications involve the possibility of spectroscopically tracing functionalized metal nanoparticles in their interaction with biosystems and cells [Hu2007, Son2012].

## 2.2.1 Electromagnetic Mechanism

Noble metal nanostructures have gained much attention in the last decades, thanks to their peculiar optoelectronic properties [KV1995]. In particular, the collective oscillation of free electrons in the metallic nanostructure can be excited using UV-visible or near infrared light. This excitation is referred to as surface plasmon resonance, and it strongly depends on the material, size and shape of the nanostructure sustaining it.

The plasmonic nature of metallic nanoparticles results in intense absorption and scattering of light. Moreover, the coupling between electromagnetic radiation and surface plasmons can give rise to a strong amplification of the optical fields close

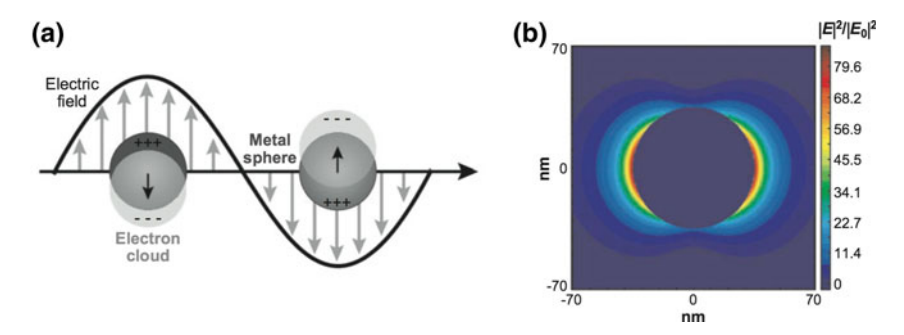


**Fig. 2.2** a Illustration of the localized surface plasmon resonance effect. **b** Extinction efficiency (ratio of cross section to effective area) of a spherical silver nanoparticle of 35 nm radius in vacuum  $|E|^2$  contours for a wavelength corresponding to the plasmon extinction maximum. Peak  $|E|^2 = 85$ . Reproduced with permission from Ref. [Sti2008]

to the metal surface. These enhanced fields are responsible for the remarkable enhancement of Raman signal of molecules located in close proximity of the metal surface (see Fig. 2.2).

As nanoparticle sizes are typically much smaller than the wavelength of light in UV-visible spectral ranges, localized surface plasmons can lead to the three dimensional confinement of light in sub-wavelength volumes. This property is originated from the coupling of photons with the electronic excitations inside the nanostructures.

Surface plasmons eigenmodes are solutions of Helmholtz equation:

$$\nabla \times \nabla \times \mathbf{E}(\mathbf{r}, \omega) - \frac{\omega^2}{c^2} \, \varepsilon(\mathbf{r}, \omega) \, \mathbf{E}(\mathbf{r}, \omega) = 0$$
 (2.31)

given the proper boundary conditions [NH2012].

If we assume that the size of the nanoparticles sustaining the plasmonic excitation is smaller than the metal's skin depth d, with  $d=\lambda/(4\pi\sqrt{\varepsilon})$ , we can use the quasi-static approximation. This means that we can neglect retardation effects by assuming that all the points of the nanoparticle will respond simultaneously to the perturbation of the external field. The whole free electron gas will therefore be periodically displaced, with the same phase, with respect to the stationary crystal lattice of the particle, as represented in Fig. 2.2a.

In the quasi-static approximation, Helmholtz equation (2.31) takes the simpler form of Laplace equation. Its solutions are quasi-static near fields: for example, the electric field of an oscillating dipole  $\mathbf{p}$ 

$$\mathbf{E}\left(r\mathbf{n},t\right) = \frac{1}{4\pi\varepsilon_{0}} \left\{ k^{2} \left(\mathbf{n} \times \mathbf{p}\right) \times \mathbf{n} \frac{e^{ikr}}{r} + \left[ 3\mathbf{n}(\mathbf{n} \cdot \mathbf{p}) - \mathbf{p} \right] \left( \frac{1}{r^{3}} - \frac{ik}{r} \right) e^{ikr} \right\} e^{i\omega t}$$
(2.32)

reduces in the near-field zone  $kr \ll 1$  to the following:

$$\mathbf{E}(r\mathbf{n},t) = \frac{1}{4\pi\varepsilon_0} \left[ 3\mathbf{n}(\mathbf{n} \cdot \mathbf{p}) - \mathbf{p} \right] \frac{e^{i\omega t}}{r^3}$$
 (2.33)

This is the electrostatic field of a static point dipole, oscillating in time with harmonic dependence  $e^{i\omega t}$ . In the quasi-static limit, the electric field can be represented by  $\mathbf{E} = -\nabla \Phi$  with the potential  $\Phi$  satisfying Laplace equation

$$\nabla^2 \Phi = 0 \tag{2.34}$$

and the boundary conditions between the metal and the dielectric material surrounding the nanoparticle. This expressions are general and can be solved for different geometries of the system: here we will focus on the simple case of a spherical nanoparticle, also considering that spherical nanocolloids are the building block of our SERS active substrates, as will be discussed in the next chapters.

#### **Single Spherical Nanoparticle Plasmonics**

Let us consider a single spherical nanoparticle of radius a, small enough to assume the quasi-static approximation. Let  $\varepsilon_1(\omega)$  be the complex dielectric constant of the metal and  $\varepsilon_2$  the dielectric constant of the medium surrounding the nanoparticle, assumed to be real and independent on the radiation frequency. Given the symmetry of the system, it is convenient to express Laplace equation 2.34 in spherical coordinates  $(r, \theta, \varphi)$ :

$$\frac{1}{r^2 \sin \theta} \left[ \sin \theta \frac{\partial}{\partial r} \left( r^2 \frac{\partial}{\partial r} \right) + \frac{\partial}{\partial \theta} \left( \sin \theta \frac{\partial}{\partial \theta} \right) + \frac{1}{\sin \theta} \frac{\partial^2}{\partial \varphi^2} \right] \Phi(r, \theta, \varphi) = 0$$
(2.35)

The solutions have the form

$$\Phi(r,\theta,\varphi) = \sum_{l,m} b_{l,m} \Phi_{l,m}(r,\theta,\varphi)$$
 (2.36)

where  $b_{l,m}$  are constant coefficients, to be determined from the boundary conditions, and the functions  $\Phi_{l,m}$  are linear combination of the Legendre functions  $P_l^m \in Q_l^m$ :

$$\Phi_{l,m} = \begin{Bmatrix} r^l \\ r^{-l-1} \end{Bmatrix} \begin{Bmatrix} P_l^m(\cos \theta) \\ Q_l^m(\cos \theta) \end{Bmatrix} \begin{Bmatrix} e^{im\varphi} \\ e^{-im\varphi} \end{Bmatrix}$$
 (2.37)

Boundary conditions imply the continuity of the tangential electric fields and of the normal components of the electric displacements  $\mathbf{D} = \varepsilon_j \mathbf{E}$  at the nanoparticle surface.

Therefore:

$$\begin{bmatrix} \frac{\partial \Phi_1}{\partial \theta} \end{bmatrix}_{r=a} = \begin{bmatrix} \frac{\partial \Phi_2}{\partial \theta} \end{bmatrix}_{r=a}$$

$$\varepsilon_1 \begin{bmatrix} \frac{\partial \Phi_1}{\partial r} \end{bmatrix}_{r=a} = \varepsilon_2 \begin{bmatrix} \frac{\partial \Phi_2}{\partial r} \end{bmatrix}_{r=a}$$
(2.38)

where  $\Phi_1$  is the electric potential inside the sphere,  $\Phi_2 = \Phi_0 + \Phi_{scatter}$  is the external potential, consisting of the potential of the incident and of the scattered fields. Assuming the incident electric field to be an *x*-polarized plane wave, we have  $\Phi_0 = -E_0 x = -E_0 r P_1^0(\cos \theta)$ . From the boundary conditions (2.38) we have:

$$\Phi_{1} = -E_{0} \frac{3\varepsilon_{2}}{\varepsilon_{1} + 2\varepsilon_{2}} r \cos \theta$$

$$\Phi_{2} = -E_{0} r \cos \theta + E_{0} \frac{\varepsilon_{1} - \varepsilon_{2}}{\varepsilon_{1} + 2\varepsilon_{2}} a^{3} \frac{\cos \theta}{r^{2}}$$
(2.39)

Solutions for  $\Phi_1$ ,  $\Phi_2$  are independent of the azimuthal angle  $\varphi$  because of the symmetry implied by the choice of the incident field.

Finally, we can calculate the expression for the electric field from  ${\bf E}=-\nabla\Phi$  and we obtain

$$\mathbf{E}_{1} = E_{0} \frac{3\varepsilon_{2}}{\varepsilon_{1} + 2\varepsilon_{2}} (\cos \theta \mathbf{n}_{r} - \sin \theta \mathbf{n}_{\theta}) = E_{0} \frac{3\varepsilon_{2}}{\varepsilon_{1} + 2\varepsilon_{2}} \mathbf{n}_{x}$$
(2.40)

$$\mathbf{E}_{2} = E_{0}(\cos\theta\mathbf{n}_{r} - \sin\theta\mathbf{n}_{\theta}) + \frac{\varepsilon_{1} - \varepsilon_{2}}{\varepsilon_{1} + 2\varepsilon_{2}} \frac{a^{3}}{r^{3}} E_{0} (2\cos\theta\mathbf{n}_{r} + \sin\theta\mathbf{n}_{\theta}) (2.41)$$

We notice that the electric field inside the nanoparticle (2.40) is homogeneous and non-zero. This is unexpected for a conductor but, as said before, we are considering a nanoparticle with a size smaller than the metal's skin depth for the given wavelength.

Another interesting feature of the solutions is that the scattered field (second term in Eq. (2.41)) has the form of an electrostatic field generated by a dipole  $\mathbf{p}$ , located at the center of the sphere. This dipole is induced by the external field  $\mathbf{E}_0$  and has the value

$$\mathbf{p} = \varepsilon_2 \,\alpha(\omega) \mathbf{E}_0 \tag{2.42}$$

being  $\alpha$  the polarizability of the nanoparticle:

$$\alpha(\omega) = 4\pi\varepsilon_0 a^3 \frac{\varepsilon_1(\omega) - \varepsilon_2}{\varepsilon_1(\omega) + 2\varepsilon_2}$$
 (2.43)

where  $\varepsilon_1(\omega)$  and  $\varepsilon_1'(\omega)$  are the real and imaginary part of the metal dielectric constant, while we assumed the dielectric constant of the surrounding medium  $\varepsilon_2$  to be real and independent from the frequency.

Notice that the polarizability diverges when the real part of the dielectric constant of the metal  $\varepsilon_1'$  equals  $-2\varepsilon_2$  and its imaginary part  $\varepsilon_1''$  is negligible. For noble metals like gold and silver, this condition is satisfied in the near ultraviolet and visible spectral ranges.

The scattering cross section for a small sphere can be easily derived by the ratio between the power radiated by the dipole

$$\overline{P} = \frac{|\mathbf{p}|^2}{4\pi\varepsilon_0\varepsilon_2} \frac{n_2^3\omega^4}{3c^3} \tag{2.44}$$

and the incident plane wave intensity  $|E_0|^2$ :

$$\sigma_{scatt} = \frac{k^4}{6\pi\varepsilon_0^2} |\alpha(\omega)|^2 \tag{2.45}$$

being  $k = \frac{\omega n_2}{c}$  the wavevector in the surrounding medium [NH2012].

Figure 2.3 shows the normalized resonance of the scattering cross section for a single nanosphere made of gold or silver and surrounded by different dielectrics. The resonance is redshifted with increasing the dielectric constant of the medium surrounding the nanosphere.

Beside the electromagnetic scattering, another important effect to consider, when dealing with electromagnetic radiation impinging on a metallic nanoparticle, is absorption. The power dissipated by the nanoparticle can be calculated using Poynting theorem, considering the nanosphere as a point dipole **p** 

$$P_{abs} = \left(\frac{\omega}{2}\right) Im \left[\mathbf{p} \cdot \mathbf{E}_0^*\right] \tag{2.46}$$

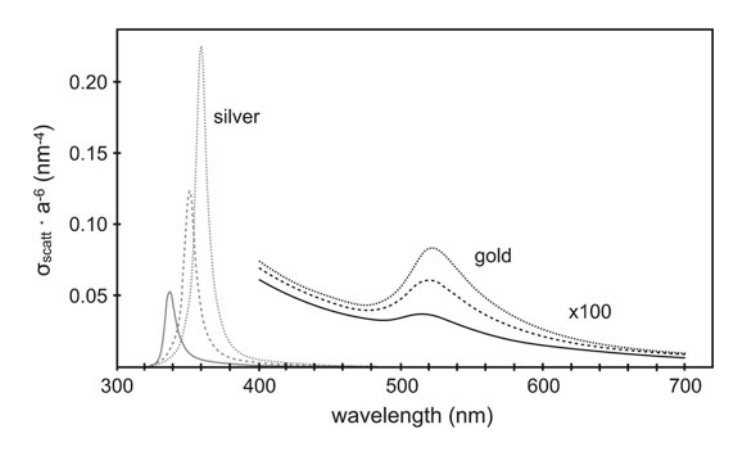


**Fig. 2.3** Scattering cross section, normalized to  $a^6$  (therefore hiding the dependence on the Np radius), for gold or silver Nps surrounded by different dielectric media. Solid line: vacuum (n = 1); dashed line: water (n = 1.33); dotted line: glass (n = 1.5). Data from reference [NH2012]

Using the expression  $\mathbf{p} = \varepsilon_2 \alpha \mathbf{E}_0$ , having assumed  $\varepsilon_2$  as real and constant, we obtain the absorption cross section

$$\sigma_{abs} = \frac{k}{\varepsilon_0} Im[\alpha(\omega)] \tag{2.47}$$

The absorption cross section scales as  $a^3$ , while the scattering cross section is proportional to  $a^6$ : for this reason, for small nanoparticle sizes absorption will be the dominant phenomenon.

In the quasi-static approximation we are neglecting the generation, by the exciting fields, of electric multipolar modes. These are non radiative excitations which do not contribute to the scattering: therefore, they do not contribute to the local field enhancement which is crucial for SERS. For nanoparticle sizes much smaller than the wavelength of the incident light, these effects can indeed be neglected with respect to the plasmonic dipole, and the argument here exposed is correct. In the case of more complex nanostructures, we cannot assume that all the points of the nanostructure will respond simultaneously to the external perturbation: retardation effects have to be considered and therefore multipolar modes need to be accounted for.

In summary, in order to optimize the SERS activity of our system, the size of the metallic features has to be carefully considered. Indeed, it has to be small enough with respect to the wavelength of the exciting light, in order to avoid the excitation of multipolar plasmonic modes. On the other hand, the metallic nanostructured features need to be big enough for the scattering contribution to dominate on the absorption phenomena.

# **Interparticle Coupling Effects**

We have seen that the illumination of metal nanoparticles with electromagnetic UV-visible radiation can excite localized plasmons inside the metal. From an experimental point of view, there is a limited interest in the study of the behavior of single non interacting, isolated nanoparticles, as real devices often imply the use of nanoparticle assemblies, such as ordered or disordered nanostructure arrays, or nanoparticle aggregates [Fas2014]. As previously discussed, if we consider particles with a diameter d much smaller than the wavelength  $\lambda$  of the exciting light ( $d \ll \lambda$ ), each excited nanoparticle will act as an electric dipole. For this reason, in these kind of systems two types of electromagnetic interactions between particles can be distinguished: near-field and far-field coupling [Mai2002, PS2008].

For very short interparticle spacing  $\Lambda$ , as in the case of nearly touching nanoparticles ( $\Lambda \sim d$ ), the near-field coupling is the most relevant effect [HS2004, Zhu2004]. In this case, the interaction of the nanostructures is driven by the electrostatic field. The single nanoparticle plasmon resonance is modified by the near-field interaction and typically broadened and redshifted [PS2008].

For particle spacings  $\Lambda \gg d$ ,  $\Lambda \sim \lambda$ , far-field dipolar interactions are dominant. In this kind of interparticle couplings, interference effects can modify the plasmon

resonance profile of each nanostructure. These collective resonances can be excited by illuminating the nanoparticle assembly with a broad beam of light [Lin2001].

While single, non interacting nanoparticles contribute almost linearly to SERS signal, both near- and far-field interparticle coupling effects can interestingly modify the local field distribution leading to higher signal enhancement [Zhu2004]. An important example is the case of SERS from colloidal systems: in nanoparticle based substrates, indeed, the strong enhancement of near-fields at the interstices between closely packed nanoparticles, called "hot-spots", are the main responsible of the increment of the spectroscopic signal [Li2003, Gun2001, Ale2009]. Therefore, nanoparticle aggregation is often induced to grant a high performance of the substrate by multiplying the number of hot-spots in the structure [Fas2014]. One- or two-dimensional arrays of far-field coupled metal nanoparticles can also give rise to high enhancements of SERS signal [Yan2009] and show other interesting features, connected with their regular geometry [Dom2016].

**Near field coupling** When nanoparticles are brought close enough to each other, an efficient near-field interaction is expected. Its effect will be a modification of the plasmon resonance of the system, as the electrostatic interaction between the nanostructures will determine a collective response to an external exciting field.

The simplest system that can be studied in this framework is a dimer of metallic nanoparticles. Pioneering works have demonstrated a strong anisotropy in the scattering spectra of nanoparticle dimers illuminated with differently polarized light [Tam2002] and a strong dependence of the effect on the interparticle distance [Rec2003]. As will be illustrated in the next Sect. 4.3, the recent advances in fabrication technologies have allowed to gain excellent control on the nanoscaled features of noble metal nanostructures [Di 1997, CK2012]. This enables a thorough investigation of the near-field coupling effect in simple systems as the pairs of identical nanoparticles designed by Rechberger and coworkers [Rec2003].

In their experimental work, they studied the influence of the interparticle distance on the plasmonic behavior of dimers illuminated by light polarized parallel (panel a of Fig. 2.4) or orthogonal (panel b) to the interparticle axis. In the case of polarization parallel to the dimer axis, as the center-to-center distance diminished, the plasmon resonance of the nanoparticles broadened and shifted towards lower frequencies. The same occurred for polarization orthogonal to the interparticle axis, but in this case the plasmon resonance was blueshifted at decreasing the interparticle distance. This anisotropic electromagnetic response was found to be more pronounced as the nanoparticles were brought closer to each other.

A simple qualitative explanation of the result is possible within a dipole-dipole interaction model, as it is sketched in the right panels of Fig. 2.4. Electromagnetic radiation, resonant with the plasmonic excitation in a single nanoparticle, causes the displacement of the electron cloud and localizes surface charges which will feel electrostatic repulsion (panel c). When a second nanoparticle is placed nearby, the polarization causes the arising of additional forces acting on both of the particles.

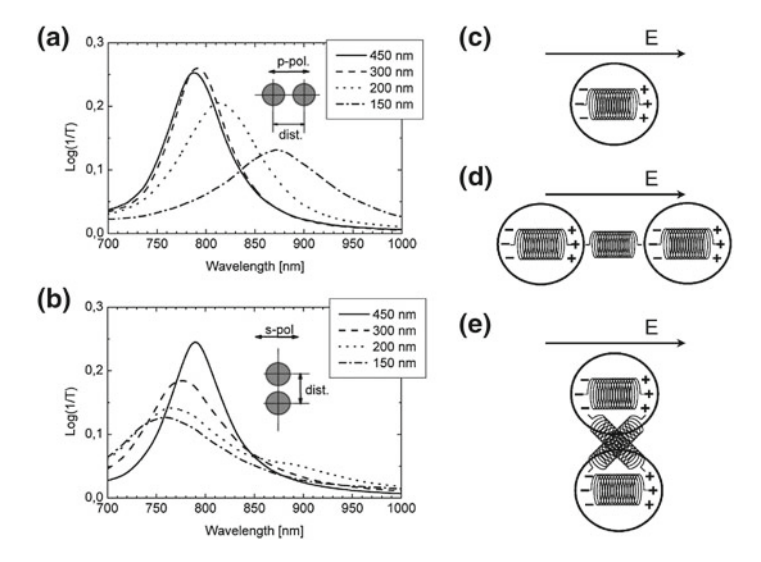
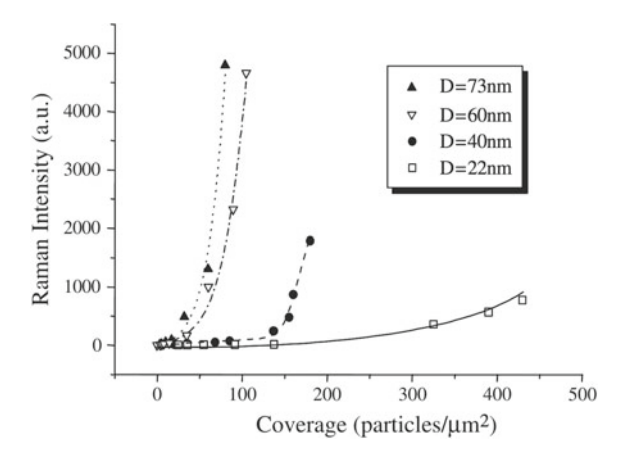


Fig. 2.4 Effect of near field coupling on dimers of cylindrical nanoparticles (150 nm diameter, 17 nm height). Left panels: extinction (=  $\log(1/\text{transmission})$ ) spectra of an array of Au nanoparticle pairs with the interparticle center-to-center distances as the parameter. The polarization direction of the exciting light is **a** parallel to interparticle axis and **b** orthogonal to it. Right panels: sketch to illustrate the electromagnetic interaction between closely spaced nanoparticles, **c** an isolated particle, **d** a dimer with the polarization of the exciting field parallel to the interparticle axis and **e** orthogonal to it. Adapted with permission from Ref. [Rec2003]

Different configurations are possible: if the field is parallel to the interparticle axis, charges of opposite sign will face on the sides of the two nanoparticles (panel d), and will weaken the repulsive forces acting on the free charges. This will lead to a lower resonance frequency (panel a). In the other case, when the field is normal to the dimer axis, the charge distribution of both the particles will increase the repulsive forces on the charges, leading to a blueshift of the plasmon resonance (panel b).

Probably the most striking characteristic of metallic nanoparticles is their capability of confining electromagnetic fields far beyond the diffraction limit, because of their coupling with electronic excitations inside matter. This effect becomes even more pronounced in near-field coupled nanostructure assemblies, as the fields can be here shrinked in very small volumes, in correspondence of the hot-spots between close-packed nanoparticles. This paves the way for interesting applications. Experimental studies on chains of near-field coupled metallic nanoparticles, for example, revealed their collective electromagnetic behavior, demonstrating their potential in acting as linear waveguides for electromagnetic radiation below the diffraction limit [Kre1999, Mai2002].

Fig. 2.5 Raman intensity versus nanoparticle coverage for different diameters D of the gold nanoparticles. The relative standard deviation of each datapoint was found within 101%. Reproduced with permission from Ref. [Zhu2004]

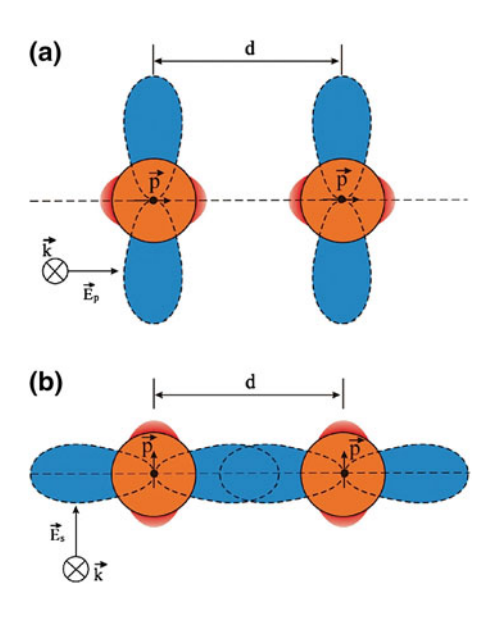


Hot-spots between shortly spaced nanoparticles are of enormous importance also in SERS, because the local field enhancement is much more pronounced in these zones [Eno2004, HS2004]. Early experimental works studied the SERS response of substrates made of gold nanoparticles, functionalized with the test molecule 4-aminothiophenol and differently assembled on glass substrates [Zhu2004]. Zhu and coworkers demonstrated that, as shown in Fig. 2.5, at low coverage of nanoparticles on the glass surface, the spectroscopic intensity was proportional to the density of nanoparticles on the substrate, being the total spectrum the sum of the contribution of isolated nanoparticles, thus suggesting a negligible interparticle coupling. A sharp nonlinear increase of SERS intensity was revealed at high surface coverages, witnessing the pivotal role of interparticle coupling when the nanoparticles were positioned close enough to each other.

The spectroscopic signal coming from molecules located inside the hot-spots is remarkably incremented with respect to the contribution of molecules located on other parts of the metal surface [JH2004, Fan2008]. Trapping molecules between aggregated nanostructures is indeed the strategy that led to the observation of single-molecule SERS [Kne1997, Xu1999]. For this reason, in order to obtain high signal enhancements, the formation of hot-spots on SERS substrates is pursued using different approaches [Kle2013], either by inducing nanoparticle aggregation [Fas2014, Pic2014] or by fabricating refined nanostructures designed to contain hot-spots [Jeo2016], such as self-similar chains of nanoparticles [Li2003, Col2015] or gold nanostars [Ind2014, Chi2014].

Far field coupling: plasmonic gratings When metal nanoparticles are organized in arrays with rather long periodicity ( $\Lambda \gg d$ , where d is the size of the nanoparticle), there is the possibility that each particle plasmon resonance couples with the other particles' via far field radiative dipole coupling. In these "plasmonic gratings", the coupling can lead to shifts in the plasmon energies [Lin2001, PS2008] and changes in Raman intensities [Chu2011]. These effects are particularly interesting when

Fig. 2.6 Radiative coupling between the particles in a chain. The applied electric field is polarized perpendicular to the axis of the chain. Blue petals are dipole-like radiative electric field. Red caps close to the surface of the particles are the near-field. In panel a, polarization of the applied electric field parallel to the axis of the chain leads to a weak radiative coupling between the particles in the chain. In panel b, polarization of the applied electric field perpendicular to the axis of the chain leads to a strong radiative coupling between the particles in the chain. Reproduced with permission from Ref. [PS2008]



considering nanoparticles disposed in arrays with interparticle distances close to the wavelength of the plasmon resonance.

Probably the first experimental work highlighting the importance of radiative dipole coupling in metal nanoparticle one- or two-dimensional arrays, at least in the visible spectral range, is the paper by Schatz and coworkers [Hay2003]. They presented evidences of a blueshift of the plasmon resonance peak occurring upon decreasing the pitch  $\Lambda$  of the array. Computational investigations showed that the effect was caused by radiative dipolar coupling between the nanoparticles. Further theoretical work on these systems demonstrated that the design of arrays with  $\Lambda \sim \lambda$ , close to the plasmon resonance wavelength, could optimize the coupling because of the hybridization of the local plasmonic excitation with the photonic modes of the array [ZS2005, Kne2006, PS2008].

The polarization of the exciting field plays an important role in the diffractive coupling of nanostructure arrays [PS2008, Vec2009]. Indeed, as as illustrated in Fig. 2.6, the emission of the nanoparticles, acting as dipolar antennas, is maximum in the direction normal to the dipole. For this reason, if we consider the model system of a one-dimensional chain of regularly spaced nanoparticles, the configuration that enhances the radiative coupling in the chain is the illumination with an electromagnetic wave propagating with both wavevector and electric field orthogonal to the chain (panel b of Fig. 2.6). It is interesting to notice that the near field coupling would be optimized instead with the electric field parallel to the chain, which would induce an electric charge displacement along the interparticle axis (panel a).

# SERS $E^4$ Dependence on the Local Field Enhancement

When a molecule is located close to a polarizable system, as for example a metallic nanoparticle, the electromagnetic interaction between these objects will affect the Raman scattering of the molecule [Jen2008]. If the polarizability of molecule and nanoparticle are respectively  $\alpha_{mol}$  and  $\alpha_{np}$ , the total polarizability of the system can be derived by Silberstein's equations [Sil1917, Jen2002].

$$\alpha_{\parallel} = \frac{\alpha_{mol} + \alpha_{np} + 4\alpha_{mol}\alpha_{np}/R^3}{1 - 4\alpha_{mol}\alpha_{np}/R^6}$$
(2.48)

$$\alpha_{\perp} = \frac{\alpha_{mol} + \alpha_{np} - 2\alpha_{mol}\alpha_{np}/R^3}{1 - \alpha_{mol}\alpha_{np}/R^6}$$
(2.49)

with R center-to-center distance between the molecule and the nanoparticle.  $\alpha_{\parallel}$  accounts for the case in which the external field is parallel to the axis between the molecule and the nanoparticle,  $\alpha_{\perp}$  for the field polarized perpendicularly to it.

As already mentioned, the Raman scattering intensity depends on the derivative of polarizability

$$I_R \propto \left| \frac{\partial \alpha}{\partial Q_{mol}} \right|^2 \tag{2.50}$$

where  $Q_{mol}$  are the normal vibrational modes of the molecule. We can reasonably assume that the nanoparticle polarizability is unaffected by the molecular normal modes. We have indeed  $\alpha_{np} \gg \alpha_{mol}$ . Hence we derive:

$$\frac{\partial \alpha_{\parallel}}{\partial Q_{mol}} = \frac{\alpha'_{mol} + 4\alpha_{np}\alpha'_{mol}/R^3}{1 - 4\alpha_{np}\alpha_{mol}/R^6} - \frac{\alpha_{mol} + \alpha_{np} + 4\alpha_{np}\alpha_{mol}/R^3}{(1 - 4\alpha_{np}\alpha_{mol}/R^6)^2} (-4\alpha_{np}\alpha'_{mol}/R^6)$$
(2.51)

$$\frac{\partial \alpha_{\perp}}{\partial Q_{mol}} = \frac{\alpha'_{mol} - 2\alpha_{np}\alpha'_{mol}/R^3}{1 - \alpha_{np}\alpha_{mol}/R^6} - \frac{\alpha_{mol} + \alpha_{np} - 2\alpha_{np}\alpha_{mol}/R^3}{(1 - \alpha_{np}\alpha_{mol}/R^6)^2} (-\alpha_{np}\alpha'_{mol}/R^6)$$
(2.52)

where  $\alpha'_{mol} = \frac{\partial \alpha_{mol}}{\partial Q_{mol}}$ . Simplyfing the expressions above, we have

$$\frac{\partial \alpha_{\parallel}}{\partial Q_{mol}} = \frac{\alpha'_{mol} (1 + 2\alpha_{np}/R^3)^2}{(1 - 4\alpha_{np}\alpha_{mol}/R^6)^2}$$
(2.53)

$$\frac{\partial \alpha_{\perp}}{\partial Q_{mol}} = \frac{\alpha'_{mol} (1 - \alpha_{np}/R^3)^2}{(1 - \alpha_{np}\alpha_{mol}/R^6)^2}$$
(2.54)

Raman intensities result then proportional to the square modulus of these expressions:

$$I_{R\parallel} \propto \left| \frac{\partial \alpha_{\parallel}}{\partial Q_{mol}} \right|^2 = \left( \frac{\partial \alpha_{mol}}{\partial Q_{mol}} \right)^2 \times \frac{(1 + 2\alpha_{np}/R^3)^4}{(1 - 4\alpha_{np}\alpha_{mol}/R^6)^4}$$
(2.55)

$$I_{R\perp} \propto \left| \frac{\partial \alpha_{\perp}}{\partial Q_{mol}} \right|^2 = \left( \frac{\partial \alpha_{mol}}{\partial Q_{mol}} \right)^2 \times \frac{(1 - \alpha_{np}/R^3)^4}{(1 - \alpha_{np}\alpha_{mol}/R^6)^4}$$
 (2.56)

The denominators in Eqs. (2.55), (2.56) are close to 1, given that  $\alpha_{mol} \ll \alpha_{np}$ . We can therefore derive the local field enhancement:

$$E_{\parallel}^{loc} = g_{\parallel}(R)E_0 \qquad \qquad E_{\perp}^{loc} = g_{\perp}(R)E_0$$
 (2.57)

with

$$g_{\parallel} = 1 + \frac{2\alpha_{np}}{R^3}$$
  $g_{\perp} = 1 - \frac{\alpha_{np}}{R^3}$  (2.58)

and we have for the Raman intensity

$$I_{R\parallel} \propto I_R^{mol} |g_{\parallel}(R)|^4$$
  $I_{R\perp} \propto I_R^{mol} |g_{\perp}(R)|^4$  (2.59)

where we have defined  $I_R^{mol} = \left(\frac{\partial \alpha_{mol}}{\partial Q_{mol}}\right)^2$  as the Raman intensity of the isolated molecule. We have therefore demonstrated that the electromagnetic contribution to SERS signal is proportional to the fourth power of the local field enhancement induced by the proximity of the molecule to the polarizable nanoparticle. This is true in both of the considered configurations, although the constant factors in Eq. (2.58) lead to larger enhancements for fields parallel to the molecule-nanoparticle axis. This is a simple dipole coupling model which needs to be integrated with other more refined methods for a more realistic evaluation of the enhanced local fields around metallic nanostructures. Among these, the most common are discrete dipole approximation (DDA) or finite difference time domain (FDTD) methods.

#### 2.2.2 Chemical Mechanism

Ever since the discovery of SERS, a participated debate regarding the origin of this effect spread in the scientific community [Ott1984, Mos1985]. A thorough comprehension of the effect was reached several decades later but the "plasmonic view", relating SERS enhancement to the electromagnetic behavior of metal nanostructures, has generally been accepted from the beginning [Mos1985, Sch2006a].

However, several features of SERS spectra (e.g. the dissimilarity between surface enhanced and conventional Raman spectra in terms of band frequencies and relative intensities, the dependence of the SERS spectral shape on the metal substrate the polarizing voltage, etc.) could not be explained in the framework of electromagnetic

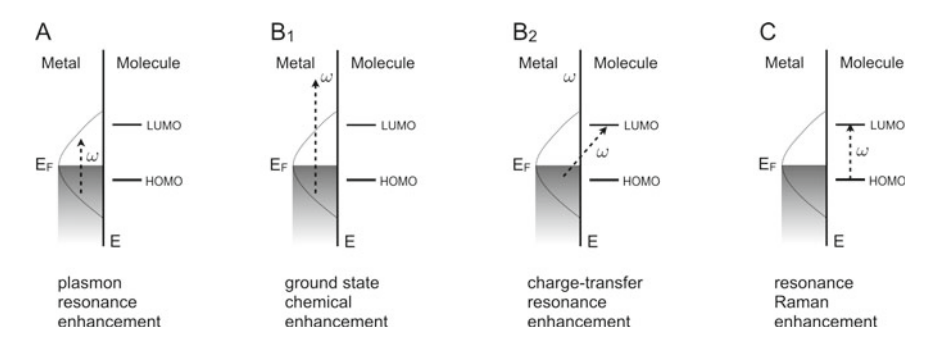


Fig. 2.7 Illustration of the different types of enhancement mechanism in SERS. A is the electromagnetic enhancement mechanism discussed in the previous Section;  $B_1$  and  $B_2$  are, respectively, the non-resonant and resonant charge transfer enhancement mechanisms, which depend on the interaction of molecule and metal; C is the molecular resonance chemical enhancement. Inspired by Ref. [Jen2008]

enhancement [Osa1994]. These experimental results thus suggested that a relevant role is played by chemical and electronic interactions between the molecule and the metallic substrate [Ott1984, Ott2005]. These aspects constitute what is called chemical enhancement.

In order to introduce chemical enhancement, we might first of all define as "chemical" effects all the phenomena contributing to the increment of SERS signal through the interaction of the molecule with the metal substrate. To simplify, the chemical mechanism of SERS includes all the not plasmon-related sources of enhancement. Chemical enhancement does not arise in the case of metal substrates only and is indeed considered the responsible for SERS signal from molecules located on semi-conductor nanostructures [Sun2007, Wan2012] or graphene [Lin2015].

Summarizing, we might state that, as illustrated in Fig. 2.7, in the molecule-metal system three sources of enhancement have to be considered:

- the **metal** nanostructure provides electromagnetic enhancement, as discussed in the previous Sect. 2.2.1 (see panel a in Fig. 2.7);
- the vibronic excitations in the **molecule** can also increment the spectroscopic signal (panel c): this is a resonant Raman process and is often reported as SERRS (Surface Enhanced Resonant Raman Scattering);
- the interaction between **metal and molecule** (panels B<sub>1</sub> and B<sub>2</sub>) can cause on one hand a change in the molecular polarizability, and on the other hand the arising of new metal-to-molecule or molecule-to-metal charge transfer resonances.

The last two aspects are usually grouped together as chemical effects.

**Molecular resonance enhancement** Regarding the resonant molecular contribution, it is worth remembering that large Raman cross sections do not necessarily imply large enhancement factors. The enhancement factor is defined as in Eq. (2.30)

and therefore, if we consider a single molecule,  $EF = I_{SERS}/I_{Raman}$ . As the resonant excitation affects the spectroscopic intensity in the case of both Raman and SERS, one might think that the mechanism depicted in Fig. 2.7c will not contribute to SERS enhancement factor. An important exception is the case of strongly fluorescent molecules: in this case, in the isolated molecule fluorescence process competes with resonant Raman and can prevent its observation [Le 2012]. When the molecule is proximal to a metal surface, fluorescence can undergo a quenching [Cha1974] and favor the Raman process, an effect that would strongly contribute to the molecular resonance chemical EF [Mos2013].

**Metal-molecule charge transfer effects** Different models are used to describe enhancement mechanisms based on the metal-molecule interaction. The discrimination between non-resonant or resonant effects is nowadays well accepted [Jen2008, Kne2016].

The "static charge transfer" mechanism points out the formation of a metal-ligand complex, which drives modifications of the molecular polarizability. These changes are therefore not connected with any resonant excitation in the system [Jen2008] but can cause the increment of the Raman cross section of the molecule [Kne2016].

The "resonant charge transfer" model involves the formation of new intermediate electronic levels in the ligand-metal complex [Lom1986]. This leads to the onset of new metal-to-molecule or molecule-to-metal charge transfer excitations, as it often happens in coordination complexes of transition metals [Ott1992, Mos2013]. As the Fermi level of metals lies between the energy of the highest occupied and the lowest unoccupied molecular orbitals (HOMO and LUMO), the formation of the ligand metal complex allows new transitions. Usually, the HOMO-LUMO transition corresponds to photon energies in the ultraviolet range, while these new transition channels are active at lower energies, and can be excited with visible photons. This phenomenon can take place upon interaction of the molecules with noble metals, but also with transition metals or semiconductors [Wan2012].

The last – and probably more discussed – phenomenon to account for is the "transient charge transfer" [Mos2013]. According to this model, Raman scattering occurs through temporary transfer of hot electrons or electron-hole pairs out of the metal on the adsorbed molecule [Ott1984]. These theories state that the excitation of plasmons in the metal nanostructure creates "ballistic" (hot) electrons [Mic1999] or electron-hole pairs [Pet1986] that, interacting with the adsorbate, eventually cause an increment of SERS signal due to the coupling of the molecular vibrations with the plasmonic transition dipole.

**Disentanglement of enhancement contributions** Theoretical approaches using electronic structure methods [Jen2008], among which time-dependent density functional theory (TDDFT), have been employed to study and interpret chemical effects. A quantitative prediction of chemical enhancement has not yet been achieved, also because of some limitations of the modelling [MJ2009, Moo2012], but a combined theoretical and experimental work can contribute to the comprehension of the observed spectral response [Val2013].

It is rather complex to disentangle the electromagnetic and chemical contributions to SERS enhancement in real problems. According to some descriptions of SERS effect, it is in facts impossible to separate the plasmon-, charge transfer- or resonance-based contribution to signal enhancement [LB2009]. In some cases, dedicated theoretical and experimental studies allowed to rule out some possibilities, or at least indicating the dominant enhancement mechanism [Osa1994, Bai2006, Val2013]. Among these works, it is worth mentioning the pioneering paper by Osawa and coworkers [Osa1994], who focused on the case of 4-aminothiophenol on silver, and pointed at the Herzberg-Teller contribution for an interpretation of charge-transfer processes.

A unified view of SERS Even though SERS enhancement mechanisms – and chemical effects in particular – are subject of extended debate, probably because of the common perception that the physics underlying SERS is not yet completely understood [Mos2013], much scientific work of the last decades has contributed to a unified description of SERS enhancement. Among these approaches, we recall the work of Lombardi and Birke [Lom1986], who derived a unified expression for the polarizability of the molecule-metal system, and hence an expression for SERS intensity, expanding the calculation of Albrecht [Alb1961] using the vibronic charge transfer coupling model, based on Herzberg-Teller theory [LB2008]. They considered the coupling between molecule and metal by including the filled and unfilled levels of the metal conduction band in the Herzberg Teller expansion [LB2009].

According to Lombardi and Birke, the polarizability of a molecule-metal system is a function of three terms, each of which is a sum over all the possible excitation-disexcitation transitions, and can be expressed as follows:

$$\alpha = A + B + C \tag{2.60}$$

where A depends upon the Franck-Condon integrals, which typically accounts for resonant Raman contribution, and vanishes far from resonance. Only totally symmetric Raman modes are allowed by this term. B and C represent Herzberg-Teller contributions and depend on molecule-to-metal and metal-to-molecule charge transfer transitions respectively. Herzberg-Teller coupling allows these charge transfer transitions at the expense of molecular ones. These terms also include transitions to both totally and non-totally symmetric vibrational modes. The resulting intensity can be enhanced by plasmon or charge-transfer resonances. The analytic expressions for these terms are rather complex, but are simplified when the excitation wavelength is in the region of charge transfer or molecular resonances (in addition to the plasmon resonance). The expression for one of the addend in the sum giving rise to B and C is

$$R_{IFK}(\omega) = \frac{\mu_{KI} \mu_{FK} h_{IF} \langle i | Q_k | f \rangle}{((\varepsilon_1(\omega) + 2\varepsilon_2)^2 + (\varepsilon_1')^2)(\omega_{FK}^2 - \omega^2 + \gamma_{FK}^2)(\omega_{IK}^2 - \omega^2 + \gamma_{IK}^2)}$$
(2.61)

where  $\mu_{IJ}$  is the electronic transition moment between the states I and J, h is the Herzberg Teller coupling constant. Here, I, F and K indicate the ground state, the charge transfer state and an excited molecular state for the hybrid moleculemetal system. At the denominator, the first term depicts the plasmon resonance when  $\varepsilon_1(\omega) = -2\varepsilon_2$  (this is the expression for a spherical metal nanoparticle, modifications are needed for more complex nanoarchitectures); the second term, which may be potential (Fermi energy) dependent, represents charge transfer resonance at  $\omega = \omega_{IK}$ . SERS intensity is proportional to the square of the polarizability and therefore, for a single term in (2.60), to  $|R_{IFK}(\omega)|^2$ .

In order to sort out the different contributions to the enhancement factor, the authors have defined an expression for the "degree of charge transfer" for vibrational mode [LB2009]. This approach leads to some interesting theoretical predictions in electrochemical SERS measurements at varying the metal potential and, therefore, its Fermi energy. Moreover, it can be generalized for non-plasmonic substrates, such as semiconductors [LB2014].

# 2.3 Current Trends in Surface Enhanced Raman Scattering

Ever since its discovery, SERS has represented an incredibly promising ultrasensitive spectroscopy. The applications of this technique are various, ranging from sensing and biosensing [Cia2014], to generic analytical analyses [Sch2014], without forgetting the possible implementation of traceable nanostructures to be exploited in biophysics and nanomedicine [Pet2003, Fas2016]. A detailed analysis of the state of the art on SERS and its applications would be a huge work and goes beyond the purpose of this thesis. For this reason, we will focus our review of the literature on the topics that are relevant for the discussion of the results reported in the next chapters.

First of all, for having SERS, a **metallic nanostructured substrate** is needed. In the last few decades, an enormous effort of the scientific community was devoted to the design and the implementation of rational plasmonic substrates [Fan2011]. These play a key role in SERS experiments, since the local field enhancement, and thus the system efficiency in the spectroscopic revelation of molecular species, basically depend on the nanoarchitecture. High SERS intensities are obtained from the structure's hot-spots, i.e. small volumes where the field is enormously incremented, as in the interstices between closely packed Nps [Mos2013].

Dlott and coworkers [Fan2008] have quantified the distribution of site **SERS enhancements** on a substrate made of silver Nps, demonstrating that the 24% of the signal measured in the overall experiment came from only 63 sites over one million. The field enhancement at these hot-spots critically depends on the interparticle distance, a quantity hardly controllable at the subnanometer scale. The crucial point is in general to find a good compromise between strong SERS enhancement and **signal reproducibility**. This can be pursued by specific statistical analysis, ensemble measurements on Np aggregates [Dom2016] or by using expressly designed measurement protocols [Str2007].

Since the SERS-active systems we have investigated are fabricated from colloidal dispersion of gold and silver nanoparticles, we will focus the discussion on the state of the art about nanoparticle-based SERS substrates [Fan2010, Fas2014]. This is presented in Sect. 2.3.1.

Highly efficient SERS substrates can be employed for **ultrasensitive molecular detection**. The first spectroscopic observations of single molecules were actually achieved with SERS [Kne1997, Xu1999], paving the way to what has now become a wide field of research. Ultrasensitive SERS is important for applications in sensing (e.g. for pollutants, explosives, drugs, etc.) and biosensing (e.g. for revealing proteins, genes, etc. which might be related to specific diseases) but also for studying the dynamical properties and the interaction with light of single molecules [BC2003, Ben2016].

SERS is a spectroscopic technique and, as conventional Raman spectroscopy, can provide information beyond the bare molecular identification, allowing to infere also structural information on the organization of analytes on the nanostructured metal substrate at varying environmental parameters [Lef1999, Cot2015]. The strong dependence of the signal enhancement on the molecular position with respect to the surface often prevents a straightforward analysis of the microscopic state of the system. For this reason, SERS experiments need to be carefully designed.

Nevertheless, they are ideal for studying specific biochemical or **biophysical processes**, as for example target-receptor biorecognition on cell membranes [Fas2016], or protein-DNA interaction [Kim2011, Li2014]. This is because of the intrinsic nanoscale nature of SERS effect, which involves near-field enhancement and charge transfer processes occurring few nanometers away from the metal surface and can therefore be used to probe physicochemical and biophysical phenomena taking place in the very same region, with an uncommonly high sensitivity [Kne2002].

This potentiality can also be exploited for inducing the **selective interaction** of properly functionalized SERS-active nanostructures with specific **cells or tissues** [QN2008]. SERS-active systems are often employed for the diagnosis and treatment of cancer. Their functionalization typically includes two types of molecules: one is a Raman label and the other is a biomolecule, able to interact with specific cellular receptors. The selective targeting of cancer cells can be used for cancer imaging [Sch2009] or for single cell diagnosis [Pal2015, Fas2016]. Moreover, therapeutic features can be added to these nanosystems [Sal2015]: for example, the biomolecules can be substituted with drugs [Fas2018], or the plasmon-enhanced absorption can be used for photothermal cancer therapy, i.e. illuminating the Nps inside the cells and killing them with the local temperature increase [Lu2010].

An emerging interest in SERS community involves the use of **non-metallic substrates**, such as semiconductor nanostructures [Wan2011] or graphene [Xu2012]. First observations of SERS effect from the surface of a GaP semiconductor nanoparticle are dated back to 1988 [Hay1988]. Since then, increasing interest has been shown in extending the range of materials available as substrates for surface-enhanced Raman scattering [Wan2012]. Being semiconductors plasmon-free, with the very

rare exception of heavily doped crystals [Bal2015], signal enhancement in these systems is mainly connected with resonant and non-resonant charge transfer processes [LB2014].

# 2.3.1 Nanoparticle-Based SERS Substrates

The arising interest in the field of surface enhanced spectroscopies is undoubtedly connected to some recently developed techniques that allow the manipulation of matter at the nanoscale. For example, nanoparticles of various shape, size and material can nowadays be fabricated and their organization on solid substrates can be achieved with a high degree of precision. In general, two different approaches can be employed for the preparation of metal nanostructures for plasmonic applications. They are generally described as "bottom-up" and "top-down" methods.

In the first case, wet chemistry approaches are employed to induce the reduction of Ag- or Au-containing ion complexes [LM1982] into colloidal form. The final product are Nps of spherical or more complex shape dispersed in a solvent, usually water. Recent preparation protocols allow a great control on their final size, shape and composition [Sch2011a, Sam2013, KV2008]. These Nps are usually stabilized in solution by an organic capping layer, providing a sufficient surface charge to prevent Np aggregation.

The second approach employs lithography techniques such as electron beam lithography (EBL), colloidal lithography, or ultraviolet photolithography to design a nanoscaled pattern inside which gold or silver are evaporated [Col2009, Hul1999]. In recent years, many different approaches in plasmonic substrate fabrication have shown competitive results in local field enhancement and SERS [De 2013, Jeo2016]: however, these novel techniques are often a rational combination of the two methods exposed above [Dom2016].

Colloidal metal Nps are probably the most common building block for efficient SERS substrates. Np aggregation is in particular crucial, as the small interstices between closely packed Nps, known as hot-spots, are responsible of most of the signal enhancement [Fan2008, TS2012]. Therefore, Np aggregation is often induced to grant a high performance of the plasmonic system by increasing the number of hot-spots in the structure [Paz2012, Sha2013]. Np aggregates are also characterized by broad surface plasmon resonances that usually result in a great versatility when used as plasmonic substrates [Gri1995, GP2007].

Electrodynamic calculations [ZS2005] and early experimental results [Yan2009] have shown a further enhancement in the plasmonic response of Nps when they are regularly disposed in one-dimensional or two-dimensional arrays. The further enhancement of the local field in specific sites of the array is related to the coupling of the Np-array photonic modes with the Np surface plasmon resonance [Gia2010, Aus2012].

**Np aggregation: why** The essential role of interparticle coupling in plasmonic has been discussed in the previous Section: one of the pioneering papers highlighting the role of interparticle coupling in SERS response of Np-based substrates is the one by

Zhu and coworkers [Zhu2004] (see also Fig. 2.5 and related comment). By studying substrates made of immobilized gold Nps on a silicon wafer, the authors demonstrated that Raman intensity (and, therefore, SERS enhancement factor) grows non-linearly at decreasing the average interparticle distance, hence suggesting that the maximum SERS intensity can be achieved in the limit of nearly touching nanoparticles. Indeed, single molecule SERS was first reported from molecules trapped in hot-spots in Np aggregates dispersed in solution [Kne1997].

To simplify, there are three main good reasons to induce Np aggregation:

- (1) **higher local field intensity**: as Nps are brought closer to each other, the increment of the local field with respect to the incident one typically scales by a factor 10 (or more) from a single Np to a Np dimer, the simplest Np aggregate achievable [HS2004]. As SERS approximately scales with the fourth power of the local field enhancement, this causes a significant gain in the spectroscopic intensity from molecules located inside interparticle hot-spots;
- (2) **increased hot-spot density**: as demonstrated by different works studying small Np aggregates, SERS enhancement factor grows linearly with the number of interparticle gaps in the cluster [Paz2012, Sha2013]. Therefore, strong enhancement factors can be reached by employing substrates made of Np clusters with high coordination number (i.e. number of aggregated particles in the structure) as illustrated in Fig. 2.8; (3) **broadband plasmon resonance**: the plasmon resonance profile depends on the size, shape and material of the Np considered. Typically, the surface plasmon resonance (SPR) peak for single Nps is in the blue-green region of the visible spectrum (with the exception of longitudinal modes in single nanorods which, however, show a strong polarization dependence). In order to avoid analyte damaging, longer excitation wavelengths for Raman experiments are usually preferred. Colloidal Np

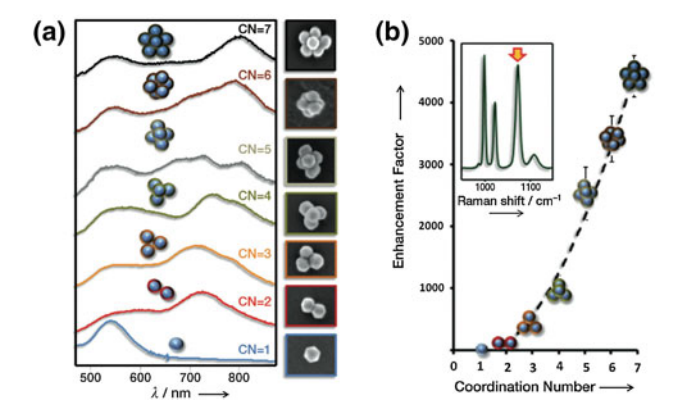


**Fig. 2.8** a Optical response of Np clusters (single Np diameter: 50 nm) with different coordination number, from 1 to 7. Darkfield scattering optical spectra measured on single Np aggregates are plotted next to their SEM images. **b** SERS enhancement factor versus coordination number. *EF* was estimated by functionalizing the clusters with benzenethiol and by measuring the intensity of the ring breathing band indicated by the arrow (inset). Adapted with permission from Ref. [Paz2012]

aggregation grants an overall homogeneous substrate for which the plasmon resonance can extend from the visible to the near IR spectral region [Paz2012, Yan2011] and with typically weak polarization dependence, especially for high coordination numbers. There is another advantage of broadband SPR for SERS, that is the possibility of comparable local field enhancement both for the incoming and for the Raman scattered fields: a narrow plasmonic excitation, indeed, could provide a high enhancement for the laser field ( $\lambda_0$ ) but not for the scattered one ( $\lambda_{Raman} > \lambda_0$ ).

**Np aggregation: how** Colloidal Np aggregation can be induced in solution by controlling the ionic strength of the dispersion [Bad2010]. It is known, for example, that salt is a good aggregating agent, as it neutralizes the electrostatic repulsion among Nps. If this is weak enough, Np aggregation can also happen spontaneously and irreversibly (see Fig. 3.5 and relative explanation): in this case, inside the solution a precipitate will probably be visibile. In a similar way, the aggregation of Nps with proper functionalization (typically with peptides) can be realized by changing the pH of the solution: this is an example of a controllable parameter, which can be used as a reversible switch between the single Np and the Np aggregate states [SM2007]. The same holds for temperature-mediated reversible aggregation of Nps linked by complementary DNA strands [Sto2000].

Np organization into clusters on substrate is similar, and can simply be achieved by the Np self-assembling [Fas2014, Liu2014]. Typically, the controlled evaporation of the solvent is induced from a droplet of Np colloidal dispersion deposited on a substrate. In this case, average interparticle distances can become considerably small (of the order of few nanometers: see Fig. 3.6) and generally depend on the modulus of the surface charge of the dispersed Nps, that is, the higher the electrostatic repulsion among Nps, the less compact the aggregation and larger the interparticle distance [Fas2014, Fas2018]. Other techniques based on self-assembly use the functionalization of the substrate to immobilize the Nps via electrostatic interaction [Zhu2004, Bai2006].

The specific approach of molecular driven self-assembly is also worth mentioning. The idea in this case is to use the interaction of molecules with the metal Np surface as a sort of "glue", to selectively induce the Np organization. The effect can be based once again on electrostatic forces [Yan2009] or on more stable, covalent binding [Dom2016]. Molecular mediated assembly can be combined with lithography techniques to further guide the Np aggregation [Alb2013, Dom2016]. A particular case of molecular driven assembly is the DNA-origami based technique for controlling the Np organization [Tha2014]. In this case, the location of Nps is controlled by the deterministic spatial conformation of complementary DNA strands, precisely designed to bind or capture the Nps into specific sites [Low1999, Hun2010].

#### **Plasmonic Grating Effect**

In recent years, a strong interest has raised around the collective electromagnetic behavior of one- (1D) or two-dimensional (2D) gratings of metallic nanostructures [Gia2010]. Some computational calculations reported indeed further enhancement of the local field close to the nanostructures in arrays due to the coupling between

the localized SPR and the photonic mode of the grating, if the nanostructures are coupled in the far field regime [ZS2005, Kne2006]. A narrowing of the plasmonic band from Nps in array is revealed when comparing its profile to the one obtained from the single Np [ZS2005, Li2009]. This can result in a further tunability of the SPR, which can allow the optimization of SERS response [Alv2007].

The idea of a plasmonic grating benefiting of both localized excitations and diffractive coupling among nanostructures has been studied in arrays of metal nanoantennas with different geometry on different dielectric and conductive substrates [Yan2009, Aug2010, Aus2012]. Diffractive coupling is typically optimized when the pitch of the array becomes closer to the wavelength of light in the medium surrounding the nanostructures ( $\Lambda \sim \lambda/n$ ) [Aug2010].

As previously discussed, the narrowing of the SPR band is not convenient for SERS experiments, as it would result in a difference in field enhancement for the incident and the scattered field. Recent theoretical [Lu2015b] and experimental works [Yan2009, Lu2015a] have underlined the role of local disorder in the broadening of the SPR band in these nanostructures organized in 1D or 2D arrays. In particular, Yan et al. [Yan2009] have demonstrated an improvement of SERS performance of self-assembled, disordered gold Np cluster when they are disposed into ordered arrays [Yan2011] due to what they call multiple scale field enhancement. Indeed, the single Nps are near-field coupled to each other inside the Np cluster, which is further coupled (on a longer distance scale) to the other clusters in the array (see Fig. 2.9).

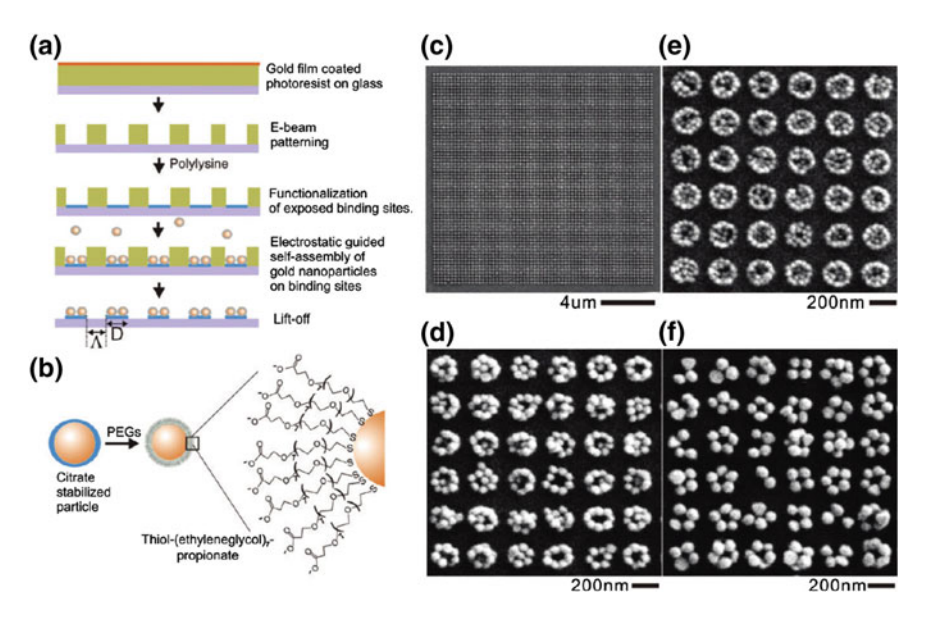
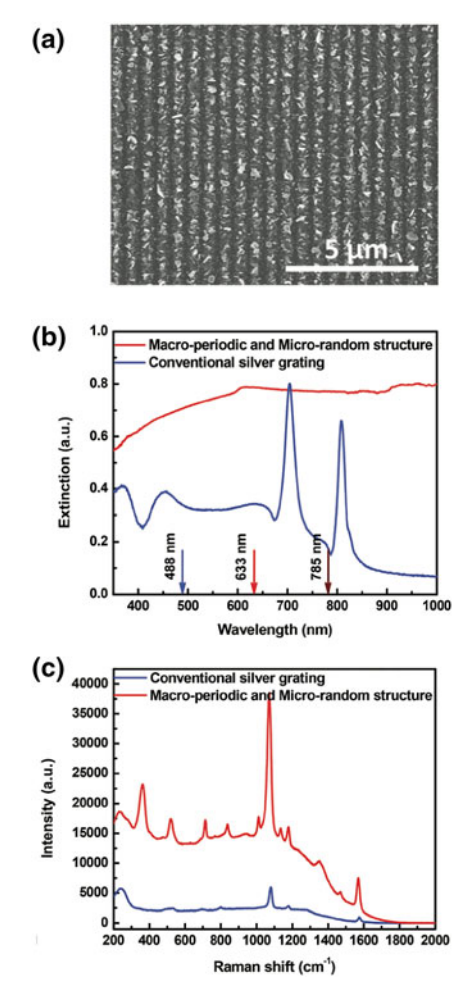


Fig. 2.9 a Fabrication protocol and **b** AuNp functionalization for the preparation of Np cluster arrays **c** with various Np diameter ( $d = 40 \text{ nm } (\mathbf{d}), d = 60 \text{ nm } (\mathbf{e}), d = 80 \text{ nm } (\mathbf{f})$ ) for a binding site of 200 nm. Reproduced with permission from Ref. [Yan2011]

Fig. 2.10 a SEM image of the macro-periodic micro-random grating (1D array of aggregated nanoplates) fabricated according to [Lu2015b]; b extinction spectra of this structure compared with a conventional silver grating of the same size and c SERS spectra acquired on the macro-periodic micro-random structure compared with the conventional Ag grating. Figure adapted with permission from [Lu2015a]



On the other hand, Lu et al. [Lu2015a] have demonstrated the role of disorder by a comparative study of SERS performances on a silver grating (1D array of Ag stripes) and on a structure made of silver nanoplates randomly arranged on a grating pattern of the same size (macro-periodic, micro-random structure). The periodicity of these structures is comparable to the wavelength used for spectroscopy (see Fig. 2.10). The broadband SPR (panel b of the figure) in these structures is due to the hybridization of localized plasmonic excitations in the aggregated nanoplates, while a further enhancement in the local field is caused by the collective modes of the grating, which the authors describe as "propagating Bloch-plasmonic" modes, and this is confirmed by the polarization-dependent SERS response of the structure.

The intriguing possibility of disposing Np-aggregates in arrays has been explored for 2D periodic arrays with submicrometer pitch [Yan2009, Yan2011]. More recent works focused on the possibility of fabricating mesoscopic arrays of Np aggregates

[Alb2013, Dom2016]. The high density of hot-spots on each binding site represents an intriguing possibility for ultrasensitive enhancement [Alb2013]. Moreover, the collective coupling of the plasmonic array, which has to be optimized by tuning the grating periodicity with the used laser wavelength, can further contribute to near field enhancement and therefore to the SERS efficiency of the system.

There is another important advantage of substrates with regular, mesoscopic geometry for SERS applications. Indeed, these nanostructures can easily be checked by visual inspection with a microscope, which facilitates the implementation of automatized measurement protocols [Alb2013]. They could also be easily inserted into microfluidic devices for cellular diagnostic applications.

# 2.3.2 SERS Applications in Nanomedicine

An extraordinary potentiality of SERS is the possibility to detect spectroscopic signal from very small volumes, much smaller than the diffraction limited scattering volumes of conventional Raman spectroscopy. For this reason, one of the natural applications of SERS-active systems has been, since the very early era of SERS, biophysics. Indeed, biophysical investigations are often interested in monitoring rare biochemical processes occurring in precise locations (e.g. in the proximity of certain molecular receptors, coding DNA sequences, etc.) and at low analyte concentration. The capability to detect specific biomolecules at low concentration in blood, bodily fluids or exhaled breath is of great interest for nanomedicine [Dom2012]. Moreover, the interaction of plasmonic, SERS-active nanostructures with single cells holds great promise for the early detection and treatment of cancer [Fas2016].

In general, a nanosensor is a system constituted by a suitable biofunctional layer, which enables the interaction with the biologically relevant target (e.g. a specific molecule or a cell) and by a recognizable element, which provides a signal containing information on the interaction with the target. The detected signal can be various: interesting results have been reported with electrochemical [Hay2014], mechanical [Arl2011], magnetic [MI2014] or optical nanosensors [Sto1998, DS2012].

In SERS, the recognizable element is obviously the metal Np, which can be labelled with a Raman active molecule and further functionalized with the biofunctional layer [Doe2007, Fas2016]. Another possibility is the direct spectroscopic study of the biofunctional layer, without any additional labelling. This is sometimes inconvenient because of the low Raman activity of certain biomolecules or the difficulties in binding them directly to the metal surface. An interesting exception are aptamer-based SERS sensors [Li2014, Cot2015]. Once the nanosensor is prepared, its interaction with the biosystem of interest needs to be investigated.

In the case of biomolecular sensing, it is sometimes possible to directly measure the spectrum of the molecule to detect, and to straightforwardly recognize its presence inside the sample. Often, it is not trivial to perform a direct spectroscopic detection of specific molecules at low concentration, due to the presence of the biolayer. This, covering the Np, increments the distance of the analyte from the nanostructured

substrate. Nevertheless, the formation of specific bonds between the nanosensor and the molecule to detect [Dom2012] or conformational changes in the biofunctional layer, induced by the presence of the analyte [Cot2015], can change the SERS spectrum of the sensor and act as control parameters. In other cases, the nanosensor is designed to monitor the presence of the analyte by strong intensity fluctuations, as in the case of gene detection performed by DNA assembly: here, the presence of the analyte induces the aggregation of Nps and the formation of hot-spots, resulting in a higher SERS intensity [Pic2014].

As for the interaction with cells, SERS nanosensors are often used to bind specifically to targeted molecular receptors on the cell membrane [Sch2006b, Fas2016]. In other cases, Nps can be transferred inside cells via sonoporation or endocytosis and can be used to monitor some properties of the cell, as for example the pH, using the modifications to the spectroscopic signal [Kne2007]. Once the Nps are located inside or in proximity of a cell, theranostic applications can be performed relying on the Np plasmonic properties, as happens for plasmonic photothermal therapy.

#### **Biomarker Detection**

One of the goals in modern medicine for the effective treatment of many diseases is to monitor their appearence and to assess their stage promptly, even before their physiological manifestation [Sal2015]. The problem of early diagnosis of cancer and other relevant pathologies can be address by monitoring the presence, inside the human body, of specific biomarkers [MR2014]. Biomarkers are molecules, such as mutant proteins or modified DNA and RNA sequences, vesicles produced by cells (e.g. exosomes), or circulating tumor cells (CTCs), that can provide information beyond the standard clinical parameters [SR2007]. The correlation between the development of pathologies and the concentration of certain biomarkers in blood or in bodily fluids is the subject of a wide field of research [Pep2001, SR2007].

Biomarkers detection can be performed with different techniques, among which the most common are the traditional fluorescence label-based immunological methods, as the enzyme-linked immunosorbent assay (ELISA) [Chi2015, Nim2016]. The sensitivity of the technique is here of crucial importance: lowering the concentration threshold for revealing the presence of a biomarker would impact on the diagnosis of the disease and, therefore, on the effectiveness of the treatment. The employment of nanoparticle-based sensors holds great promise for developing novel biosensing methods [Pal2015] or improving the sensitivity of traditional assays, as in the case of "plasmonic ELISA" by De La Rica and Stevens [DS2012].

SERS based nanosensors have proved to be competitive in the detection of specific molecules at sub-picomolar concentration [Dom2012]. Moreover, the combination of SERS active Nps with microfluidic devices has allowed great improvements in the detection of CTCs inside human blood. In the work by Pallaoro et al. [Pal2015], SERS nanotags were functionalized to selectively bind to cancer cell receptors, which were then separated by the normal cells via Raman activated cell-sorting [Doc2011] based on SERS signal.

## **Therapeutic Drug Monitoring**

Therapeutic drug monitoring (TDM) consists of the determination of a drug concentration inside a biological matrix (e.g. plasma, blood, etc.) as a function of time during the patient treatment period, starting from administration. A precise interpretation of the results is required in relation to the target range and the pharmacokinetics of the drug, in order to proceed to a personalized redosage of the drug, depending on the patient response. Not all drugs require such a precise monitoring, because for most of them the concentration threshold for effective therapeutic action and the one for toxicity usually differ significantly (i.e. the drug has wide therapeutic range). TDM is required for drugs with a very narrow therapeutic window, which practically means that a slight overdosage will be easily causing significant side-effects, as typically happens for chemotherapeutic drugs.

Serious consequences for drug under- or overdosing may be avoided by TDM. Unfortunately, the current methods for this analysis are time-consuming and expensive. In this framework, point-of care SERS sensors can overcome the difficulties and long time required for the execution of multi-step analyses like high performance liquid chromatography (HPLC) and mass spectrometry. Interesting results have been recently obtained using microfluidic devices on SERS detection of various farmaceutical compounds in urine and blood [Ack2007, Str2007, WC2014], also in the specific case of methotrexate, an antifolate drug for cancer treatment on which we will focus in the next chapters [Hid2014].

### **Selective Interaction of Nps with Cells**

Surface enhanced Raman scattering is an ideal candidate for the study of cells and tissues with very high spatial resolution. Spectroscopic imaging, diagnostics and theranostics, i.e. the combination of diagnosis and therapy, can be performed at single cell level with a high level of control on both the sample and the interpretation of the results [Ste2013, Gal2014].

• **Tissue and cell imaging** Raman spectroscopy is a label free technique which allows monitoring the chemical composition of samples, through the recognition of molecular vibrational fingerprints. As discussed above, however, Raman spectroscopy suffers from the small cross section of Raman process and the consequent low signal intensity. This, from an experimental point of view, means that it requires long acquisition times.

Moreover, the spatial resolution of Raman imaging is controlled by the diffraction limit in the visible range ( $\sim$ 200 nm at best). There are several approaches that can be used to improve the performances of Raman, as for example the use of Coherent Stokes/Antistokes Raman microSpectroscopy (CSRS/CARS), which involves two-photon coherent processes that can upgrade both the intensity and the spatial resolution [EX2008, Yon2015].

A further possibility is represented by TERS, Tip Enhanced Raman Scattering: here, a metallic nanostructured tip is mounted on a scanning probe microscope and used to map the morphology of a sample while collecting the colocalized surface-enhanced spectroscopic signal [Stö2000]. This technique leads to remarkable results in imaging cell membranes, but it is limited to surface investigation [Neu2006]. Moreover, the scanning probe approach usually requires very long acquisition times.

Another suitable approach is investigating cells and tissues by collecting signal from subdiffractive confined volumes, nanometer-close to a SERS-active substrate. SERS provides high spectroscopic intensity and the possibility of label-free investigation [Gre2011]. Obviously, the essential drawback of SERS-based imaging is the necessity of inducing the interaction of the cell with a SERS-active substrate, which might perturbate the cellular activity. Examples in this respect are nanostructured macroscopic metal substrates for cell growth [Zit2015] or, more commonly, metallic Nps to be introduced inside the cells [Kne2007].

In SERS cellular imaging, as actually happens in all SERS applications, the design of a proper metal nanostructured substrate is crucial. Considerations are not limited to the performances in signal enhancement and reproducibility: in biophysical applications, the effects on the cell of the nanosystem are to be carefully monitored. Cytotoxicity is a very important issue in these studies. In the case of metal Nps that are localized onto or internalized inside cells, it typically depends on the Np material, its capping layer - if it is present -, and on the Np concentration [Ste2013, Mat2010, DK2013]. In order to limit the Np cytotoxicity, usually gold Nps are preferred to silver ones; for the same reason, and to improve the Np stability, they are often coated with an organic, biocompatible capping layer [Mat2010, Fra2015].

The capping layer can act as a spectroscopic label [Hu2007], also enabling to probe the cell conditions, by monitoring modifications to the reported molecule induced by molecular binding events or a change in the cellular environment, as in the case of intracellular pH mapping reported by Kneipp and coworkers [Kne2007]. The molecular layer can also facilitate the interaction of the Nps with cells [DK2013]. Gregas et al., for example, demonstrated that charged Nps are more easily internalized inside cells the neutral-charged ones [Gre2011]. Moreover, the Np biofunctionalization is often exploited for inducing the selective interaction of the Nps with certain receptors on the membrane or inside the cells: to this aim, peptide, protein or antibody are used for the Np conjugation, with interesting results [Sch2006b]. Finally, time resolved SERS imaging gives the possibility of following the molecular pathways inside the cell by the simultaneous optical tracking and spectroscopic analysis of gold Nps [And2011].

• Single-cell diagnostics Given the potentialities of SERS in the study of cells [Ste2013], and given the results already obtained in the discrimination between normal and cancer cells from their Raman spectral features [Doc2011, Gal2014], a considerable interest has raised in developing highly sensitive SERS-based methods of cancer diagnosis at single cell level. This approach seems promising for early cancer detection, as it is possible to design strategies for simple and fast screening protocols for single cells [Pal2011, Fas2016].

A possible approach for SERS based diagnosis is the functionalization of SERS-labelled Nps with a specific molecule to target cellular markers that are overexpressed on cancer cell membrane [Sam2011]. The selective biorecognition of the SERS active Nps is induced by incubating cell cultures with a suitable nanovector. Many examples of such strategy involve protein-antigen interaction [Sch2011b]. Starting from this idea, the group of Moskovits developed a protocol for distinguishing cancerous epithelium prostate cells from normal cells [Pal2011]. Protein/antigen interaction is not the only type of biorecognition which can be exploited in this respect. Indeed, protein-based nanovectors can suffer from a lack of stability of the biolayer, as it has been demonstrated that these nanosensors are highly sensible to environmental conditions (e.g. temperature, pH) and are subject to assembly with other proteins in complex biological media like serum [Ehr2009], therefore inhibiting the specific biorecognition of the target receptors [Sal2013].

An alternative to protein based nanosensors is represented by the choice of other smaller, more stable molecules, like folic acid [Luc2000]. The overexpression of folate binding protein of different types has been widely studied in the last decades [Des2012], and folate-functionalized nanovectors have been synthesized [Boc2013, Li2013]. We have recently developed a folate nanovector-based procedure for single cell screening [Fas2016]. We demonstrated that folate-Nps bind to different types of cells with different efficiency, which were found to reflect folate-receptor expression level on the cell membranes. This is described in Chap. 5.

Single cell SERS diagnostics can be combined with other tools like microfluidics to achieve additional features to the diagnosis. An example is SERS-base cell sorting and separation [Doc2011, Pal2015].

• SERS and theranostics Theranostics is the combination of diagnosis and therapy, performed within the same process. In nanomedicine, a common approach to theranostics is the design of nanosystems composed by a recognizable element, which is often a biolayer able to selectively interact with morbid or cancer tissues, and a therapeutic element, which can be activated by external stimuli once in contact with the target cell. In recent years, several kind of theranostic nanovectors have been designed. Some of them are based on therapeutic drugs, which are either loaded onto the Np surface [Bes2016, Fas2018] or transported inside vescicles and then released locally in a controlled way. This happens through pH gradients [Cho2005] or by targeting the nanovescicle with ultrasounds [Lin2014].

In other cases, the therapeutic action of the nanovectors relies on the nanomaterial intrinsic properties, as it happens for metal Nps employed in plasmonic photothermal cancer therapy [Hua2008]. Once the Nps are located inside or in close proximity of cancer cells, the illumination with light (usually in the near IR spectral range), which is strongly absorbed, has the effect of increasing of the temperature of the Np and its environment, which eventually kills the cells [Boc2013].

The traceability of these nanovector, during their interaction with cells, is to be considered. To this aim, theranostic nanovectors are often conjugated with labels like fluorescent molecules. In the case of SERS active systems, the location of the nanovectors can be monitored following their spectroscopic signal [Fas2016, Fas2018].

# 2.3.3 Non Metallic Substrates: SERS from Semiconductor Nanostructures

As discussed in this Section, the applications of SERS active nanostructures range from the spectroscopic detection of molecules at ultra-low concentrations, to the study of molecular adsorbates on different surfaces, to the fabrication of suitably functionalized nanosystems, capable to target specific kind of cells and to act as drug carriers for biomedical applications. In this framework, some drawbacks of the use of metal nanostructures need to be considered. Among them, the cytotoxicity of metal nanoparticles has been widely studied [Fra2015]. Moreover, there is a limited choice in the chemical functionalization approaches that can be used to bind molecules to a metallic surface [NS2008].

In recent years, the scientific community has expressed interest in studying SERS effect from non-metallic nanostructures, excluding the well understood plasmonic excitation from the picture and focusing on understanding - and better controlling - the charge transfer (CT) enhancement mechanism [Wan2012, LB2014]. In this respect, a possibility can be the implementation of semiconducting nanostructures. Despite a less intense enhancement of the spectroscopic signal, indeed, this approach implies some interesting advantages. First of all, a lower cytotoxicity of semiconducting nanostructures would facilitate the application of these systems in drug delivery or nanomedicine. Then, a wider choice of molecules can be conjugated to semiconductor surfaces. Moreover, the functionalization of semiconductor nanostructures with organic molecules and the study of molecule-to-surface CT processes are of great interest for applications (e.g. photovoltaic [Wan2015] or electrochemical [Cat2012]).

Semiconductor nanostructures are intriguing systems, because of their potential in exhibiting unique physical and chemical properties compared to their bulk counterparts [Arb2007]. In particular, nanowires, which are filamentary crystals, are characterized by high surface-to-volume ratio, which can cause their crystallization in phases that are not stable in the bulk form, with effects on electronic and optical properties, due to the change in the bandstructure [Fon2007]. Many efforts have been devoted to improving of the tunability of optical and electronic properties of the nanowires. In this framework, different approaches have been developed. Some of them act on the nature of the materials, for example by implementing doping or utilizing alloys in order to tune the carrier density [Ass2013]. An important possibility is also to focus on the crystalline structure, by introducing mechanical strains (e.g. in core-shell systems [Hau2015]) derived by the combined presence of different

materials in the same nanostructured object. Another approach involves the covering of the nanowire inorganic scaffold with an organic molecular layer [Cat2012].

Functionalized semiconductor nanostructures offer great advantages from different points of view. First of all, the molecular covering acts as a passivating layer, preventing the surface oxidation and the formation of defects which could result in compromised carrier mobility [San1987]. Secondly, such hybrid materials can present different characteristics with respect to the bare semiconductor [Yaf2013], resulting in improved performances of the nanowires for applications and devices [Odo2013]. In this framework, a better understanding of the dynamic CT phenomena occurring at the molecule/semiconductor interface is crucial for the optimized design of such systems.

Ackermann KR, Henkel T et al (2007) Quantitative online detection of low-

#### References

[Ack2007]

[Ack2007]	concentrated drugs via a SERS microfluidic system. ChemPhysChem 8(18):2665–2670
[Alb1961]	Albrecht AC (1961) On the theory of Raman intensities. J Chem Phys 34(5):1476–1484
[Alb2013]	Alba M, Pazos-Perez N et al (2013) Macroscale Plasmonic Substrates for Highly Sensitive Surface-Enhanced Raman Scattering. Angewandte Chemie International Edition 52(25):6459–6463
[Ale2009]	Alexander KD, Hampton MJ et al (2009) A high-throughput method for controlled hot-spot fabrication in SERS-active gold nanoparticle dimer arrays. J Raman Spectrosc 40(12):2171–2175
[Alv2007]	Alvarez-Puebla R, Cui B (2007) Nanoimprinted SERS-active substrates with tunable surface plasmon resonances. J Phys Chem C 111(18):6720–6723
[And2011]	Ando J, Fujita K (2011) Dynamic SERS imaging of cellular transport pathways with endocytosed gold nanoparticles. Nano Lett 11(12):5344–5348
[Arb2007]	Arbiol J, Kalache B et al (2007) Influence of Cu as a catalyst on the properties of silicon nanowires synthesized by the vapour-solid-solid mechanism. Nanotechnology 18(30):305606
[Arl2011]	Arlett JL, Myers EB (2011) Comparative advantages of mechanical biosensors. Nat Nanotechnol 6(4):203–215
[Ass2013]	Assali S, Zardo I (2013) Direct band gap wurtzite gallium phosphide nanowires. Nano Lett 13(4):1559–1563
[Aug2010]	Auguié B, Bendana XM et al (2010) Diffractive arrays of gold nanoparticles near an interface: critical role of the substrate. Phys Rev B 82(15):155447
[Aus2012]	Ausman LK, Li S et al (2012) Structural effects in the electromagnetic enhancement mechanism of surface-enhanced Raman scattering: Dipole reradiation and rectangular symmetry effects for nanoparticle arrays. J Phys Chem C 116(33):17318–17327
[Bad2010]	El Badawy AM, Luxton TP et al (2010) Impact of environmental conditions (pH, ionic strength, and electrolyte type) on the surface charge and aggregation of silver nanoparticles suspensions. Environ Sci Technol 44(4):1260–1266
[Bai2006]	Baia M, Toderas F (2006) Probing the enhancement mechanisms of SERS with p-aminothiophenol molecules adsorbed on self-assembled gold colloidal nanoparticles. Chem Phys Lett 422(1):127–132

ovarian cancer cells. Mol Pharma 11(2):391-399

biomolecules. Nat Comm 7:12189

ence 354(6313):726-729

erfaces 141:141-147

Baldassarre L, Sakat E (2015) Midinfrared plasmon-enhanced spectroscopy with germanium antennas on silicon substrates. Nano Lett 15(11):7225–7231

Bizzarri AR, Cannistraro S (2003) Temporal fluctuations in the SERRS spectra of single iron-protoporphyrin IX molecule. Chem Phys 290(2):297–306

Benz F, Schmidt MK et al Single-molecule optomechanics in "picocavities". Sci-

Bessar H, Venditti I (2016) Functionalized gold nanoparticles for topical delivery of methotrexate for the possible treatment of psoriasis. Colloids Surf B: Bioint-

Boca-Farcau S, Potara M (2013) Folic acid-conjugated, SERS-labeled silver nanotriangles for multimodal detection and targeted photothermal treatment on human

Ben-Jaber S, Peveler WJ et al (2016) Photo-induced enhanced Raman spectroscopy for universal ultra-trace detection of explosives, pollutants and

Cattani-Scholz A, Liao K-C et al (2012) Molecular architecture: construction of self-assembled organophosphonate duplexes and their electrochemical character-

[Bal2015]

[BC2003]

[Ben2016]

[Bes2016]

[Boc2013]

[BP2016]

[Cat2012]

	ization. Langmuir 28(20):/889–7896
[Cha1974]	Chance RR, Prock A (1974) Lifetime of an emitting molecule near a partially
	reflecting surface. J Chem Phys 60(7):2744–2748
[Cha2011]	Chapman HN, Fromme P et al (2011) Femtosecond X-ray protein nanocrystal-
	lography. Nature 470(7332):73–77
[Chi2014]	Chirumamilla M, Toma A (2014) 3D nanostar dimers with a Sub-10-nm
	gap for single-/few-molecule surface-enhanced raman scattering. Adv Mater
	26(15):2353–2358
[Chi2015]	Chinen AB, Guan CM et al (2015) Nanoparticle probes for the detection of cancer
	biomarkers, cells, and tissues by fluorescence. Chem Rev 115(19):10530–10574
[Cho2005]	Choucair A, Soo PL et al (2005) Active loading and tunable release of doxorubicin
_	from block copolymer vesicles. Langmuir 21(20):9308–9313
[Chu2011]	Chu Y, Zhu W (2011) Beamed Raman: directional excitation and emission
	enhancement in a plasmonic crystal double resonance SERS substrate. Optics
	Express 19(21):20054–20068
[Cia2014]	Cialla D, Pollok S et al (2014) SERS-based detection of biomolecules. Nanopho-
	tonics 3(6):383–411
[CK2007]	Chen S-H, Kotlarchyk M (2007) Interactions of photons and neutrons with matter.
	World Scientific, Singapore
[CK2012]	Cabrini S, Kawata S (2012) Nanofabrication handbook. CRC Press, Boca Raton
[Col1975]	Colthup N, Daly LH et al (1975) Introduction to infrared and Raman spectroscopy.
	Elsevier, Amsterdam
[Col2009]	Coluccio ML, Das G et al (2009) Silver-based surface enhanced Raman scattering
	(SERS) substrate fabrication using nanolithography and site selective electroless
	deposition. Microelectron Eng 86(4):1085–1088
[Col2015]	Coluccio ML, Gentile F et al (2015) Detection of single amino acid mutation
	in human breast cancer by disordered plasmonic self-similar chain. Sci Adv
	1(8):e1500487
[Cot2015]	Cottat M, D'Andrea C (2015) High sensitivity, high selectivity SERS detection of
	MnSOD using optical nanoantennas functionalized with aptamers. J Phys Chem
	C 119(27):15532–15540
[Das2012]	Das G, Patra N et al (2012) Fabrication of large-area ordered and reproducible
	nanostructures for SERS biosensor application. Analyst 137(8):1785–1792
[De 2013]	De Angelis F, Malerba M (2013) 3D hollow nanostructures as building blocks for
	multifunctional plasmonics. Nano Lett 13(8):3553-3558
[Des2012]	Desmoulin SK, Hou Z et al (2012) The human proton-coupled folate transporter:
	biology and therapeutic applications to cancer. Cancer Biol Ther 13(14):1355-
	1373

- [Di 1997] Di Fabrizio E, Grella L et al (1997) Nanometer biodevice fabrication by electron beam lithography. J Vac Sci Technol B 15(6):2892–2896
- [DK2013] Dykman LA, Khlebtsov NG (2013) Uptake of engineered gold nanoparticles into mammalian cells. Chem Rev 114(2):1258–1288
- [Doc2011] Dochow S, Krafft C (2011) Tumour cell identification by means of Raman spectroscopy in combination with optical traps and microfluidic environments. Lab Chip 11(8):1484–1490
- [Doe2007] Doering WE, Piotti ME et al (2007) SERS as a foundation for nanoscale, optically detected biological labels. Adv Mater 19(20):3100–3108
- [Dom2012] Domenici F, Bizzarri AR et al (2012) Surface-enhanced Raman scattering detection of wild-type and mutant p53 proteins at very low concentration in human serum. Anal Biochem 421(1):9–15
- [Dom2016] Domenici F, Fasolato C (2016) Engineering microscale two-dimensional gold nanoparticle cluster arrays for advanced Raman sensing: an AFM study. Colloids Surf A: Physicochem Eng Asp 498:168–175
- [DS2012] De La Rica R, Stevens MM (2012) Plasmonic ELISA for the ultrasensitive detection of disease biomarkers with the naked eye. Nat Nanotechnol 7(12):821–824
- [Ehr2009] Ehrenberg MS, Friedman AE et al (2009) The influence of protein adsorption on nanoparticle association with cultured endothelial cells. Biomaterials 30(4):603–610
- [Eno2004] Enoch S, Quidant R (2004) Optical sensing based on plasmon coupling in nanoparticle arrays. Optics Express 12(15):3422–3427
- [EX2008] Evans CL, Xie XS (2008) Coherent anti-Stokes Raman scattering microscopy: chemical imaging for biology and medicine. Ann Rev Anal Chem 1:883–909
- [Fan2008] Fang Y, Seong N-H et al (2008) Measurement of the distribution of site enhancements in surface-enhanced Raman scattering. Science 321(5887):388–392
- [Fan2010] Fan JA, Wu C et al (2010) Self-assembled plasmonic nanoparticle clusters. Science 328(5982):1135–1138
- [Fan2011] Fan M, Andrade GFS et al (2011) A review on the fabrication of substrates for surface enhanced Raman spectroscopy and their applications in analytical chemistry.

  Anal Chimica Acta 693(1):7–25
- [Fas2014] Fasolato C, Domenici F et al (2014) Dimensional scale effects on surface enhanced Raman scattering efficiency of self-assembled silver nanoparticle clusters. Appl Phys Lett 105(7):073105
- [Fas2016] Fasolato C, Giantulli S et al (2016) Folate-based single cell screening using surface enhanced Raman microimaging. Nanoscale 8(39):17304–17313
- [Fas2018] Fasolato C, Giantulli S et al (2018) Antifolate functionalized nanovectors: SERS investigation motivates effective theranostics, In preparation
- [Fle1974] Fleischmann M, Hendra PJ et al (1974) Raman spectra of pyridine adsorbed at a silver electrode. Chem Phys Lett 26(2):163–166
- [Fon2007] Morral AF, i, Arbiol J, et al (2007) Synthesis of silicon nanowires with wurtzite crystalline structure by using standard chemical vapor deposition. Adv Mater 19(10):1347–1351
- [Fra1979] Frauenfelder H, Petsko GA et al (1979) Temperature-dependent X-ray diffraction as a probe of protein structural dynamics
- [Fra2015] Fratoddi I, Venditti I (2015) How toxic are gold nanoparticles? The state-of-theart. Nano Res 8(6):1771–1799
- [Gal2014] Galler K, Bräutigam K et al (2014) Making a big thing of a small cell-recent advances in single cell analysis. Analyst 139(6):1237–1273
- [Gia2010] Giannini V, Vecchi G et al (2010) Lighting up multipolar surface Plasmon polaritons by collective resonances in arrays of nanoantennas. Phys Rev Lett 105(26):266801
- [GP1977] Gaber BP, Peticolas WL (1977) On the quantitative interpretation of biomembrane structure by Raman spectroscopy. Biochimica et Biophysica. Acta (BBA)-Biomembranes 465(2):260–274

References 51

[GP2007] Ghosh SK, Pal T (2007) Interparticle coupling effect on the surface plasmon resonance of gold nanoparticles: from theory to applications. Chem Rev 107(11):4797–4862

- [Gre2011] Gregas MK, Yan F et al (2011) Characterization of nanoprobe uptake in single cells: spatial and temporal tracking via SERS labeling and modulation of surface charge. Nanomed: Nanotechnol Biol Med 7(1):115–122
- [Gri1995] Freeman RG, Grabar KC et al (1995) Self-assembled metal colloid monolayers: an approach to SERS substrates. Science 267(5204):1629
- [Gun2001] Gunnarsson LK, Bjerneld EJ (2001) Interparticle coupling effects in nanofabricated substrates for surface-enhanced Raman scattering. Appl Phys Lett 78(6):802–804
- [Hau2015] Hauge HIT, Verheijen MA et al (2015) Hexagonal silicon realized. Nano Lett 15(9):5855–5860
- [Hay1988] Hayashi S, Koh R et al (1988) Evidence for surface-enhanced Raman scattering on nonmetallic surfaces: Copper phthalocyanine molecules on GaP small particles. Phys Rev Lett 60(11):1085
- [Hay2003] Haynes CL, McFarland AD et al (2003) Nanoparticle optics: the importance of radiative dipole coupling in two-dimensional nanoparticle arrays. J Phys Chem B 107(30):7337–7342
- [Hay2014] Hayat A, Catanante G et al (2014) Current trends in nanomaterial-based amperometric biosensors. Sensors 14(12):23439–23461
- [Hid2014] Hidi IJ, Mühlig A (2014) LOC-SERS: towards point-of-care diagnostic of methotrexate. Anal Methods 6(12):3943–3947
- [HS2004] Hao E, Schatz GC (2004) Electromagnetic fields around silver nanoparticles and dimers. J Chem Phys 120(1):357–366
- [Hu2007] Qingyan H, Tay L-L (2007) Mammalian cell surface imaging with nitrilefunctionalized nanoprobes: biophysical characterization of aggregation and polarization anisotropy in SERS imaging. J Am Chem Soc 129(1):14–15
- [Hua2008] Huang X, Jain PK et al (2008) Plasmonic photothermal therapy (PPTT) using gold nanoparticles. Lasers Med Sci 23(3):217–228
- [Hul1999] Hulteen JC, Treichel DA et al (1999) Nanosphere lithography: size-tunable silver nanoparticle and surface cluster arrays. J Phys Chem B 103(19):3854–3863
- [Hun2010] Hung AM, Micheel CM et al (2010) Large-area spatially ordered arrays of gold nanoparticles directed by lithographically confined DNA origami. Nat Nanotechnol 5(2):121–126
- [Ind2014] Swarnapali A, Indrasekara DS, Meyers S et al (2010) Gold nanostar substrates for SERS based chemical sensing in the femtomolar regime. Nanoscale 6(15):8891–8899
- [Jen2002] Jensen L, Strand P-O et al (2002) Polarizability of molecular clusters as calculated by a dipole interaction model. J Chem Phys 116(10):4001–4010
- [Jen2008] Jensen L, Aikens CM et al (2008) Electronic structure methods for studying surface-enhanced Raman scattering. Chem Soc Rev 37(5):1061–1073
- [Jeo2016] Won Jeong J, Masud Parvez Arnob M et al (2016) 3D Cross-point plasmonic nanoarchitectures containing dense and regular hot spots for surface-enhanced raman spectroscopy analysis. Adv Mater 28:8695
- [JH2004] Jackson JB, Halas NJ (2004) Surface-enhanced Raman scattering on tunable plasmonic nanoparticle substrates. Proc Natl Acad Sci 101(52):17930–17935
- [Kim2011] Kim NH, Lee SJ et al (2011) Reversible tuning of SERS hot spots with aptamers. Adv Mater 23(36):4152–4156
- [Kle2013] Kleinman SL, Frontiera RR et al (2013) Creating, characterizing, and controlling chemistry with SERS hot spots. Phys Chem Chem Phys 15(1):21–36
- [Kne1997] Kneipp K, Wang Y et al (1997) Single molecule detection using surface-enhanced Raman scattering (SERS). Phys Rev Lett 78(9):1667

- [Kne2002] Kneipp K, Kneipp H et al (2002) Surface-enhanced Raman scattering and biophysics. J Phys: Condens Matter 14(18):R597
- [Kne2006] Kneipp K, Moskovits M et al (2006) Surface-enhanced Raman scattering: physics and applications, vol 103. Springer Science & Business Media, Berlin
- [Kne2007] Kneipp J, Kneipp H (2007) One-and two-photon excited optical pH probing for cells using surface-enhanced Raman and hyper-Raman nanosensors. Nano Lett 7(9):2819–2823
- [Kne2016] Kneipp K (2016) Chemical contribution to SERS enhancement: an experimental study on a series of polymethine dyes on silver nanoaggregates. J Phys Chem C
- [Kre1999] Krenn JR, Dereux A et al (1999) Squeezing the optical near-field zone by plasmon coupling of metallic nanoparticles. Phys Rev Lett 82(12):2590
- [KV1995] Kreibig U, Vollmer M (1995) Optical properties of metal clusters, vol 25. Springer Science & Business Media, Berlin
- [KV2008] Khoury CG, Vo-Dinh T (2008) Gold nanostars for surface-enhanced Raman scattering: synthesis, characterization and optimization. J Phys Chem C 112(48):18849–18859
- [LB2008] Lombardi JR, Birke RL (2008) A unified approach to surface-enhanced Raman spectroscopy. J Phys Chem C 112(14):5605–5617
- [LB2009] Lombardi JR, Birke RL (2009) A unified view of surface-enhanced Raman scattering. Acc Chem Res 42(6):734–742
- [LB2014] Lombardi JR, Birke RL (2014) Theory of surface-enhanced Raman scattering in semiconductors. J Phys Chem C 118(20):11120–11130
- [Le 2007] Le Ru EC, Blackie EJ (2007) Surface enhanced Raman scattering enhancement factors: a comprehensive study. J Phys Chem C 111(37):13794–13803
- [Le 2012] Le Ru EC, Schroeter LC et al (2012) Direct measurement of resonance Raman spectra and cross sections by a polarization difference technique. Anal Chem 84(11):5074–5079
- [Lef1999] Lefrant S, Baltog I (1999) Structural properties of some conducting polymers and carbon nanotubes investigated by SERS spectroscopy. Synth Metals 100(1):13–27
- [Li2003] Li K, Stockman MI et al (2003) Self-similar chain of metal nanospheres as an efficient nanolens. Phys Rev Lett 91(22):227402
- [Li2009] Li J, Fattal D et al (2009) Plasmonic optical antennas on dielectric gratings with high field enhancement for surface enhanced Raman spectroscopy. Appl Phys Lett 94(26):263114
- [Li Q, Jiang Y (2013) High surface-enhanced Raman scattering performance of individual gold nanoflowers and their application in live cell imaging. Small 9(6):927–932
- [Li2014] Li F, Zhang H (2014) Aptamers facilitating amplified detection of biomolecules. Anal Chem 87(1):274–292
- [Lin2001] Linden S, Kuehl J et al (2001) Controlling the interaction between light and gold nanoparticles: selective suppression of extinction. Phys Rev Lett 86(20):4688
- [Lin2014] Lin C-Y, Javadi M et al (2014) Ultrasound sensitive eLiposomes containing doxorubicin for drug targeting therapy. Nanomed: Nanotechnol Biol Med 10(1):67–76
- [Lin2015] Ling X, Huang S (2015) Lighting up the Raman signal of molecules in the vicinity of graphene related materials. Acc Chem Res 48(7):1862–1870
- [Liu 2014] Liu H, Yang Z (2014) Three-dimensional and time-ordered surface-enhanced Raman scattering hotspot matrix. J Am Chem Soc 136(14):5332–5341
- [LM1982] Lee PC, Meisel D (1982) Adsorption and surface-enhanced Raman of dyes on silver and gold sols. J Phys Chem 86(17):3391–3395
- [Lom1986] Lombardi JR, Birke RL et al (1986) Charge-transfer theory of surface enhanced Raman spectroscopy: Herzberg-Teller contributions. J Chem Phys 84(8):4174–4180
- [Lon2002] Long DA (2002) The Raman effect: a unified treatment of the theory of Raman scattering by molecules. Wiley, New York

Loweth CJ, Caldwell WB et al (1999) DNA-based assembly of gold nanocrystals.

[Low1999]

[LOW 1999]	Lowelli C3, Caldwell w B et al (1999) DivA-based assembly of gold halloerystals.
	Angewandte Chemie International Edition 38(12):1808–1812
[Lu2010]	Lu W, Singh AK et al (2010) Gold nano-popcorn-based targeted diagnosis, nan-
[	otherapy treatment, and in situ monitoring of photothermal therapy response of
	prostate cancer cells using surface-enhanced Raman spectroscopy. J Am Chem
	Soc 132(51):18103–18114
[Lu2015a]	Lu H, Ren X et al (2015) Broadband near-field enhancement in the macroperiodic
[2020100]	•
	and micro-random structure with a hybridized excitation of propagating Bloch-
	plasmonic and localized surface-plasmonic modes. Nanoscale 7(40):16798-
	16804
[Lu2015b]	Lu H, Ren X et al (2015) Experimental and theoretical investigation of macro-
[2420100]	periodic and micro-random nanostructures with simultaneously spatial transla-
	tional symmetry and long-range order breaking. Sci Rep 5
[Luc2000]	Lucock M (2000) Folic acid: nutritional biochemistry, molecular biology, and role
	in disease processes. Mol Genet Metab 71(1):121–138
[Mai2002]	Maier SA, Brongersma ML et al (2002) Observation of near-field coupling in
[141412002]	
	metal nanoparticle chains using far-field polarization spectroscopy. Phys Rev B
	65(19):193408
[Man2012]	Mangialardo S, Gontrani L et al (2012) Role of ionic liquids in protein refolding:
	native/fibrillar versus treated lysozyme. RSC Adv 2(32):12329–12336
[Mat2010]	Matschulat A, Drescher D et al (2010) Surface-enhanced Raman scattering hybrid
[Mat2010]	
	nanoprobe multiplexing and imaging in biological systems. ACS Nano 4(6):3259–
	3269
[McP1976]	McPherson A (1976) The growth and preliminary investigation of protein and
	nucleic acid crystals for X-ray diffraction analysis. Methods Biochem Anal
	23:249–345
D #1001 41	
[MI2014]	Muluneh M, Issadore D (2014) Microchip-based detection of magnetically labeled
	cancer biomarkers. Adv Drug Deliv Rev 66:101–109
[Mia2008]	Miao J, Ishikawa T (2008) Extending x-ray crystallography to allow the imaging
	of noncrystalline materials, cells, and single protein complexes. Ann Rev Phys
	Chem 59:387–410
D.C. 10001	
[Mic1999]	Michaels AM, Nirmal M (1999) Surface enhanced Raman spectroscopy of indi-
	vidual rhodamine 6G molecules on large Ag nanocrystals. J Am Chem Soc
	121(43):9932–9939
[MJ2009]	Morton SM, Jensen L (2009) Understanding the molecule- surface chemical cou-
[1:102007]	pling in SERS. J Am Chem Soc 131(11):4090–4098
D. f. 00101	
[Moo2012]	Moore JE, Morton SM et al Importance of correctly describing charge-transfer
	excitations for understanding the chemical effect in SERS. J Phys Chem Lett
	3(17):2470–2475
[Mos1985]	Moskovits M (1985) Surface-enhanced spectroscopy. Rev Mod Phys 57(3):783
	1 10
[Mos2013]	Moskovits M (2013) Persistent misconceptions regarding SERS. Phys Chem
	Chem Phys 15(15):5301–5311
[MR2014]	Maroto P, Rini B (2014) Molecular biomarkers in advanced renal cell carcinoma.
	Clin Cancer Res 20(8):2060–2071
[Neu2006]	Neugebauer U, Rösch P et al (2006) On the way to nanometer-sized information
[002000]	of the bacterial surface by tip-enhanced Raman spectroscopy. ChemPhysChem
	7(7):1428–1430
[NH2012]	Novotny L, Hecht B (2012) Principles of nano-optics. Cambridge University
	December 1.

Nimse SB, Sonawane MD et al (2016) Biomarker detection technologies and

Neouze MA, Schubert U (2008) Surface modification and functionalization of

metal and metal oxide nanoparticles by organic ligands. Monatshefte für Chemie-

Press, Cambridge

Chem Mon 139(3):183–195

future directions. Analyst 141(3):740–755

[Nim2016]

[NS2008]

- [Odo2013] Odobel F, Pellegrin Y (2013) Bio-inspired artificial light-harvesting antennas for enhancement of solar energy capture in dye-sensitized solar cells. Energy EnvironSci 6(7):2041–2052
- [Osa1994] Osawa M, Matsuda N (1994) Charge transfer resonance Raman process in surface-enhanced Raman scattering from p-aminothiophenol adsorbed on silver: Herzberg-Teller contribution. J Phys Chem 98(48):12702–12707
- [Ott1984] Otto A (1984) Surface-enhanced Raman scattering: "Classical" and "Chemical" origins. Light scattering in solids IV. Springer, pp 289–418
- [Ott1992] Otto A, Mrozek I et al (1992) Surface-enhanced Raman scattering. J Phys: Condens Matter 4(5):1143
- [Ott2005] Otto A (2005) The 'chemical'(electronic) contribution to surface-enhanced Raman scattering. J Raman Spectrosc 36(6–7):497–509
- [Pal2011] Pallaoro A, Braun GB et al (2011) Quantitative ratiometric discrimination between noncancerous and cancerous prostate cells based on neuropilin-1 overexpression. Proc Natl Acad Sci 108(40):16559–16564
- [Pal2015] Pallaoro A, Hoonejani MR et al (2015) Rapid identification by surface-enhanced Raman spectroscopy of cancer cells at low concentrations flowing in a microfluidic channel. ACS Nano 9(4):4328–4336
- [Paz2012] Pazos-Perez N, Wagner CS et al (2012) Organized plasmonic clusters with high coordination number and extraordinary enhancement in Surface-Enhanced Raman Scattering (SERS). Angewandte Chemie International Edition 51(51):12688–12693
- [Pep2001] Pepe MS, Etzioni R et al (2001) Phases of biomarker development for early detection of cancer. J Natl Cancer Inst 93(14):1054–1061
- [Pet1986] Pettinger B (1986) Light scattering by adsorbates at Ag particles: Quantummechanical approach for energy transfer induced interfacial optical processes involving surface plasmons, multipoles, and electron-hole pairs. J Chem Phys 85(12):7442–7451
- [Pet2003] Petry R, Schmitt M et al (2003) Raman spectroscopy-a prospective tool in the life sciences. ChemPhysChem 4(1):14–30
- [Pic2012] Piccirilli F, Mangialardo S et al (2012) Sequential dissociation of insulin amyloids probed by high pressure Fourier transform infrared spectroscopy. Soft Matter 8(47):11863–11870
- [Pic2014] Picciolini S, Mehn D (2014) Polymer nanopillar-gold arrays as surface- enhanced raman spectroscopy substrate for the simultaneous detection of multiple genes. ACS Nano 8(10):10496–10506
- [PS2008] Pinchuk AO, Schatz GC (2008) Nanoparticle optical properties: Far-and near-field electrodynamic coupling in a chain of silver spherical nanoparticles. Mater Sci Eng: B 149(3):251–258
- [QN2008] Ximei Qian and Shinning Ming Nie (2008) Single-molecule and single-nanoparticle SERS: from fundamental mechanisms to biomedical applications. Chem Soc Rev 37(5):912–920
- [Rec2003] Rechberger W, Hohenau A (2003) Optical properties of two interacting gold nanoparticles. Optics Commun 220(1):137–141
- [Sal2013] Salvati A, Pitek AS et al (2013) Transferrin-functionalized nanoparticles lose their targeting capabilities when a biomolecule corona adsorbs on the surface. Nat Nanotechnol 8(2):137–143
- [Sal2015] Salvati E, Stellacci F et al (2015) Nanosensors for early cancer detection and for therapeutic drug monitoring. Nanomedicine 10(23):3495–3512
- [Sam2011] Samanta A, Maiti KK et al (2011) Ultrasensitive near-infrared raman reporters for SERS-based in vivo cancer detection. Angewandte Chemie International Edition 50(27):6089–6092
- [Sam2013] Samal AK, Polavarapu L et al (2013) Size Tunable Au@ Ag core- shell nanoparticles: synthesis and surface-enhanced raman scattering properties. Langmuir 29(48):15076–15082

References 55

[San1987]	Sandroff CJ, Nottenburg RN (1987) Dramatic enhancement in the gain of a
[	GaAs/AlGaAs heterostructure bipolar transistor by surface chemical passivation.
	Appl Phys Lett 51(1):33–35
[Sch2006a]	Schatz GC, Young MA et al (2006) Electromagnetic mechanism of SERS.
	Surface-enhanced Raman scattering. Springer, pp 19–45
[Sch2006b]	Schlücker S, Küstner B (2006) Immuno-Raman microspectroscopy: in situ detec-
	tion of antigens in tissue specimens by surface-enhanced Raman scattering. J
	Raman Spectrosc 37(7):719–721
[Sch2009]	Schlücker S (2009) SERS microscopy: nanoparticle probes and biomedical appli-
	cations. ChemPhysChem 10(9–10):1344–1354
[Sch2011a]	Schmid G (2011) Nanoparticles: from theory to application. Wiley, New York
[Sch2011b]	Schuetz M, Mueller CI et al (2011) Design and synthesis of Raman reporter
	molecules for tissue imaging by immuno-SERS microscopy. J Biophotonics
FC 1 201 41	4(6):453–463
[Sch2014]	Schlücker S (2014) Surface-Enhanced raman spectroscopy: Concepts and chemical and isotome. An accuse the Chemical International Edition 52(10):4756-4705
[Cho2012]	ical applications. Angewandte Chemie International Edition 53(19):4756–4795 Shaw CP, Fan M et al (2013) Statistical correlation between SERS intensity and
[Sha2013]	nanoparticle cluster size. J Phys Chem C 117(32):16596–16605
[Sig2016]	Signorelli S, Cannistraro S et al (2016) Structural characterization of the
[51g2010]	intrinsically disordered protein p53 using Raman spectroscopy. Appl Spectrosc
	0003702816651891
[Sil1917]	Silberstein L (1917) Molecular refractivity and atomic interaction. II. Lond Edinb
[5111717]	Dublin Philos Mag J 33(198):521–533
[SM2007]	Si S, Mandal TK (2007) pH-controlled reversible assembly of peptide-
. ,	functionalized gold nanoparticles. Langmuir 23(1):190–195
[Son2012]	Song J, Zhou J (2012) Self-assembled plasmonic vesicles of SERS-encoded
	amphiphilic gold nanoparticles for cancer cell targeting and traceable intracel-
	lular drug delivery. J Am Chem Soc 134(32):13458–13469
[SR2007]	Swarup V, Rajeswari MR (2007) Circulating (cell-free) nucleic acids-a promis-
	ing, non-invasive tool for early detection of several human diseases. FEBS Lett
	581(5):795–799
[Ste2013]	Stender AS, Marchuk K et al (2013) Single cell optical imaging and spectroscopy.
FG. 100001	Chem Rev 113(4):2469–2527
[Sti2008]	Stiles PL, Dieringer JA et al (2008) Surface-enhanced Raman spectroscopy. Ann
FG4 - 10001	Rev Anal Chem 1:601–626
[Sto1998]	Storhoff JJ, Elghanian R (1998) One-pot colorimetric differentiation of polynucleotides with single base imperfections using gold nanoparticle probes. J Am
	Chem Soc 120(9):1959–1964
[Sto2000]	Storhoff JJ, Lazarides AA (2000) What controls the optical properties of DNA-
[5102000]	linked gold nanoparticle assemblies? J Am Chem Soc 122(19):4640–4650
[Stö2000]	Stöckle RM, Suh YD et al (2000) Nanoscale chemical analysis by tip-enhanced
[5102000]	Raman spectroscopy. Chem Phys Lett 318(1):131–136
[Str2007]	Strehle KR, Cialla D et al (2007) A reproducible surface-enhanced Raman spec-
[]	troscopy approach. Online SERS measurements in a segmented microfluidic sys-
	tem. Anal Chem 79(4):1542–1547

- [Sun1997] Sunde M, Serpell LC et al (1997) Common core structure of amyloid fibrils by synchrotron X-ray diffraction. J Mol Biol 273(3):729–739
- [Sun2007] Sun Z, Zhao B et al (2007) ZnO nanoparticle size-dependent excitation of surface Raman signal from adsorbed molecules: observation of a charge-transfer resonance. Appl Phys Lett 91(22):221106
- [Tam2002] Tamaru H, Kuwata H (2002) Resonant light scattering from individual Ag nanoparticles and particle pairs. Appl Phys Lett 80(10):1826–1828
- [Tha2014] Thacker VV, Herrmann LO et al (2014) DNA origami based assembly of gold nanoparticle dimers for surface-enhanced Raman scattering. Nat Commun 5

- [TS2012] Thomas R, Swathi RS (2012) Organization of metal nanoparticles for surfaceenhanced spectroscopy: a difference in size matters. J Phys Chem C 116(41):21982– 21991
- [Val2013] Valley N, Greeneltch N (2013) A look at the origin and magnitude of the chemical contribution to the enhancement mechanism of surface-enhanced Raman spectroscopy (SERS): Theory and experiment. J Phys Chem Lett 4(16):2599–2604
- [Vec2009] Vecchi G, Giannini V et al (2009) Surface modes in plasmonic crystals induced by diffractive coupling of nanoantennas. Phys Rev B 80(20):201401
- [W1953] Watson JD, Crick FHC et al (1953) Molecular structure of nucleic acids. Nature 171(4356):737–738
- [Wan2011] Wang X, Shi W (2011) Using Si and Ge nanostructures as substrates for surfaceenhanced Raman scattering based on photoinduced charge transfer mechanism. J Am Chem Soc 133(41):16518–16523
- [Wan2012] Wang X, Shi W (2012) Surface-enhanced Raman scattering (SERS) on transition metal and semiconductor nanostructures. Phys Chem Chem Phys 14(17):5891–5901
- [Wan2015] Wang X, Liow C (2015) Engineering interfacial photo-induced charge transfer based on nanobamboo array architecture for efficient solar-to-chemical energy conversion. Adv Mater 27(13):2207–2214
- [WC2014] Wu H-Y, Cunningham BT (2014) Point-of-care detection and real-time monitoring of intravenously delivered drugs via tubing with an integrated SERS sensor. Nanoscale 6(10):5162–5171
- [Xu1999] Xu H, Bjerneld EJ et al (1999) Spectroscopy of single hemoglobin molecules by surface enhanced Raman scattering. Phys Rev Lett 83(21):4357
- [Xu2012] Weigao X, Ling X (2012) Surface enhanced Raman spectroscopy on a flat grapheme surface. Proc Natl Acad Sci 109(24):9281–9286
- [Yaf2013] Yaffe O, Ely T (2013) Effect of molecule-surface reaction mechanism on the electronic characteristics and photovoltaic performance of molecularly modified Si. J Phys Chem C 117(43):22351–22361
- [Yan 2009] Yan B, Thubagere A et al (2009) Engineered SERS substrates with multiscale signal enhancement: nanoparticle cluster arrays. Acs Nano 3(5):1190–1202
- [Yan 2011] Yan B, Boriskina SV et al (2011) Design and implementation of noble metal nanoparticle cluster arrays for plasmon enhanced biosensing. J Phys Chem C 115(50):24437–24453
- [Yon2015] Yonemaru Y, Palonpon AF et al (2015) Super-spatial-and-spectral-resolution in vibrational imaging via saturated coherent anti-stokes raman scattering. Phys Rev Appl 4(1):014010
- [Zhu 2004] Zhu Z, Zhu T et al (2004) Raman scattering enhancement contributed from individual gold nanoparticles and interparticle coupling. Nanotechnology 15(3):357
- [Zit2015] Zito G, Rusciano G et al (2015) Surface-enhanced Raman imaging of cell membrane by a highly homogeneous and isotropic silver nanostructure. Nanoscale 7(18):8593–8606
- [ZS2005] Zou S, Schatz GC (2005) Silver nanoparticle array structures that produce giant enhancements in electromagnetic fields. Chem Phys Lett 403(1):62–67

# Chapter 3 Investigation on Nanoparticles and Their Molecular Functionalization



The essential building blocks of SERS-active systems we have studied are noble metal nanoparticles (Nps). They constitute the metallic substrate crucially contributing to SERS amplification thanks to the enhancement of the local electromagnetic field. Nowadays, Nps of various shape, size and material can be fabricated with a high degree of precision [Sch2011, Sam2013, KV2008] and their chemical properties can be tuned by employing different ligands [Per2009, Vit2011, Car2017]. In addition, nanolithography techniques as electron beam lithography (EBL) and photolithography (PL) allow to manipulate metallic and non-metallic substrates and to engineer their chemical properties at the nanoscale [Col2009, Hul1999].

Spherical, water dispersed Nps are probably the simplest SERS substrate available. Nevertheless, their low-cost and readiness, along with the possibility to form hot-spots by inducing their aggregation, leading to huge local field intensity, represent a great advantage for applications. For these reasons, in terms of performances they can be considered competitive with the other most refinely fabricated nanosystems. Nanoparticles used for SERS application are typically sized between 20 and 100 nm. This aspect is interesting for biological applications, as the small Np size facilitates the interaction with living cells [Kne2010].

For what concern SERS purposes, the essential feature of these nanostructures is their surface plasmon resonance (SPR), which directly affects the Np optical response. As discussed in Chap. 2, the plasmon resonance is strongly influenced by shape and size of the nanostructure, as well as its material and dielectric environment. These aspects need to be controlled for SERS substrate preparation. It is also important to test the stability of the nanostructures both in the colloidal and in the solid form (i.e. organized on a substrate), because it is well known that Np uncontrolled aggregation can result in a strong modification of the nanostructure SPR, due to the hybridization of the single Np plasmonic modes [Nor2004, Sön2005]. Hence, a thorough characterization of the Nps implies the combined use of different techiniques.

In particular, one can obtain information on a number of characteristics of the Np, among which:

#### • size and morphology

When the Nps are in dispersed in solution, dynamic light scattering (DLS) presents as a straightforward technique for monitoring their hydrodynamic radius [BP1976]. On the other hand, when investigating metallic nanostructures in the solid form (i.e. fixed on a dried sample) electron microscopies such as Scanning Electron Microscopy (SEM) or Transmission Electron Microscopy (TEM) are more appropriate. In particular, TEM allows achieving better resolution but requires a rather demanding sample preparation, while SEM is more versatile. Scanning probe microscopies are also useful, primarily for their non desruptivity: among these, Atomic Force Microscopy (AFM) can be performed at ambient conditions (without the need of a vacuum environment) and also in liquid, provided that the Nps are bound to a substrate [Dom2016].

### • surface charge

The  $\zeta$ -potential is the electric potential around a Np in solution, relative to a point in the bulk fluid away from the Np surface. It is a key indicator of the stability of colloidal dispersions. The magnitude of the  $\zeta$ -potential indicates the degree of electrostatic repulsion between adjacent, similarly charged particles in a dispersion. For molecules and particles that are small enough, a high  $\zeta$ -potential will confer stability and the dispersion will resist aggregation [Hun2013].

## • plasmon resonance and dielectric environment

UV-Visible measurements are the most direct approach to investigate the plasmon resonance of metal nanostructures. Extinction measurements can be easily performed on nanocolloids in suspension to monitor their SPR: in the case of spherical Nps (with diameters  $d=20 \div 100\,\mathrm{nm}$ ), the plasmon peak of silver colloids is centered in the blue region of the spectrum, while for gold Nps it is found in the green region. The SPR peak is sensitive to the Np dielectric environment, and its frequency shift is often used to control the molecular conjugation of the Nps, as it happens in SPR sensors [NC2002]. Np aggregation dramatically influences the plasmon resonance. Typically, hybridized inter-Np plasmonic modes cause the appearence of a large peak at lower frequency, with respect to single Np SPR, resulting in an overall broadening of the plasmon band [Nor2002].

#### • molecular conjugation

For what concerns the binding or location of molecules on the Np surface, indirect information can be deduced from the frequency shift of the plasmonic peak. UV-Visible spectra also contain absorption bands relative to the electronic excitations of most of the organic molecules. Other elemental techniques for surface investigation, such as photoemission spectroscopy, can be employed for monitoring the chemical processes occurring at the metal surface [Bat2012]. However, more precise structural information can be derived from surface enhanced spectroscopies. Surface Enhanced Infrared Absorption (SEIRA) and SERS techniques can provide information on the molecular environment surrounding the Nps, including

**Fig. 3.1** 4-aminothiophenol and its possible conjugations

structural signatures indicating the molecular organization, the orientation on the substrate, etc. [Cot2015].

We will here present the results concerning the functionalization of different noble metal nanocolloids and the characterization procedures which allowed us to study these systems. In Sect. 3.1, as an example, we will examine the covalent functionalization of Nps with the well-known ligand 4-aminothiophenol (4ATP), which was also used as a test probe for the design of SERS substrates described in Chap. 4. Beside its stability, the main advantage of using this molecule is the fact that 4ATP is a hetero-bifunctional linker. Indeed, as shown in Fig. 3.1, thiol group (-SH) allows to realize a simple covalent bond with a metal (e.g. S-Ag, S-Au), while the exposed amine group (-NH<sub>2</sub>) enables the further conjugation with other organic molecules.

In the following Sect. 3.2, the biofunctionalization of 4ATP-Nps with folate and antifolate molecules via amide bond will be probed with SERS: the structural information, that can be indirectly inferred from the spectroscopic analysis, are of great relevance for the application of these systems in the nanomedical context.

#### 3.1 Model Functionalization with 4ATP Linker

# 3.1.1 Preparation and Control Characterization

The preparation of 4ATP conjugated Nps is a rather simple process, as the functionalization of noble metal surfaces with molecules exposing a thiol group takes place spontaneously via S-Au or S-Ag covalent binding. To do so, we have purchased water-dispersed, citrate stabilized gold and silver nanocolloids of 60 and 100 nm size (Ted Pella Inc., Redding, CA). An ethanol solution of 4ATP at the concentration of 0.1 mg/mL was prepared and added to the water-dispersed colloid in a volume of  $5\,\mu\text{L}$  (see panel a of Fig. 3.3). The relatively high concentration of 4ATP in solution ensured that the final dispersion contained enough molecules to reach the complete covering of the Np surface. The number of molecules needed was estimated from geometrical considerations. The covalent binding of 4ATP molecules on the Np surface was followed over time by monitoring the sensitive localized SPR absorption modes with UV-Vis absorption measurements as a function of time (see Fig. 3.2).

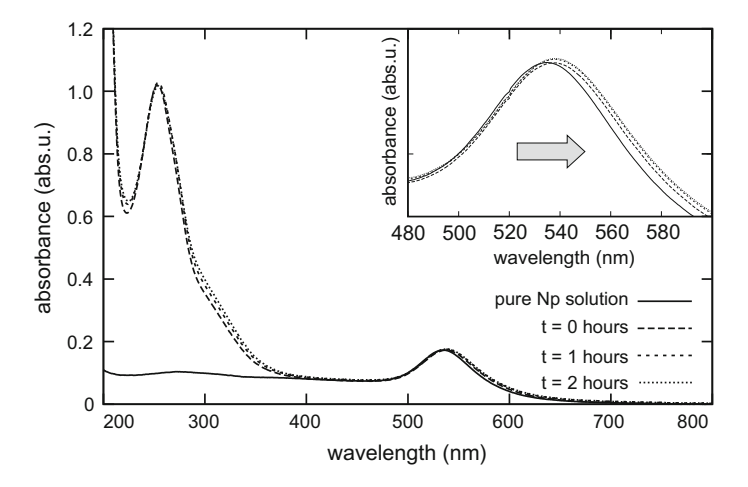


**Fig. 3.2** UV-Visible absorption acquired on a solution of AuNps (60 nm diameter) as a function of time, while monitoring their functionalization with 4ATP molecules (absorption bands of 4ATP are well visible below 300 nm wavelength). In the inset, the zoom allows monitoring the shift of the plasmonic peak of the Nps upon chemical conjugation

The change in the local dielectric environment at the metallic interface, occurring upon binding of the 4ATP molecules, caused the single particle plasmonic peak to broaden and red-shift [HV2001, Yos2009, Dom2011].

The absorption band for 60 nm diameter AgNps shifted indeed from 430 nm for bare (as purchased, citrate capped) Nps to 445 nm for conjugated Nps (in the case of 100 nm Nps, the peak shifted from 497 nm to 534 nm). Similarly, the plasmonic peak of AuNps shifted from 535 nm to 538.5 nm. This phenomenology is commonly observed in plasmonic nanostructure conjugation protocols, although the absolute plasmon frequencies and the amount of the shifts obviously change from sample to sample. Since we can reasonably assume that the red-shift is roughly proportional to the number of molecules adsorbed onto the Nps, we can state that, at the maximum shift, the Np surface covering by 4ATP molecules is complete (i.e., the surface is "saturated"). Considering the steric hindrance of 4ATP molecules, we estimate that about 5000–10000 4ATP molecules can fully cover a single 60 nm Np (15000–30000 for a 100 nm Np) [HV2001].

The complete functionalization of Nps with 4ATP typically takes place over few (2.5) hours. The following preparation step is the purification of the obtained nanocolloid. To do so, the samples were dialyzed against deionized (MilliQ) water for 12 hours, to eliminate from the suspension the residual 4ATP molecules, not bound to the Np surface, and the Np citrate capping agent (panel b in Fig. 3.3).

As explained in previous Sections,  $\zeta$  potential and DLS measurements can assess the size and the stability of the dispersed Nps. Generally, a low absolute value (negative or positive) of the  $\zeta$  potential in a nanocolloid indicates a very low electrostatic repulsion among the Nps, which tend to aggregate (threshold value for the stability is

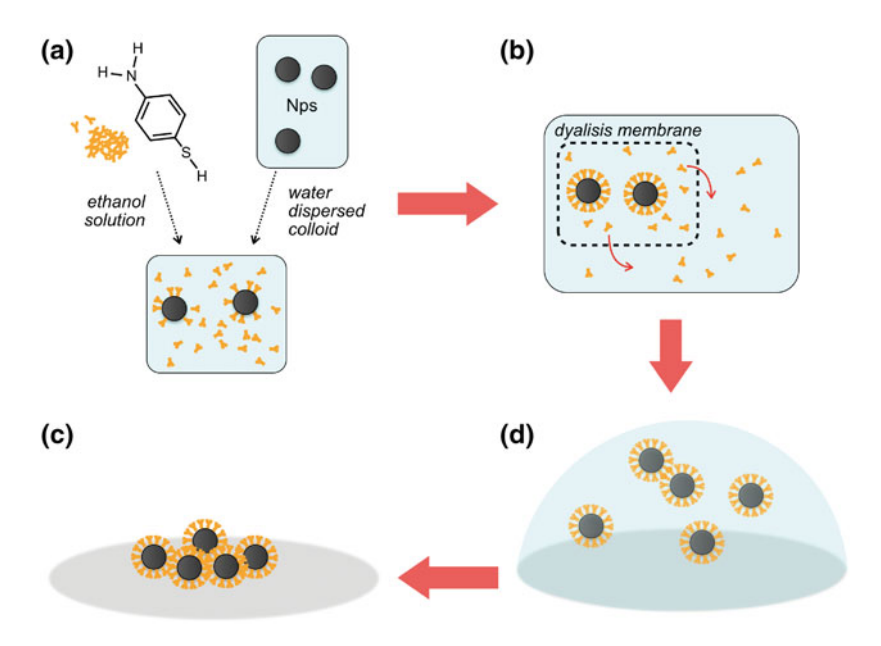
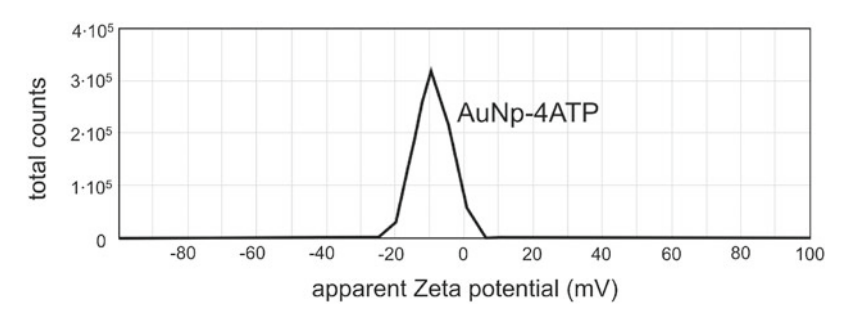


Fig. 3.3 Schematic sketch illustrating the process of nanoparticle functionalization with 4-ATP molecules



**Fig. 3.4** ζ potential measurement on 4ATP functionalized AuNps (60 nm diameter)

 $\sim \pm 30\, \mathrm{mV}$ ). When purchased, the nanocolloids are very stable dispersions, but once the Nps are functionalized with 4ATP, as can be seen in Fig. 3.4 in the case of AuNps (60 nm diameter), the value of  $\zeta$  potential decreases to  $-10\,\mathrm{mV}$ . As a result the 4ATP-AuNps, which size is initially centered around  $\sim\!60\,\mathrm{nm}$  (see Fig. 3.5, black spectrum), aggregate in larger structures: this is witnessed by the retarded DLS measurements, performed on the same sample during the following 12 hours (Fig. 3.5).

The 4ATP conjugated, purified colloids were then induced to self-organize in clusters on the surface of a coverslip glass. Water evaporation took place in a climatized chamber at 45°C. The aggregation of the Nps in mesoscopic clusters on the substrate

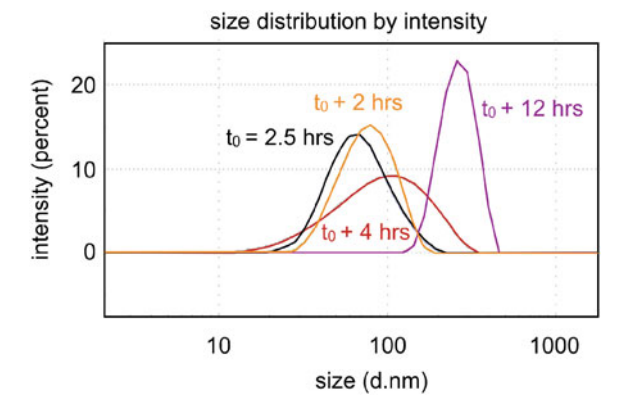
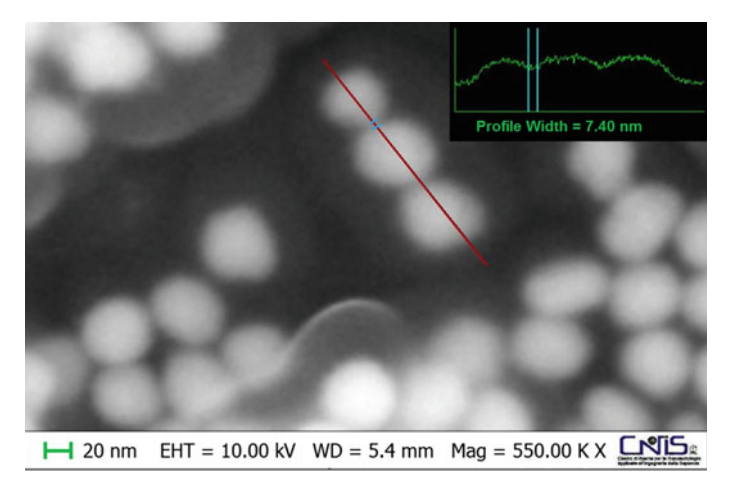


Fig. 3.5 DLS measurements on 4ATP functionalized AuNps (60 nm diameter) as the reaction was completed (2.5 h) and after 2, 4 and 12 h



**Fig. 3.6** SEM image of a 60 nm nanoparticle cluster showing the typical interparticle distance (approximately 5–7 nm)

was observed by SEM imaging, as shown in Fig. 3.6. The clusters are closely packed, with a very small interparticle spacing (5–7 nm, comparable with the instrumental resolution considering the non-conductive nature of the glass substrate). This suggests a very high density of hot-spots in the structure. SERS measurements were performed on these dried, stable samples. A more detailed discussion about the field enhancement and signal amplification provided by these substrates, in relation with the aggregate morphology, will be presented in Chap. 4.

# 3.1.2 SERS Versus Raman Spectrum

In Fig. 3.7, we compare surface-enhanced Raman spectra acquired on representative 4ATP-Np clusters (solid lines) with the Raman spectrum of bulk 4ATP (dashed spectrum). For sake of visualization, the spectral intensities were normalized to the most intense spectroscopic band on the range. The 4ATP-Nps functionalization via Smetal covalent bond is witnessed by the disappearance of the Raman band assigned to the S-H stretching of the thiol group, around 2560 cm<sup>-1</sup>[Fas2014, Dom2011]. Marked differences are noticeable between the SERS spectrum of 4ATP from the mesoscopic Np clusters and its conventional Raman signature, particularly when comparing the spectral intensities (see the caption of Fig. 3.7). Indeed, all peaks exhibit a huge enhancement with a strong spectral weight redistribution.

In particular, SERS spectra feature around 1400 cm<sup>-1</sup>a large and intense spectral structure with two main bands, ascribed to C–C stretching and C–H bending in the molecule [Osa1994]. These are hardly detectable in the Raman spectrum in Fig. 3.7. Moreover, all the SERS bands exhibit an appreciable red-shift (typically 15–20 cm<sup>-1</sup>) with respect to the conventional Raman peaks. This is an expected characteristic of SERS spectra [Osa1994]. The frequency of the main Raman and SERS bands was estimated with a Lorentzian fitting procedure (see Fig. 3.8). The results of the analysis are reported in Table 3.1, together with the assignment and mode symmetry.

The different measured intensities were found to be related primarily, as expected, to the Np material. It is well known, indeed, that silver substrates provide higher enhancements with respect to their gold counterparts: in our case, the difference is

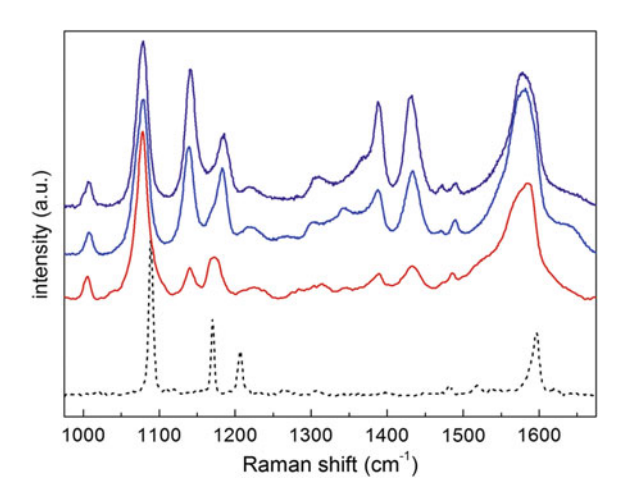
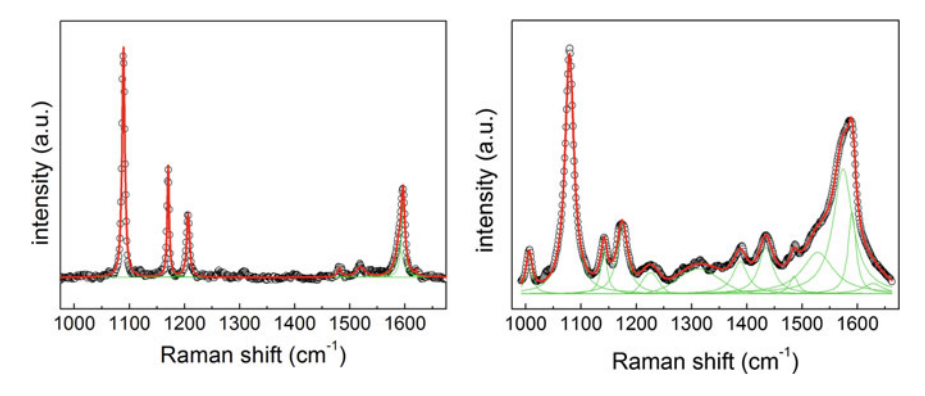


Fig. 3.7 Raman and SERS spectra of 4-aminothiophenol, obtained by bulk 4ATP and by 60 nm 4ATP-AuNps and by 60 nm,  $100 \, \mathrm{nm} \, 4ATP$ -AgNps, respectively. Spectra are normalized to the height of the most intense band (C-S stretching, at  $1078 \, \mathrm{cm}^{-1}$ ). Scale factors of  $10^6$  for 4ATP-Au and of  $10^8$  for 4ATP-Au, with respect to the bulk 4ATP spectrum, are to be considered. The spectral region shown here includes the most intense spectroscopic signature of 4ATP, for both SERS and Raman



**Fig. 3.8** Fitting of Raman spectrum of 4ATP in powder (bulk) form (left) and SERS spectra obtained on a cluster of aggregated 4ATP-AuNps (right). Similar results are obtained for SERS from Ag substrates

**Table 3.1** Frequency of the principal Raman and SERS band of 4ATP estimated through a careful fitting procedure (see Fig. 3.8). The band assignment is reported, together with the indication of the vibrational mode symmetry ( $C_{2v}$ ) for the benzene ring, according to Refs. [Osa1994, Kho2012]. In detail:  $\nu$ , stretching;  $\gamma$  and  $\delta$ , bending;  $\rho$ , rocking

Raman frequency (cm <sup>-1</sup> )	SERS frequency (cm <sup>-1</sup> )	Assignment
-	1006	$\gamma$ (CCC), $\gamma$ (CC) ( $a_1$ )
1089	1078	$\nu(CS)(a_1)$
_	1138	$\delta$ (CH) $(b_2)$
1170	1174	$\delta$ (CH) $(a_1)$
1206	_	
_	1388	$\rho$ (CH) + $\nu$ (CC) ( $b_2$ )
_	1434	$\nu(\text{CC}) + \rho(\text{CH}) (b_2)$
1590	1574	$\nu(CC)(b_2)$
1597	1590	$\nu(CC)(a_1)$
1620	1628	$\rho(\text{NH}_2)$
2560	_	$\nu(SH)$

on average of 2 orders of magnitude (see the next Chapter). In the case of AgNps of different diameter, the changes in intensity seemed to be related to the different cluster morphologies rather than to the Np diameters (see Sect. 4.1 for a thorough discussion).

The most evident difference among SERS spectra in Fig. 3.7 is related to the relative intensity of the bands in the spectrum. The peaks of the modes with  $b_2$  symmetry (in particular the ones centered at 1138, 1388, 1343 cm<sup>-1</sup> and the low frequency component of the CC stretching band at 1574 cm<sup>-1</sup>) seem to experience variable enhancement. This is related to the physical mechanism of signal amplification. For 4ATP molecules bound to nanostructured silver or gold, the enhancement of the  $b_2$ 

bands has been the subject of a heated debate. Indeed, some works suggested the arising of the bands to be related with 4ATP photodimerization via azo bond [Hua2010] or to be pH sensitive when the measurements are performed in solution [Kim2012]. Nevertheless, there seem to be a strong consensus around the idea of a Herzberg Teller charge transfer enhancement of these bands [Osa1994, Bai2006]. In agreement with this hypothesis, the paper of Zheng and coworkers [Zho2006] ascribed the appearence of  $b_2$  bands to the compression of 4ATP molecules in Np interstices and suggested that the metal bound both the thiol and the NH<sub>2</sub> ends of the molecule. This was confirmed by Moskovits and coworkers, with the observation of alternating appearance of these modes when reversibly tuning the inteparticle distance of 4ATP-Nps [Kim2010, Kim2011]. In summary, we think that the CT mechanism is responsible for the enhancement of  $b_2$  peaks, being the effect probably modulated by the molecular orientation with respect to the surface and by the width of the inter-Np gap.

To summarize, SERS spectra intrinsically show several differences with respect to their Raman analogues:

- Enhanced intensity The remarkable amplification of SERS intensity is straightforwardly observable, as very short acquisition times in SERS experiments, compared to conventional Raman ones, lead to very good signal to noise ratios. This effect can be quantitatively estimated by calculating SERS enhancement factor EF: several approaches to this problem are possible [Le 2007], but the most common definition for EF is given by Eq. 2.30. EF is there defined as the ratio between SERS and Raman intensity, obtained by peak integration, normalized to the single molecule contribution. In our Np-aggregates, it is of the order of 109 for silver Nps and of 107 for gold Nps. Enhancement factors can be used to quantify SERS efficiency of different substrates, and will be deeply discussed in the next Chapter.
- New bands Raman and SERS spectra are not discriminated just for their different intensity. Indeed, SERS experiments are characterized by a strong modification of the system under investigation, due to the molecular proximity to a metal surface. This can cause a relaxation of Raman scattering selection rules, and the appearence in SERS spectrum of bands which are not detectable in the conventional Raman signature of the molecule [Kne2006].
- Frequency shift For the same reasons, the bands commonly undergo a frequency shift. This can be related to charge transfer mechanisms that can modify the electronic polarizability and/or the strength of chemical bonds inside the molecule [Kho2012].
- Intensity ratio As discussed in the case of  $b_2$  modes of 4ATP, the intensity ratio between specific peaks can undergo a certain variability in SERS experiments. This is related to the different signal amplification mechanisms in SERS. Nevertheless, electromagnetic-enhanced peaks always show reproducible intensity ratios, and constitute the stable scaffold of the SERS spectroscopic response of the molecules. In other words, the SERS fingerprint of a molecule, although different from the Raman one, can be identified, provided to expect a certain intrinsic variability, generally related to the CT processes.

# 3.2 Further Conjugation: Folate and Antifolates

As described in the previous Section, functionalizing noble metal Nps with 4ATP SERS probe enables the possibility of further chemical conjugation via the formation of an amide bond, exploiting the NH<sub>2</sub> group exposed by 4ATP. This is useful for applications implying the interaction of SERS-active nanostructures with cells. Several approaches for the biofunctionalization of SERS-labelled nanostructures have been reported in the literature. Often, they rely on the physisorption of biologically relevant molecules, that are conjugated through electrostatic interaction, hydrogen bond or similar interactions [Wan2014]. Nevertheless, for bioapplications a stable functionalization, based on a covalent bond, is usually preferable.

Taking these aspects into account, we have developed a procedure for binding folic acid to our 4ATP-AuNp, via amide bond [Fas2016]. This folate nanovector was designed for cancer diagnostics applications, that are thoroughly described in Chap. 5. The functionalization approach, described in the following paragraph 3.2.1, can be extended to molecules similar to folate, as folate binding competitors, as antifolate drugs. If properly employed, these antifolates can add therapeutic features to the nanovector: their cytotoxicity, for example, can be exploited for the selective elimination of targeted cancer cells [Far1948]. We will show that a SERS spectroscopic characterization of the system can be exploited for monitoring the functionalization procedure, also in terms of a quantitative analysis of folate/antifolate binding efficiency.

# 3.2.1 Nanovector Functionalization: The Case of Folate

The functionalization protocol for the preparation of folate/antifolate conjugated theranostic nanovectors is herein presented in detail: we provide the complete description and characterization results in the case of FA. As cytotoxic agents, we have chosen antifolates primarily because of their structural similarity to folate: this is also the reason for their toxic action against cancer cells. Indeed, they are recognized by the cellular receptors as folate molecules and, once internalized inside the cells, they bind irreversibly to the enzymes responsible for folate metabolism, eventually leading the cell to death [Wib2013, Che2013]. Owing to the similarity between folate and antifolates, the present protocol can be adopted, without substantial modifications, for antifolate conjugation.

## **Nanovector Preparation**

The functionalization reaction employed for the nanovector preparation takes place in water, without the addition of any other solvent: avoiding contamination is a great advantage for the application of this system in the treatment of cells.

A solution of folic acid (FA) is prepared in MilliQ water ( $c = 8 \cdot 10^{-3}$  M) and is stirred at each step to avoid FA precipitation. The molecule of FA contains two

carboxylic groups (-COOH), which constitute the reactive electrophilic centers involved in the nanovector biofunctionalization.

The conjugation of FA is achieved with the activation of these groups by means of 2 cross-linker specific molecules, that react with FA in sequence: *EDC* (1-ethyl-3-[-dimethylaminopropyl]carbodiimidehydrochloride) is a "coupling" reagent, which forms a highly unstable intermediate (O-Acilisourea active ester). Subsequently another activator, *NHS* (N-hydroxy-succinimide) reacts to form a less labile complex (activated ester succinate). In order to ensure the activation of the carboxylic groups of FA, EDC and NHS are added to the folate solution with the ratios FA/EDC (1:1) and EDC/NHS (3:1) [Cos2010]. The final solution is incubated for 30 minutes at room temperature (25°C) to form the stable covalent adduct FA-NHS.

The last stage is the reaction between the FA-NHS adduct and the functionalized 4ATP-AuNps, prepared as described in Sect. 3.1.1. FA is kept in excess to favor the most efficient covering of the Nps. It is important to stress that the reaction of covalent functionalization between FA and 4ATP does not occur with a stoichiometric ratio of 1:1 as a result of steric hindrance. The reaction is carried out at 4°C, for 12 hours. Then, the solution is dialyzed for 24 hours against MilliQ water in order to remove the residual FA. During dyalisis, the presence of FA in the dialysis water can be monitored over time by means UV-Visible absorption spectroscopy.

**Chemical details** As already explained, the reaction mechanism discussed above requires a first activation, of one of the carboxyl groups of FA, by the reactive portion of EDC (carbon-heteroatom double bond) (Fig. 3.9).

Fig. 3.9 1, 2 nucleophilic addition

This is a 1, 2 nucleophilic addition (i.e., a  $\pi$  bond is removed in favor of the formation of 2 new covalent bonds). The intermediate that is formed is an active "high-energy" ester. Then, the second activation of the carboxylic group via NHS takes place. This molecule is used in organic synthesis and in biochemical reactions, mostly assisted by a coupling reagent as EDC, chosen here. The activated acids can react with amines to form, for example, amides, while an ordinary carboxylic acid reacting with an amine can form a salt compound only.

In the second step, the intermediate *O-acilisourea active ester* undergoes a *SN2 substitution* reaction (i.e. a reaction where a bond is broken and a new bond is formed simultaneously, in the absence of the carbocationic intermediate), where *EDC* is substituted with *NHS* to form a *NHS* ester. Therefore, the carbonyl carbon of FA is now electrophilic enough to be attacked by a nucleophilic agent which, in our case, is the amino group of 4ATP (Fig. 3.10).

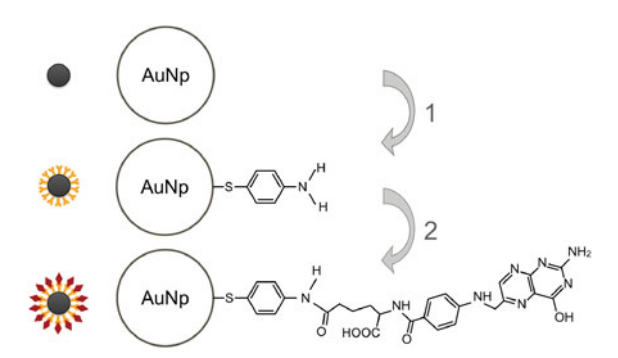
$$R_1$$
 $R_1$ 
 $R_2$ 
 $R_3$ 
 $R_3$ 

Fig. 3.10 First SN2 reaction

The last step can be summarized in a second *SN2 nucleophilic substitution* which, if occurring at slightly basic pH, allows the release of NHS by breaking a second ester bond, with the formation of an amide bond. The group R' in Fig. 3.11 obviously represents 4ATP. The complex FA-4ATP-Np results therefore successfully formed.

Fig. 3.11 Second SN2 reaction

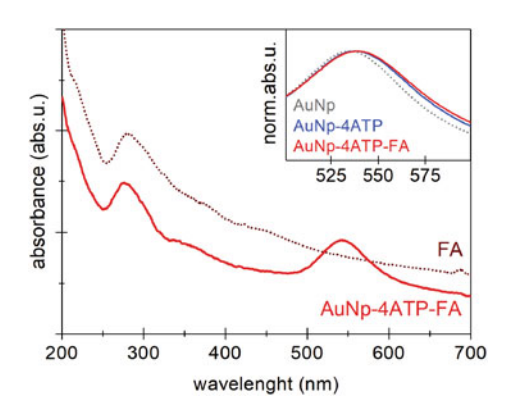
A sketch of the two main steps of the Np functionalization reaction is shown in Fig. 3.12. As can be noticed, the final structure of the nanovector there schematized is one of the possible binding configurations (being thought the most probable [Man2010]) involving the two carboxyl groups of folic acid. Both the configurations constitute an oriented binding, as the interacting part of the folate molecule, the heterocyclic part, is the farthest from the Np, being left externally with respect to the Np surface, ready for biointeractions.

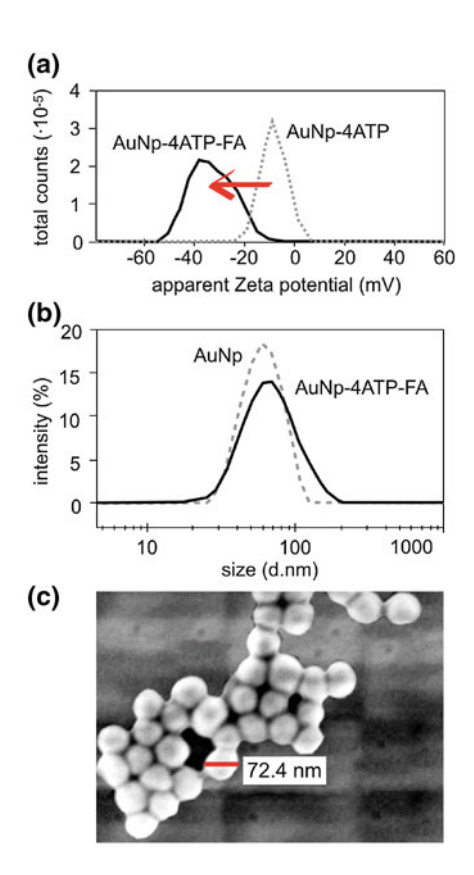


**Fig. 3.12** Main steps of the gold nanoparticle functionalization: AuNp are firstly conjugated with the Raman reporter 4ATP (1), than conjugated to folic acid (2). The sketch of the final structure is a result of one of the possible oriented binding configurations involving the carboxilic moieties of folic acid. In such configurations the folate pteroyl group is kept exposed to water and free to bind to membrane receptors

Fig. 3.13 Optical absorption of the nanovector: UV-Visible spectra of bulk folic acid (wine, dotted line) and of the complete nanovector dispersion at low concentration (solid red line). Inset: shift of the plasmonic peak of AuNps at different steps of the functionalization: bare Np (gray, dotted), 4ATP-Np (blue, solid) and FA-4ATP-Np (red, solid line). Spectra in the inset are normalized to the plasmonic peak intensity

Fig. 3.14 Nanovector characterization during the functionalization. Panel a  $\zeta$ Potential measurements at different intermediate functionalization steps. Panel **b** Dynamic Light Scattering size measurement of bare Np (gray, dashed) compared to FA-4ATP-Np (black, solid line). The final size distribution is centered around 70 nm, as revealed also by FESEM measurements shown in panel c. The latter image was acquired from a Np deposition on a glass slide, without any metallization of the substrate, at low voltage (1 kV) to avoid sample degradation





#### **Control Characterization**

After preparation, the folate nanovector was characterized in solution. First of all, its optical absorption was monitored with UV-Visible spectroscopy, as shown in Fig. 3.13. In the absorption spectra, we can recognize the presence of folate absorption bands as well as the plasmonic peak of the conjugated Nps, which is shifted compared to one detected on bare Np and 4ATP-Np. This is due to the change in the dielectric environment at the Np surface related to the FA biofunctionalization. The final size and colloidal stability of the nanovector were then tested by  $\zeta$  potential and DLS measurements. The results are shown in Fig. 3.14.

Owing to the conjugation with FA, the nanovector is highly stable in water solution, as witnessed by a high negative value ( $-38\,\text{mV}$ ) of its  $\zeta$  potential. This implies that the nanovector aggregation will be prevented by the Np surface charge. Indeed, DLS measurements detected a size distribution centred around 70 nm diameter (see Fig. 3.14b). This result for a single Np size is compatible with estimates obtained by SEM imaging (panel c). Similar results on the nanovector dispersed in PBS and even in cell culture medium imply a remarkable stability and a nice versatility of the system [Fas2016].

A complementary spectroscopic characterization was obtained by Fourier transform infrared absorption measurements performed at different steps of functionalization and shown in Fig. 3.15. The spectrum of the complete nanovector features an extra peak (highlighted by the arrow in the Figure) with respect to the signature

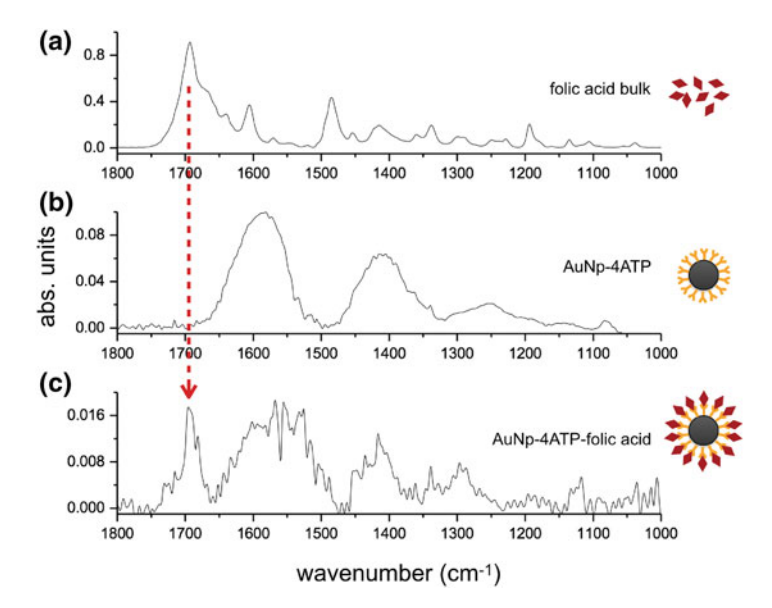


Fig. 3.15 FTIR measurements on folic acid bulk (a), 4ATP-Nps (b) and FA-4ATP-Nps (c). The red arrow highlights the absorption band assigned to the carbonyl group of folic acid

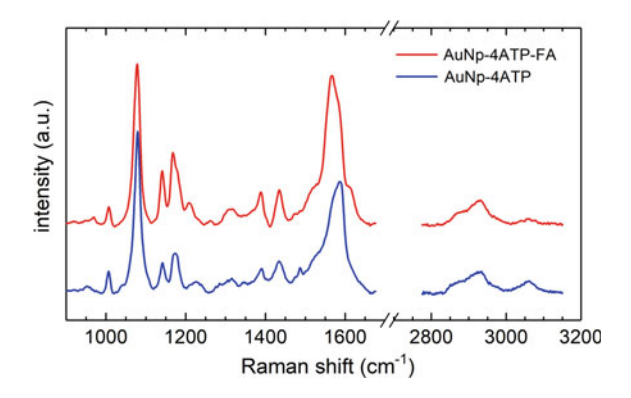
of 4ATP-Nps (panel b): this can be related to the FA shell. The new band indeed corresponds to the IR absorption peak assigned to the carbonyl group (—CONH—in the case of FA-4ATP-Np complex) [Sha2010]. It is centered around 1700 cm<sup>-1</sup>: slight intensity modification and frequency shifts in the nanovector spectrum (panel c) with respect to the bulk (panel a) are ascribed to the gold Np surface enhanced infrared absorption effect [Bai2009].

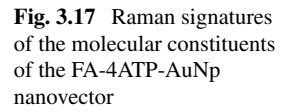
# 3.2.2 SERS Signature of Folate/Antifolate Nanovectors

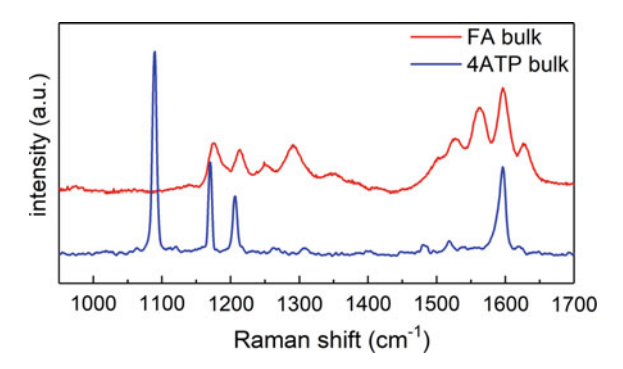
Representative SERS spectra acquired on assemblies of functionalized FA-4ATP-AuNps and 4ATP-AuNps are displayed in Fig. 3.16. The main recognizeable spectroscopic fingerprint on both spectra can be ascribed to the 4ATP linker. As a reference, we reported the conventional Raman fingerprint of 4ATP and folic acid in the bulk form in Fig. 3.17. The predominance of the 4ATP signature, with respect to the one of folic acid, can be motivated by several reasons: (i) the higher distance of FA molecules from the Np surface, which lowers the signal enhancement; (ii) the lower Raman cross section of FA and (iii) the lower amount of FA molecules. According to our estimate, indeed, the covalent conjugation between FA and 4ATP onto the Np surface occurrs with a stoichiometric ratio of around 1:6 (see the next Section).

SERS spectra on FA conjugated 4ATP-AuNps feature rather weak but clear and reproducible modifications with respect to the 4ATP-Nps spectroscopic reference. Literature on SERS spectroscopy has demonstrated that few cm<sup>-1</sup>shifts of specific peaks, as well as reproducible changes in the lineshapes of SERS bands, can be related to chemical conjugation events. This is particularly true in the case of widely studied molecular SERS probes as 4ATP [Kho2012, Güh2015]. In benzene-like molecules, in particular, the phenyl ring C–C stretching Raman mode results in a strong intense SERS band observed around 1580 cm<sup>-1</sup> and composed of two distinct components with different symmetry (see Table 3.1). This band is particularly susceptible to the type of chemical substituents in the molecule and their electronic properties [Jia2005, Bai2006, Dav2013, Sch1977, TS1988].

Fig. 3.16 SERS spectra acquired on 4ATP-AuNps (blue) and FA-4ATP-Nps (red) aggregated on a glass substrate







Starting from these considerations, we have focused on the C–C stretching band to perform a high resolution spectral analysis comparing the signature of FA bioconjugated and reference 4ATP-Nps. Signal was acquired using a  $100\times$  objective upon illumination of the sample with 1 mW incident power of a 633 nm HeNe laser. A diffraction grating with 1800 groves/mm ensured a spectral resolution better than 1 cm<sup>-1</sup>. The average SERS spectra were obtained by mediating several sets of spectra acquired from different, 2  $\mu$ m spaced points in a two-dimensional scan, typically over a  $16\times16$   $\mu$ m<sup>2</sup> area on the sample. Measurements on distinct points did not differ in the spectral shape but by an overall intensity factor: this is expected in a self-assembled SERS substrate, as will be discussed in the next chapter. The average spectra of FA conjugated and reference 4ATP-Nps are displayed in Fig. 3.18.

It is revealed that folate conjugation induces a strong change in the relative weight of the two band components, that are highlighted in the spectra in Fig. 3.18 ( $\nu_a = 1568.0 \pm 1.0 \, \mathrm{cm^{-1}}$ ,  $\nu_s = 1586.7 \pm 0.4 \, \mathrm{cm^{-1}}$ ). This change increases the relative weight of the low frequency component in the biofunctionalized sample. As previously mentioned, the two band components are assigned to different symmetries of the C–C stretching mode [Kho2012], being the low frequency one assigned to the antisymmetric vibration, the high frequency to the symmetric one. It is well known that a change in the relative weight of these two spectral components is associated to a modification in the charge distribution in the molecule. This can be driven by a mechanical stress or, more commonly, by the onset of charge transfer processes due to molecular modifications [Kho2012, Güh2015] as in our case, because of 4ATP-FA covalent binding. In particular, as displayed in the simplified scheme in Fig. 3.19, the modification of the primary aromatic amine occurring upon the formation of the amide bond triggers the mesomeric delocalization of the amide nitrogen lone pair and hence the occurrence of multiple aromatic resonance structures [SF2010].

By comparing the spectra in Fig. 3.18 it is also possible to distinguish some side bands. These are less intense spectral structures reproducibly detected in the case of folate and antifolate functionalization (see also Fig. 3.23 in the next paragraph and related comment). References from literature [Ren2011, Hid2014] and conventional Raman signal of folic acid (see Fig. 3.17) allow to ascribe these peaks to the SERS signature of folate and antifolate molecules.

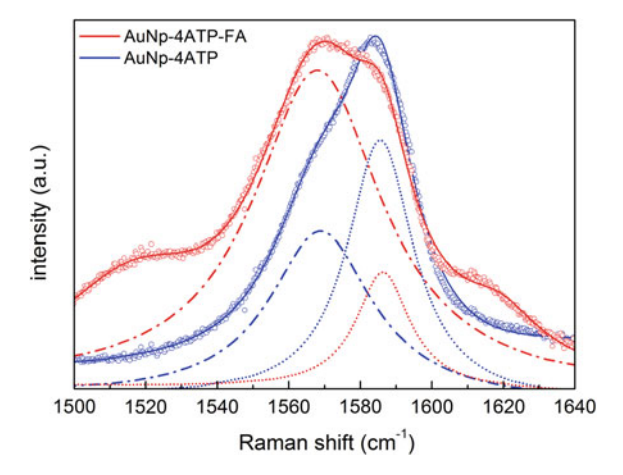


**Fig. 3.18** High resolution SERS spectra of the spectral region around the C–C stretching band acquired on 4ATP-AuNps (blue) and on FA-4ATP-AuNps (red). The fitting curve (solid line) is superimposed to the experimental data (scatter plot). Dashed-dotted and dotted lines identify the two main spectral components revealed in the fitting (lorentzian curves). They are assigned to the antisymmetric and symmetric modes of C–C stretching, respectively

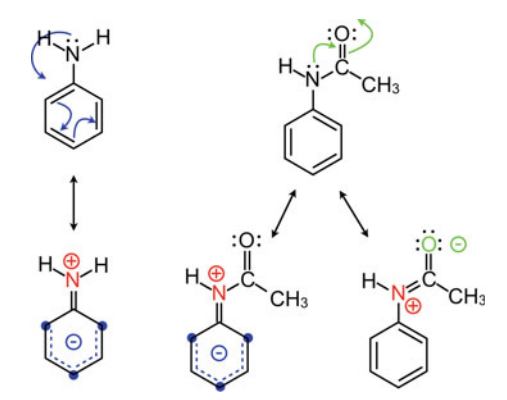


**Fig. 3.19** The typical resonance structures of acetanilide are shown. These derive from the non-bonding valence electron pair of the aromatic amino substituent diverted to the adjacent carbonyl group of the amide bond, and provide in turn an electronic delocalization change along the Raman active aromatic CC bonds

As anticipated in Sect. 3.1, employing SERS for investigating metal Np functionalization has the advantage, compared to other techniques, of granting the specific identification of the molecular species that are in close proximity to the metal surface. In fortunate cases, SERS can allow the direct monitoring of chemical conjugation through the appearence of new peaks related to the formed chemical bond. This is for example the case of diazotization (with the formation of a N=N bond) [Dom2012]. Unluckily, in the case of 4ATP-folate conjugation, such an approach would imply

the binding to involve the pteroyl part of the molecule (see Fig. 5.4), which is the one involved in the biorecognition of folate by cellular receptors [Che2013]. On the contrary, folate conjugation via amide bond, involving one of the two carboxile groups of the molecule, ensures not only the structural integrity of the ligand moiety driving the interaction with receptors, but also the correct molecular orientation which optimizes this interaction, as deeply discussed in Chap. 5.

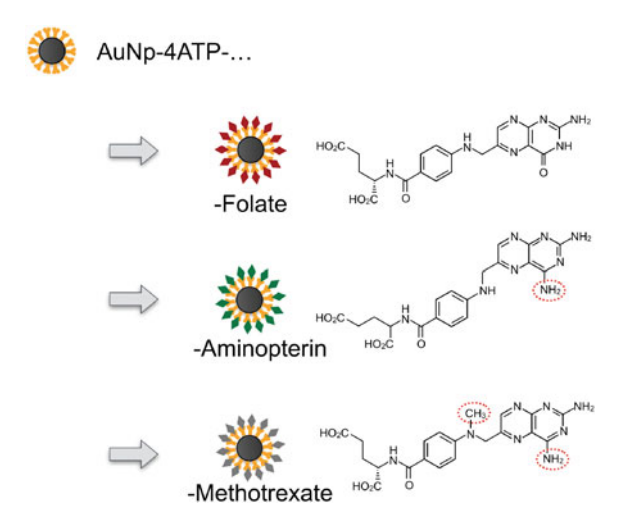
## **Folate Substitution with Antifolate Drugs**

In principle, the functionalization approach illustrated is very general and can be adopted for inducing the conjugation of 4ATP-AuNps, via amide bond, also with molecules different from folate. Here we present the results obtained in the binding of 4ATP-AuNps with antifolate drugs aminopterin (AMT) and methotrexate (MTX), as sketched in Fig. 3.20. The results obtained by applying these systems for cancer theranostics purposes will be discussed in Sect. 5.3.

Here, we will focus in particular on the SERS characterization of these nanovectors. The functionalization strategy adopted for these conjugations is chosen because it grants an enhanced interaction with folate cellular receptors due to the oriented binding of folate/antifolate molecules on the Np surface (see Sect. 5.3). As already discussed, the identification of a SERS marker for the conjugation of folate/antifolate via amide bond is difficultly achievable. Nevertheless, a careful SERS analysis allowed to point out the success of the biofunctionalization and demonstrated eventually that SERS signal can provide information on the efficiency of folate/antifolate binding to the 4ATP-Nps, without requiring the employment of more demanding methods, such as UV-Visible based titration assays.

The control characterization previously described was performed on all the functionalized samples with positive results. As an example, we have reported in Fig. 3.21 the results of UV-Visible absorption measurements, showing the shift of the plas-

Fig. 3.20 Sketch illustrating the possibilities of chemical conjugation of 4ATP-Nps with folate and antifolate drugs



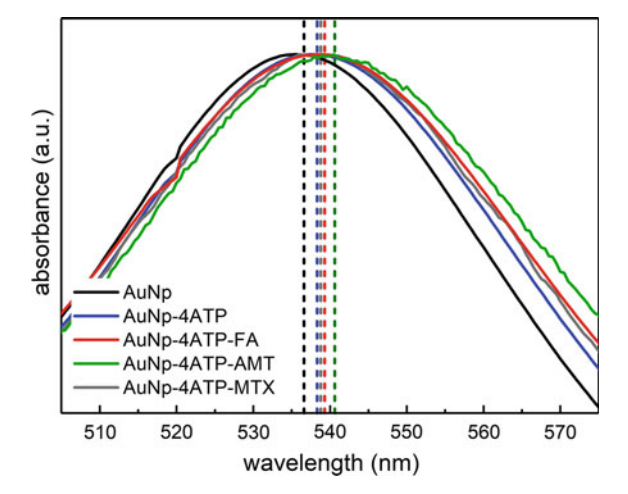


**Fig. 3.21** UV-Visible absorption measurements witnessing the shift of the plasmonic peak of AuNps upon different steps of functionalization: bare AuNp (black), 4ATP-AuNp (blue), FA-4ATP-AuNp (red), AMT-4ATP-AuNp (green), MTX-4ATP-AuNp (gray). Data have been normalized to the maximum of the plasmonic peak intensity, and dashed vertical lines mark the shift of the peak center

monic peak at different steps of the Np functionalization process. After checking the sample preparation, we have focused on the characterization of the SERS response: the results are reported in Fig. 3.22. The spectra were obtained from the average of 10 independent acquisitions and are normalized to the maximum intensity detected

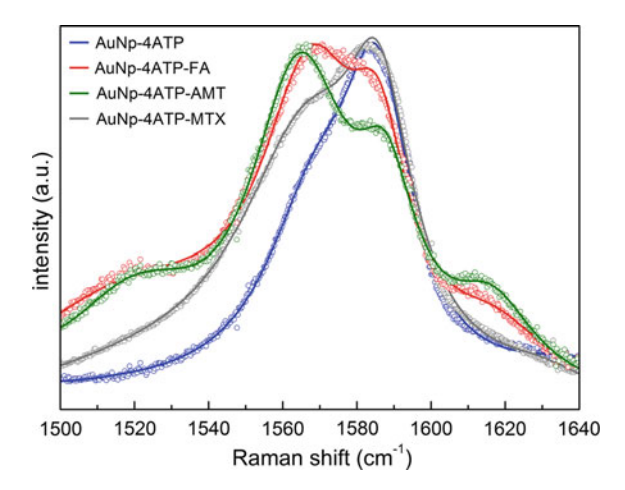


**Fig. 3.22** Experimental data (scatter) and fit (solid line) relative to the high resolution analysis of the band centered around 1580 cm<sup>-1</sup> in the cases of 4ATP-AuNps (blue), FA-4ATP-AuNps (red), AMT-4ATP-AuNps (green), MTX-4ATP-AuNps (gray). Data are normalized to the maximum detected intensity. The data reported are the mean of 10 acquisitions performed with the same experimental conditions (see the previous paragraph)

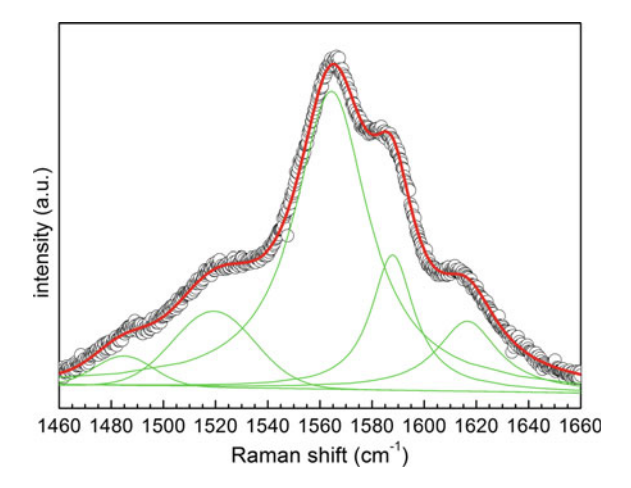


**Fig. 3.23** Experimental data (scatter) and cumulative fit (red solid line) of the SERS spectrum acquired on AMT-4ATP-AuNps assemblies. All the spectral components of the fit are plotted in green. The high intensity components of the C–C stretching of 4ATP are evident, while the weaker bands at the side of the spectral structure are to be ascribed to the SERS signature of AMT

(see the previous paragraph for experimental details on the measurement protocol). The spectra show analogue modifications in the case of folate-, aminopterin- and methotrexate-conjugated samples, in terms of both the modification to the strong C–C band and the appearence of other weak spectral structures close to the C–C stretching peak. These become evident by fitting this spectral region (see Fig. 3.23). In the case of methotrexate conjugation, the changes in the spectral shape and the appearence of the sidebands are weaker, but can still be recognized.

In our opinion, the differences between the spectra of FA-, AMT- and MTX-4ATP-AuNps evident in Fig. 3.22, depend on a different binding efficiency for the various folate/antifolate molecules, due to a different yield of the chemical functionalization reaction. This is qualitatively confirmed by UV-Visible absorption measuremens presented in Fig. 3.21, showing a weaker shift for the MTX-4ATP-AuNps bands. To bring further support to our hypothesis, we have compared SERS results with another titration approach, based on UV-Visible absorption spectroscopy.

## Molecular Conjugation Efficiency and Semiquantitative SERS

The binding efficiency in the folate/antifolate bioconjugation reaction was tested by realizing titration experiments, and counting the number of folate/antifolate molecules actually bound to the amines of the 4ATP molecules on the Np surface. Considerations based on steric hindrance arguments, estimating the covering of a 4ATP-AuNp with FA molecules, had led us to the rough estimate of approximately 2300 folate molecules bound to a single Np, at best. This estimate is in agreement with the results obtained experimentally.

The number of conjugated folic acid molecules was derived from the difference in the number of available 4ATP molecules before and after folate functionalization. The number of 4ATP primary amines (and therefore unconjugated 4ATP molecules) was quantified by using Coomassie Brilliant Blue (CBB) dye standard addition method [Cou2009].

A CBB solution at pH 2.2 was prepared in (H<sub>2</sub>O, MeOH, CH<sub>3</sub>COOH) with (80, 15, 5%) proportions respectively. The Np suspension was sonicated for typically 2 min in a sonicator bath, then CBB was gradually added until saturation. At each addition step, the suspension was incubated for 10 min at room temperature in the dark, then followed by centrifugation at 3900 rpm for 15 min. The absorbance of free CBB in the supernatant was measured by UV-Visible spectrophotometry at  $\lambda = 610$  nm with a 1 cm cell. Measurements were performed in triplicates.

Every CBB molecule is able to bind one single primary amine site [Cou2009]. Therefore, the amount of CBB bound to form the 4ATP-CBB complex is directly equivalent to the amount of 4ATP groups available on the Nps surface. This allows as well an indirect quantification of FA attached on the Nps, from the difference between the results obtained before and after FA conjugation. The number of FA molecules per Np is calculated from the following equation

$$N = \frac{(nc_1 - nc_2) \cdot N_A}{C} \tag{3.1}$$

where  $nc_1$ ,  $nc_2$  are the molar amounts of CBB bound to 4ATP-AuNps and to FA-4ATP-AuNps, estimated from the black and red trends in Fig. 3.24, respectively;  $N_A$  is the Avogadro number, and C is the number of AuNps.

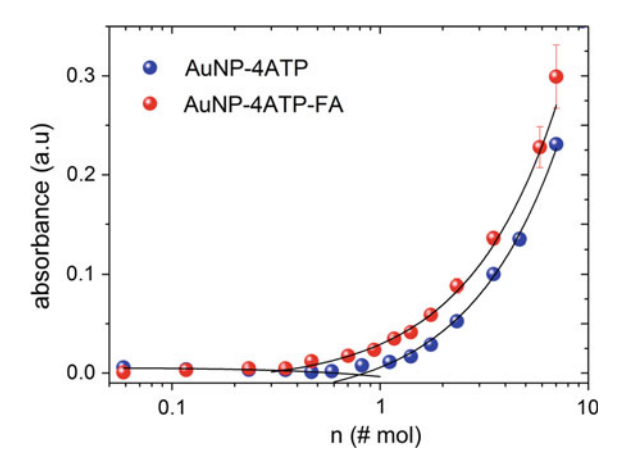


**Fig. 3.24** Titration of 4ATP primary amine groups available on the AuNps surface: supernatant absorbance is reported in function of the amount of CBB added to the Np dispersion. The red (FA-4ATP-AuNps) and black (4ATP-AuNps) lines are the linear titration fits before and after CBB saturation. The intersection corresponds to the critical saturation value, which determined the maximum amount of bound CBB

Accordingly, the mean number of 4ATP molecules bound to a single AuNp  $N_{4ATP}$  was estimated to be  $12000 \pm 1000$ . Similarly, the average number of tethered FA molecules  $N_{FA}$  was quantified as equal to  $1900 \pm 200$  molecules per nanovector. We can define the conjugation efficiency as the ratio of 4ATP molecules actually bound to folate, with respect to the total:

$$r_{titr}|_{FA} = \frac{N_{FA}}{N_{4ATP}} = (1.6 \pm 0.3) \cdot 10^{-1}$$

The same experimental procedure, performed with a different dye molecule (Orange II) led to a similar result in the case of aminopterin conjugation. Indeed, according to our estimate  $N_{4ATP}=14600\pm1500$  and  $N_{AMT}=2760\pm300$ . Therefore,

$$r_{titr}|_{AMT} = \frac{N_{AMT}}{N_{4ATP}} = (1.9 \pm 0.4) \cdot 10^{-1}$$

In studying the effect of folate conjugation on 4ATP-AuNps SERS signature, the most evident feature is the change in the spectral shape of the C–C stretching band, due to the modification to the relative weight of the two spectral components of the peak. In Fig. 3.25 we have evidenced the fit spectral components relative to the C–C stretching peak in the reference case of 4ATP-AuNps and in the cases of functionalized samples. An effective way to quantify the spectral modification occurring upon folate/antifolate binding is to calculate the intensity ratio  $\rho$  between

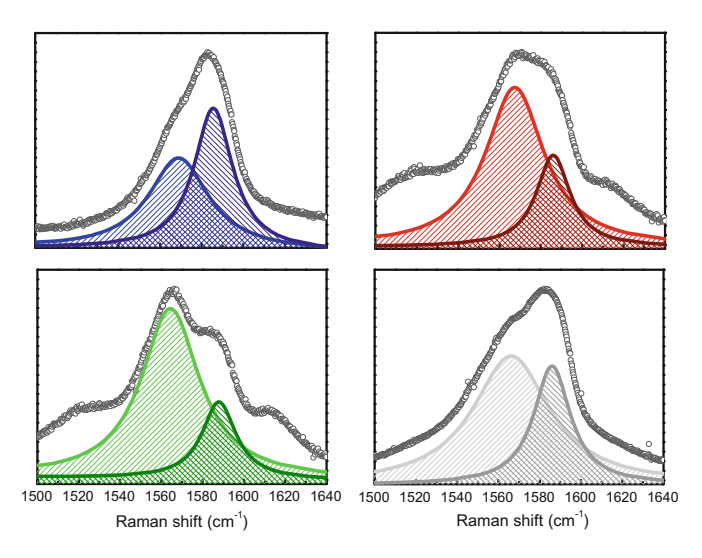


**Fig. 3.25** The spectral components of the fit used for the quantitative SERS analysis are evidenced for the four samples: 4ATP-AuNps (**a**), FA-4ATP-AuNps (**b**), AMT-4ATP-AuNps (**c**), and MTX-4ATP-AuNps (**d**). Scatter plot are experimental data

the antysimmetric (low frequency) and symmetric (high frequency) components of the band. From data analysis on the four samples (Fig. 3.25), we derive that

$$\rho_{FA} = 3.16 \pm 0.36$$
  $\rho_{AMT} = 3.79 \pm 0.51$   $\rho_{MTX} = 2.12 \pm 0.41$ 

We can then define a SERS titration factor as

$$r_{SERS} = \frac{\rho_{conj}}{\rho_{4ATP}} = \frac{I_{anti}/I_{sym}|_{conj}}{I_{anti}/I_{sym}|_{4ATP}}$$

leading to the following estimates:

$$r_{SERS}|_{FA} = 3.5 \pm 0.4$$
  $r_{SERS}|_{AMT} = 4.2 \pm 0.5$   $r_{SERS}|_{MTX} = 2.3 \pm 0.4$ 

It is now possible to compare the two different titration estimates, and we find:

$$\alpha_{FA} = \left[\frac{r_{SERS}}{r_{titr}}\right]_{FA} = 21.7 \pm 6.5$$
  $\alpha_{AMT} = \left[\frac{r_{SERS}}{r_{titr}}\right]_{AMT} = 21.9 \pm 6.6$ 

The ratio between  $r_{titr}$  and  $r_{SERS}$  is in very good agreement for the two samples, which suggest we can use the estimate for inferring the conjugation efficiency in the case of MTX

$$r_{titr}|_{MTX} = \frac{r_{SERS}|_{MTX}}{\langle \alpha \rangle} = (1.1 \pm 0.5) \cdot 10^{-1}$$

Methotrexate is characterized by a lower yield of the chemical conjugation reaction (approximately 1 conjugated molecule every 10 4ATP free amine groups) with respect to FA (1:6) and AMT (1:5).

Concluding, these results suggest the possibility of using SERS analysis to quantitatively estimate the efficiency of the bioconjugation in this kind of systems. This is a great advantage from an experimental point of view. Indeed, while UV-Visible-based titration assays need to be performed on massive samples (volumes of Np solution employed here are of the order of 1 mL), SERS can give reliable results on samples at least 100 times smaller. This means that SERS characterization can be easily performed on the very same Np dispersion used for cell treatment, enhancing the control and reproducibility of the final result.

# 3.3 Experimental Details

In this Section, most of the experimental details and instrumental setups used are presented. These apply also to the following Chapters. Any further details are reported in specific discussions.

**UV-visible absorption measurements** The Np molecular conjugation was estimated by monitoring the changes in the optical absorption spectra and in particular in the frequency position of the Np localized surface plasmon resonance. The UV-Visible absorption measurements were performed on the Np dispersion at room temperature (RT) using a double beam Jasco V-570 spectrophotometer, set with a 0.5 nm bandwidth.

**Dynamic light scattering** Dynamic light scattering (DLS) was used to characterize the size distribution of the Nps in solution. Our Malvern NanoZetaSizer apparatus is equipped with a 5 mW HeNe laser (Malvern Instruments Ltd, UK) and uses quasibackscatter detection, i.e. the scattered light is collected at an angle of 173°, the backscattering being less sensitive to multiple scattering effects. The CONTIN algorithm was emplyed for analyzing the measured autocorrelation functions in order to obtain the size distributions. Decay times are used to determine the distribution of the diffusion coefficients D of the particles, which in turn are converted to a distribution of apparent hydrodynamic radii  $R_H$  using the Stokes Einstein relationship  $R_H = K_B T / 6\pi \eta D$ , where  $K_B T$  is the thermal energy and  $\eta$  the solvent viscosity. The reported radius values are the average of several measurements and are obtained from intensity-weighted distributions.

 $\zeta$  potential The  $\zeta$  potential of the suspended Nps was measured at 25.0°C temperature (0.1°C, T accuracy), adopting the Phase Analysis Light Scattering (PALS) technique of a Malvern NanoZetaSizer apparatus (Malvern Instruments Ltd, UK). This enables the measurement of the electrophoretic mobility, and from this the  $\zeta$  potential, which we provided herein in the Helmholtz/Smoluchowski approximation. The measurements were performed employing a palladium electrode dip cell ZEN 1002 (Malvern, UK). The runs were set up in triplicate, each consisting of at least 30 sub-runs.

Infrared measurements The infrared characterization was performed at RT on  $150 \times 150 \, \mu m^2$  microsized regions using a JASCO Irtron IRT-30 Fourier Transform infrared (FTIR) microscope, equipped with a nitrogen cooled MCT detector, a Cassegrain objective  $16 \times$ . The acquisition was set up in transmission mode,  $512 \, scans$ , with a spectral resolution of  $4 \, cm^{-1}$ . The microscope is coupled with a FTIR/410 Jasco spectrometer equipped with a conductive ceramic coil mounted in a water-cooled copper jacket source and a KBr beamsplitter. The optical path was purged continuously with gaseous nitrogen. For the microFTIR measurements, the Np solution was dried at  $37^{\circ}$ C on CaF<sub>2</sub> substrates.

**Raman/SERS measurements** Raman measurements were performed employing a Horiba HR-Evolution microspectrometer, equipped with a 25 mW He-Ne laser (632.8 nm wavelength) and a set of neutral power attenuating filters. The spectrometer is coupled with a confocal microscope equipped with a set of objectives at different magnifications ( $50 \times -0.50 \, \text{NA}$  and  $100 \times -0.8 \, \text{NA}$  were typically used for SERS experiments). A 600 lines per mm diffraction grating ensured a spectral resolution better than  $3 \, \text{cm}^{-1}$ . Spectroscopic maps, i.e. measurements acquired systematically on two-dimensional scans, were acquired by employing a software

controlled mapping stage with submicrometric precision. Keeping fixed focusing and confocal diaphragm, a constant scattering volume can be assumed whose transverse surface is defined by the laser spot on the sample (approximately 3 and 1  $\mu m$  for the  $50\times$  and  $100\times$  respectively). Exploiting the high confocality of the setup, micrometric sampling along the optical axis can also be realized (see for example Fig. 5.7 in the following Chapter). All the spectroscopic data are herein presented after processing, which consisted of a polynomial baseline subtraction (usually 3rd degree) performed with the acquisition software, LabSpec 6.1. Fitting and other types of quantitative data analysis were performed with OriginPro 8.1 software.

**Atomic Force Microscopy** Tapping-mode AFM images, using a cantilever with a spring constant,  $k = 42 \, \text{N/m}$ , a scan rate of  $0.3 \div 0.7 \, \text{Hz}$  and an extremely sharp tip (nominal radius of curvature of  $2 \, \text{nm}$ ), were recorded by an Atomic Force Microscope Dimension Icon Bruker equipped with a Nanoscope V Controller (c/o SNN-Lab-Sapienza Nanoscience & Nanotechnology Lab). All the AFM images shown herein are accompanied with a colour bar for the height scale. Data analysis was performed by NanoScope Analysis Version 1.4 (Bruker Corporation).

## References

[Cou2009]

[Bai2006]	Baia M, Toderas F et al (2006) Probing the enhancement mechanisms of SERS with p-aminothiophenol molecules adsorbed on self-assembled gold colloidal nanopar-
	ticles. Chem Phys Lett 422(1):127–132
[Bai2009]	Baia M, Toderas F et al (2009) Multilayer structures of self-assembled
	gold nanoparticles as a unique SERS and SEIRA substrate. ChemPhysChem
	10(7):1106–1111
[Bat2012]	Battocchio C, Meneghini C et al (2012) Silver nanoparticles stabilized with thi-
	ols: a close look at the local chemistry and chemical structure. J Phys Chem C
	116(36):19571–19578
[BP1976]	Berne BJ, Pecora R (1976) Dynamic light scattering: with applications to chem-
	istry, biology, and physics. Courier Corporation
[Car2017]	Carlini L, Fasolato C et al (2017) Comparison between silver and gold nanoparti-
	cles stabilized with negatively charged hydrophilic thiols: SR-XPS and SERS as
	probes for structural differences and similarities. Colloids Surf A: Physicochem
	Eng Asp 532:183–188
[Che2013]	Chen C, Ke J et al (2013) Structural basis for molecular recognition of folic acid
	by folate receptors. Nature 500(7463):486–489
[Col2009]	Coluccio ML, Das G et al (2009) Silver-based surface enhanced Raman scattering
	(SERS) substrate fabrication using nanolithography and site selective electroless
	deposition. Microelectron Eng 86(4):1085–1088
[Cos2010]	Costantini F, Benetti EM et al (2010) Enzyme-functionalized polymer brush films
	on the inner wall of silicon-glass microreactors with tunable biocatalytic activity.
	Lab on a Chip 10(24):3407–3412
[Cot2015]	Cottat M, D'Andrea C et al (2015) High sensitivity, high selectivity SERS detection
	of MnSOD using optical nanoantennas functionalized with aptamers. J Phys Chem
	C 119(27):15532–15540

linear and dendritic structures. Polym Int 58(5):511-518

Coussot G, Nicol E et al (2009) Colorimetric quantification of amino groups in

- [Dav2013] Davies RA, Chong NS et al (2013) Chemical enhancement of the surface enhanced Raman scattering signals of anilines via their ortho-substituents
- [Dom2011] Domenici F, Bizzarri AR et al (2011) SERS-based nanobiosensing for ultrasensitive detection of the p53 tumor suppressor. Int J Nanomed 6:2033–2042
- [Dom2012] Domenici F, Bizzarri AR et al (2012) Surface-enhanced Raman scattering detection of wild-type and mutant p53 proteins at very low concentration in human serum. Anal Biochem 421(1):9–15
- [Dom2016] Domenici F, Fasolato C et al (2016) Engineering microscale two-dimensional gold nanoparticle cluster arrays for advanced Raman sensing: an AFM study. Colloids Surf A: Physicochem Eng Asp 498:168–175
- [Far1948] Farber S, Diamond LK et al (1948) Temporary remissions in acute leukemia in children produced by folic acid antagonist, 4-aminopteroyl-glutamic acid (aminopterin). New Engl J Med 238(23):787–793
- [Fas2014] Fasolato C, Domenici F et al (2014) Dimensional scale effects on surface enhanced Raman scattering efficiency of self-assembled silver nanoparticle clusters. Appl Phys Lett 105(7):073105
- [Fas2016] Fasolato C, Giantulli S et al (2016) Folate-based single cell screening using surface enhanced Raman microimaging. Nanoscale 8(39):17304–17313
- [Güh2015] Gühlke M, Heiner Z et al (2015) Combined near-infrared excited SEHRS and SERS spectra of pH sensors using silver nanostructures. Phys Chem Chem Phys 17(39):26093–26100
- [Hid2014] Hidi IJ, Mühlig A et al (2014) LOC-SERS: towards point-of-care diagnostic of methotrexate. Anal Methods 6(12):3943–3947
- [Hua2010] Huang Y-F, Zhu H-P et al (2010) When the signal is not from the original molecule to be detected: chemical transformation of para-aminothiophenol on Ag during the SERS measurement. J Am Chem Soc 132(27):9244–9246
- [Hul1999] Hulteen JC, Treichel DA et al (1999) Nanosphere lithography: size-tunable silver nanoparticle and surface cluster arrays. J Phys Chem B 103(19):3854–3863
- [Hun2013] Hunter RJ (2013) Zeta potential in colloid science: principles and applications, vol 2. Academic press, London
- [HV2001] Haynes CL, Van Duyne RP (2001) Nanosphere lithography: a versatile nanofabrication tool for studies of size-dependent nanoparticle optics. J Phys Chem B 105(24):5599–5611
- [Jia2005] Jiao L, Niu L et al (2005) Simple azo derivatization on 4-aminothiophenol/Au monolayer. Electrochem Commun 7(2):219–222
- [Kho2012] Kho KW, Dinish US et al (2012) Frequency shifts in SERS for biosensing. ACS Nano 6(6):4892–4902
- [Kim 2010] Kim NH, Lee SJ et al (2010) Aptamer-mediated surface-enhanced Raman spectroscopy intensity amplification. Nano Lett 10(10):4181–4185
- [Kim2011] Kim NH, Lee SJ et al (2011) Reversible tuning of SERS hot spots with aptamers. Adv Mater 23(36):4152–4156
- [Kim 2012] Kim K, Kim KL et al (2012) Surface-enhanced Raman Scattering of 4-Aminobenzenethiol on Ag and Au: pH dependence of b 2-type bands. J Phys Chem C 116(7):4774–4779
- [Kne2006] Kneipp K, Moskovits M et al (2006) Surface-enhanced Raman scattering: physics and applications, vol 103. Springer Science & Business Media, Berlin
- [Kne2010] Kneipp J, Kneipp H et al (2010) Novel optical nanosensors for probing and imaging live cells. Nanomed Nanotechnol Biol Med 6(2):214–226
- [KV2008] Khoury CG, Vo-Dinh T (2008) Gold nanostars for surface-enhanced Raman scattering: synthesis, characterization and optimization. J Phys Chem C 112(48):18849–18859
- [Le 2007] Le Ru EC, Blackie EJ et al (2007) Surface enhanced Raman scattering enhancement factors: a comprehensive study. J Phys Chem C 111(37):13794–13803

[Man2010]	Mansoori GA, Brandenburg KS et al (2010) A comparative study of two folate-conjugated gold nanoparticles for cancer nanotechnology applications. Cancers 2(4):1911–1928
[NC2002]	Nath N, Chilkoti A (2002) A colorimetric gold nanoparticle sensor to interrogate
. ,	biomolecular interactions in real time on a surface. Anal Chem 74(3):504–509
[Nor2002]	Norman TJ, Grant CD et al (2002) Near infrared optical absorption of gold
	nanoparticle aggregates. J Phys Chem B 106(28):7005–7012
[Nor2004]	Nordlander P, Oubre C et al (2004) Plasmon hybridization in nanoparticle dimers.
	Nano Lett 4(5):899–903
[Osa1994]	Osawa M, Matsuda N et al (1994) Charge transfer resonance Raman process in
	surface-enhanced Raman scattering from p-aminothiophenol adsorbed on silver:
	Herzberg-Teller contribution. J Phys Chem 98(48):12702–12707
[Per2009]	Perrault SD, Walkey C et al (2009) Mediating tumor targeting efficiency of
	nanoparticles through design. Nano Lett 9(5):1909–1915
[Ren2011]	Ren W, Fang Y et al (2011) A binary functional substrate for enrichment and
	ultrasensitive SERS spectroscopic detection of folic acid using graphene oxide/Ag

[Sam2013] Samal AK, Polavarapu L et al (2013) Size tunable Au@ Ag core- shell nanoparticles: synthesis and surface-enhanced Raman scattering properties. Langmuir 29(48):15076–15082

nanoparticle hybrids. Acs Nano 5(8):6425-6433

- [Sch1977] Schmid ED, Schlenker P et al (1977) Raman intensity and conjugation. IV-determination of the conjugation between a phenyl ring and a carbonyl group by Raman intensity. J Raman Spectrosc 6(6):314–318
- [Sch2011] Schmid G (2011) Nanoparticles: from theory to application. Wiley, New York Solomons JTG, Fryhle CB (2010) Organic chemistry, 2000. Prentice Hall, Englewood Cliffs
- [Sha2010] Shakeri-Zadeh A, Mansoori GA et al (2010) Cancerous cells targeting and destruction using folate conjugated gold nanoparticles. Dyn Biochem Process Biotechnol Mol Biol 4(1):06–12
- [Sön2005] Sönnichsen C, Reinhard BM et al (2005) A molecular ruler based on Plasmon coupling of single gold and silver nanoparticles. Nat Biotechnol 23(6):741–745
- [TS1988] Tripathi GNR, Schuler RH (1988) Resonance Raman studies of substituent effects on the electronic structure of phenoxyl radicals. J Phys Chem 92(18):5129–5133
- [Vit2011] Vitale F, Fratoddi I et al (2011) Mono-and bi-functional arenethiols as surfactants for gold nanoparticles: synthesis and characterization. Nanoscale Res Lett 6(1):103
- [Wan2014] Wang Y, Ji W et al (2014) Exploring the effect of intermolecular H-bonding: a study on charge-transfer contribution to surface-enhanced Raman scattering of p-Mercaptobenzoic acid. J Phys Chem C 118(19):10191–10197
- [Wib2013] Wibowo AS, Singh M et al (2013) Structures of human folate receptors reveal biological trafficking states and diversity in folate and antifolate recognition. Proc Natl Acad Sci 110(38):15180–15188
- [Yos2009] Yoshida K, Itoh T et al (2009) Spectral shapes of surface-enhanced resonance Raman scattering sensitive to the refractive index of media around single Ag nanoaggregates. Appl Phys Lett 95(26):263104
- [Zho2006] Zhou Q, Li X et al (2006) Charge transfer between metal nanoparticles interconnected with a functionalized molecule probed by surface-enhanced Raman spectroscopy. Angew Chem Int Ed 45(24):3970–3973

# **Chapter 4 Nanoparticle-Based SERS Substrates for Molecular Sensing Applications**



As already discussed in the introductory chapters, the wide interest and research focused on plasmonic nanostructures for near field coupling and enhanced field confinement has paved the way for the development of numerous specific applications in diverse fields, from sensors technology to medical diagnostics. Among these applications, plasmonic substrates for SERS spectroscopy, sensing and SERS-based chemical analysis have attracted much interest [Sti2008, Kne1997, SN2012].

Although single, isolated metallic Nps induce strong and predictable scattered field profiles and can therefore enhance predictably also the Raman signal, the huge enhancement factors necessary to approach the single molecule spectroscopic limit are only produced by the very close proximity of multiple metal Nps, shrinking the enhanced fields in the so-called *hot-spots* [Kne2006]. From dimers [Fra2012] to more complex architectures [Yan2009], inter-particle plasmonics give rise to a modified, broader surface plasmon resonance (SPR) that results in better performances and a bigger versatility of the SERS system. The plasmonic behavior underlying SERS has indeed shown a strong dependence upon both size and shape of Np clusters [Yos2010, ZW2012].

In this Chapter, we describe the development of SERS active substrates based on the aggregation of colloidal silver and gold nanoparticles. We will mostly focus on the influence of the metal nanoarchitecture on SERS efficiency, investigating therefore the characteristics of the substrate which positively affect the electromagnetic enhancement in these systems. Of course, as already mentioned, the Np material choice also plays an important role in the final performance of the SERS substrate, being higher (typically, a couple of orders of magnitude) in the case of AgNps. AuNps are usually preferred for their better chemical stability, which makes them better candidates for the preparation of SERS substrates when this requires multiple fabrication steps. The plasmonic performace of the systems considered was tested by functionalizing the substrates with the conventional SERS label 4ATP.

In the first Sect. 4.1, we begin our analysis by focusing on Np self-assembly from a water dispersion [Fas2014]. As discussed in Chap. 3, Nps tend to aggregate in microscopic, disordered clusters, typically formed by layers of superimposed Nps. A combined microscopic (AFM) and spectroscopic investigation allowed to

correlate the morphological parameters of the Np cluster with its SERS efficiency, and pointed out a linear increase of the maximum SERS intensity revealed on a cluster with its surface area, up to very large values ( $\sim\!30~\mu\text{m}^2$ ). The number of Np layers composing the aggregate also plays a role in the SERS response of the system. The outlined results coherently point out a cooperative plasmonic effect of the entire Np aggregate, up to the mesoscopic scale, in enhancing the local field and producing the overall SERS response.

In order to support our interpretation of the experimental data, we also carried out electromagnetic simulations on multilayer Np structures, described in Sect. 4.2. For these electrodynamics simulations we employed a finite difference time domain (FDTD) software. The FDTD simulation of a complex structure such as a microsized, self-assembled (i.e. disordered) Np cluster, containing thousands of Nps, can hardly be achieved with common computational resources. Nevertheless, the effect of multiple Np layers can be monitored by simulating a simpler structure, as a multilayered assembly of Nps organized in a regular, simple cubic crystal lattice. Our simulations indeed led to a qualitative validation of our interpretation.

The final Sect. 4.3 is dedicated to the development of SERS substrates based on a template-guided self-assembly approach. Considering the influence on SERS efficiency of the self-assembled cluster morphology, we induced the Np spontaneous aggregation inside mesoscopic cavities prepared using electron beam lithography (EBL). For this multi-step preparation protocol, we used gold Nps instead of silver ones for their higher chemical stability. EBL-driven self-assembly granted a good control on the aggregate morphologies, therefore boosting the signal reproducibility of the system, while reaching overall a high enhancement factor [Dom2016].

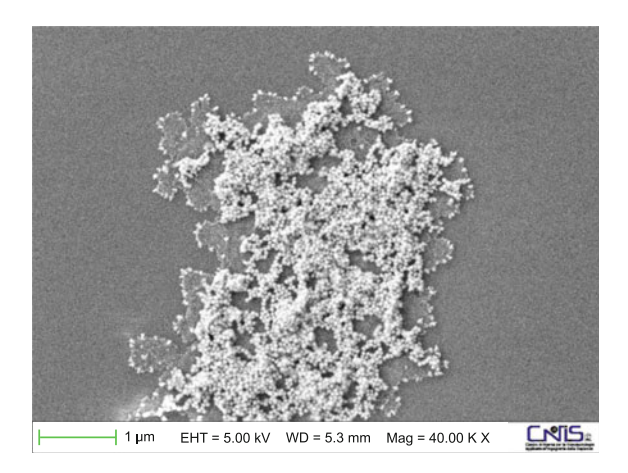
# 4.1 Self-assembled Mesoscopic Silver Nanoparticle Clusters

In studying the SERS response from mesoscopic, disordered Np clusters obtained by self-assembly, one of the key points to monitor is the relationship between the aggregate morphology and its SERS efficiency. This is indeed the path to follow for the design of high performance, reproducible SERS substrates [DJ2014].

The first insight on the role of the local plasmonic nanoarchitecture in the SERS response of diverse noble metal systems was provided by some pioneering works exploiting scanning probe microscopy in conjunction with Raman spectroscopy [BC2009, Van1993, NE1997]. Despite these considerable efforts, a clear framework and specific engineering recipes are still far from being identified. Our approach exploits as well a synergic high resolution topographic micro-Raman and Atomic Force Microscopy (AFM) investigation. Probing this correlation, we can associate the SERS spectroscopic efficiency, based on local field enhancement, through far field optical illumination/detection measurements, with the corresponding nanoscale morphology of the plasmonic substrate.

The system investigated in this study consists of microsized Np clusters obtained by the self-organization of AgNps functionalized with the well known SERS probe

**Fig. 4.1** SEM image of a 60 nm nanoparticle cluster showing the typical micrometric cluster size



4ATP [Osa1994, Bai2006]. AgNps with 60 and 100 nm nominal diameters are functionalized in solution, as described in Sect. 3.1.1. Their self-organization in clusters takes place during the environmentally controlled water evaporation, once a droplet of Np dispersion is deposited on a clean glass slide. The straightforward and well reproducible process is sketched in Fig. 3.3. The self-assembly process has the great advantage of being a very simple and cheap method for inducing the Np aggregation. It has been shown that self-assembled Np aggregates represent hot-spot rich, high performance SERS-active substrates [Liu2014, Fas2014].

At the end of the drying process, the so-obtained plasmonic systems were analyzed by scanning electron microscopy and X-ray microanalysis. These revealed the presence of self-assembled, microsized clusters made of 4ATP functionalized AgNps on the glass slide (see Figs. 4.1 and 3.6). Regardless of the Np diameter, all the sample showed a similar distribution of typical cluster sizes and a similar, close packing organization of the Nps, with interparticle distances typically of 5–7 nm (see the inset of Fig. 3.6).

# 4.1.1 Coupled AFM and Raman Analysis

Since the local field enhancement is directly linked to the plasmonic response of the metallic substrate, the EM SERS enhancement is affected by even the smallest peculiarity or difference in the Np assembly from cluster to cluster, as these changes will affect the collective electronic excitation in the structure (SPR). Unraveling the correlation between Np aggregate morphologies and their SERS activity is therefore a pivotal challenge towards the development of performing and efficient sensing devices. To enlighten this relationship, AFM measurements were carried out on several samples with clusters providing different extents of EM-enhancement.

The Np clusters obtained by self-assembly exhibited a consistent morphology regardless of the different size of the Nps used. The typical cluster height ranged between 2 and 3 layers of Nps, where larger areas favored the thicker configuration. Self-assembled particle aggregates are disordered on a large scale and feature interparticle junctions and crevices which are expected to strongly affect the local field distribution and, therefore, the SERS signal enhancement. The wide dispersion observed on the investigated cluster population in terms of particle number and overall geometry results from both the randomness of the self-assembly process and the intrinsic size-dispersion of the nanocolloid used (<20%).

On several samples, both spatially resolved Raman and AFM measurements were carried out on the same clusters using a fine grating as a reference to identify the cluster positions. The use of a red exciting laser is not suitable for observing SERS from isolated AgNps, which display a SPR in the green region of the spectrum, as witnessed by the optical absorption of functionalized AgNps in water dispersion (see Fig. 3.2). The comparison between AFM topography and Raman maps collected on the same sample surface revealed indeed the absence of a detectable SERS signal from single Nps. Instead, a strong SERS activity was revealed in correspondence of micrometric Np aggregates. This is expected, since it is known that a pronounced red-shift of the SPR is driven by Np aggregation [Lu2005].

The AFM topography and the corresponding Raman intensity map acquired on a representative,  $100\,\mathrm{nm}$  Np cluster are shown in Fig. 4.2. The Raman map was produced by integrating the acquired spectrum over the C-S stretching band ( $\sim 1078\,\mathrm{cm}^{-1}$ ), that is known to be enhanced exclusively by EM mechanism [Osa1994, Bai2006]. Consequently, the Raman intensity map can be considered a map of the EM enhancement within the cluster. Notably, when the different spatial resolution of Raman and AFM is accounted for, the shapes emerging from the two measurements are well consistent. Such consistency has been thoroughly and successfully checked for several aggregates, thus indicating that the cluster area can be estimated straight from the Raman intensity maps.

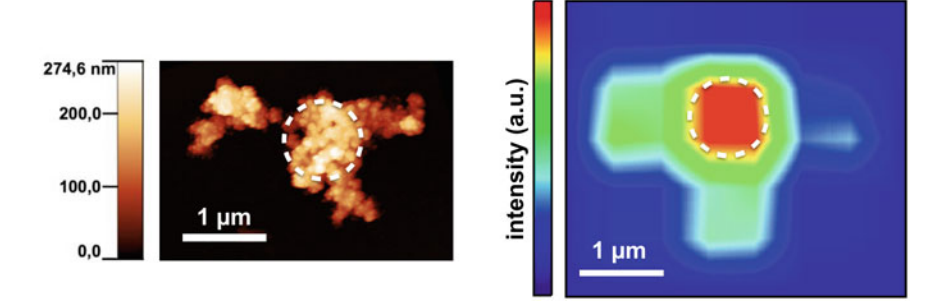


**Fig. 4.2** AFM topography (left) and Raman map of the EM-enhanced SERS signal (right) acquired on a micrometric 100 nm nanoparticle cluster. The point where the maximum intensity was acquired is highlighted. The average cluster height is 2 stacking planes of Nps

# 4.1.2 Dimensional Scale Effect on SERS Efficiency

The SERS EM enhancement produced by a Np cluster can be effectively quantified by evaluating the integrated intensity of the C-S stretching band on the most intense spectrum in the spectroscopic map of the aggregate,  $I_{Max}$ . The values of  $I_{Max}$  are displayed in Fig. 4.3 as a function of the cluster area. Regardless of the diameter of the Nps used, the experimental points seem to gather around two definite increasing linear dependences.

Such a qualitative observation can be substantiated by a quantitative analysis. To do so, we first calculated the quantity  $I_{Max}/area$  for each experimental point. The whole dataset was then analyzed using a simple cluster analysis algorithm, seeking for a bipartition of the data which minimized the square deviation from the group averages [Nil1967, But1986]. For these two separate groups, a linear fit was then calculated, with the intercept value fixed at zero. The ratio between the slopes of the two regression lines is  $\sim$ 2.7, both data sets showing an excellent linear correlation (R=0.979 and 0.945, respectively).

Our hypothesis is that the double-slope linear dependence is to be ascribed to the different average heights of the clusters. Indeed, AFM measurements on clusters with similar areas (see arrows in Fig. 4.3) showed that the lower slope trend can be associated to an average height of 2 Np planes, while the higher slope trend to 3 Np-layer structures. These results suggest that the whole aggregate is participating to the SERS response of any individual spot over the cluster surface. And this implies that, apart from the specific nanoscale organization, the collective plasmonic response

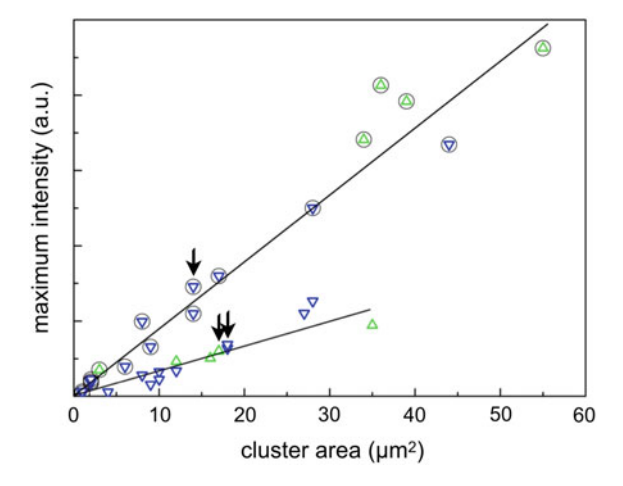


Fig. 4.3 Maximum SERS intensity versus cluster area detected on  $60\,\mathrm{nm}$  (blue  $\triangledown$ ) and  $100\,\mathrm{nm}$  (green  $\triangle$ ) Np clusters, respectively. The ratio of the slopes of the two linear regression curves obtained by the two data subset (circled and not circled symbols), is  $\sim$ 2.7, with correlation coefficients 0.979 (circled) and 0.945. The black arrows indicate clusters of similar area showing a two (lower fit) or three Np-layer composition by AFM measurements

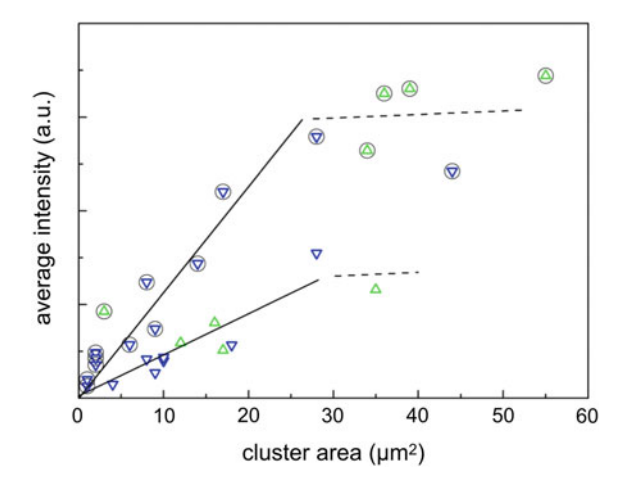
of the whole structure drastically affects the EM signal enhancement. The evidence that the linear trends do not depend upon the different Np diameters brings in further support to this interpretation.

We might expect that the linear trend of  $I_{Max}$  vs cluster area would bend down to an asymptotic value for aggregates large enough. A threshold for the saturating size can be estimated considering the propagation length of surface plasmon polaritons, i.e. coupled plasmonic-photonic excitations that exist in correspondence of a planar surface of contact between different materials. In the case of the silver-air interface, a propagation length at the micron scale is expected for such excitations [NH2012]. Considering this, one could argue that the linear dependence of  $I_{Max}$  from the cluster area may not hold for the larger aggregates. Interestingly, such deviations become actually more evident when the average intensity scattered from the whole aggregate,  $I_{ave}$ , is calculated. Although a linear increasing trend for  $I_{ave}$  is found for cluster areas smaller than  $\sim 30~\mu m^2$ , an almost constant value for larger aggregates is obtained (Fig. 4.4).

The idea of the Np vertical assembly in layers influencing the SERS activity of the cluster, suggested by the double slope in Fig. 4.3, is confirmed by the correlation between AFM topography and SERS mapping (Fig. 4.2). This "more material, more signal" relation might seem intuitive, but in this respect it is worth to stress that the few-nm separation among Nps revealed by SEM would not allow, in principle, radiation to cross the impinging Nps layer and reach the layers below. This, unless the light is coupled with an excitation inside matter, so that subdiffraction light focusing can take place. The dependence of signal enhancement on the number of Np layers thus suggests an effect of plasmonic waveguiding of radiation across the Np layers. This effect can increase the number of molecular scatterers actually contributing to the signal and, therefore, the overall SERS intensity.

To quantitatively investigate this effect, combining spectroscopic and morphological data, we calculated over the whole aggregate surface the local SERS enhance-

Fig. 4.4 Average SERS intensity versus cluster area for 60 nm (blue  $\nabla$ ) and 100 nm (green  $\triangle$ ) Np clusters, made of three (circled symbols) or two Np layers. The lines are guides for the eye



ment factor, defined as  $EF = I_{SERS}/I_{Raman}$  where the intensities are normalized to the single molecule contribution. Different EF values were found from aggregate to aggregate, depending on the cluster morphology (typically,  $10^8 < EF < 10^9$ ). Interestingly, the experimental values of the enhancement factor seem to increase for clusters with higher number of planes, faster than the increase of Np number in the cluster (which is in principle included in the normalization to single molecule contribution). Therefore, higher clusters appear to benefit of other contributions to th EF, beyond the increase in the number of scattering molecules.

These experimental results are confirmed by preliminary FDTD calculations [KL1993] on multilayer structures of AgNps, where remarkable cooperative effects are observed. The simulations were performed on Np ensembles organized in a cubic lattice made of different Np layers. The results indeed show that going from 1 to 3 stacking Nps planes the EM enhancement rapidly increases, whereas for thicker aggregates a saturation effect is observed. This effect is in agreement with the picture considering the cluster as a single plasmonic object. These results, which are presented in detail in the next Sect. 4.2, confirm the strong interaction between the localized Np SPR inside metal aggregates to be the main driver of SERS, but also point out that the local field enhancement of SERS hot-spots may be more correctly defined within the cluster assembly if we would consider it as a single near-field optical connected entity.

In conclusion, a combined Raman and AFM investigation allowed to relate the nanoscale morphology of plasmonic, self-assembled Np aggregates with the SERS intensity these structure can provide. The results coherently pointed out a cooperative effect of the complete Np cluster structure in the SERS response. Indeed, the maximum SERS intensity, as well as the average intensity scattered by the whole cluster, grow linearly with the cluster area up to at least  $\sim 30 \, \mu m^2$ , which can be considered the cluster dimension for optimal SERS performances. The cooperative effects and the size scale at which they take place are consistent with the theoretical predictions of the surface plasmonic polariton description. SERS efficiency also reveals to be proportional to the number of Np layers composing the cluster, both locally ( $I_{Max}$ ) and on average ( $I_{ave}$ ). These features clearly indicate that the cluster behaves as a single plasmonic object, that is the SERS response of the structure is affected by the whole aggregate geometry, in terms of both surface area and local height, up to a size of 30  $\mu$ m<sup>2</sup> and a height of 3 Np planes.

These results can be the starting point for interesting developments. Indeed, on one side, we provide a significant dataset that can be the basis for theoretical calculations aimed at testing and modeling cooperative plasmonic behavior in large structures made of multiple, near field coupled, nanosized objects. On the other side, the preparation protocol based on self-assembly, which ensures the close packing of

the Nps up to the micrometric scale, can be further optimized, for example by driving the self-assembly into patterned, designed cavities of proper size. These two aspects will be the subject of the following Sections.

#### 4.2 FDTD Simulation: Theoretical Predictions

As discussed in Sect. 2.2, the electromagnetic mechanism of SERS enhancement can be described with a classical approach, based on Maxwell's equations. It can be useful, for checking the working hypotheses on SERS results, to simulate the electromagnetic behavior of the plasmonic substrate. We chose to perform such an investigation to test the cooperative plasmonic behavior of Nps arranged in multilayer structures.

Electromagnetic simulations can be conveniently carried out with the employment of commercial softwares, like Lumerical FDTD Solutions, <sup>1</sup> which we chose. This software allows solving electrodynamics problems in a discrete space, by using the Finite Difference Time Domain (FDTD) method [KL1993, HT2000]. It also provides a Computer-Aided Design (CAD) environment for the easy three dimensional design of the plasmonic system.

FDTD computational approach, which is described in the next paragraph, is ideal for the study of structures with a high degree of spatial symmetry (e.g. ordered Np layers), while the simulation of large disordered structures, like mesoscopic self-assembled aggregates, is rather demanding in terms of computational resources. The thorough electrodynamic study of these structures requires other methods, such as those based on the discrete dipole approximation. Nevertheless, this is beyond the purpose of our investigation. Indeed, the results obtained for ordered multilayer Np structures are in qualitative agreement with our experimental results (see the previous Sect. 4.1).

# 4.2.1 The FDTD Software

The FDTD method is a state-of-the-art algorithm for the direct resolution in terms of space and time of problems in the field of electrodynamics and photonics [Ged2011, Sul2013]. By exploiting the Fourier transform, the software automatically provides the results in the frequency domain, which is essential for calculating physical properties like transmission and reflection of light.

FDTD algorithm solves Maxwell's equations (4.1) in non-magnetic materials:

$$\frac{\partial \mathbf{D}}{\partial t} = \nabla \times \mathbf{H} \qquad \mathbf{D}(\omega) = \varepsilon_0 \varepsilon_r(\omega) \qquad \frac{\partial \mathbf{H}}{\partial t} = -\frac{1}{\mu_0} \nabla \times \mathbf{E} \qquad (4.1)$$

<sup>&</sup>lt;sup>1</sup>Lumerical FDTD Solutions, https://www.lumerical.com/tcad-products/fdtd/, last visited 01.11.2016

where **H**, **E** and **D** are the magnetic and electric fields and the electrical displacement, respectively, and  $\varepsilon_r(\omega)$  is the relative dielectric constant.

In three-dimensional space, Maxwell's equations are solved in terms of the six components of the electromagnetic field:  $E_x$ ,  $E_y$ ,  $E_y$ , and  $H_x$ ,  $H_y$ ,  $H_z$ . Let us assume the structure to be infinite along the z axis and the fields to be independent from z:

$$\varepsilon(\omega, x, y, z) = \varepsilon(\omega, x, y)$$
  $\frac{\partial \mathbf{E}}{\partial z} = \frac{\partial \mathbf{H}}{\partial z} = 0$  (4.2)

Then, Maxwell's equations can be divided into two groups of independent equations, composed by three vectorial quantities, which can be solved independently in the x-y plane. These are usually referred to as *transverse electric* (TE) and *transverse magnetic* (TM) equations. The components involved are the following:

$$TE \rightarrow E_x, E_y, H_z \qquad TM \rightarrow H_x, H_y, E_z$$
 (4.3)

For example, in the TM case, Maxwell's equations become:

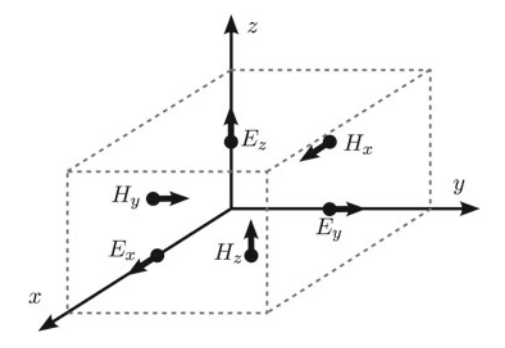
$$\frac{\partial D_z}{\partial t} = \frac{\partial H_y}{\partial x} - \frac{\partial H_x}{\partial y} \qquad D_z(\omega) = \varepsilon_0 \varepsilon_r(\omega) E_z$$

$$\frac{\partial H_x}{\partial t} = -\frac{1}{\mu_0} \frac{\partial E_z}{\partial y} \qquad \frac{\partial H_y}{\partial t} = \frac{1}{\mu_0} \frac{\partial E_z}{\partial x} \tag{4.4}$$

The FDTD method solves these TM, TE equations in a discrete space-time. Every field component is calculated in a slightly different position inside a rectangular unit cell of a cartesian computational grid, namely the Yee cell (see Fig. 4.5). The solutions obtained are automatically interpolated by the software to their values in the origin of the cell (this procedure works well in cases where the presence of singularities can be neglected).

**Sources of electromagnetic radiation** As explained above, the simulation software works in the time domain to investigate the system response in the frequency domain.

**Fig. 4.5** Example of a Yee cell for the resolution of TM equation with FDTD method



Once defined the spectral range in which the investigation has to be performed, Lumerical elaborates the parameters of the electromagnetic radiation pulse (duration, shape) which are necessary for a complete response on the selected spectral range. The incident radiation can either be a plane wave or a gaussian beam. Once these parameters are defined, the user selects the total simulation time, which has to be long enough to cover the whole electromagnetic response of the system, but reasonably short in order to limit the simulation execution time.

**Monitors** The observation of the electromagnetic behavior of the system is performed by placing inside the Yee cell monitors (2D surfaces), lines (1D) or points (0D) in which the value of the fields are detected. In this way, the spectral profiles of the local fields can be exported. Moreover, monitors properly positioned can allow to calculate macroscopic properties of the system like the transmission or reflection of an incident electromagnetic wave.

System definition and discretization The design of the system in terms of morphology and geometry can be performed in a CAD environment. The real-time three-dimensional visualization of the object allows a simple control on the simulated structure. As for the material, its definition usually relies on a database containing the optical properties of most of the common materials. In the simulation presented here, we used the optical properties measured by Johnson and Christy for gold [JC1972], and the results of Palik for silver [Pal1998]. Once the system is defined, a proper discretization of space, necessarily cartesian, needs to be chosen. The software authomatically sets a non-uniform discretization, with a thickened mesh in correspondance of materials with high values of absorbance or refraction index. The mesh can be modified in order to deepen the investigation in areas containing complex structures, in which a strong change/discontinuity of the fields is expected.

**Boundary conditions** The definition of the boundary conditions for the simulated cell (necessarily of finite size) is of crucial importance. In this respect, several options can be chosen, among which the most common are the periodic boundary conditions, useful for the simulation of infinite Np planes, and the *PML* conditions, which are suitable for the simulation of isolated nanostructures and consist of placing a layer of perfectly absorbent material on the sides of the cell [Ber1994]. The selected boundary conditions will affect the choice of the exciting source, which needs to be a plane wave, or a gaussian beam, respectively. This will prevent the arising or artifacts from diffraction effects.

## Modeling a Multilayer Np Structure

The simulation of a system of Nps regularly arranged on an xy plane can be efficiently performed using periodic boundary conditions. We chose first of all to simulate a single, infinite plane of 60 nm diameter Nps in a cubic lattice, with interparticle gap of 2 nm. For the simulation of this system, we located a 60 nm sized sphere at the origin of a 62 nm sized cell (a square in the xy plane), and we placed periodic boundary conditions in the x and y directions (see Fig. 4.6). As widely discussed in literature [FS1996], this approach allows to simulate a plane wave incident in the z direction on an infinite two dimensional (xy) grating of Nps.

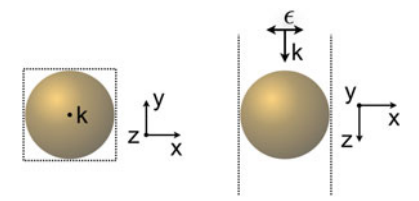


**Fig. 4.6** Sketch of the important part of the FDTD cell used for investigating the electromagnetic response of an infinite plane of Nps. Periodic boundary conditions allow to limit the simulation to a single Np

With the same approach, infinite multilayer structures of Nps disposed in a cubic lattice can be simulated by adding sequentially one or more Nps inside the cell depicted in Fig. 4.6 along the z axis, with the same interparticle gap (in principle, the Np spacing along z can be modified, but our aim here was to simulate a model structure).

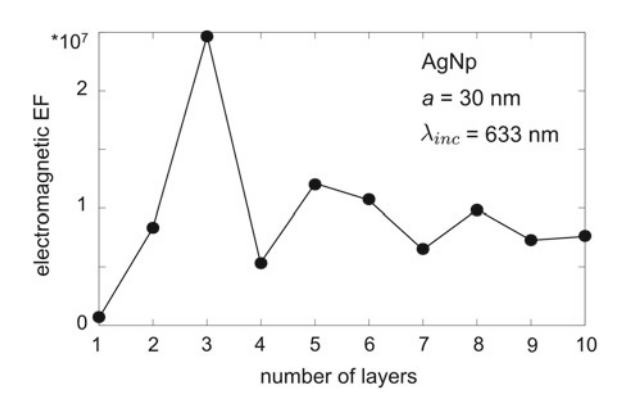
#### 4.2.2 Results on Silver and Gold Np Multilayers

**Silver: comparison with experiments** The first purpose of the electromagnetic simulation performed was to confirm, at least from a qualitative point of view, the experimental results presented in the previous Sect. 4.1. In particular, we focused on the data reported in Fig. 4.3: based on AFM experimental results, we had ascribed the double linear trend of the maximum SERS intensity  $I_{max}$  measured on mesoscopic AgNp clusters to the cooperative plasmonic behavior of the superimposed Np layers forming the aggregate, contributing to the determination of the electromagnetic enhancement factor. In a simplified picture, we could ascribe the growing trend for  $I_{max}$ , both depending on the area and on the number of layers, as the effect of the incremented number of hot-spots in the cluster. Nevertheless, it is not trivial to predict how the local field distribution in such a large structure will contribute to SERS signal enhancement.

We therefore simulated a multilayer ordered structure of AgNps with 60 nm diameter, as previously described. In Fig. 4.7, we have reported the trend of the electromagnetic enhancement factor (EF) in the system as a function of the number of Np layers. This has been calculated as the sum of EF values inside the hot-spots (hs), with the reasonable assumption that only hot-spots will significantly contribute to SERS intensity [Fan2008, Mos2013]. Electromagnetic EF in these sites is estimated from the fourth power of the local field enhancement g:

$$\sum_{hs} |g[hs]|^4 = \sum_{hs} |E/E_0|^4 \tag{4.5}$$

Fig. 4.7 Electromagnetic enhancement factor for an infinite multilayer structure of AgNps, arranged in a simple cubic crystal. EF was estimated by exclusively considering the hot-spot contribution



With this definition, we are probably overestimating EF, as we are assuming the Raman scattered field ( $\lambda_{Raman}$ ) to undergo the same enhancement as the incident field ( $\lambda_0$ ): this assumption implies a systematic error, due to the fact that we are neglecting the wavelength-dependence of the electromagnetic scattering response. Nevertheless, the (4.5) allows estimating the plasmonic behavior with considerations that are independent on the spectral band chosen for SERS observations. Moreover, experimental evidences show that to the neat plasmonic profiles estimated through electromagnetic simulations usually correspond strongly broadened resonances in real samples (due to irregularities in the geometry, impurities, etc.) leading, in real plasmonic substrates, to a less sharp wavelenght-dependence of the scattering profile.

As evident from the plot in Fig. 4.7, the exciting wavelength of 633 nm seems to be convenient to exploit the maximum local field enhancement. Moreover, the

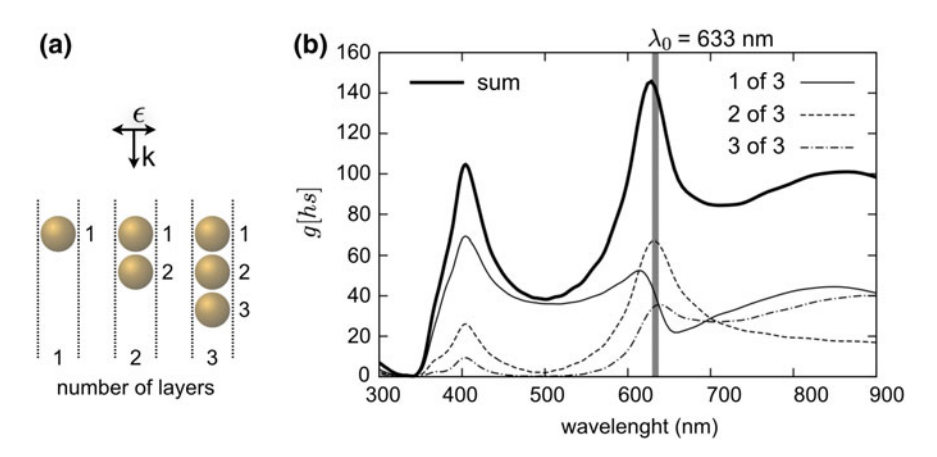
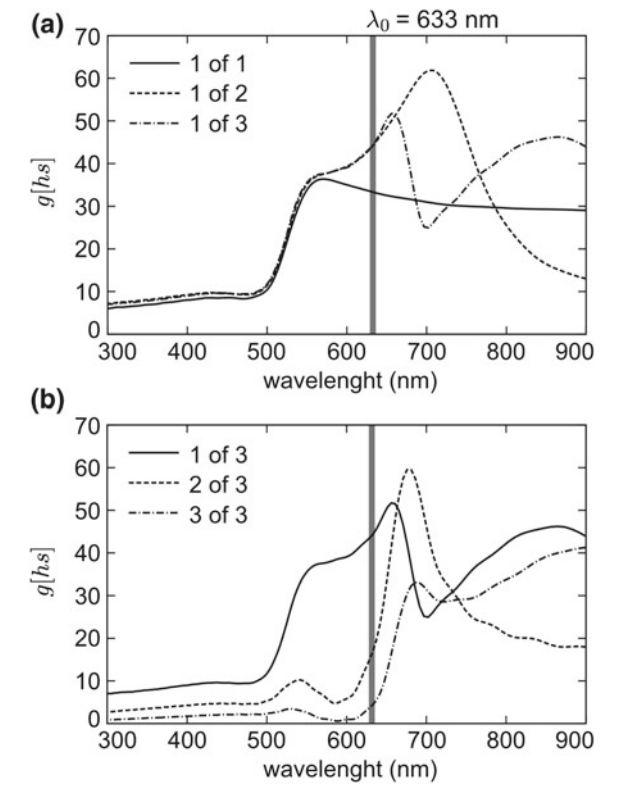


Fig. 4.8 Panel a sketch to clarify the structures and labels simulated. Panel b local field amplification g observed in the hot-spots of an infinite three-layer structure of AgNps, arranged in the simple cubic crystals. The spectral contribution of the different Np layers are highlighted. The laser wavelenght  $\lambda_0$  is highlighted

Fig. 4.9 Electromagnetic enhancement factor for a multilayer structure of AuNps, arranged in a simple cubic crystal, as a function of the number of layers

Fig. 4.10 Spectral dependence of the local field enhancement g in the hot-spots of a multilayer structure of AuNps, arranged in a simple cubic crystal. Panel a the contribution from hot-spots of the first Np layer encountered by radiation is plotted in the case of one-, two- and three-layer structure. Panel b contribution to the local field enhancement g of the first, second and third Np plane encountered by electromagnetic radiation. Np planes are labelled as in Fig. 4.8a



cooperative effect of superimposed Np planes leads to a remarkable growth of the EF up to three Np planes (see also Fig. 4.8), actually reproducing the trend revealed from experimental data. Then the value seem to stabilize around a lower value. The ratio between the angular coefficients  $c_2$ ,  $c_3$  of the linear fits in Fig. 4.3 is actually similar to the ratio between the simulated EF for 2 and 3 Np layers:

$$\frac{c_3}{c_2} = 2.7$$
  $\frac{EF_3}{EF_2} = 2.9$ 

**Gold: planning future design** As will be discussed in Sect. 4.3, in order to improve the signal reproducibility from self-assembled Np aggregates, we developed a template-guided self-assembly strategy for better controlling the Np-aggregate morphology, therefore enhancing the signal reproducibility. In order to optimize the design of such structures, we conducted the same electromagnetic simulations discussed above on structures made of gold Nps. As can be seen from Fig. 4.9, a less sharp dependence on the number of Np layers is revealed in gold based structures (see also reference [Jeo2016]). Moreover, the plots in Fig. 4.10a highlight that the enhancement factor in a one-layer Np structure is substantially homogeneous over the whole region of Raman excitations ( $\lambda_{Raman} > \lambda_0$ ).

#### 4.3 Electron Beam Lithography Driven Self-assembly

In the previous Sections, we have discussed the role of spontaneously assembled mesoscopic architectures, as Np clusters self-assembled on solid supports, in providing a huge and size dependent enhancement of the SERS signal of test molecules confined within (see Sect. 4.1). By behaving as single plasmonic objects, close packed, micrometric sized Np aggregates illuminated by visible light induce the confinement of an intense electromagnetic field at their surface that is used for exciting surface enhanced Raman scattering of molecules nearby [Fas2014]. In the previous Sect. 4.1 we have discussed how the SERS intensity on these structures increases linearly with the cluster area (up to  $\sim$ 30 µm²), exhibiting different increase rate depending on the aggregate thickness. Such an influence of the thickness on the SERS enhancement allows to ascribe the increased variability of the Raman intensity revealed on larger aggregates to their intrinsically higher inhomogeneity (variability in the number of Np layers within a single cluster) [Fas2014, Fas2015].

Our results suggest that ordered, closely packed Np aggregates composed of a single Np layer and displaying a few  $\mu m^2$  size can be easily recognized and manipulated within the resolution of an optical microscope. More importantly, they can provide a good SERS signal enhancement, and a reduced variability in the spectral intensity in a sampling over the whole substrate [Yan2009, Yan2011a, Alb2013]. However, although micrometric assemblies are easy and cheap to generate, the reproducibility of giant signal enhancements is difficult to control in such completely random structures.

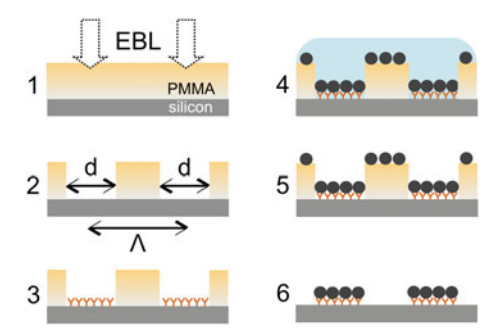


Fig. 4.11 Schematic process flow of the template-assisted assembly of NCAs. After the developing process, the e-beam patterning is followed by the functionalization of the exposed binding sites to allow the chemical bonding guided self-assembly of NPs; the lift-off process leaves on the substrate the particles patches of diameter d with a periodical spacing  $\Lambda$ 

It is possible to induce the controlled assembly of colloidal Np into well defined arrays, achieved with excellent reproducibility using top-down lithographic methods, as focused ion beam (FIB) or electron beam lithography (EBL) [Utk2012, Bre2012]. EBL in particular has emerged in the last few years as a flexible and quick tool to perform extensive nano- and micro-patterning, with the additional advantage, with respect to FIB, of avoiding ion implantation into exposed sites [Utk2012]. Unfortunately, up to date, the control over the spatial resolution reached by EBL patterning is typically limited to few nanometers. For this reason, it is tricky to generate by EBL Np assemblies with interparticle gaps of less than ~10 nm. This has a negative implication on the generated SERS intensities, which are significantly smaller than those achieved in "chemically" assembled clusters of nearly touching Nps [Yan2011b].

In order to reach challenging results in molecular and cellular sensing, the nanofabrication method adopted needs to produce the close packed aggregation of strongly packed Nps into clusters of defined morphology on a microscale area [Alb2013]. Proceeding from these considerations, we combined EBL and self-assembly strategies [TK1993, MT2003, Pre2007] to develop a SERS substrate made of two-dimensional arrays of mesoscopic Nps aggregates with well-defined shape, yielding well-predictable SERS enhancement. The adopted procedure is sketched in Fig. 4.11.

Self-assembly, when it is guided into a designed template, can produce the aggregation of AuNps into different, regular Nanoparticle Cluster Arrays (NCAs). These NCA platforms are very promising for applications, provided the achievement of a good reproducibility in terms of shape, size and thickness of the clustered Np patches. As demonstrated, these morphological characteristics crucially affect the induced optical - and, therefore, spectroscopic - response of the structures. A great advantage of these systems is that the flexibility of the NCA fabrication approach makes it straightforward to adjust the electromagnetic response of NCAs, varying the value of the characteristic geometrical parameters [Yan2009, Yan2011a, Alb2013, Kim2011].

The first step to implement a successful NCA fabrication is the optimization of the electron beam (e-beam) dose value with respect to the geometry adopted for the lithographic NCA mask. There is a tradeoff among speed, complexity and accuracy in the EBL writing of a desired mask. High energy e-beam is used for optimal resolution, although electron scattering limits its application, particularly due to the "proximity effect", where electrons writing a feature at one location overexpose a nearby feature, affecting the pattern geometry [Hu2006, Moh2012]. The second step is to determine the optimal chemical derivatization protocol, to be used to induce the aggregation of colloidal (typically, water dispersed) Nps into the EBL designed patterns on the substrate. The aim of the procedure, as discussed above, is to ensure a selective and tight packing of the Nps (60 nm sized) into the printed pattern.

We have fabricated NCAs composed of microsized AuNp clusters, that can easily be localized on the macroscopic substrate by optical imaging. However, in order to gain detailed information on the shape of the patches and the ordering and thickness within the Np aggregates we performed an accurate AFM analysis. The AFM, optical and SERS combined imaging on the NCA, properly functionalized with a SERS label, show an excellent correspondence between the spectroscopic and the topographic array maps. The high enhancement factor and the quite good reproducibility of the SERS sensing on our NCAs are promising for the implementation of multiplexed sensing based on this kind of systems. Indeed, the regular, geometrical planar distribution of the aggregates on the substrate allows to perform multiple measurements on a single sample, with the possibility of enhancing the sensitivity through a careful statistical analysis of the collected data.

# 4.3.1 Nanoparticle Cluster Array Preparation

**Electron Beam Lithography** EBL was performed using a Zeiss Auriga 405 Field Emission Microscope equipped with a Raith Elphy Quantum EBL module (c/o SNN-Lab-Sapienza Nanoscience & Nanotechnology Lab). The EBL patterns were designed on (100)-oriented silicon wafers. Prior to the lithographic process, the Si surface was cleaned in absolute ethanol (organic cleaning) and then sonicated (mechanical cleaning) for 2 min. Boiling in 1,1,1-trichloroethane for 10 min and then rinsing with ultrapure (milliQ) water followed. The treatment of the Si surface with an oxidizing solution increases the number of the exposed Si-OH bonds, involved in the linkage with Nps.

The positive resist AR P632.04 (purchased from ALLRESIST GmbH, Germany) was spin-coated on the Si wafer to obtain a poly-methylmethacrylate (PMMA) film. Preliminary tests allowed to establish a working protocol with a spin rate of 3000 r.p.m., that ensured the deposition of a thin and uniform solid polymer layer. After the resist coating, the sample was baked in the oven at 120 °C for 1 h. This thermal annealing stabilizes the film structure by cross-linking the chemical groups. It also removes the residual solvent and the stress built up in the resist during the spinning session [HC2001].

Atomic Force Microscopy (AFM) was performed to evaluate the thickness profiles on the obtained sample. It revealed an almost constant resist thickness of  $\sim$ 60 nm (see also Sect. 4.3.2). This controlled thickness guarantees an accurate result in the lithography, yielding a regular, nicely defined micro-patterning of the substrate into micrometric wells. As the thickness of the e-beam written PMMA is comparable or smaller (Fig. 4.11) than the Nps diameter, once the substrate has been developed, the surface has been functionalized and the particles have been deposited, the Nps partially protrude out of the well, above the resist surface. This allowed a detailed AFM investigation aimed at monitoring the effective immobilization and the packing of the Nps on the masked PMMA surface. Therefore, AFM analysis allowed to check the reproducibility of the whole substrate fabrication procedure at different steps of the preparation.

The design of the patterns for the NCA realization was performed using the CAD software of the EBL module. Each sample consists of multiple pattern configurations, organized in sectors, each one featuring different sizes of the diameter of the binding sites (d) and of the pitch of the array ( $\Lambda$ ). The EBL working parameters were a step size and line spacing of 24 nm, a dwell time of  $6 \cdot 10^{-4}$  ms and two different area dose values (100 and 20  $\mu$ C/cm²). The dose is defined as the product of the beam current by the beam dwell time, that is the time taken for the electrons to penetrate the resist.

The substrates exposed to e-beam were then treated with the developer AR 600-55 (ALLRESIST GmbH, Germany) for 60 s. This favors a high solubility of the resist degradated by the e-beam writing. After this, the substrates were transferred into the stopper bath AR 600-60 (ALLRESIST GmbH, Germany) for 30 s, to interrupt the development process. Afterwards, the substrates were rinsed in milliQ water and dried. After the development, the substrates were baked again for 30 min to thermally anneal the exposed regions, for reducing the unwanted chemical changes taking place within the resist layer during the exposure [HC2001].

Nanoparticle cluster preparation and functionalization The self-assembly of AuNps into clusters of the designed shape was induced through a chemical binding strategy. The part of the silicon surface exposed by lithography was functionalized using two different protocols, both aimed at the chemical anchoring of the Nps to the substrate surface.

In the first protocol, the exposed Si surface was derivatized using an ethanol solution of the organosilane 3-amino-propyltriethoxy-silane (APTS) (3%, incubation performed at RT for 90 min). The treated substrates were then thoroughly rinsed with ethanol and then baked at 110 °C for 10 min to stabilize further the silanized silicon silane. Afterwards, the further derivatization of the surface with glutaraldehyde (Glu) was obtained by incubating the substrates in a 1% Glu solution for 30 min at RT (see also [HC2001]), and eventually purified by rinsing abundantly with milliQ water. Exploiting the bifunctionality of the SERS 4-aminothiophenol probe, the aldehydemodified surfaces were conjugated with 4ATP [Dom2012] in water solution (0.05 g/l 4ATP, 1 h incubation and then rinsing). Free thiol moieties resulted thus available to covalently bind the AuNps on the exposed Si surfaces, allowing the controlled Np

assembly into clusters. The same APTS-Glu chemical linking strategy was successfully adopted also to build up SERS biosensing platforms being sensitive and stable in air and water environments [Dom2012]. In the second protocol, the thiol-driven covalent bridging of the bare AuNp surface and the Si surface was instead promoted directly by using a layer of 3-mercapto-propyltriethoxy-silane (MPTS) molecules. The EBL exposed Si substrates were incubated with 3% MPTS solution in ethanol for 90 min, and thus rinsed and baked, as performed according to the first protocol. In both cases, the nanocolloid incubation was performed with consecutive steps of Np deposition (at 25 °C, for at least 3 h) and thorough rinsing in milliQ water, to ensure a high Np density to covalently bind to the silicon. At the end of the incubation, the samples were rinsed and dried under pure nitrogen gas. The prepared samples were stored at 4 °C and a good stability in the SERS signal was revealed by repeated measurements on the same sample area. All the chemicals used for the preparation, if not specified otherwise, were purchased from Sigma-Aldrich at analytical grade. Each step of the preparation was checked by AFM (see the following Sect. 4.3.2).

For the SERS spectroscopy investigation, the surface of the NCAs obtained by both protocols was labelled with the standard 4ATP probe through a three hours incubation with a 0.05 g/l water solution of the molecule, again followed by rinsing with milliQ water in order to remove the unbound molecules, and drying under pure nitrogen gas [Dom2011]. In the spectroscopic maps presented in this Section, the step of the scan was set at 0.5  $\mu m$ . The intensity of a selected Raman/SERS band (details are discussed in the following) was then calculated by integrating the spectrum around the band frequency and plotted against the spatial coordinates.

# 4.3.2 Analysis of the Patterned Arrays

We have prepared four replicates per sector, each one consisting of a squared two dimensional array of wells with variable size and pitch (d and  $\Lambda$ , respectively). Each e-beam preparated sector - denoted by specific values of d and  $\Lambda$  - was identified with a capital letter (see Fig. 4.12). In Fig. 4.12 we report the results of the AFM analysis of the lithographically prepared patterns at two values of the area dose (100 and 20  $\mu$ C/cm<sup>2</sup>). Atomic force microscopy was performed in order to compare the CAD nominal characteristics of the template patterns with the ones obtained experimentally.

No significant discrepancies were revealed between the nominal and the measured  $\Lambda$ . On the contrary, nominal and experimental d values were found to be markedly different for both doses (see Table 4.1). These differences increased at smaller values of  $\Lambda$ . When the higher dose was used, in particular, the correspondence between the nominal and obtained masks was significantly degraded (see for example the well size d, detected on the sectors with the higher  $\Lambda$  values,  $\Lambda$  and  $\Lambda$  in the following Table 4.1). As the Np binding size is the Si surface exposed at the bottom of the well, the experimental value of d corresponds to the size of the Np cluster eventually formed. In Fig. 4.13 we report the  $\Lambda$  imaging and the corresponding height profiles

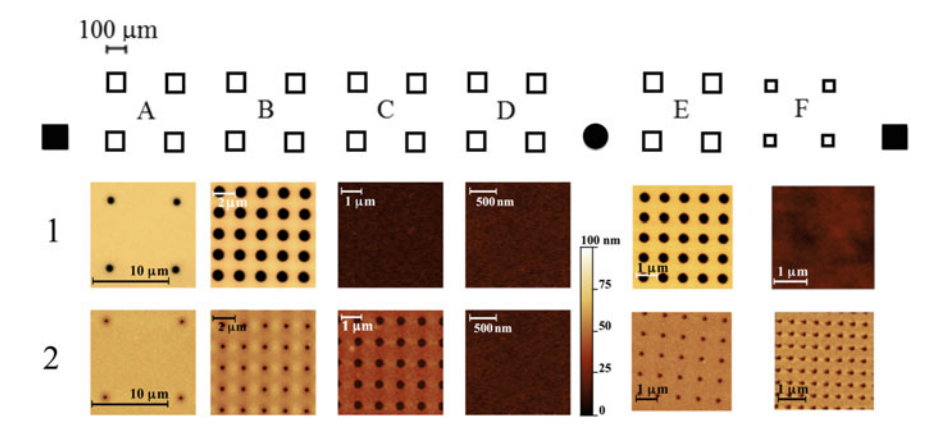


**Fig. 4.12** Arrangement of the designed sectors (four replicates for sector) together with the AFM topography on a single representative sector (type  $\mathbf{a}$ – $\mathbf{f}$ ) lithographed using an area dose value of  $100 \,\mu\text{C/cm}^2$  (row 1) and of  $20 \,\mu\text{C/cm}^2$  (row 2). Reproduced with permission from [Dom2016]

**Table 4.1** Geometric features of the different sectors realized at variable e-beam dose. Uncertainties on the experimental d values are standard deviations calculated on 5 profiles for each sector. The parameter  $\Lambda - d$  is critical for a successful design of the lithographic mask (see Sect. 3.1)

Sector	Dose value	Λ	Nominal d	$\Lambda - d$	measured d
	(μC/cm <sup>2</sup> )	(µm)	(µm)	(µm)	(µm)
(A,1)	100	10	0.500	9.500	$0.70 \pm 0.06$
(A,2)	20	10	0.250	9.750	$0.25 \pm 0.02$
$(A,2)^a$	20	10	0.500	9.500	$0.44 \pm 0.03$
(B,1)	100	2	0.500	1.500	$0.87 \pm 0.07$
(B,2)	20	2	0.250	1.750	$0.30 \pm 0.03$
$(B,2)^a$	20	2	0.500	1.500	$0.57 \pm 0.04$
(C,1)	100	1	0.500	$0.500^{b}$	"bowl"
(C,1) <sup>a</sup>	100	1	0.250	0.750	$0.7 \pm 0.1$
(C,2)	20	1	0.250	0.750	$0.33 \pm 0.05$
(D,1)	100	0.75	0.500	0.250	"bowl"
(D,2)	20	0.75	0.500	$0.250^{c}$	"bowl"
$(D,2)^a$	20	0.75	0.250	0.500	$0.23 \pm 0.07$
(E,1)	100	1	0.250	0.750	not reproducible
(E,2)	20	1	0.125	0.850	0.040 (not uniform)
(F,1)	100	0.50	0.250	0.250	"bowl"
(F,2)	20	0.50	0.125	0.375	0.040 (not uniform)

<sup>&</sup>lt;sup>a</sup>Sectors with nominal d halved or doubled with respect to those shown in Fig. 4.12

<sup>&</sup>lt;sup>b</sup>RS<sub>100</sub>

 $<sup>^{</sup>c}$ RS<sub>20</sub>

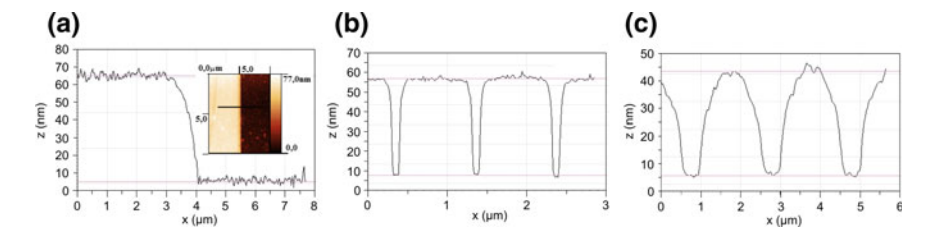


Fig. 4.13 AFM profiles monitor the thickness of the resist film after the spin-coating process (a), and after the e-beam writing ( $100 \,\mu\text{C/cm}^2$  dose) on the sectors (A,1) and (B,1), corresponding to the larger  $\Lambda = 10 \,\mu\text{m}$  (b) and the smaller  $\Lambda = 2 \,\mu\text{m}$  (c) (see Table)

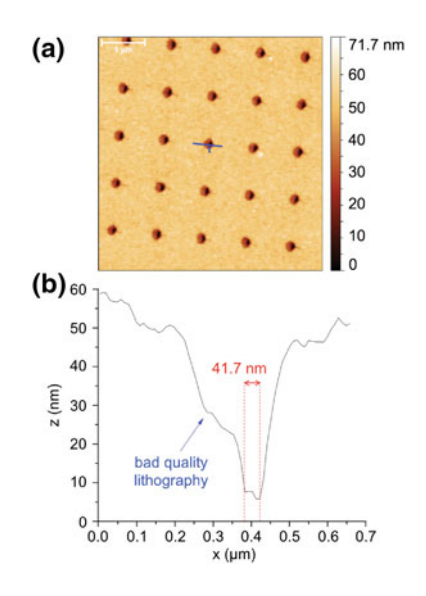
acquired on sectors A an B, demonstrating the effect of the e-beam process at varying doses on the resist coating the silicon substrates. As noticeable from the AFM profiles in Fig. 4.13b, c, despite the offset in the expected d values discussed above, the e-beam writing at the intense dose of  $100\,\mu\text{C/cm}^2$  resulted in symmetric wells, regularly disposed on the thin resist film.

The enlargement of the single e-beam written site is called *intraproximity* and it is caused by the strong electron scattering, degrading the polymer on a region wider than expected [Hu2006]. At smaller values of the pitch  $\Lambda$ , the scattering can also affect the shape of the sites: this is the *interproximity* effect [Hu2006]. Both these phenomena generate and uneven and difficultly predictable degradation of the the resist within individual sites, eventually affecting even the overall thickness of the lithographed resist film (compare the profile scales in Fig. 4.13a–c).

While the effect of a reduction of  $\Lambda$  is to increase the interproximity effect and therefore a reduced precision in the e-beam writing, a decrease of the nominal d by a factor 2 for a given  $\Lambda$  markedly reduces the mismatch between the nominal and measured values of d. This can be explained with a reduced electron scattering, motivated by the fact that a shorter exposure time is required to write a smaller well. This can be expected as the energy absorbed by the polymeric resist depends on both the exposure time and the e-beam intensity, and their product defines the dose. Coherent considerations can be made in commenting the results of AFM on sectors C and D, where  $\Lambda$  is reduced by a factor 2 compared to A and B, respectively. At higer doses, the resist was degraded on the whole array area due to the interproximity effect: a single "bowl" was therefore formed over the whole sector (see Fig. 4.12). A similar effect was observed on sector (F,1) ( $\Lambda$  and d halved compared to (C,1)).

Adopting an empirical approach, we can define a dose-dependent threshold value for the resist sinking,  $RS_{dose} = \Lambda - d$ , below which the proximity effect takes over and prevents to resolve the single sites for Np binding, thus resulting in a blurred EBL escavated "bowl" in the resist. At high doses (100  $\mu$ C/cm²),  $RS_{100} \sim 0.5 \mu$ m. At smaller dose values, RS is expected to be smaller: indeed, we can successfully obtain patterns that are more densely structured (see e.g. masks C and F, Fig. 4.12). For a dose of 20  $\mu$ C/cm²,  $RS_{20} \sim 0.25 \mu$ m. Further reducing the dose with the aim of lowering RS is not advisable, as this could prevent the resist complete writing, down

Fig. 4.14 AFM imaging (a) and profilometry (b) acquired on part of the lithographed E sector ( $\Lambda$ =1  $\mu$ m; d = 0.125) that was realized using an e-beam dose of 20  $\mu$ C/cm². The dashed red lines delimit the region where the resist development reached the Si wafer: the silicon surface exposed effectively achievable for Np deposition is much smaller than expected



to the silicon surface. This happened for example in correspondence of sector E: when writing using a dose of  $20~\mu\text{C/cm}^2$ , a large asymmetric degradation of the resist is obtained (see the AFM profile in Fig. 4.14): the escavated area partially overlaps the site designed for Np functionalization. In order to avoid the problem, it might be necessary to increase the dose by prolonging the exposure time (i.e., the dwell time). Increasing the e-beam intensity can cause an unexpected, irregular enlargement of the obtained wells, while the writing process results poorly reproducible (see sector (E,1) in Fig. 4.12).

This analysis demonstrates that very accurate and reproducible microstructures can be realized if the dose values are adjusted properly. This preliminar study was the basis for the preparation of Np aggregates of micrometric and submicrometric size, ordered according to the patterns in sectors (A,1), (B,1) and (B,2), i.e. with a 2 and 10  $\mu$ m spacing.

# 4.3.3 Analysis of the Ordered Nanoparticle Cluster Arrays

Two-dimensional arrays of Np clusters were produced by functionalizing the Si surface within the e-beam designed binding sites in order to favor the Np binding (Fig. 4.11). As discussed in Sect. 4.3.1, two different chemical protocols were adopted, being the first based on APTS/Glu/4ATP and the second on MPTS functionalization. We realized NCAs according to the patterns labelled as A and B sectors. After the resist lift off, AFM topography allowed to investigate the result of the NCA formation in the two cases (see Fig. 4.15). In part (a) of the Figure, we notice that in the APTS/Glu/4ATP case, while the organization of the Np clusters is ordered

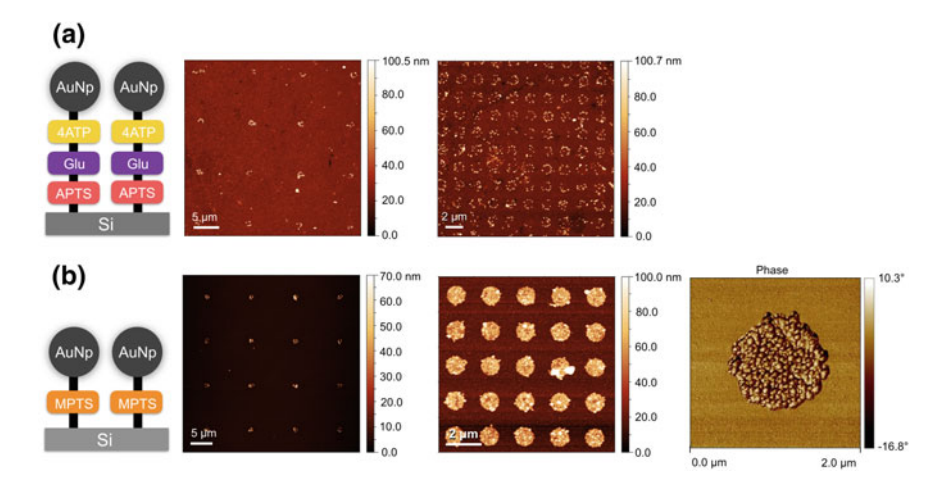


**Fig. 4.15** AFM images of NCAs obtained from a and b sectors using APTS-Glu-4ATP (panel (a)) or MPTS (panel b) for linking the Nps onto the Si-OH binding sites. Panel a, from left to right: the functionalization scheme, the topography of array areas from (A,1) and (B,1) sectors specified in the Table. Panel b, from left to right: the functionalization scheme, the topography of array portions of (A,1) and (B,1), and the phase image of a representative Np cluster from (B,1)

in the long range order, the number of Nps linked within the single binding sites is insufficient to obtain a close packed cluster of the type discussed in Sect. 4.1. In part (b) of the Figure the better results achieved with the MPTS linker are shown. The second protocol allowed obtaining regular arrays of densely packed Np clusters: AFM profiles acquired on a representative aggregate are displayed in Fig. 4.16a and show a nicely defined structure formed by a single Np layer. In some cases we observed an overlayer structure formed by an excess of Nps, as reported in Fig. 4.16b (see also Fig. 4.15, part B, 2  $\mu$ m spaced array). These irregular structures might be explained by physisorption during the incubation process. Nevertheless, we cannot exclude the overlayer growth to be related to the rare occurrence of Np clustering before the deposition, already within the nanocolloid used for the incubation. Notably, we can instead rule out the presence of impurities at atomic resolution, by combining the high resolution AFM topography and the phase image (Fig. 4.15b). The fine control of the vertical Np assembly in these cluster remains an open challenge.

In 4.15 the different efficiency in Np binding of the two NCA preparation protocols is evident if we compare part a and b. This is the effect of differences in the number of steps and chemicals involved in the two protocols and is probably partially related to a different concentration of the anchoring agent. The lower number of steps and the stability of the product seem favorable in the case of the MPTS protocol. Indeed, the SERS substrates obtained by MPTS covalently linking the Nps are very stable, also in water, for several days.

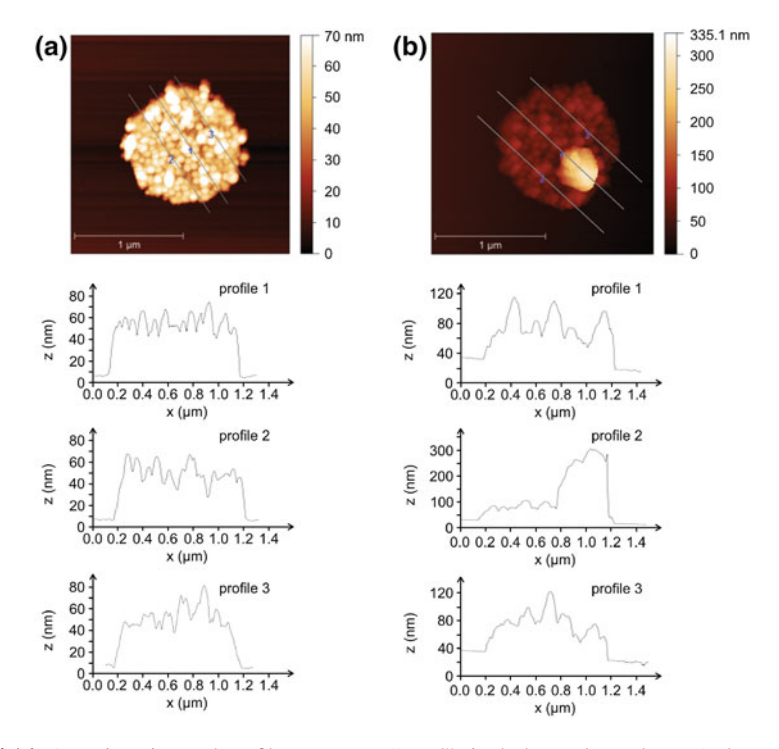


**Fig. 4.16** AFM imaging and profilometry on a "good" single-layered Np cluster (column a) and on a "bad" Np cluster featuring an overlayer Np disposition (column b). Both aggregates belong to sector (B,1) ( $\Lambda=2~\mu m$  and  $d=1~\mu m$ ) of the MPTS functionalized substrates. Notice from the scale of the profiles that the height values are compatible with a single layer **a** or an overlap **b** of several 60 nm sized Nps

Notably, both protocols expose the AuNps surface unfunctionalized, and therefore ready for physi- or chemi-sorption of different analytes, although the Np tight arrangement in clusters partially reduces the portions of the Np area available for analyte binding. An alternative approach could be to engineer the Np binding of analytes, as proteins and cells, in solution [Jia2009] and consequently induce the Np arrangement in clusters (e.g. with the APTS-Glu linker for the detection of 4ATP or similar molecules).

As discussed, we tested the potentiality of the characterized NCA in SERS sensing by functionalizing the available Np surface with the usual 4ATP probe and by monitoring its spectroscopic signal upon illumination with a 633 nm He-Ne laser. We mainly focused on the (A,1) sectors, so that the separation between clusters  $\Lambda$  was large enough to avoid the possibility of optical interferences in the signal from the clusters within the array. In Fig. 4.17 we report the results of the optimized spectroscopic mapping.

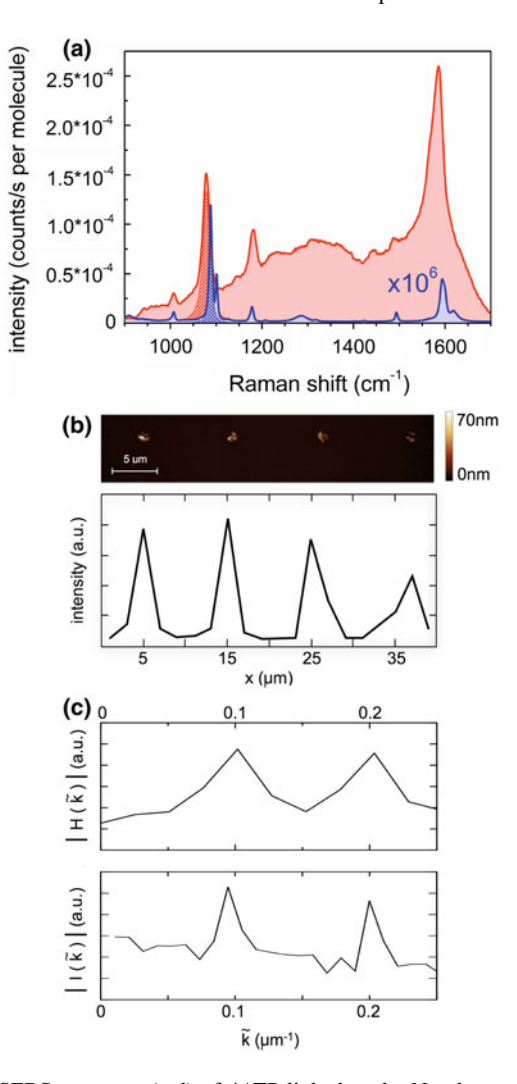


**Fig. 4.17** Panel A: SERS spectrum (red) of 4ATP linked to the Np clusters is compared to the molecule conventional Raman spectrum (blue). Both spectra are normalized to the number of molecular scatterers within the scattering volume, thus contributing to the spectroscopic signal. The conventional Raman spectrum is multiplied by a scaling factor of  $10^6$  to allow its visibility. The integrated intensities used to estimate the enhancement factors are highlighted: the whole spectral integral is coloured in light red (SERS) and light blue (Raman spectrum), while the area of the band centered at  $1078 \text{ cm}^{-1}(1089 \text{ cm}^{-1}\text{in Raman spectrum})$ , estimated through a Lorentzian fitting, is shown using a squared pattern, again in red and blue, respectively. Panel B: a representative SERS (C-S stretching) intensity trend measured along a row of the sector A (Λ = 10 μm, d = 1 μm), compared with the corresponding AFM topography. Panel C: FFT of the AFM height signal of sector A (upper plot, |H(k)|) is compared to the FFT of the SERS signal on the same sector (lower plot, |I(k)|). Notice the peak at the periodicity of 10 μm (centered at  $0.1 \text{ μm}^{-1}$ ) and its second harmonic (at  $0.2 \text{ μm}^{-1}$ ). The comparatively larger width of the AFM FFT peaks is related to the different size of the frame measured (40 μm and 75 μm for AFM and SERS acquisition, respectively)

#### 4.3.4 SERS Reproducibility

In Fig. 4.17a we present a representative SERS spectrum of 4ATP, acquired on a Np cluster of  $d=1~\mu m$  size from a sector with inter-cluster spacing of  $\Lambda=10~\mu m$ , and we compare it with the conventional Raman spectrum of the molecule (see Chap. 3 for the band assignment). As expected, the SERS effect strongly increases the Raman cross section of the 4ATP molecule when this is bound to the nanostructured metal surface [Ank2008, Dom2012]. The strong SERS signal allowed the quick realization of spatially resolved scans, identifying the Np cluster position on the substrates and revealing experimentally a full correspondence between the AFM topography and SERS intensity maps that is displayed in Fig. 4.17b. In panel (c) we demonstrate that the periodicity of the AFM height signal and the SERS intensity is the same by comparing their fast Fourier transform (FFT).

In order to evaluate the efficiency in signal enhancing of our plasmonic substrate, we can calculate the enhancement factor (EF) that is the ratio of SERS and Raman spectroscopic intensity per single molecule, as explained in the previous Sections. In this analysis, we have estimated the number of molecules contributing to the spectroscopic signal via geometrical considerations (for a detailed discussion, see [Fas2014]). We have then calculated an *overall* EF by integrating the whole 4ATP SERS/Raman spectrum over the *fingerprint* spectral region (shown in Fig. 4.17a) and a *band* EF, obtained by comparing the integrated intensity of the strong C-S stretching band, centered at 1089 cm<sup>-1</sup> in the Raman spectrum and red-shifted to  $1078 \text{ cm}^{-1}$  in the SERS spectrum.

Notably, while integrating over the whole spectrum we are considering both the electromagnetic and the chemical contributions to the SERS enhancement, the band EF is expected to account exclusively for the electromagnetic mechanism, as reported for the enhancement of the C-S stretching band [Osa1994]. The overall EF is to be used for molecules bound covalently to the metal surface, allowing charge-transfer phenomena to take place. On the contrary, the intrinsically smaller band, electromagnetic EF is representative for molecules physisorbed to the metal surface.

It is worth mentioning that some significant drops or raises in SERS intensity (>20%) were occasionally detected: we ascribe these fluctuations to the uneven surface packing exhibited by isolated Np assemblies, as confirmed by both optical inspection and AFM topography (see Fig. 4.16b). Nevertheless, the large number of clusters within a  $100 \times 100 \ \mu m^2$  sector allows discarding the worst data, enabling a contained variability of the SERS intensity (within the 20% on ensembles up to 30 clusters, measured consequently). As also reported in the scale of Fig. 4.17a, we have estimated on our NCAs an *overall E F* of  $(1.1 \pm 0.2) \times 10^7$ , which is to be considered very positively if compared to the performances of other gold-based SERS substrates, as reported in the literature [Yan2009, Yan2011b]. We also estimated a *band* EF of  $(0.30 \pm 0.06) \times 10^7$ . The order of magnitude of our *band* EF is in agreement with what is predicted by simulations on similar systems, consisting of layers of closely packed AuNps (see Sect. 4.2).

These experimental observations confirm the idea that Np clusters of micrometric, controlled areas can provide quite regular, reproducible, and highly enhanced Raman signals. On top of these notable results from the spectroscopic point of view, these periodically arranged structures present a strong potential for the integration within portable devices, capable of parallel operation for multiple and automated analyses [Str2007, Jia2009, Cos2014]. We therefore believe that they might represent step further towards effective, SERS-based, Lab-on-Chip devices [Cos2014].

#### References

[Alb2013]	Alba M, Pazos-Perez N et al (2013) Macroscale plasmonic substrates for highly sensitive surface-enhanced Raman scattering. Angew Chem Int Ed 52(25):6459–6463
[Ank2008]	Anker JN, Hall WP et al (2008) Biosensing with plasmonic nanosensors. Nat Mater 7(6):442–453
[Bai2006]	Baia M, Toderas F et al (2006) Probing the enhancement mechanisms of SERS with p-aminothiophenol molecules adsorbed on self-assembled gold colloidal nanoparticles. Chem Phys Lett 422(1):127–132
[BC2009]	Bizzarri AR, Cannistraro S (2009) Surface-enhanced Raman spectroscopy combined with atomic force microscopy for ultrasensitive detection of thrombin. Anal

[Ber1994] Berenger J-P (1994) A perfectly matched layer for the absorption of electromagnetic waves. J Comput Phys 114(2):185–200

Biochem 393(2):149-154

- [Bre2012] Brewer G (2012) Electron-beam technology in microelectronic fabrication. Elsevier, Amsterdam
- [But1986] Butler RW (1986) Optimal stratification and clustering on the line using the L1norm. J Multivar Anal 19(1):142–155
- [Cos2014] Costantini F, Nascetti A et al (2014) On-chip detection of multiple serum antibodies against epitopes of celiac disease by an array of amorphous silicon sensors. RSC Adv 4(4):2073–2080
- [DJ2014] Deng Y-L, Juang Y-J (2014) Black silicon SERS substrate: effect of surface morphology on SERS detection and application of single algal cell analysis. Biosens Bioelectron 53:37–42
- [Dom2011] Domenici F, Bizzarri AR et al (2011) SERS-based nanobiosensing for ultrasensitive detection of the p53 tumor suppressor. Int J Nanomed 6:2033–2042
- [Dom2012] Domenici F, Bizzarri AR et al (2012) Surface-enhanced Raman scattering detection of wild-type and mutant p53 proteins at very low concentration in human serum. Anal Biochem 421(1):9–15
- [Dom2016] Domenici F, Fasolato C et al (2016) Engineering microscale two-dimensional gold nanoparticle cluster arrays for advanced Raman sensing: an AFM study. Colloids Surf A PhysChemical Eng Asp 498:168–175
- [Fan2008] Fang Y, Seong N-H et al (2008) Measurement of the distribution of site enhancements in surface-enhanced Raman scattering. Science 321(5887):388–392
- [Fas2014] Fasolato C, Domenici F et al (2014) Dimensional scale effects on surface enhanced Raman scattering efficiency of self-assembled silver nanoparticle clusters. Appl Phys Lett 105(7):073105
- [Fas2015] Fasolato C, Domenici F et al (2015) Self-assembled nanoparticle aggregates: organizing disorder for high performance surface-enhanced spectroscopy. In: NANOFORUM 2014, vol. 1667. AIP Publishing, p 020012

Fraire JC, Pérez LA et al (2012) Rational design of plasmonic nanostructures for

[Fra2012]

[Lu2005]

L	,
	biomolecular detection: interplay between theory and experiments. ACS Nano 6(4):3441–3452
[FS1996]	Frenkel D, Smit B (1996) Understanding molecular simulations: from algorithms
	to applications. Academic, San Diego
[Ged2011]	Gedney SD (2011) Introduction to the finite-difference time-domain (FDTD)
	method for electromagnetics. Synth Lect Comput Electromagn 6(1):1-250
[HC2001]	Halliwell CM, Cass AEG (2001) A factorial analysis of silanization conditions for
	the immobilization of oligonucleotides on glass surfaces. Anal Chem 73(11):2476–
	2483
[HT2000]	Hagness SC, Taflove A (2000) Computational electrodynamics: the finite differ-
	ence time-domain method. Artech House, Norwood
[Hu2006]	Shu-Fen H, Huang K-D (2006) Proximity effect of electron beam lithography on
FT.G1.0=01	single-electron transistors. Pramana 67(1):57–65
[JC1972]	Johnson PB, Christy RW (1972) Optical constants of the noble metals. Phys Rev
FT 20161	B 6(12):4370
[Jeo2016]	Jeong JW, Arnob MMP et al (2016) 3D cross-point plasmonic nanoarchitectures
	containing dense and regular hot spots for surface-enhanced Raman spectroscopy
[Jia2009]	analysis. Adv Mater 28:8695
[J1a2009]	Jia C-P, Zhong X-Q et al (2009) Nano-ELISA for highly sensitive protein detection. Biosens Bioelectron 24(9):2836–2841
[Kim2011]	Kim NH, Lee SJ et al (2011) Reversible tuning of SERS hot spots with aptamers.
[Kiiii2011]	Adv Mater 23(36):4152–4156
[KL1993]	Kunz KS, Luebbers RJ (1993) The finite difference time domain method for elec-
[1221//0]	tromagnetics. CRC Press, Boca Raton
[Kne1997]	Kneipp K, Wang Y et al (1997) Single molecule detection using surface-enhanced
,	Raman scattering (SERS). Phys Rev Lett 78(9):1667
[Kne2006]	Kneipp K, Moskovits M et al (2006) Surface-enhanced Raman scattering: physics
	and applications, vol 103. Springer Science & Business Media, Berlin
[Liu2014]	Liu H, Yang Z et al (2014) Three-dimensional and time-ordered surface-enhanced

substrate. Nano Lett 5(1):5–9
[Moh2012] Mohammad MA, Muhammad M et al (2012) Fundamentals of electron beam exposure and development. Nanofabrication. Springer, Berlin, pp 11–41

Raman scattering hotspot matrix. J Am Chem Soc 136(14):5332-5341

Lu Y, Liu GL et al (2005) High-density silver nanoparticle film with temperature controllable interparticle spacing for a tunable surface enhanced Raman scattering

- [Mos2013] Moskovits M (2013) Persistent misconceptions regarding SERS. Phys Chem Chem Phys 15(15):5301–5311
- [MT2003] Marrian CRK, Tennant DM (2003) Nanofabrication. J Vac Sci Technol A 21(5):S207–S215
- [NE1997] Nie S, Emory SR (1997) Probing single molecules and single nanoparticles by surface-enhanced Raman scattering. Science 275(5303):1102–1106
- [NH2012] Novotny L, Hecht B (2012) Principles of nano-optics. Cambridge University Press, Cambridge
- [Nil1967] Nilsson G (1967) Optimal stratification according to the method of least squares. Scand Actuar J 1967(3–4):128–136
- [Osa1994] Osawa M, Matsuda N et al (1994) Charge transfer resonance Raman process in surface-enhanced Raman scattering from p-aminothiophenol adsorbed on silver: Herzberg-Teller contribution. J Phys Chem 98(48):12702–12707
- [Pal1998] Palik ED (1998) Handbook of optical constants of solids. Academic, Cambridge [Pre2007] Prevo BG, Kuncicky DM et al (2007) Engineered deposition of coatings from nanoand micro-particles: a brief review of convective assembly at high volume fraction. Colloids Surf A PhysChemical Eng Asp 311(1):2–10

[SN2012]	Siddhanta S (2012) Surface enhanced Raman spectroscopy of proteins: implica-
C J	tions in drug designing. Nanomater Nanotechnol 2(2012):2–1
[Sti2008]	Stiles PL, Dieringer JA et al (2008) Surface-enhanced Raman spectroscopy. Ann
	Rev Anal Chem 1:601–626
[Str2007]	Strehle KR, Cialla D et al (2007) A reproducible surface-enhanced Raman spec-
	troscopy approach. Online SERS measurements in a segmented microfluidic sys-
	tem. Anal Chem 79(4):1542–1547
[Sul2013]	Sullivan DM (2013) Electromagnetic simulation using the FDTD method. Wiley,
	New Jercy
[TK1993]	Tandon US, Khokle WS (1993) Patterning of material layers in submicron region.
	Halsted Press, Sydney
[Utk2012]	Utke I, Moshkalev S et al (2012) Nanofabrication using focused ion and electron
	beams: principles and applications. Oxford University Press, Oxford
[Van1993]	Van Duyne RP, Hulteen JC et al (1993) Atomic force microscopy and surface-
	enhanced Raman spectroscopy. I. Ag island films and Ag film over polymer
	nanosphere surfaces supported on glass. J Chem Phys 99(3):2101–2115
[Yan2009]	Yan B, Thubagere A et al (2009) Engineered SERS substrates with multiscale
DV 0011 1	signal enhancement: nanoparticle cluster arrays. ACS Nano 3(5):1190–1202
[Yan2011a]	Yan B, Boriskina SV et al (2011) Design and implementation of noble metal
	nanoparticle cluster arrays for plasmon enhanced biosensing. J Phys Chem C
FN7 - 001111	115(50):24437–24453
[Yan2011b]	Yan B, Boriskina B et al (2011) Optimizing gold nanoparticle cluster configurations
[Vee2010]	(n ≤ 7) for array applications. J Phys Chem C 115(11):4578–4583
[Yos2010]	Yoshida KI, Itoh T et al (2010) Quantitative evaluation of electromagnetic enhance-
	ment in surface-enhanced resonance Raman scattering from plasmonic properties
[7W2012]	and morphologies of individual Ag nanostructures. Phys Rev B 81(11):115406
[ZW2012]	Zhang Z, Wen Y (2012) Controllable aggregates of silver nanoparticle induced by

methanol for surface-enhanced Raman scattering. Appl Phys Lett 101(17):173109

# Chapter 5 SERS-Active Nanovectors for Single-Cell Cancer Screening and Theranostics



In Chap. 3, we have presented the synthesis and thorough characterization of SERS active nanovectors based on gold Nps functionalized with folate and antifolate molecules. We will here report on the application of these systems for cancer diagnostics and therapy at single cell level. Section 5.1 contains a brief introduction to the problem and the motivation for our work.

In Sect. 5.2, we will discuss the potentialities of SERS-active, folate conjugated Nps in cancer early diagnostics. Folic acid plays an essential role in cellular metabolism and reproduction. For this reason, cancer cells tend to overexpress folate binding proteins on their membrane when compared to healthy ones. As an effect of the different receptor expression level, our nanovector selectively targets cancer cells and localizes on their membrane. Measuring SERS signal from cells treated with the nanovector allows for monitoring the density of folate binding proteins on their membrane. We will describe the SERS-based single-cell screening procedure we have developed. This protocol allowed the discrimination of different normal and cancer lines chosen based on their folate receptor expression [Fas2016].

In the final Sect. 5.3, results regarding the interaction of theranostic, antifolate-based nanovectors are presented. The toxic action of aminopterin and methotrexate loaded gold Nps, labelled with SERS reporter 4ATP, was preliminary tested on cancer cells: as expected, a strong cytotoxicity was revealed when compared to folate functionalized Nps [Fas2018]. In order to investigate the effect of nanostructuring, a comparative study on aminopterin was performed by treating the cells with the same amount of drug either fixed on the nanovector or in the free molecular form. The enhanced cytotoxicity revealed for the nanostructured drug was explained in relation to the oriented binding induced by Np functionalization. Furthermore, an investigation on the nanovector selectivity was carried out by comparing the results of the treatment on cancer and normal cells [Fas2018].

The studies we present are proof of principle experiments, performed on cell culture grown at a laboratory level. The successful results obtained are promising of further interesting developments: as a first step, we are planning to test these methods on primary cell lines.

#### **5.1** Early Cancer Diagnostics and Theranostics

At the frontiers of oncology in recent years, much interest has been attracted by the early detection of cancer, that is the capability to reveal the presence of the disease at the first stages of its progression: undoubtedly, a prompt diagnosis opens the way to more effective treatments [Smi2015]. In this framework, a growing need has been expressed for the development of highly sensitive and specific detection methodologies [Chi2015]. The current challenge is to detect the presence of extremely few cancer cells in small, stable biological samples, granting low invasiveness, sensing reproducibility and high versatility with respect to the different tumor types and metastatic spread [Bac2000, Har2003]. However, because of tumor heterogeneity, cancer cells can often elude even specific analyses: for this reason, the implementation of novel detection methodologies [Mir2015, Cao2011] can be crucial to address effective diagnosis [Cao2011].

A strategy for the identification of cancer cells within a screening is represented by the recognition of characteristics that are specific of cancer cell, as their peculiar morphology [Boe2004] or their mechanical properties [Cro2007]. Another possibility is to selectively target cancer cells by means of traceable markers, contrast agents that, in the case of optical screening, can be fluorophores or spectroscopically active molecules [Chi2015, Mit2011]. The achieved traceability of cancer cells can be exploited for cell sorting, as realized in flow-cytometry assays [Bar1983, Krü2002]. The targeting method relies on the different bioaffinity of cancer cells for certain molecules, that depends on the higher density of specific receptors on their membrane [Mit2011]. This peculiarity has already been exploited for diagnostics, by targeting these receptors with objects, featuring therapeutic features, functionalized with specific proteins or antibodies [Fan2012, Baz2015].

Unfortunately, these macromolecules are highly sensitive to temperature, pH and other environmental conditions: their functionality is therefore rather unstable. Moreover, they often tend to form assemblies with other proteins in human serum [Ehr2009], inhibiting both sensitivity and specificity of the biorecognition [Sal2013]. An alternative to proteins for biotargeting is the use of small and more stable molecules, such as folic acid (FA) [Luc2000]. Also FA binding proteins are, indeed, differently expressed depending on the cell type [Wei1992], and more frequent on cancer cell membranes. Cancer cells express a large number of FA-receptors due to the crucial role of FA in cellular metabolism and replication [Wei1992], while in healthy cells their expression is relatively low [Luc2000, Par2005, Wib2013]. For this reason, one can think of identifying a suitable technique that highlights the different densities of FA receptors that can be found on different cells.

In this framework, SERS-based methods can offer interesting opportunities towards the ultrasensitive detection of selected cancer cells through a specific, biomolecular-mediated interaction with a properly designed plasmonic object [VoD2010, Kah2007]. Gold nanocolloids have been widely used in the design of biosensors for tumor markers [Kah2007], owing to their peculiar properties, as a high surface-to-volume ratio, which enables a versatile biomolecular conjuga-

tion [Dom2011, Dom2012] (see also Chap. 3), their desirable chemical stability [GP2007] and relatively low cytotoxicity [Fra2015]. Displaying high signal enhancement capabilities, properly functionalized Nps [Kne2010, Li2015] can be successfully employed for highlighting the differences among cancer and normal cells in terms of density and even type, as will be discussed, of FA receptors [Kan2013], therefore making the first step in the direction of cancer detection at single cell level [And2011, Pal2015, Wer2011].

Moreover, both the plasmonic nature and the bioconjugation of metal Np based nanovectors can be exploited for adding some therapeutic features to the system. In this way, diagnostics can be coupled with therapy. At single cell level, cancer therapy consists of selectively killing cancer cells without damaging the healthy tissue surrounding them. This can be performed in different ways, exploiting the localized properties of the nanovector.

Photothermal-induced cancer therapy exploits the strong absorption of plasmonic nanostructures for inducing a local heating in the proximity of Np illuminated with radiation (usually in the near infrared spectral range, to exploit the transparency spectral window of biomaterials). If the Nps have been selectively bound or internalized by cancer cells, this local increase of temperature will result in the selective killing of these cells [Hua2008, Lu2010, Boc2013]. Another possible approach is to exploit the versatility of Np biofunctionalization for loading chemotherapic drugs onto the Np surface: for their low-toxicity and traceability, gold Np based systems are interesting candidates for selective drug delivery applications [Gho2008, Dre2012].

## **5.2 Folate-Based SERS Diagnostics**

Targeting strategies for inducing the selective interaction of cells with a nanosensor are usually based on molecular biorecognition. In this framework protein/antigen interactions are widely exploited, although protein based biofunctionalization can suffer from stability issues, which can prevent the success of the method, as previously discussed (Sect. 2.3.2). An alternative choice for nanovector bioconjugation is represented by small, stable molecules such as folic acid (FA) [Sam2016].

FA is a group B vitamin, commonly used as a therapy for some types of anemia and as a supplement during pregnancy. Its action in several coenzyme forms is related to the acceptance, redox processing and transfer of one-carbon units. Folate metabolism reactions are essential for amino acid metabolism, purine and pyrimidine synthesis and for the formation of the primary methylating agent, S-adenosylmethionine [BG1999, Luc2000].

FA binding proteins are differently expressed depending on the cell type [Wei1992]. As an effect of the crucial role of folate in cell metabolism and replication [Luc2000], cancer cells tend to express a large number of FA-receptors compared to their relatively low expression level in healthy tissues [Wei1992, Par2005].

#### 5.2.1 Idea of the Experiment

We illustrate here an approach that combines the high sensitivity of SERS with the selective recognition of FA operated by several types of cells through the different expression of their molecular receptors [Par2005, Wib2013]. A sketch of the experiment is presented in Fig. 5.1.

We propose a cellular screening based on the intensity of the SERS signal provided by a folate conjugated SERS-active nanovector [Boc2013, Sam2016]. By treating different cell lines with this FA-nanovector, one expects a different binding efficiency depending on the density of FA receptors on the membrane of the specific cell type. A measurement of the overall SERS signal intensity from a single cell can provide an estimate of the nanovector binding efficiency and therefore, indirectly, of the level of FA receptor expression. As illustrated in Chap. 3, we have thus realized a folate nanovector by functionalizing gold Nps with the Raman active bifunctional linker 4ATP, which was further conjugated with FA molecules. The synthesis, characterization and SERS signature of such system has been thoroughly presented in Sect. 3.2.1.

We treated three different cell lines - two cancerous, one normal as control - with our folate nanovector, by adding it to the cell culture while maintaining physiological conditions. Cell lines were chosen based on their well studied differences in the folate receptor expression, in terms of both density and types. After the treatment with the SERS nanovector, we monitored the SERS response on the different cell types. A thorough analysis revealed that we reached a clear discrimination between cancer and normal cells based on the spectroscopic signal. The data acquired on the three cell populations were also found to reflect clearly the folate receptor expression levels expected in the corresponding cell lines.

Fig. 5.1 Sketch illustrating the folate-based approach for single-cell cancer screening by SERS intensity

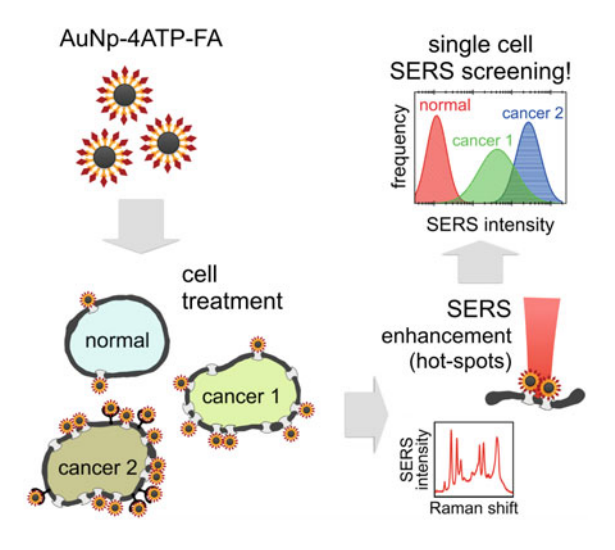
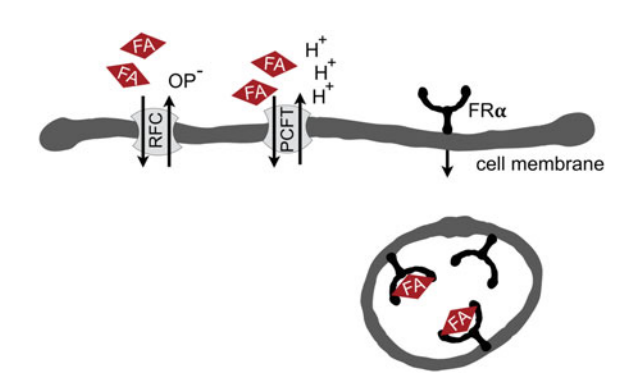


Fig. 5.2 The sketch illustrates the most common folate binding proteins and their internalization mechanisms. RFC and PCFT are solute carriers, while  $FR\alpha$  is a receptor, responsible for folate internalization via endocytosis. Inspired by [Des2012]



#### **Folate Binding Proteins on Normal and Cancer Cells**

The interaction of folate with cells is mediated by two widely expressed facilitative transporters, solute carrier (SLC) proteins, that are the reduced folate carrier (RFC) and the proton-coupled folate transporter (PCFT), and via a family of high affinity folate receptors (FRs), that transport folate via endocytosis [Wu1999, Kel2006] (see Fig. 5.2). There are three isoforms of folate receptor, called FR $\alpha$ , FR $\beta$  and FR $\gamma$ . Among them, FR $\alpha$  is highly expressed in specific malignant tumors of epithelial origin (for example, it is strongly expressed in cervical uterine and ovarian carcinomas, while it is less frequent in prostate carcinoma) [Kel2006, Jos2013].

Choice of cell lines for SERS screening In order to test the folate-based targeting strategy, we chose three different cell lines which are known for their different folate receptor expression, in terms of both density and types. Two of these lines are stable and well studied tumor models: the prostatic cancer cells PC-3 and the cervical cancer cells HeLa [Man2010, Jos2013]. Both the cell lines are known to overexpress the solute carries, but it is FR $\alpha$  that has the highest affinity to folate. The level of expression of FR $\alpha$  has been investigated by Yoshi and coworkers with immunoblotting experiments specifically targeting this receptor with its antibody [Jos2013]. The results are shown in Fig. 5.3. As can be seen, a strong band characterizes the signal of HeLa cells, while a much lower signal is associated to PC-3, in which FR $\alpha$  expression is strongly doubted [Des2012, Jos2013, Fen2013].

For a comparative study on non-cancer cells, we chose HaCaT immortalized keratinocytes, because they were used in a previous work [Kan2013] as a control cell line for fluorescence-based experiments on bioaffinity with folate. Gene expression

Fig. 5.3 Western blot showing the presence of FR $\alpha$  on different cell lines, cancer and non-cancer, compared to a control. Reproduced with permission from [Jos2013]

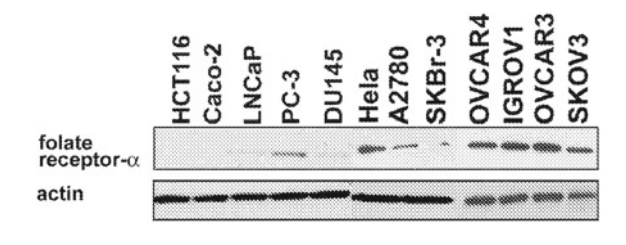


**Fig. 5.4** FA-4ATP-Np complex: AuNp are firstly covered with the Raman reporter 4ATP, than conjugated to folic acid. The red circle identifies the heterocyclic part of the molecule, involved in the biorecognition by folate receptors [Che2013]

investigations recently proved that PCFT is the binding protein responsible for folate supply in HaCaT line, and that its expression level is rather low [Fuj2014].

**Folate biofunctionalization of gold Nps: advantages** The preparation of the gold Np based folate nanovector was thoroughly described in the previous Sect. 3.2. To summarize, the biofunctionalization is a two step process: gold Nps (60 nm diameter) are labelled with SERS reporter 4ATP, and then further conjugated with folic acid (see Fig. 5.4) through covalent bonds. From a biophysical point of view, this functionalization approach has different advantages:

- the colloidal stability of the Np dispersion, which was also proved in cell culture medium [Fas2016]. This is due to the high surface charge conferred to the system by the unbound carboxile moieties (see Fig. 5.4);
- the recognizable and intense SERS signal of the complex FA-4ATP-AuNps, mainly motivated by the presence of highly SERS-active 4ATP molecules close to the Np surface (see Fig. 3.16);
- the oriented binding of folate on the Np surface (see Fig. 5.4), which exposes the pteroyl part of the molecule, active in the biorecognition by folate receptors.

Cell proliferation assay The three cell lines used in the experiment were obtained from Interlab Cell Line Collection (ICLC) (Istituto Nazionale per la Ricerca sul Cancro, Genova, Italy). HaCaT, a human normal keratinocyte cell line, HeLa, a human cervical cancer cell line, and PC-3, an androgen-independent human prostate cancer cell line were grown in DMEM (Euroclone, Life Science Division, GB, Pero, Italy). All media were supplemented with 100 µg mL<sup>-1</sup> penicillin, 100 µg mL<sup>-1</sup> 250 streptomycin and 10% fetal bovine serum (Euroclone). Cells were maintained in a tissue culture incubator at 37°C, 5% CO<sub>2</sub>. The experiments were performed by plating the cells at a density of  $5 \times 10^3$  mL<sup>-1</sup> in 96-well flat plates in the culture medium and then incubated at 37 °C under 5% CO<sub>2</sub>. After 24 h, different concentrations of FA-4ATP-Nps, ranging from 1 to 2 pM, were added in triplicate. We performed different time courses: a 2 h pulse and 24 h of treatment. The cells were then incubated with MTT (3-[4,5-dimethylthiazol-2-yl]-2,5-diphenyltetrazolium) (Sigma-Aldrich, Saint Louis, Missouri, USA) for 4h. The formed crystals were dissolved in 100 μL of DMSO and further incubated for 15 minutes. The absorbance was measured in a plate reader spectrophotometer (Labsystem Multiskan MS), using a test wavelength of 540 nm and a reference wavelength of 690 nm. The cells incubated with

culture medium alone represented the controls, and wells containing the medium alone served as blanks. All the results were analyzed by ANOVA. The significance was evaluated by the Tukey honestly significant difference (HSD) *post hoc* test and data were expressed as means  $\pm$  standard deviation of independent samplings from different experiments. The level of significance was established at p value <0.05.

#### 5.2.2 Cell Treatment and Viability Tests

We treated the cells by adding the nanovector - in a concentrated water dispersion - to the cell culture. The cells were incubated in this condition for two hours, then rinsed with PBS and stabilized for Raman/SERS measurements by drying under a laminar flow at the controlled temperature of 37 °C. Any other chemical fixing agent was avoided in order to minimize the effects of the fixing treatment on the spectroscopic response.

MTT is a standard colorimetric assay used for the assessment of the cellular metabolic activity: its result reflects the number of viable cells within a determined cell culture. For this reason, MTT can be used for determining the cytotoxic level of a certain agent. MTT cytotoxicity assays were used to monitor the effect on the cells of both the nanovector and the other aspects of the treatment itself, as the stress caused by adding a water dispersion to the cell culture. Results obtained on HaCaT, PC-3 and HeLa lines are shown in Fig. 5.5.

All cell lines were treated with 1 pM FA-4ATP-Np solution, only HeLa cell line was also treated with 2 pM Np solution. MTT tests were performed after incubations lasting 2 and 24h at each concentration. In order to determine if the lower viability recorded after the treatment was caused by the presence of the nanovector or to the osmotic stress due to water addition, ultrapure water was added to the HeLa cell culture at different concentrations and incubated for 2h.

In the case of HeLa cells (panel c in Fig. 5.5), the results of MTT assays show the same, very small decrease in viability on water-treated and nanovector-treated wells: this proves that the toxic effect is not correlated with the action of the Nps. As a final check, PC-3 and HaCaT lines were treated with the highest concentration of ultrapure water (50 parts of milliQ water in 50 parts of medium culture) for 2 and 24 h and they did not show any decrease in viability.

# 5.2.3 Raman and SERS Imaging on Treated Cells

Raman spectroscopy was used to measure all the cell lines, both treated ad not treated. In Fig. 5.6, we present representative spectra of PC-3 cancer cells and HaCaT normal cells, focusing on the fingerprint region between 1000 and 1700 cm<sup>-1</sup>. In particular, the spectrum of an untreated PC-3 cell is compared with two spectra acquired on treated PC-3 cancer cells, displaying higher or lower intensity of the SERS signal, and

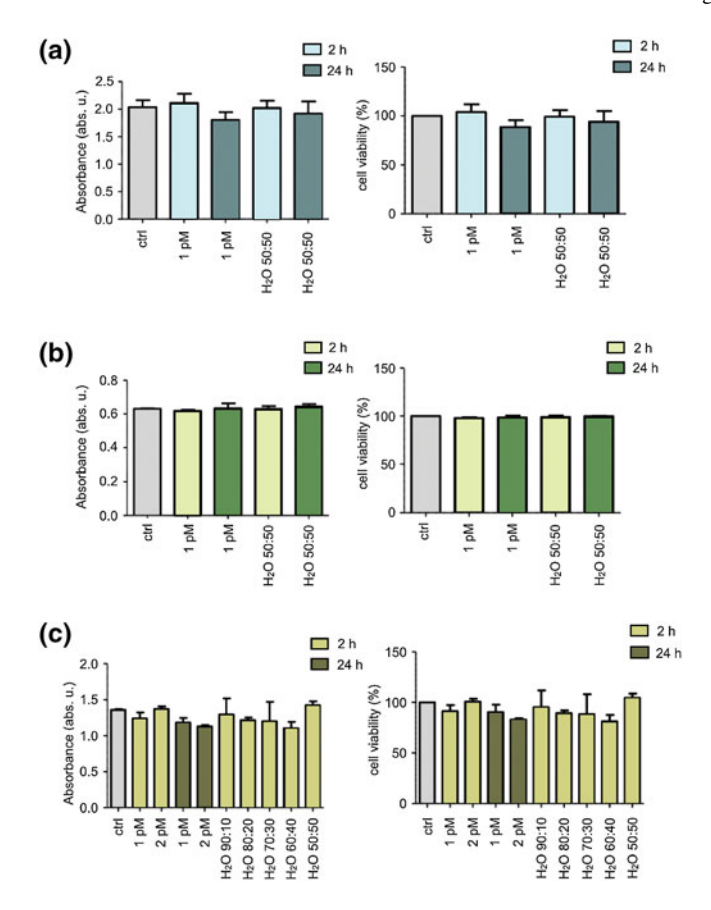
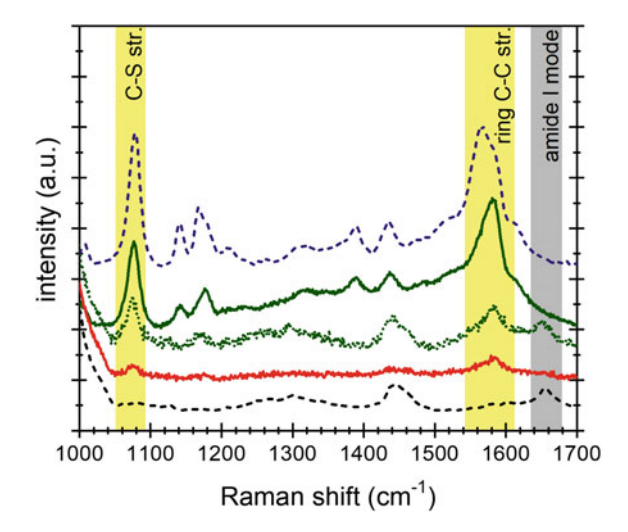


Fig. 5.5 Results of MTT assays on HaCaT (a), PC-3 (b) and HeLa cell lines (c). Columns and bars are mean and standard deviation values from 3 independent experiments. All results were analyzed by ANOVA, and the significance was evaluated by the Tukey honestly significant difference (HSD) post hoc test. The level of significance was established at p < 0.05. Statistical analyses were performed using GraphPad Prism 5 Software

with the one collected on treated HaCaT normal cells. We also present the reference spectrum of the nanovector. Intuitively, we can ascribe the strong bands in the treated cell spectra - within the yellow shaded region - to the presence of the nanovector. In the case of low SERS signal, it is possible to recognize within these spectra - in the gray region - the features typical of the cell signal, not masked by the SERS peaks.

The highlighted spectral features allow the clear identification of the signal from the nanovector within the spectra collected on each cell. As a first qualitative comparison, we noticed that the nanovector signal revealed on PC-3 and HeLa cells is much stronger than that measured on HaCaT cells (the latter expresses FA binding protein PCFT only). This observation confirms the feasibility of a spectroscopic discrimination between cancer and normal cells based on their different expression



**Fig. 5.6** The typical Raman spectrum (dashed-black) of PC-3 cancer cells is compared with the spectra of treated PC-3 cells: dotted-green and solid-green lines refer to low and high SERS intensities. The spectrum of a normal HaCaT treated cell (solid-red) and the one of the nanovector (dashed-navy) are shown for comparison. The peaks centered at 1078 and 1580 cm<sup>-1</sup>(see the yellow-shaded areas) are the SERS markers of the nanovector bound to the cell membrane

level of FA binding proteins. The SERS-based single cell screening procedure will be carefully discussed in the next Subsection. Meanwhile, it is worth noticing that a detailed investigation of the nanovector–cell interaction is possible with a careful spectroscopic study.

Raman imaging in particular allows understanding where and how the Nps bind to the cell membranes. Moreover, by exploiting the high confocality of our microspectrometer, it was possible to optimize the spatial resolution along the optical axes to a few microns, collecting the signal from a very thin focus region. Combining SERS with the micrometric resolution either along the vertical axes or over the sample surface allows investigating the distribution of the Nps all over the cell surface. The representative result for a PC-3 cell is shown in Fig. 5.7.

If we plot on a colour scale the integrated spectral intensity of the cellular CH<sub>2</sub>-CH<sub>3</sub> stretching peaks as a function of the position on the cell, we obtain a Raman spectroscopic map that is in very good correspondance with the optical image of the cell, reported in Fig. 5.7d. This makes us confident to fully exploit spectroscopic imaging also using SERS signal. In Fig. 5.7a, we present the SERS intensity maps (integrated intensity of a nanovector specific peak vs. horizontal position), compared with optical images (Fig. 5.7b), both collected moving the focus plane of a few microns along the optical axes. The schematic of the procedure is shown in panel c, where we also show a detailed stratigraphic analysis of the cell, obtained by plotting the normalized intensity of the nanovector-, cell- and substrate-specific peaks versus the vertical position z. The relative maximum of these three signals is found at

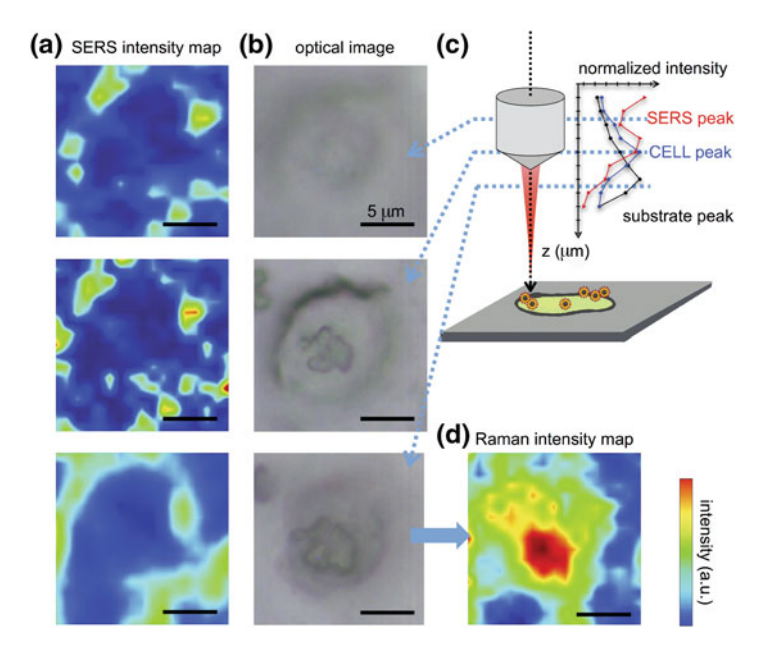


**Fig. 5.7** a SERS imaging obtained by integrating the C-S stretching peak of 4ATP and plotted in thermal scale is correlated with the optical image of the cell (**b**). The measurements were performed varying the focus of the objective at different values of z. Nps seem to be located at the margins of the cell, as pointed out in [Boc2013] (**c**) Intensity of SERS and Raman peaks relative to the different components of the system acquired varying the objective focus (versus z). **d** The imaging of the cell performed integrating the CH<sub>2</sub>-CH<sub>3</sub> stretching peaks shows a good correspondence with the optical image, giving information on the location of the cell nucleus (double membrane and higher signal). Reproduced with permission from [Fas2016]

different vertical positions, being that of the nanovector located  $\sim 1~\mu m$  above that of the cell, which in turn is located  $\sim 2~\mu m$  above that of the substrate. The data reported in Fig. 5.7 were acquired by varying the focus along the vertical axis using a 50  $\mu m$  confocal hole aperture. The dependence of the signal on the position along the optical axis suggests a vertical arrangement of the components: the nanovector is probably located outside the cell, but close to the membrane. This picture is in agreement with the results we obtained from FESEM imaging, where the great majority of the Nps is clearly visible outside the cell membrane, while only a few of them are apparently located inside the cell.

# 5.2.4 SEM Imaging on Treated Cells

FESEM imaging allowed a fair comparison with SERS imaging in the characterization of the measured, treated cells on their Si substrate. It also allowed a deeper insight in monitoring the possible internalization of Nps, which was suggested by

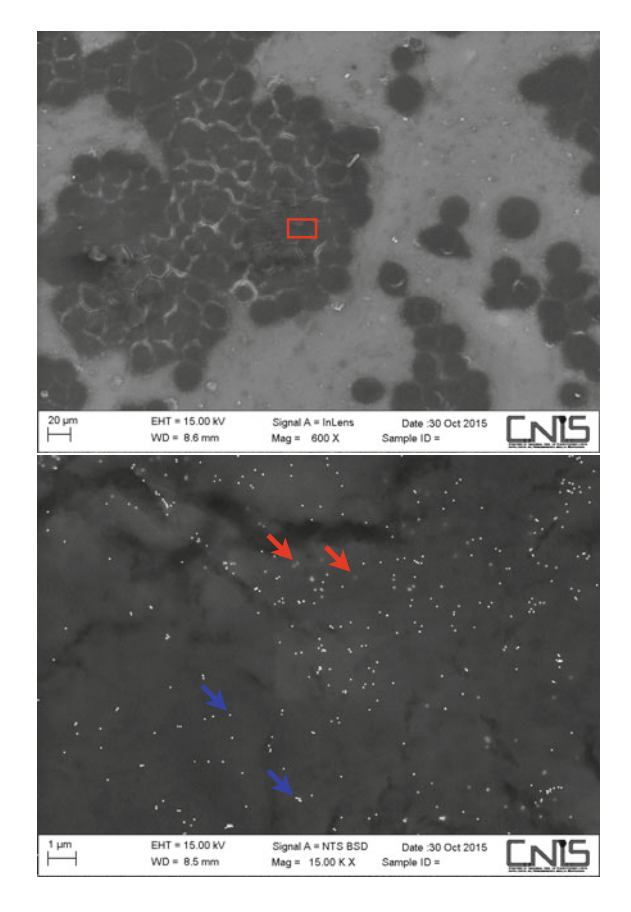


**Fig. 5.8** SEM imaging acquired on HeLa cells at different magnification. In the upper panel (lower magnification), the area of the subsequent zoom is evidenced by the red rectangle. In the lower panel (higher magnification), Nps on the cell membranes are visible. Blue arrows indicate examples of bright Nps, which are probably lying externally with respect to the membrane. Red arrows, instead, indicate shadowed Np, which could be covered by the cell membrane because of their internalization inside the cell

SERS confocal imaging. The backscattering FESEM mode was chosen for the analysis: this ensured a high contrast visibility for Au on the cell sample, being the scattering cross section higher for gold than for the other materials on the sample, as it is proportional to the third power of the elemental atomic number [Kri2005]. In Fig. 5.8, we present the results of FESEM imaging on treated HeLa cells, acquired at different magnification. The results confirm that the Nps are located on the cell membrane (see the blue arrows in the lower panel of the Figure). It also seems that some Nps are internalized inside the cell, as witnessed by the halo which covers the bright Np image (see the red arrows). We are confident that this effect is due to the presence of the membrane layered over the Np. Indeed, the power of the incident

electron beam during the acquisition (15 keV), according to the literature, exceeds the threshold of "transparency" of the cell membrane to electron beams [Kri2005].

#### 5.2.5 SERS Screening and Results

The SERS screening protocol was developed in order to get an estimate of the SERS intensity from single, treated cells. A quick and automatized sampling of the cell spectroscopic signal was carried out, by collecting 9 spectra all over the cell area (see Fig. 5.9a). The spectroscopic mapping was realized using a low magnification objective ( $50\times$ ) using a spacing of 3 µm for the map. Given this choice for the optical parameters, our estimate is that the sampling covers around the 50% of the cell surface. We then calculated a simple *control parameter* for each cell. It is proportional to the integrated intensity of the nanovector-specific SERS band (centred at  $1580~\rm cm^{-1}$ ): this  $I_{SERS}$  was calculated for all the spectra, and its value was normalized to the substrate integrated intensity,  $I_{substrate}$ , to account for slightly different experimental conditions from cell to cell.

The control parameter is defined by  $C=1000 \cdot I_{SERS}/I_{substrate}$ . Its values recorded for a hundred cell population for each cell line confirmed the qualitative observation discussed above: the selective targeting of the different cell populations is induced by folate specific biorecognition. The mean of the control parameter value indeed systematically increases going from HaCaT (non-cancer,  $\langle C \rangle = 5$ ) to PC-3 (cancer,  $\langle C \rangle = 75$ ) to HeLa (cancer, with the highest expression of FA receptors,  $\langle C \rangle = 196$ ).

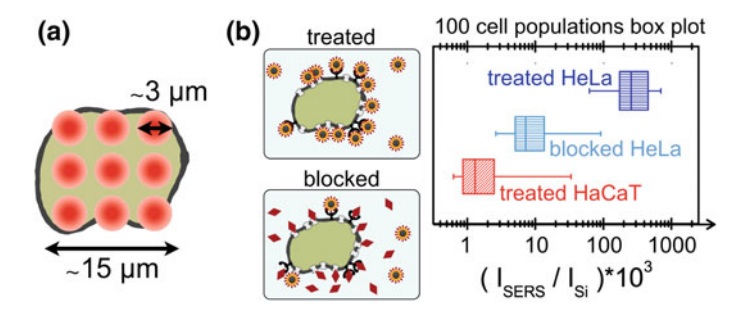
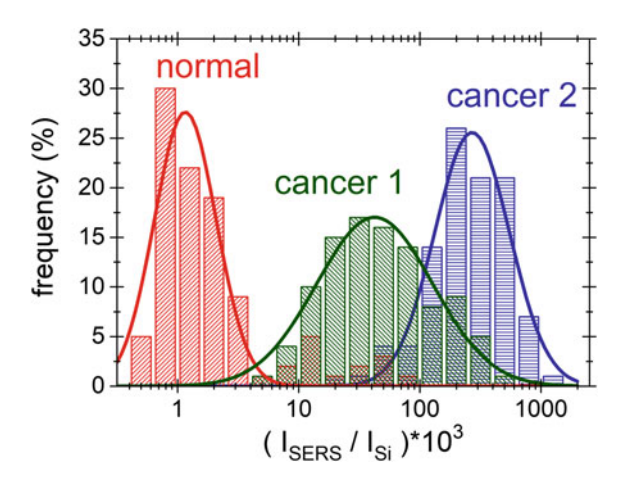


**Fig. 5.9** Panel **a** Sketch of the screening measurement protocol performed on measured cells. Panel **b** In a schematics, the experimental procedure adopted for the ordinary treatment with the nanovector (top) is compared to the blocking experiment (bottom), performed by adding to the culture free FA molecules to compete with the nanovector in reaching the cell receptors. On the right, the boxplot shows the distribution of SERS intensity measured on screened treated HeLa cells (blue box) and blocked HeLa cells (light blue box). For reference, we also report the SERS intensity detected on ordinarily treated normal HaCaT cells (red box)

**Blocking experiment** A blocking experiment provided the killing proof in favour of our interpretation, that is, the SERS results discussed above are induced by FA specific biorecognition. To realize this, HeLa cells were incubated with the nanovector in presence of a high concentration of unbound folate molecules in the cell culture. The usual treatment protocol was followed (see the previous paragraph for details), and then a population of 100 cells from the ordinarily treated sample was screened and compared with a 100-cell population of the *blocked* sample. In Fig. 5.9b we compare the results of the SERS screening with a box plot. The results demonstrate that there is a clear decrease of the signal in the folate-blocked cells, almost reaching the low SERS response of HaCaT normal cells. This is caused by the competition between free folate molecules and FA nanovector for the molecular binding sites on the cell membrane. As a consequence, a smaller amount of Nps is found on the blocked cells, giving rise therefore to a lower overall SERS signal.

Screening results In Fig. 5.10, we display the results of the SERS screening on three 100-cell populations of HeLa, PC-3 and HaCaT cells in a histogram. A logarithmic binning is chosen to cover the wide range of C values recorded experimentally; the frequency of occurrence of the C values is evident by the height of the columns. The data for the three cell populations follow the same statistical behaviour, that can be modeled as a lognormal distribution [WI2014], with largely different parameters for the three cell lines. The optimal fitting curves are plotted in Fig. 5.10 as solid lines over the histograms. There are clear differences among the distributions for the three cell populations. First of all, the distribution of C values recorded on HaCaT cells is peaked around small values, the result reflecting the very low density of FA binding proteins on the surface of normal cells. Moreover, the two populations of cancer cells can be well discriminated, being the expected value of PC-3 control parameter quite lower than the one of HeLa cells.

Fig. 5.10 Histogram showing the occurrence of different values of the control parameter, related to the different SERS intensities recorded on the three cell populations. The logarithmic binning was chosen because of the wide range of C parameter revealed experimentally. Here normal refers to HaCaT line, cancer 1 to PC-3 and cancer 2 to Hela. Adapted with permission from [Fas2016]



A semi-quantitative interpretation of the experimental data in terms of density and type of FA binding proteins on the cell membrane is possible [WI2014]. Biological investigations on indeedthe overexpression of folate receptor  $\alpha$  on the cell membrane, as well as a high density of the FA solute carriers, as RFC and PCFT [Jos2013, Des2012]. More controversial is the case of PC-3, about which there are different hypothesis on the expression of folate binding proteins on these cells [Par2005, HM2005, Jos2013, Sin2015]. Most probably, the overexpression of the folate SLC is the one responsible for the enhanced targeting of PC-3 cells with respect to the HaCaT population. The higher signal recorded on HeLa cells with respect to PC-3 is in agreement with the idea of the of the overexpression of FR $\alpha$ , in addition to the solute carriers overexpression that is also present on PC-3 cells. The statistical interpretation of our data could be further improved by implementing statistical modeling, and paves the way for hypothesis testing on new data.

In summary, the design of a screening procedure, based on the SERS spectroscopic imaging of the cells, allowed for monitoring the overall SERS response, at the single cell level, on 100-cell populations. A proper statistical analysis allowed to identify the typical SERS signal induced from our treatment on the chosen human cell models: the non-tumorigenic keratinocyte HaCaT line, metastatic prostate cancer PC-3 line and uterine cervical cancer HeLa line. The low SERS signal we were capable of detecting on HaCaT cells demonstrates the sensitivity of our method, that enables detecting the presence of the few folate solute PCFT carriers expressed and responsible for the cellular folate supply [Fuj2014]. As discussed, the different responses of the HeLa and PC-3 cells is ascribed mainly to the presence of the FR $\alpha$  receptor, which is known to be present in a comparatively higher density on the HeLa membrane [Fen2013, Kel2006, Jos2013].

Our method presents several advantages compared to similar studies [Man2010]. In particular:

- the time of incubation with the nanovector is rather rapid, therefore we can state that there is no change in the cell population during the treatment;
- the treatment of the cells is realized under physiological conditions (cell culture medium, 37 °C temperature), without preventing the selective binding of the nanoparticle to the folate receptors;
- as witnessed by our cytotoxicity measurement, the viability of the cell culture is unvaried during and after the treatment with the nanovector, granting the reliability of the procedure (see Sect. 5.2.2);
- lastly, the cellular sample is stabilized only by drying it, without further addition of fixing agents, which could affect the spectroscopic response of the system.

Owing to its characteristics, our nanovector is not only suitable for SERS studies, but also for near field microscopy, scanning probe and electronic microscopy imaging. FESEM imaging on HeLa cells (see Sect. 5.2.4) allowed to estimate, upon our treatment, approximately 100 Np-receptor binding events per cell. This estimate is in good agreement with the expected high (approximately nM) folate-receptor affinity.

It is well known that using a red HeNe laser for SERS excitation reduces the light-induced sample damaging and ensures therefore a good reproducibility of the spectroscopic analysis. Moreover, red light couples more favorably to the plasmon resonance of gold Nps aggregates rather than to that of isolated Nps [GP2007]. Consequently, the SERS screening results (Fig. 5.10) will reflect more thoroughly the distribution of the folate receptor density rather than the presence of single, isolated receptors. On the positive side, this reduces the risk of having single, non-specific binding events affecting the measurement; on the negative side, though, it prevents the detection of many single, isolated Nps (see Fig. 5.8). With the aim of further enhancing the diagnostic sensitivity, a possibility could be to induce the nanovector aggregation (e.g. in dimers) prior to cell treatment.

The presented results prove the possibility of achieving statistically relevant responses even starting from rather small cell populations, if compared with the numbers required e.g. for fluorescence-based methods. The small size, the stability and the negligible cytotoxicity of the nanovector makes it promising for the applications for the realization of in vivo studies, also in view of possible theranostic applications. In particular, given the positive correlation between the FR $\alpha$  expression and tumor stage and grade, the role of FA in tumor progression was evidenced [Kel2006]. In this respect, folate binding competitors, known as antifolate drugs, as aminopterin (AMT) and methotrexate (MTX), have been developed over several decades for the treatment of cancer and inflammatory diseases [Par2005, Wib2013, Che2013, Far1948]. To date, antifolates approved for clinical use enter cells via RFC (primarily) and PCFT solute carriers and by folate receptors [Wib2013, Des2012]. As an overexpression of FR $\alpha$  seems a typical characteristic of cancer cells, a predominant internalization of antifolate loaded nanovectors via FR $\alpha$  would be desirable in order to improve the treatment specificity, while limiting collateral damage on normal cells. The test of the same Np functionalization protocol substituting/including folate and antifolate drug AMT and MTX will be presented in the next Sect. 5.3. Our tests revealed an intriguing, significant increase in HeLa cell mortality after incubation with the AMT- and MTX-nanovectors. This suggests a valuable role of SERS (anti) folate-Nps to design traceable multi-therapeutics carriers.

# 5.3 From Selectivity to Theranostics: Antifolate Nanovectors

Once the high selectivity and sensitivity of our method was proved, we could speculate about adding some theranostics features to our plasmonic nanovector. As already discussed (Sect. 2.3.2), this can be realized in several ways: one of the most common is to exploit the strong absorption of gold for the photothermal selective killing of cancer cells [Hua2008, Lu2010, Boc2013]. Another possibility is represented by drug delivery: thanks to the versatile functionalization of gold Np, therapeutic drugs can be loaded onto the Nps together with the molecules active in cancer cell biorecognition [Gho2008, Dre2012].

We chose to follow this second approach, using the same molecule for both biorecognition and therapeutic action. To do so, we substituted folate molecules with two different chemotherapeutic drugs, aminopterin (AMT) and methotrexate (MTX) [Far1948]. Being folate binding competitors, molecules like AMT and MTX are commonly called antifolates. Once internalized inside the cell as folate molecules, their toxic action consists of the irreversible binding to the folate metabolic enzymes: by preventing folate metabolism, the action of antifolates eventually leads the cells to death [Par2005, Wib2013, Che2013]. As many other chemotherapeutic substances, antifolates are typically used to selectively kill cancer cells: the problem of limiting the amount of drug administered to the patients is crucial for avoiding collateral effects.

The preparation of AMT- and MTX-4ATP-AuNp nanovectors was performed using the approach developed for folate, as described in Sect. 3.2.1. Cytotoxicity assays prove the strong toxic effect of these nanovectors, compared to the folate one. Moreover, the results show an enhanced toxicity of AMT molecules when conjugated (and optimally oriented) onto a Np surface, compared to the free molecular form.

An important characteristic of antifolates - at least of the ones approved, to date, for clinical use - is their stronger affinity for solute carriers RFC (primarily) and PCFT, rather than for folate receptor FR $\alpha$  [Des2012, Wib2013]. To some extent, this represents a disadvantage, because normal cells typically provide for folate supply through the very same PCFT and RFC solute carriers [Des2012, Fuj2014]. Instead, it is FR $\alpha$  overexpression that has been proved to be a transversal feature of many types of malignant carcinomas [Kel2006, Jos2013]. Some selectivity issues could therefore arise in the employment of antifolate nanovectors in cancer theranostics. A possible solution is to separate the molecular agents responsible for biorecognition and therapy, by co-loading folate (which shows the highest affinity for FR $\alpha$ ) and antifolate molecules (for their strong cytotoxicity).

## 5.3.1 Preliminary Cytotoxicity Results

MTT technique was employed for a preliminar characterization of antifolate nanovector cytotoxicity. HeLa cells were chosen for this investigation, because of their strong efficiency in binding the folate nanovector, as demonstrated by SERS screening (Fig. 5.10). In commenting the cytotoxicity of our folate nanovector, we had stated that the decrease in the viability of HeLa cells was related to the osmotic stress for the addition of the nanovector, and that FA-4ATP-AuNps did not cause any harm to the cell culture. In treating the cells with the same amount of AMT- and MTX-nanovectors, instead, we reveal a significant drop in the cell viability, even after only 2 h (see Fig. 5.11).

As expected from biochemical considerations, both the antifolate nanovectors synthesized show a toxic action when interacting with cells. The results shown in Fig. 5.11 bring further support to the idea that, despite their quite large size (diameter is 60 nm), the Nps are somehow internalized inside the cells. This could happen

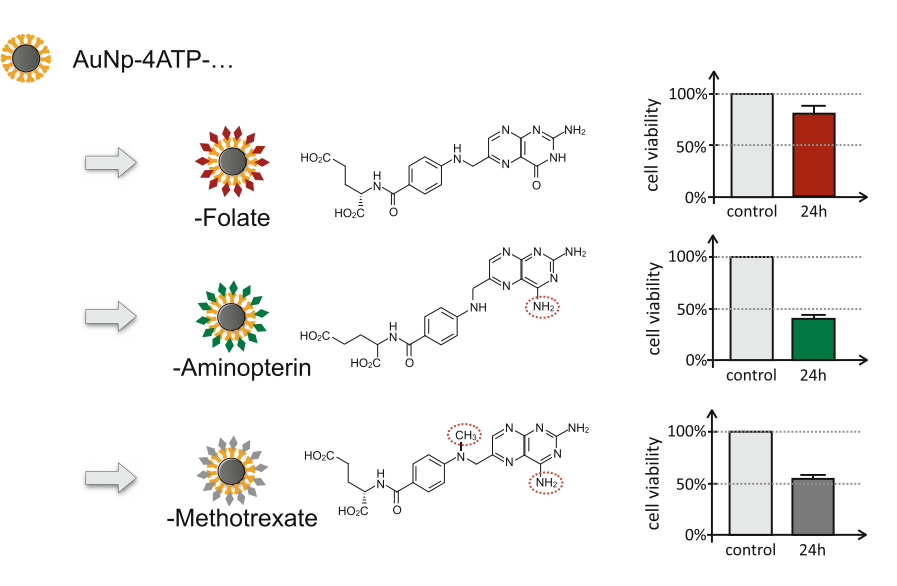


**Fig. 5.11** Sketch of folate/antifolate based nanovector with their relative cytotoxicity results. Cell viability was estimated with MTT assays by treating HeLa cells for 2 and 24h with AMT-4ATP-AuNp water solution in 1:2 volume ratio with the cell culture medium (corresponding to 5 pM concentration)

for example by receptor mediated endocytosis in the case of FR $\alpha$ . Even without a direct investigation on the mechanism of internalization, we can derive indirect information on the subject from the nanovector cytotoxicity. Indeed, the cytotoxic effect of AMT and MTX is triggered by their irreversible binding to folate metabolic enzymes, which prevents folate action in DNA and protein synthesis inside the cell.

# 5.3.2 Enhanced Toxicity of Nanostructured Drugs

In order to move towards the application of these systems, their therapeutic efficiency and selectivity need to be tested. As for the first aspect, we performed a comparative study by administering to the cells the drug in the free molecular form and in the nanostructured form, bound to the Nps. Meanwhile, the drug selectivity was probed by comparing the response from HeLa cancer cells with that of HaCaT normal cells. MTT assays performed at different drug concentration allowed to estimate for both the cell lines the  $IC_{50}$  value, that is the drug concentration necessary to kill the 50% of the cells in the culture.

Repeated nanovector preparations and SERS characterization (Fig. 3.22) show that the nanovector with AMT results more stable than that with MTX. For this reason, the systematic cytotoxicity investigation was performed using the AMT-4ATP-AuNp nanovector. Results are shown in Fig. 5.12. Cytotoxicity results obtained by treating

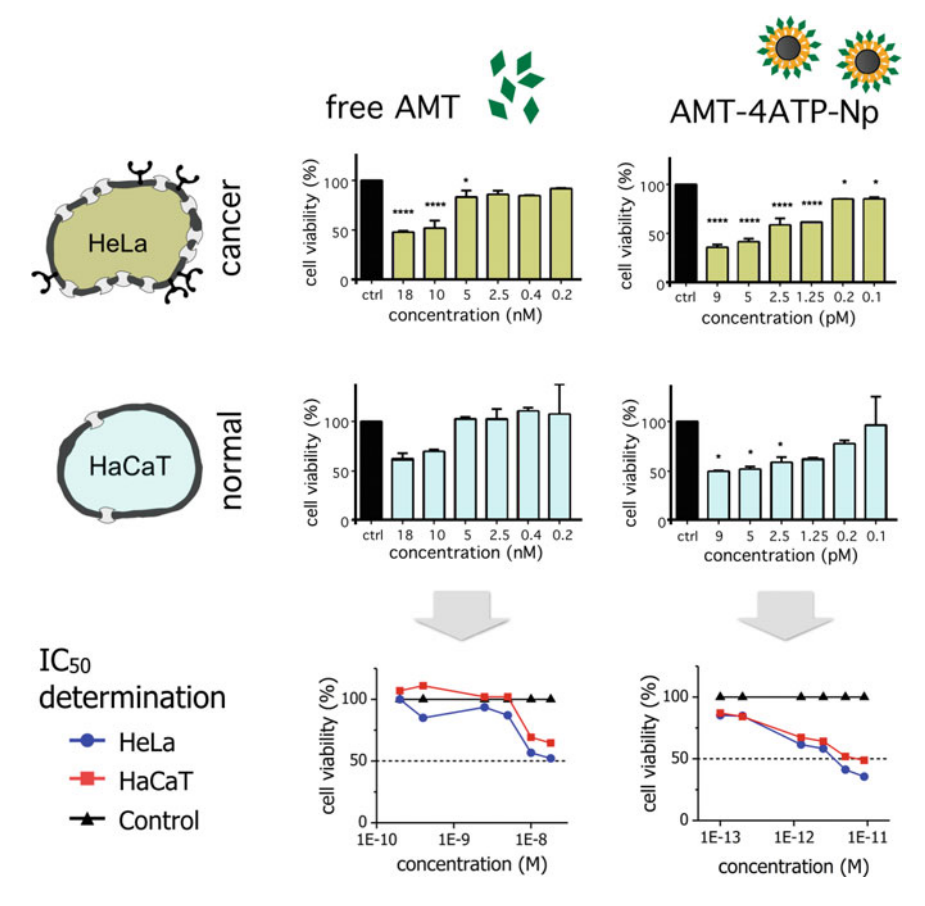


Fig. 5.12 MTT assay showing the cell viability of HeLa (first row) and HaCaT cell lines (second row) treated with different concentration of AMT-Nps (first column) and free AMT (second column) for 24h. The percentage of cell viability was determined by normalizing the absorbance of controls to 100%. Columns and bars represent mean and standard deviation value for 3 independent experiments. \*\*\*\*  $p \le 0.0001$ , \*  $p \le 0.05$ ; all results were analyzed by ANOVA, and the significance was evaluated by the Tukey honestly significant difference (HSD) post hoc test. Third row: summary of the cell viability, leading to an estimate of an  $IC_{50}$  value equal to respectively 18.71 nM and 36.91 nM in HeLa and HaCaT cell lines treated with molecular AMT (first column) and equal to 3.23 pM and 4.43 pM for the treatment with AMT-Nps (second column). All data were elaborated with Graph Pad Prism 6.0

HeLa and HaCaT cells with the AMT-4ATP-Nps are compared with the effect of treatment with AMT in the free molecular form.

The first, striking result is that comparable loss of cell viability are obtained from very different concentrations of AMT in nanostructured and molecular forms. Values on the x axes of the graphs in Fig. 5.12, indeed, differ for about three orders of magnitude. In order to quantify this effect, we extrapolated the  $IC_{50}$  values in all

the examined cases (lower row in the Figure).  $IC_{50}$  values for AMT were found to be equal to 3.23 pM and 4.43 pM in HeLa and HaCaT cell lines treated with the nanovector and equal to 18.71 nM and 36.91 nM with free AMT treatment.

According to our considerations, this difference can be explained accounting for two reasons, related to the nanovector properties. The first is a structural reason: AMT molecules, when covalently conjugated with 4ATP through amide bond, are optimally oriented, exposing the pteroyl part of the molecule to the interaction with the cellular receptors (see also Fig. 5.4). The second possible argument is that the internalization of a single AMT-Np, operated by the cellular receptor, brings inside the cell around two thousand AMT molecules. Once again, these molecules are oriented so to enable a very easy biorecognition by folate metabolic enzymes inside the cells. In principle, even accounting for their steric hindrance, several enzymes can bind to a single Np in an irreversible manner, enhancing and speeding up the blocking of folate metabolism that eventually leads the cell to death.

The results reported in Fig. 5.12 also bring to a second consideration about the rather small difference between the  $IC_{50}$  values for HeLa and HaCaT cell lines, for both nanostructured and molecular AMT form. This lack of selectivity was expected from the biochemical considerations already exposed. Indeed, it is known that, differently from folate, both AMT and MTX show a stronger affinity for RFC and PCFT folate solute carriers than for FR $\alpha$ . The latter is strongly expressed on cancer cells and typically absent on normal ones [Des2012, Wib2013, Jos2013]. The remarkable selectivity revealed for folate nanovector is therefore strongly reduced in the case of AMT.

#### Estimating the Np Binding Efficiency with SEM Imaging

In principle, cytotoxicity results do not allow to state the cause of the low specificity of our treatment. Indeed, it could be either that the nanovector bound to both the cell lines with the same efficiency, or that AMT-4ATP-AuNps show a higher toxic effect on normal HaCaT cells, while HeLa are more resilient. Once again, we can exploit SEM imaging for investigating both the density of Nps on normal and cancer cells, and their location with respect to the cell membrane.

In Fig. 5.13, we have reported representative SEM images acquired on HaCaT and HeLa cell lines, treated with the AMT nanovector at concentrations below (1.25 pM) and above (5 pM) the  $IC_{50}$  threshold, for 24 h. As evident from the comparison of panels a and b in the Figure, there is no significant difference in Np binding in the case of HaCaT and HeLa. This is most probably causing the same toxic effect of the Nps in both the cell lines.

This confirms the need of a strategy for a selective targeting of  $FR\alpha$ , which could enhance the specificity of this method. To do so, we are currently working on a functionalization protocol which could enable the co-loading of folate and antifolate molecules on the same Np. FA could induce a predominant internalization of the AMT-loaded nanovectors via  $FR\alpha$ , leading to an improvement of the treatment specificity.

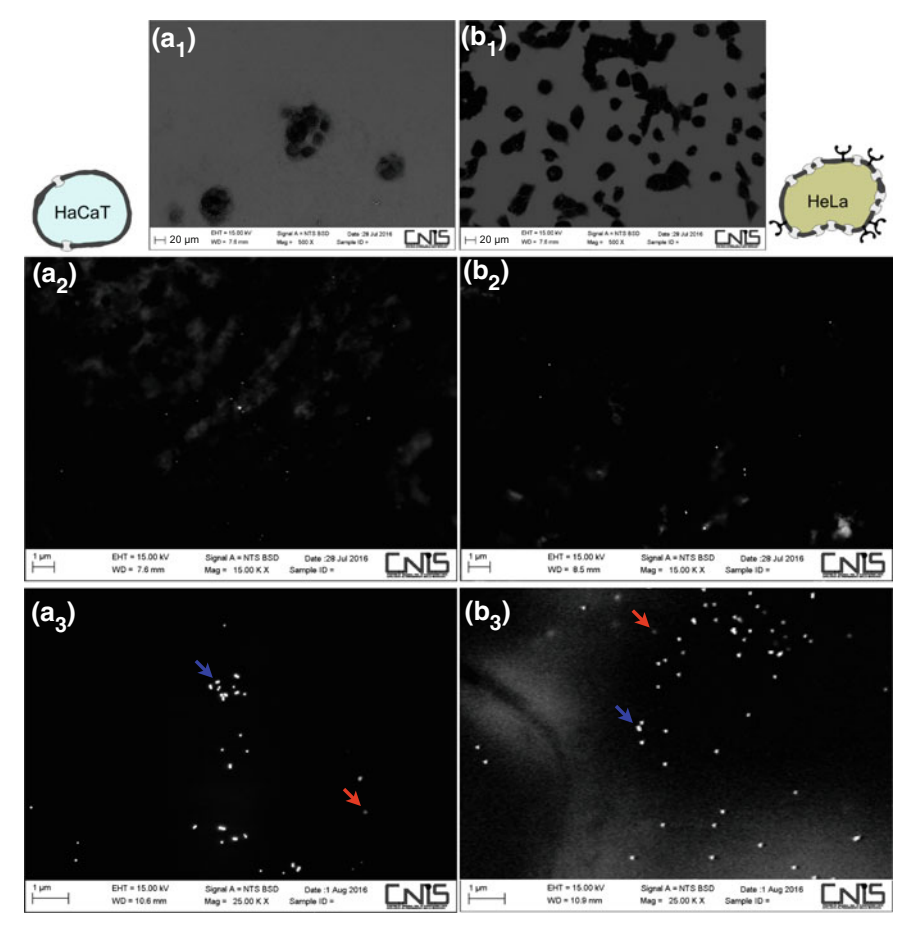


**Fig. 5.13** SEM imaging acquired in backscattering mode on HaCaT (panels  $(a_i)$ ) and HeLa (panels  $(b_i)$ ) cells, treated with AMT-4ATP-AuNps for 24h at the AMT concentrations of 1.25 pM  $(a_1, a_2, b_1, b_2)$  and 5 pM  $(a_3, b_3)$ .  $a_1$  and  $b_1$  are field visions, allowing to distinguish the cells on the Si substrate. In panels  $a_3$  and  $b_3$ , the red arrows highlight Nps probably covered by the cell membrane, while blue arrows indicate the Nps that are left externally with respect to the membrane

#### References

- [And2011] Ando J, Fujita K et al (2011) Dynamic SERS imaging of cellular transport pathways with endocytosed gold nanoparticles. Nano Lett 11(12):5344–5348
- [Bac2000] Backman V, Wallace MB et al (2000) Detection of preinvasive cancer cells. Nature 406(6791):35–36
- [Bar1983] Barlogie B, Raber MN et al (1983) Flow cytometry in clinical cancer research. Cancer Res 43(9):3982–3997
- [Baz2015] Bazak R, Houri M et al (2015) Cancer active targeting by nanoparticles: a comprehensive review of literature. J Cancer Res Clin Oncol 141(5):769–784

[BG1999] Bailey LB, Gregory JF et al (1999) Folate metabolism and requirements. J Nutr 129(4):779–782

- [Boc2013] Boca-Farcau S, Potara M et al (2013) Folic acid-conjugated, SERS-labeled silver nanotriangles for multimodal detection and targeted photothermal treatment on human ovarian cancer cells. Mol Pharm 11(2):391–399
- [Boe2004] Boecking A, Stockhausen J et al (2004) Towards a single cell cancer diagnosis. Multi-modal and monocellular measurements of markers and morphology (5M). Cell Oncol 26(1–2):73–80
- [Cao2011] Cao D-L, Ye D-W et al (2011) A multiplex model of combining gene-based, protein-based, and metabolite-based with positive and negative markers in urine for the early diagnosis of prostate cancer. Prostate 71(7):700–710
- [Che2013] Chen C, Ke J et al (2013) Structural basis for molecular recognition of folic acid by folate receptors. Nature 500(7463):486–489
- [Chi2015] Chinen AB, Guan CM et al (2015) Nanoparticle probes for the detection of cancer biomarkers, cells, and tissues by fluorescence. Chem Rev 115(19):10530–10574
- [Cro2007] Cross SE, Jin Y-S et al (2007) Nanomechanical analysis of cells from cancer patients. Nat Nanotechnol 2(12):780–783
- [Des2012] Desmoulin SK, Hou Z et al (2012) The human proton-coupled folate transporter: biology and therapeutic applications to cancer. Cancer Biol Ther 13(14):1355–1373
- [Dom2011] Domenici F, Bizzarri AR et al (2011) SERS-based nanobiosensing for ultrasensitive detection of the p53 tumor suppressor. Int J Nanomed 6:2033–2042
- [Dom2012] Domenici F, Bizzarri AR et al (2012) Surface-enhanced Raman scattering detection of wild-type and mutant p53 proteins at very low concentration in human serum. Anal Biochem 421(1):9–15
- [Dre2012] Dreaden EC, Alkilany AM et al (2012) The golden age: gold nanoparticles for biomedicine. Chem Soc Rev 41(7):2740–2779
- [Ehr2009] Ehrenberg MS, Friedman AE et al (2009) The influence of protein adsorption on nanoparticle association with cultured endothelial cells. Biomaterials 30(4):603–610
- [Fan2012] Fan K, Cao C et al (2012) Magnetoferritin nanoparticles for targeting and visualizing tumour tissues. Nat Nanotechnol 7(7):459–464
- [Far1948] Farber S, Diamond LK et al (1948) Temporary remissions in acute leukemia in children produced by folic acid antagonist, 4-aminopteroyl-glutamic acid (aminopterin). N Engl J Med 238(23):787–793
- [Fas2016] Fasolato C, Giantulli S et al (2016) Folate-based single cell screening using surface enhanced Raman microimaging. Nanoscale 8(39):17304–17313
- [Fas2018] Fasolato C, Giantulli S et al (2018) Antifolate functionalized nanovectors: SERS investigation motivates effective theranostics (in preparation)
- [Fen2013] Feng D, Song Y et al (2013) Distinguishing folate-receptor-positive cells from folate-receptor-negative cells using a fluorescence off-on nanoprobe. Anal Chem 85(13):6530–6535
- [Fra2015] Fratoddi I, Venditti I et al (2015) How toxic are gold nanoparticles? the state-of theart. Nano Res 8(6):1771–1799
- [Fuj2014] Fujiwara R, Takenaka S et al (2014) Expression of human solute carrier family transporters in skin: possible contributor to drug-induced skin disorders. Sci Rep 4:5251
- [Gho2008] Ghosh P, Han G et al (2008) Gold nanoparticles in delivery applications. Adv Drug Deliv Rev 60(11):1307–1315
- [GP2007] Ghosh SK, Pal T (2007) Interparticle coupling effect on the surface plasmon resonance of gold nanoparticles: from theory to applications. Chem Rev 107(11):4797–4862
- [Har2003] Harisinghani MG, Barentsz J et al (2003) Noninvasive detection of clinically occult lymph-node metastases in prostate cancer. N Engl J Med 348(25):2491–2499
- [HM2005] Hattori Y, Maitani Y (2005) Folate-linked nanoparticle-mediated suicide gene therapy in human prostate cancer and nasopharyngeal cancer with herpes simplex virus thymidine kinase. Cancer Gene Ther 12(10):796–809

- [Hua2008] Huang X, Jain PK et al (2008) Plasmonic photothermal therapy (PPTT) using gold nanoparticles. Lasers Med Sci 23(3):217–228
- [Jos2013] Joshi HC, Vangapandu SN et al (2013) Conjugates of noscapine and folic acid and their use in treating cancer. US Patent 8,426,398
- [Kah2007] Kah JCY, Kho KW et al (2007) Early diagnosis of oral cancer based on the surface plasmon resonance of gold nanoparticles. Int J Nanomed 2(4):785
- [Kan2013] Kang MJ, Park SH et al (2013) Folic acid-tethered Pep-1 peptide-conjugated liposomal nanocarrier for enhanced intracellular drug delivery to cancer cells: conformational characterization and in vitro cellular uptake evaluation. Int J Nanomed 8:1155
- [Kel2006] Kelemen LE (2006) The role of folate receptor a in cancer development, progression and treatment: cause, consequence or innocent bystander? Int J Cancer 119(2): 243–250
- [Kne2010] Kneipp J, Kneipp H et al (2010) Novel optical nanosensors for probing and imaging live cells. Nanomed Nanotechnol Biol Med 6(2):214–226
- [Kri2005] Krinsley DH, Pye K et al (2005) Backscattered scanning electron microscopy and image analysis of sediments and sedimentary rocks. Cambridge University Press, Cambridge
- [Krü2002] Krüger J, Singh K et al (2002) Development of a microfluidic device for fluorescence activated cell sorting. J Micromech Microeng 12(4):486
- [Li2015] Li Y, Heo J et al (2015) Organelle specific imaging in live cells and immunolabeling using resonance Raman probe. Biomaterials 53:25–31
- [Lu2010] Lu W, Singh AK et al (2010) Gold nano-popcorn-based targeted diagnosis, nanotherapy treatment, and in situ monitoring of photothermal therapy response of prostate cancer cells using surface-enhanced Raman spectroscopy. J Am Chem Soc 132(51):18103–18114
- [Luc2000] Lucock M (2000) Folic acid: nutritional biochemistry, molecular biology, and role in disease processes. Mol Genet Metab 71(1):121–138
- [Man2010] Mansoori GA, Brandenburg KS et al (2010) A comparative study of two folateconjugated gold nanoparticles for cancer nanotechnology applications. Cancers 2(4): 1911–1928
- [Mir2015] Mirkin CA, Meade TJ et al (2015) Nanotechnology-based precision tools for the detection and treatment of cancer. Springer, Cham
- [Mit2011] Mitsunaga M, Ogawa M et al (2011) Cancer cell-selective in vivo near infrared photoimmunotherapy targeting specific membrane molecules. Nat Med 17(12): 1685–1691
- [Pal2015] Pallaoro A, Hoonejani MR et al (2015) Rapid identification by surface-enhanced Raman spectroscopy of cancer cells at low concentrations flowing in a microfluidic channel. ACS Nano 9(4):4328–4336
- [Par2005] Parker N, Turk MJ et al (2005) Folate receptor expression in carcinomas and normal tissues determined by a quantitative radioligand binding assay. Anal Biochem 338(2):284–293
- [Sal2013] Salvati A, Pitek AS et al (2013) Transferrin-functionalized nanoparticles lose their targeting capabilities when a biomolecule corona adsorbs on the surface. Nat Nanotechnol 8(2):137–143
- [Sam2016] Samadian H, Hosseini-Nami S et al (2016) Folate-conjugated gold nanoparticle as a new nanoplatform for targeted cancer therapy. J Cancer Res Clin Oncol 142(11):1–13
- [Sin2015] Singh R, Kesharwani P et al (2015) Development and characterization of folate anchored Saquinavir entrapped PLGA nanoparticles for anti-tumor activity. Drug Dev Ind Pharm 41(11):1888–1901
- [Smi2015] Smith RA, Manassaram-Baptiste D et al (2015) Cancer screening in the United States, 2015: a review of current American Cancer Society guidelines and current issues in cancer screening. CA: Cancer J Clin 65(1):30–54
- [VoD2010] Vo-Dinh T, Wang H-N et al (2010) Plasmonic nanoprobes for SERS biosensing and bioimaging. J Biophotonics 3(1–2):89–102

References 135

[Wei1992] Weitman SD, Lark RH et al (1992) Distribution of the folate receptor GP38 in normal and malignant cell lines and tissues. Cancer Res 52(12):3396–3401

- [Wer2011] Werner ME, Karve S et al (2011) Folate-targeted nanoparticle delivery of chemo-and radiotherapeutics for the treatment of ovarian cancer peritoneal metastasis. Biomaterials 32(33):8548–8554
- [WI2014] Weddell JC, Imoukhuede PI (2014) Quantitative characterization of cellular membrane-receptor heterogeneity through statistical and computational modeling. PloS one 9(5):e97271
- [Wib2013] Wibowo AS, Singh M et al (2013) Structures of human folate receptors reveal biological trafficking states and diversity in folate and antifolate recognition. Proc Natl Acad Sci 110(38):15180–15188
- [Wu1999] Marietta W, Gunning W et al (1999) Expression of folate receptor type a in relation to cell type, malignancy, and differentiation in ovary, uterus, and cervix. Cancer Epidemiol Biomark Prev 8(9):775–782

# Chapter 6 Conclusions



Surface Enhanced Raman Scattering represents a promising technique to overcome the limitations of optical vibrational spectroscopy in terms of signal intensity and spatial resolution. Its potentialities as an ultrasensitive spectroscopy are particularly well expressed in the field of biophysics. Indeed, biophysical investigations typically target specific interactions between biomolecules (receptor/target, protein/antigen,...), rarely occurring at precise locations. In the last years, SERS-based platforms for molecular detection at ultra-low concentrations, sometimes integrated in microfluidic devices, have been developed achieving impressive results. Similarly, SERS-active nanosensors, specifically interacting with cells, have been developed for diagnostics, drug delivery and other biomedical applications.

Nevertheless, it is worth to remind that SERS spectroscopy, as often happens for the powerful tools, needs to be handled with care since a straightforward interpretation of the spectral response is not always achievable. Indeed, in order to extract specific information on relevant biomolecules, it is usually required to take into account many different aspects: the investigated system, the SERS substrate, the environment and the interplay among them at the nanoscale level.

In this Thesis, colloidal dispersions of gold and silver nanoparticles were used as a building block for implementing SERS-active systems for bioapplications, in particular in the fields of molecular sensing and cellular diagnostics. In general, we have tried to combine the applicative goal with more fundamental studies on the microscopic behavior of SERS active systems, in order to gain as much information as possible from the spectroscopic response.

The utmost original results achieved in this work, together with the related future perspectives, can be summarized as follows.

Self-assembly of noble metal Np into clusters is probably the simplest route
to obtain high SERS signal enhancement from molecules located at the hotspots, in the interparticle gaps. Unfortunately, these aggregates are characterized
by high variability of the local nanoarchitecture, causing different spectroscopic
performances. A possible and promising way to reach signal predictability and
reproducibility, is to correlate the intensities measured on Np clusters with their

138 6 Conclusions

morphological parameters. The self-assembly on a substrate of functionalized silver nanoparticles, starting from a colloidal dispersion, leads to the formation of aggregates of micrometric size, typically composed by a few Np superimposed layers. The correlation of SERS and AFM measurements on these Np aggregates shows a linear increasing trend of the maximum spectroscopic intensity as a function of the cluster surface up to very large areas ( $\sim 30\,\mu\text{m}^2$ ) and a further dependence on the number of Np layers stacked in cluster. Experimental results have been supported by electromagnetic simulations showing a comparable shape-dependencies on similar structures. The whole of the results coherently suggests that the SERS intensity arises from the onset of cooperative effects involving the entire cluster: the mesoscopic aggregate seems to behave as a single, near-field optical connected entity.

- Once clarified the connection between morphology and SERS efficiency of the Np aggregate, a strategy for template-mediated cluster formation can be developed, by driving Np aggregation inside mesoscopic cavities produced by electron beam lithography. EBL-guided self-assembly allows the preparation of SERS-active substrates made of Np aggregates of micrometric size, arranged in ordered two dimensional arrays on large areas (100 µm size). AFM and SERS measurements demonstrate a very good correspondence between the morphology and the spectroscopic signal, with a precise periodicity given by the array spatial organization. Clusters are characterized by very close Np packing: the high hot-spot density leads to very large enhancement factors and good signal reproducibility from cluster to cluster. The regular spatial organization and the high number of cluster can enable implementing systematic statistical analyses on the spectroscopic response. The perspective of this work is the investigation of the long range coupling among the aggregates: in principle, indeed, by tuning the array periodicity with the exciting wavelength used for Raman excitation, the diffractive coupling in the array can be optimized, possibly leading to a further enhancement of SERS signal.
- The functionalization protocol used to test the SERS-active substrates implies the covalent conjugation of metal Nps with the molecular label 4-aminothiophenol. This molecule is a bifunctional linker, binding the metal with a thiol group and exposing an  $-NH_2$  end for further biofunctionalization, for example via amide bond or diazotization (-N=N-). This possibility was exploited for the preparation of SERS-active nanovectors conjugated with folic acid (FA) or with its binding competitors, namely antifolate drugs, for biomedical applications. The pursued functionalization strategy leads to the oriented binding of folate/antifolates on the Np surface, exposing on the structure surface the hydrophobic part of the molecule, active in the biorecognition by cellular receptors or enzimes. A thorough characterization of the system allowed to estimate the molecular conjugation efficiency, demonstrating the potential of a quantitative SERS investigation, which results can be competitive with other titration techniques.
- Folic acid plays an essential role in cellular metabolism and reproduction. For
  this reason, cancer cells typically overexpress FA binding proteins on their membrane with respect to normal cells. On these bases, we developed a protocol for
  SERS-based early diagnosis of cancer, by selectively targeting cancer cells with

6 Conclusions 139

the FA-nanovector. Three different cell lines (cancer HeLa and PC-3, and normal HaCaT lines), chosen for their different expression of FA binding proteins, were treated with the nanovector and showed a very different efficiency in the Np uptake, resulting in different SERS signal intensity on the samples. Experimental results were found in good agreement with the expectations from biological considerations: a screening procedure based on SERS microimaging allowed the net discrimination of normal and cancer cells. Moreover, the values of SERS intensity measured on single cells of different lines were found to belong to statistical distributions with very different parameters. Reproducible measurements carried out on relatively small populations (100 cells) demonstrate the potential of this technique, compared to other fluorescence-based methods, for single cell diagnostics on real bioptic samples.

• The strong selectivity of FA nanovector opened the way for the possible implementation of additional therapeutic features, in order to reach theranostics, that is the combination of diagnosis and therapy. The adopted approach is based on the substitution of FA with its binding toxic competitors aminopterin (AMT) and methotrexate (MTX). The comparative cytotoxicity investigation performed by treating HeLa cancer cells with FA-, AMT- and MTX-nanovectors proved a high toxicity of antifolate based nanovectors. A systematic study comparing the treatment with AMT in the free molecular form or loaded onto Nps demonstrated a remarkable enhancement of the action of the drug in the nanostructured case. This means that the use of the AMT-nanovector allows reducing the drug concentration over one thousand times, therefore limiting the collateral damages of the treatment. The selectivity of AMT-nanovector, tested by comparing its effect on cancer (HeLa) and normal (HaCaT) cells, seems reduced with respect to the FA case. This is related to the stronger biochemical affinity of FA with folate receptor FR $\alpha$ , which is typically found exclusively on cancer cells. A possible solution, which is also a close perspective of this Thesis work, is the co-loading of folate and antifolate on the same nanovector, for a more efficient biorecognition and therapeutic action, respectively.

In conclusion, noble metal nanoparticles were functionalized, characterized and employed for the development of different biophysical applications. A detailed, fundamental study of all the factors affecting the spectroscopic response of our SERS-active systems proved to be crucial for implementing systematic measurement and data analysis protocols. The discussed results were obtained not only on the applicative side, but also on more fundamental topics: the same ambivalence holds for the perspectives of this Thesis. On one side, indeed, we aim at moving from the proof-of-principle study to more realistic and scalable applications. On the other side, we are working to gain deeper insight in the mechanisms of plasmonic interparticle coupling and molecular interactions at the nanoscale.

# Appendix A SERS Application in Cultural Heritage

In the framework of a collaboration with Dr. L. Lombardi, of the Chemistry Department of Sapienza University, we have carried out SERS experiments for studies in cultural heritage and diagnostics, where SERS spectroscopy often represented the first, quick step within a multianalytical investigation [Ser2016].

In the first Section, we discuss an experiment aimed at the identification of the molecular components of natural lake pigments, used in the ancient time for both painting and tissue dyeing. To do this, a systematic, combined characterization by SERS spectroscopy, coupled with other techniques, such as high performance thin layer chromatography (HPTLC), was employed with interesting results.

In the second Section, we present a multianalytical study on a historical dress from the 19th century. SERS analysis on purple dyed yarns of the dress helped detecting on the artwork both the natural purple dye orchein and its synthetic alternative, mauveine.

### A.1 HPTLC-SERS Investigation of Madder Lake Ammonia Extract

Ever since its development, planar chromatography has attracted great interest in the field of the analysis of natural products, as it provides chromatograms that are a fingerprint of the natural raw materials. Even more importantly, it can be used as a preliminary separation step for a wider, multi-analytical approach, as the single chromatographic traces obtained can be investigated employing other techniques, among which various optical spectroscopies [Bia2016].

In this Section, we describe the HPTLC-based approach for the creation of a SERS database of the isolated compounds present in ammonia extracts of Madder lake. The present analytical method can be scaled to the analysis other natural lake pigments and the spectral database can be helpful in attributing the different features of the spectroscopic signals measured on unknown mixtures.

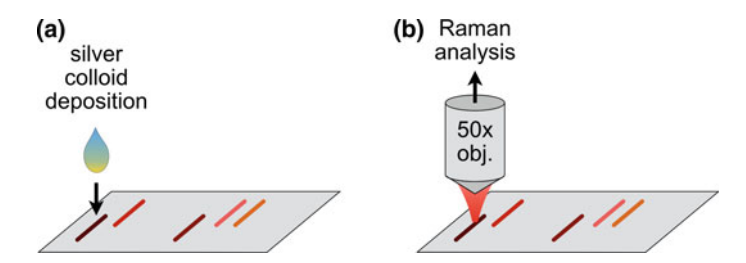


Fig. A.1 Schematic representation of HPTLC-SERS protocol of analysis

Hezel was the first proposing the coupling of TLC and SERS [HZ1977] for the separation and detection of analytes: since then, the approach was applied successfully to numerous compounds [Kog1988, Cau1995, Ist2003]. Although the great potential of this technique for the study of dye mixtures has been highlighted in literature [Bro2009, Gei2009], its application in the conservation science field has not yet become well-established [Poz2011].

In HPTLC-SERS, analytes are isolated and preliminarily purified through the classic HPTLC separation method. Afterwards, the SERS spectral response of the single traces on the TLC plate is identified. In order to achieve SERS from the molecular traces on the plate, a droplet of AgNp colloidal dispersion is deposited onto each spot and dried. The Np aggregation induced on the substrate favors an efficient SERS detection of the substances on the TLC plate. The experimental protocol is sketched in Fig. A.1.

The low cost, high throughput and specificity are among the advantages of HPTLC-SERS, compared to other common separation methods, such as those based on liquid chromatography. Even more important is the remarkable sensitivity of SERS, which allows to probe very small sample volumes, enabling the microinvasive study of historical materials and artworks [Poz2011].

## A.1.1 HPTLC-SERS Analytical Method

The HPTLC-SERS experimental protocol is here discussed. First of all, the ammonia extract of Madder lake, as well as the purified single fractions of this lake, obtained as described by Lombardi and coworkers [Lom2016], were applied on HPTLC plate with pre-concentrating zone (Silica gel 60 with concentrating zone  $10\times2.5$  cm, Merck) using 5  $\mu L$  Camag micropipettes (Muttenz, Switzerland) (examples for Madder lake in Figs. A.2, A.3, A.4 and A.5). The eluent used are ethyl acetate, dichloromethane, glacial acetic acid, formic acid, water, in the ratios (100:25:8:8). Solvents and acids were purchased from Sigma-Aldrich.

SERS analyses were performed by focusing the laser beam on the TLC plate in correspondence of each spot, after the deposition and drying of 25  $\mu$ L (in 5 consequent steps) of AgNp colloidal dispersion prepared with the Lee-Meisel protocol

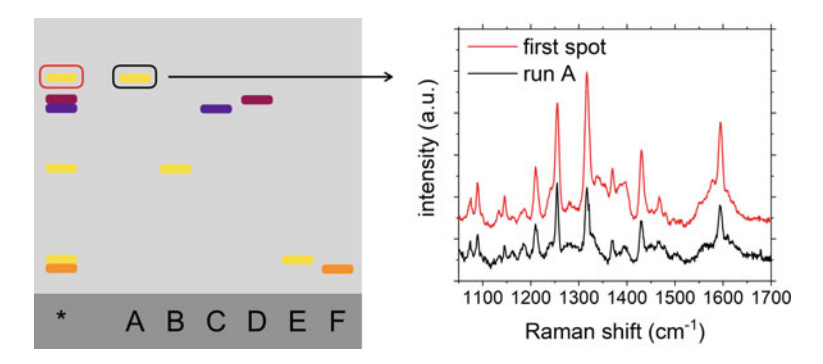


**Fig. A.2** Left panel: Schematic representation of HPTLC chromatographic separation of madder lake ammonia extract. Right panel: HPTLC-SERS results for the first spot of madder lake ammonia extract (munjistin methyl ester), which spectrum (red) results in excellent agreement with munjistin methyl ester standard spectrum (black)

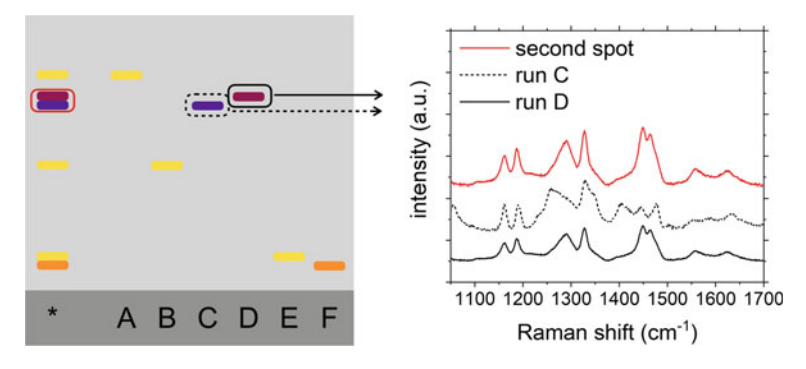


**Fig. A.3** HPTLC-SERS results for the second spot of madder lake ammonia extract. The TLC trace here resulted a bit broadened, corresponding to both the TLC runs of alizarin and purpurin (runs C and D). Nevertheless, the HPTLC-SERS signal acquired on the lake spot (red spectrum) was found to be rather homogeneous. It resulted in excellent agreement with the spectrum of alizarin standard (solid black), while we cannot safely rule out the presence of purpurin (dashed black)

[LM1982]. SERS spectra were acquired keeping the incident power below 0.25 mW, using 50× objective. For each spot, the spectroscopic mapping of an area of 5 × 5  $\mu m^2$  (step 1  $\mu m$ , 2 s acquisition time) allowed the determination of an average spectrum. Spectra are here presented without pretreatement, except for a polynomial background subtraction.

## A.1.2 Experimental Results

We present here the results on the identification of the molecular compounds contained in the ammonia extract of Madder lake.

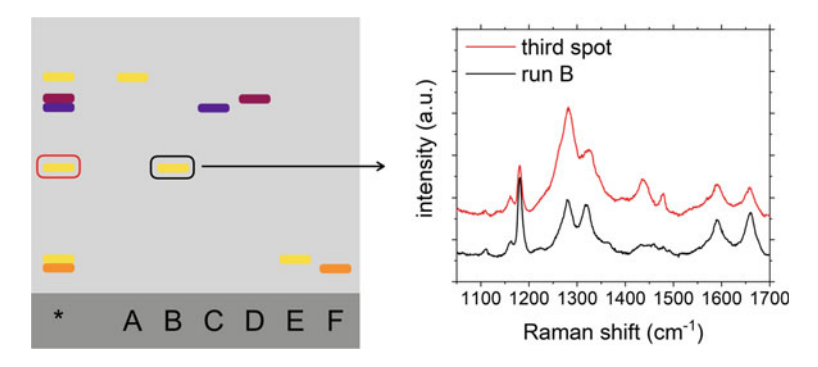
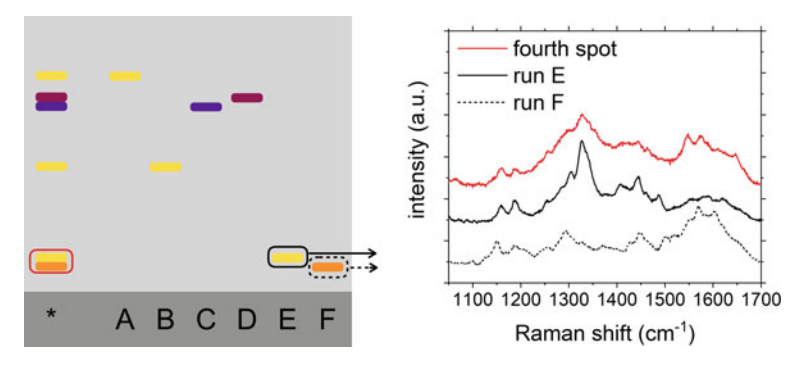


Fig. A.4 HPTLC-SERS results on the third isolated spot of madder lake ammonia extract. HPTLC-SERS spectrum acquired on it (red) is in very good agreement with the signature of munjistin standard (black)



**Fig. A.5** HPTLC-SERS results for the fourth isolated spot of madder lake ammonia extract, corresponding to the TLC spots of ruberythric acid (run E) and lucidin primeveroside (run F). Here, the HPTLC-SERS spectrum of the lake spot (red) seems to derive from an overlap of two different components, as results from the comparison with the spectra of ruberythric acid (solid black) and lucidin primeveroside standards (dashed black)

In order to compare the traces obtained from the lake extract with already analized standards, we applied on the same HPTLC plate the following substances (see the sketches on the left in Figs. A.2, A.3, A.4 and A.5): total ammonia madder lake extract (run \*), standard of munjistin methyl ester (run A), standard of munjistin (run B), standard of purpurin (run C), standard of alizarin (run D), standard of ruberythric acid (run E), standard of lucidin primeveroside (run F). All these standards are obtained from the chromatographic separation of the ammonia madder lake extract, previously analyzed by nuclear magnetic resonance and electrospray ionization-mass spectrometry (ESI-MS) to confirm the purity of the isolated compounds.

The SERS spectra obtained from each HPTLC spot in the total ammonia Madder lake extract and that of the corresponding isolated compound are presented in Figs. A.2, A.3, A.4 and A.5.

The HPTLC analyses conducted allowed to identify the SERS signature of the isolated compounds present in the ammonia extract of Madder lake. This lake was selected for its rich variety of glycosylated compounds. At the best our knowledge, at the present moment the SERS response of these type of compounds has not yet been reported in literature. Using this approach, a preliminary SERS database of isolated compounds was created. This can be helpful in attributing the different signals revealed on an unknown mixture to specific dyes. As a future perspective of this work, the present approach will be applied also to the extracts of other lake pigments, thus expanding the SERS database.

## A.2 A Multianalytical Study Unravels Purple Dyeing Processes: The Case of a Historical Dress from the 19th Century

#### A.2.1 Introduction

Orchein, or orchil, is a purple dye derived from lichens of the genus Roccella. It was widely adopted up to the first half of nineteenth century when Perkin succeded in sythesizing mauveine, or analine purple, in 1856 [Bal2004, Woo2016]. Mauveine resulted soon available inexpensively and in large amounts, and orchein was rapidly replaced by its synthetic alternative.

As many dyeing molecules, mauveine can be successfully detected with a remarkable sensitivity by SERS analyses [Woo2016, Cañ2014, Poz2016]. The high sensitivity of SERS is even more important to detect orchil which, as other phenoxazone compounds, is characterized by a low photo-stability, that causes its significant degradation and makes it unusually difficult to detect on historical samples [Ros2013].

For addressing this and analogous problems in the cultural heritage and conservation fields, considerable efforts of the scientific community are aimed at developing highly sensitive non- or micro-invasive techniques for art diagnostics, that are often based on optical spectroscopy (e.g. Raman or UV fluorimetry). Among these recent possible analytical tools, SERS plays a major role, combining its sensitivity with the specificity of Raman spectroscopy [Ros2013, Cle2006, Cle2009, Ace2015, Doh2014].

In this Section, we present a study carried out on a historical dress that belonged to a Sicilian noblewoman, Donna Concetta Tomasi di Lampedusa. The artwork is dated back to 1865-1870 and is now part of a private collection. It consists of a shaped bodice and a wide skirt, decorated with black lace applications in silk. In order to unravel the dyeing technique used for obtaining the purple fabric of the dress, a multianalytical approach was adopted. Preliminary SERS measurements were performed directly on the fibers of the dress, by depositing nanocolloids on dyed yarns, and served as molecular screening. This analysis was followed by

the selective extraction of dye molecules and mass spectrometric measurements. The ammonia extraction method proposed by Lombardi and coworkers allowed the detection of orchil, revealed despite its presence in small amount [Lom2016]. This confirmed the results obtained by SERS spectroscopy. Proton nuclear magnetic resonance (<sup>1</sup>H-NMR) and matrix-assisted laser desorption/ionization time-of-flight (MALDI-ToF) mass spectrometry analyses finally determined that orchein was employed in the dyeing process alongside its synthetic alternative. These results testify the widespread diffusion of mauveine all over Europe after only ten years from its discovery.

# A.2.2 Sicilian Noblewoman Dress: Microscopy, Sampling, Experimental Details

The analysis we here present was carried out on a historical dress that belonged to Donna Concetta Tomasi di Lampedusa. The item is dated back to 1865–1870, and consists of a single piece, made of a shaped bodice attached to a wide skirt, decorated with black silk lace and a crinoline petticoat (see Fig. A.6a). At the time when the dress was first restorated, it resulted strongly deteriorated, and even the handling was a difficult task. The external fabric, made of silk taffeta, with Chinee floral print, was visibly subject to a depolymerization of the fiber and a marked discolouration. In correspondence of printed applications, holes were found on the fabric and caused a partial loss of the decoration. The five different types of lace applications were also

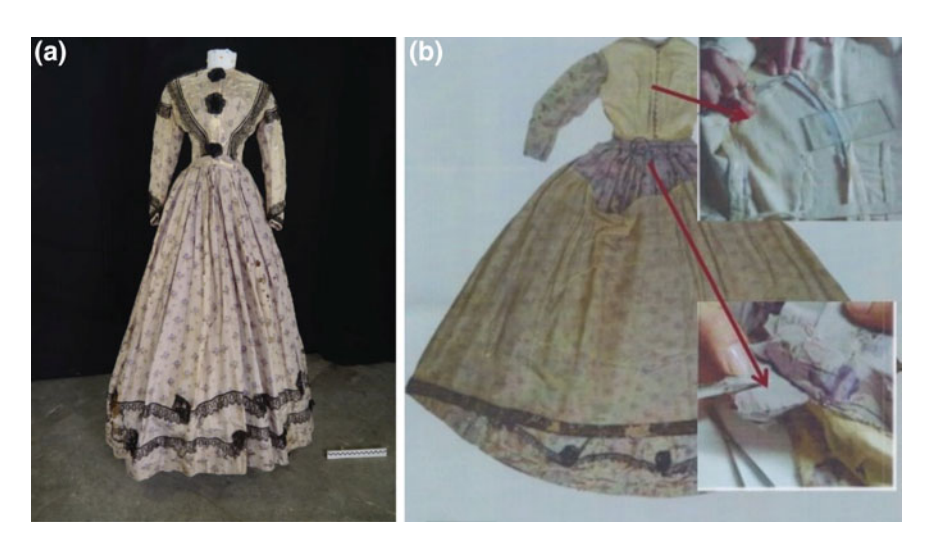


**Fig. A.6** Panel **a** the historical dress that belonged to Donna Concetta Tomasi di Lampedusa. Panel **b** particular of the verso of the dress, highlighting the points of sampling, from the corset and the skirt

affected by deformation and degradation. It is the liner fabrics that remained intact, and allowed the preservation of the fragile silk covering to date. For our study, we collected two taffeta samples from the verso of the dress. One came from the corset and a second from the internal part of the skirt (see Fig. A.6b).

As a preliminary investigation, silver nanocolloid was deposited and dried on the dyed yarns of a small fabric sample, and SERS measurements performed on the sample allowed for specific molecular detection. Subsequently, solvent extraction from another portion of the fabric provided dispersed samples for NMR and mass spectrometry investigations. For details on the materials and methods for the colloid preparation and on the dye extraction, as well as for the experimental specifications on Raman, NMR and mass spectrometry please refer to reference [Ser2016].

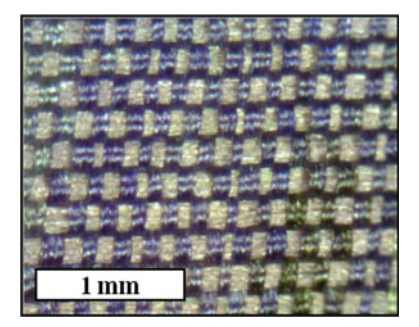
#### A.2.3 Results and Discussion

Two taffeta samples were collected from the verso of the dress for the analysis. Sample 1 was obtained from the corset, belonging to the decorative part of the dress and it is coloured in a dark violet. Sample 2 was collected from the background of the skirt and is coloured in a lighter violet.

Optical microscopy on the samples (Fig. A.7) showed a very complex texture of coloured yarns. In Sample 1 one can observe dark violet, light violet, green and light blue fibers. In Sample 2 two different shades of purple-pink were observed: darker fibers were more intense and visible, while lighter ones showed traces of another violet colour.

Extremely interesting results came from the SERS analysis of the purple yarns present in both samples (see Fig. A.8). SERS measurements performed directly on the dyed fibers allowed to recognize signals compatible with what is reported in the literature as the SERS spectrum of mauveine [Cañ2014]. The spectrum obtained on Sample 2 recalls the one collected on Sample 1, but presents additional peaks that can be explained by the presence of a small amount orcein dye [Ace2015; Doh2014; Kok1966]. These features are marked with arrows in Fig. A.8.

**Fig. A.7** Particular of textile in taffeta (Sample 1, magnification 40×)



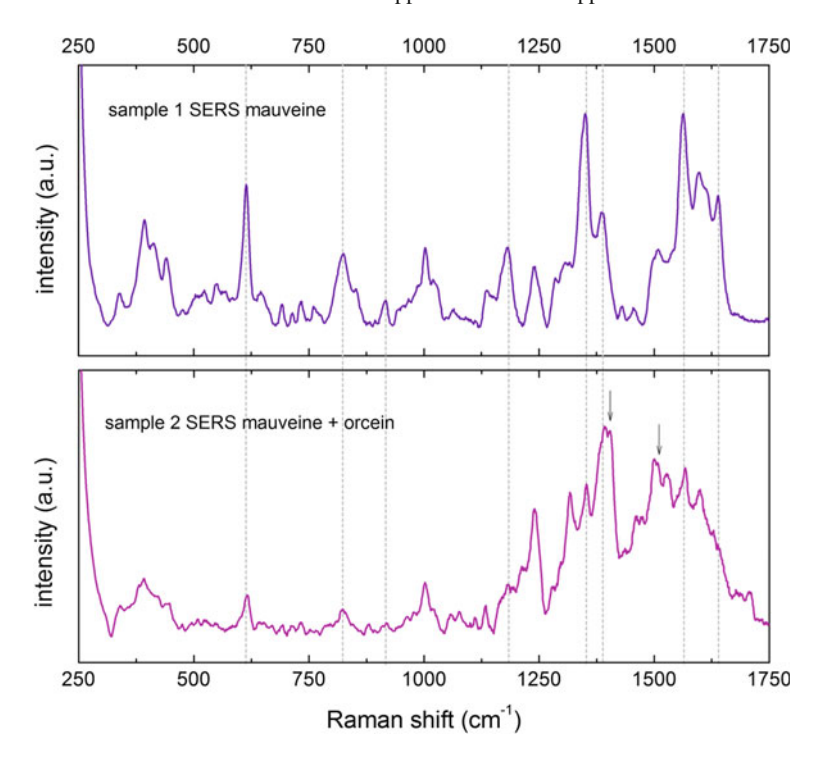


**Fig. A.8** SERS spectra collected on Sample 1 (top panel) and 2 (bottom panel). Grey lines in the background identify the mauveine peaks, revealed on both samples, while grey arrows highlight the peaks ascribed to orcein (see text for details)

The preliminary SERS analysis allowed to hypothesize the presence of two different classes of purple dyes in the sample. Consequently, a proper analytical approach was design to confirm these observations and gain further insight in the sample composition. In particular, different extraction protocols were adopted and followed by NMR and mass spectrometry analyses. Based on SERS preliminary investigation, an extraction with formic acid, specifically suitable for mauveine dyes, was carried out on Sample 1 [Sou2008, ZL2005]. The MALDI-ToF analysis indeed confirmed the presence of mauveine dyes.

SERS results suggested that orcein could have possibly been employed in association with mauveine for the dyeing process of part of the yarns. For this reason, the ammonia protocol, specific for the extraction of natural dyes [Lom2016], was fistly performed on Sample 2. After this extraction, a second one based on formic acid was carried out as well [Ros2013, Sou2008, ZL2005]. The residue obtained from the first extraction was analysed by ESI-MS and MALDI-ToF techniques. From the MALDI-ToF spectrum, no signals associable to either of the two classes of dyes was recognized. Interestingly, instead, the ESI-MS spectrum showed a peak at [M-H]<sup>-</sup> = 361.32, that can be ascribed to an  $\alpha$ -amino orcein. The extraction in formic acid, on the other hand, provided sufficient material to perform an additional

analysis by NMR. This reveals signals that can be ascribed to a mixture of mauveine dyes according to previous results in the literature [De 2007]. MALDI-ToF spectra confirmed the identification of the dyes present as the same mixture of mauveine molecules detected in Sample 1.

#### A.2.4 Conclusions

The multianalytical investigation discussed above enabled the identification of a mixture of orcein and mauveine dyes in a historical sample. The SERS screening performed on fiber allowed for a preliminary assessment of the sample composition. Based on the first step, two different extraction protocols were properly selected for producing residues to be analyzed by NMR and mass spectrometry. In particular, the ammonia based protocol allowed to selectively extract orchil dyes. The second extraction treatment, based on formic acid, allowed to select mauveine dyes.

The successful investigation detected the presence of orchil dyes in the sample despite their low concentration. If one had performed the exctraction with formic acid alone, the signal from orchil could have been covered by the strong signature of mauveine in the final product. This study demonstrates that synthetic and natural dyes were used in association for colouring this precious dress. Even more interestingly, the conducted analyses prove that mauveine was already widely employed as a purple dye only nine years after Perkin's discovery.

#### References

[Ace2015]	Aceto M, Arrais A et al (2015) A diagnostic study on folium and orchil dyes
	with non-invasive and micro-destructive methods. Spectrochim. Acta Part A: Mol.
	Biomol. Spectrosc. 142:159–168

- [Bal2004] Ball P (2003) Bright earth: art and the invention of color. University of Chicago Press
- [Bia2016] Bianco A, Serrilli AM et al (2016) Chapter 7. Endemic plants of Italy and their peculiar molecular pattern. Studies in natural products chemistry. Elsevier
- [Bro2009] Brosseau CL, Gambardella A et al (2009) Ad-hoc surface-enhanced Raman spectroscopy methodologies for the detection of artist dyestuffs: thin layer chromatographysurface enhanced Raman spectroscopy and in situ on the fiber analysis. Anal Chem 81(8):3056–3062
- [Cañ2014] Cañamares MV, Reagan DA et al (2014) TLC-SERS of mauve, the first synthetic dye. J Raman Spectrosc 45(11–12):1147–1152
- [Cau1995] Caudin JP, Beljebbar A et al (1995) Coupling FT Raman and FT SERS microscopy with TLC plates for in situ identification of chemical compounds. Spectrochim Acta Part A: Mol Biomol Spectros 51(12):1977–1983
- [Cle2006] Clementi C, Miliani C et al (2006) In situ fluorimetry: a powerful non-invasive diagnostic technique for natural dyes used in artefacts: Part I. Spectral characterization of orcein in solution, on silk and wool laboratory-standards and a fragment of Renaissance tapestry. Spectrochim Acta Part A Mol Biomol Spectrosc 64(4):906–912

- [Cle2009] Clementi C, Miliani C et al (2009) In-situ fluorimetry: a powerful non-invasive diagnostic technique for natural dyes used in artefacts: Part II. Identification of orcein and indigo in Renaissance tapestries. Spectrochim Acta Part A Mol Biomol Spectrosc 71(5):2057–2062
- [De 2007] Seixas De Melo J, Takato S et al (2007) Revisiting Perkin's dye(s): the spectroscopy and photophysics of two new mauveine compounds (B2 and C). Chem Commun 25:2624–2626
- [Doh2014] Doherty B, Gabrieli F et al (2014) Surface enhanced Raman spectroscopic investigation of orchil dyed wool from Roccella tinctoria and Lasallia pustulata. J Raman Spectrosc 45(9):723–729
- [Gei2009] Geiman I, Leona M et al (2009) Application of Raman Spectroscopy and surfaceenhanced Raman scattering to the analysis of synthetic dyes found in ballpoint pen inks. J Forensic Sci 54(4):947–952
- [HZ1977] Hezel UB, Zeiss C (1997) Potential and experience in quantitative "high performance thin-layer chromatography" HPTLC. J Chromatogr Libr 9:147–188
- [Ist2003] István K, Keresztury G et al (2003) Normal Raman and surface enhanced Raman spectroscopic experiments with thin layer chromatography spots of essential amino acids using different laser excitation sources. Spectrochim Acta Part A Mol Biomol Spectrosc 59(8):1709–1723
- [Kog1988] Koglin E (1988) Combining surface enhanced Raman scattering (SERS) and high-performance thin-layer chromatography (HPTLC). J Mol Struct 173:369–376
- [Kok 1966] Kok A (1966) A short history of the orchil dyes. Lichenologist 3(02):248–272
- [LM1982] Lee PC, Meisel D (1982) Adsorption and surface-enhanced Raman of dyes on silver and gold sols. J Phys Chem 86(17):3391–3395
- [Lom2016] Lombardi L, Serafini I et al (2016) A new approach to the mild extraction of madder dyes from lake and textile. Microchem J 126:373–380
- [Poz2011] Pozzi F, Bruni S et al (2011) Development of innovative analytical procedures for the identification of organic colorants of interest in art and archaeology. The University of Milan
- [Poz2016] Pozzi F, Zaleski S et al (2016) Surface-enhanced Raman spectroscopy: using nanoparticles to detect trace amounts of colorants in works of art. Nanoscience and cultural heritage. Springer, Berlin, pp 161–204
- [Ros2013] Rosi F, Clementi C et al (2013) Study of Raman scattering and luminescence properties of orchil dye for its nondestructive identification on artworks. J Raman Spectrosc 44(10):1451–1456
- [Ser2016] Serafini I, Lombardi L et al (2016) A new multianalytical approach for the identification of synthetic and natural dyes mixtures. The case of orcein-mauveine mixture in a historical dress of a Sicilian noblewoman of XIX century. In: Natural Product Research (in press)
- [Sou2008] Sousa MM, Melo MJ et al (2008) A study in mauve: unveiling Perkin's dye in historic samples. Chem-A Eur J 14(28):8507–8513
- [Woo2016] Woodhead AL, Cosgrove B et al (2016) The purple coloration of four late 19th century silk dresses: a spectroscopic investigation. Spectrochim Acta Part A Mol Biomol Spectrosc 154:185–192
- [ZL2005] Zhang X, Laursen RA (2005) Development of mild extraction methods for the analysis of natural dyes in textiles of historical interest using LC-diode array detector-MS. Anal Chem 77(7):2022–2025



#### Claudia Fasolato

# **Experience** Vocational

2018 – **Fixed-term Assistant Professor (rtd-A),**Dipartimento di Fisica e Geologia, Università degli Studi di Perugia,

Perugia, Italy.

2017–2018 **Postdoc @Nanophononics Lab,**Department Physik, Universitaet Basel, Basel, Switzerland

2016–2017 **Research Fellow** @**NOXXS Project**, *Dipartimento di Fisica*, *Università degli Studi di Milano*, Milan, Italy.

#### Miscellaneous

2015 – **President** @ *The Science Zone* nonprofit organization, *The Science Zone Associazione di Divulgazione Scientifica*, Rome, Italy.

#### Ph.D. Thesis

Title Plasmonic nanostructure assemblies: Surface-Enhanced Spectroscopy for Biophysical Applications

Supervisor Prof. Dr. Paolo Postorino Defense Rome, February 17th, 2017

#### Education

2013–2017 **Ph.D. in Experimental Condensed Matter Physics,** *Università Sapienza*, Rome, Italy, *summa cum laude*.
2010–2013 **Master Degree in Condensed Matter Physics** 

2010–2013 Master Degree in Condensed Matter Physics, Università Sapienza, Rome, Italy, 110/110.

© Springer Nature Switzerland AG 2018 C. Fasolato, *Surface Enhanced Raman Spectroscopy for Biophysical Applications*, Springer Theses, https://doi.org/10.1007/978-3-030-03556-3

#### 2007–2010 Bachelor Degree in Physics,

Università Sapienza, Rome, Italy, 110/110 cum laude.

2002-2007 High School Diploma, scientific curriculum,

Liceo Scientifico Statale G.B. Quadri, Vicenza, Italy, 100/100 cum laude.

#### **Publications and Conferences**

- Author of 14 peer reviewed publications (+3 in preparation) on international scientific journals (Nano Letters, Nanoscale, Applied Physics Letters, and others).
- Presenter at 13 national and international conferences (1 invited presentation, 5 oral presentations, 7 poster presentations).
- Member of the local organizing committee of the workshop Plasmonica 2014 (Rome, July 2014).

#### **Funding and Scholarships**

- "Borsa di perfezionamento all'estero" 2016–2017, Sapienza University
- "Angelo Della Riccia" Fellowship 2017, Fondazione Angelo Della Riccia
- Starting grant "Avvio alla Ricerca" 2016, Sapienza University
- Starting grant "Avvio alla Ricerca" 2014, Sapienza University

#### Awards

- Springer Prize for Best Ph.D. Thesis, Sapienza University, 2017
- Best poster presentation at ECIS 2016 conference (Rome, 4–9.09.2016)
- Best student talk at the School of Photonics 2016 (Cortona, 11–14.07.2016)
- Best poster presentation at Ramanfest 2016 conference (Berlin, 19–20.05.2016)
- Best poster presentation at Plasmonica 2013 workshop (Milan, 1–3.07.2013)

#### Ph.D. Schools and Training

- 20th International Winterschool on New Developments in Solid State Physics, Feb. 2018, Mauterndorf (Austria) chair prof. dr. A. Rastelli
- Winter School of Photophysics of Hybrid Interfaces, Jan. 2017,
   Ambroz pod Krvavcem (Slovenia) chair dr. C. Gadermaier, dr. J Gierschner
- Inelastic Neutron Scattering: Scientific Opportunities from Innovative Instrumentation, Sept. 2016, Perugia (Italy) chair dr. D. Colognesi, prof. dr. A. Orecchini
- School of Photonics 2016: Plasmonics and Nano-Optics, July 2016, Cortona (AR) (Italy) chair dr. A. Belardini, prof. dr. P. Biagioni, prof. dr. R. Sapienza
- Experimental School of Science Communication, 2015–2016, Rome (Italy) – chair dr. A. Parisi (Libreria AsSaggi)
- International School of Physics and Technology of Matter: New frontiers in downscaled materials and devices: realization and investigation by advanced methods, Sept. 2014, Otranto (LE) (Italy) – chair dr. M. Saviano, prof. dr. P. Siciliano

#### Languages

Italian Mothertongue English Excellent German Intermediate

#### **Didactic Activities**

Courses "Condensed Matter Physics" (T.A.) (Master Degree in

Physics, Univ. Basel, 2017); "Math Basics" (Bachelor Degree in Natural Sciences, Univ. Sapienza, 2014).

Topical seminaries "Plasmonic nanostructures and applications" and "Sur-

face Enhanced Raman Spectroscopy" for the course *Experimental Physics of Biosystems*. "Vibrations in solids, harmonic approximation" for the course *Condensed* 

Matter Physics.

Theses supervision Master Thesis in Physics of Biosystems (Dr. Francesca

Ripanti, Oct. 2015). Master Thesis in Nanotechnology Engineering (Dr. Francesco Pomponi, Oct. 2017). Bachelor Theses in Physics (Eleonora Bonaventura,

Oct. 2015 and Giulio Danella, Oct. 2018).

Lab training/supervision Training and supervision of several master and Ph.D.

students in HPS Research Group (Univ. Sapienza) and Nanophononics Lab (Univ. Basel). Supervision of 5 student teams in their experimental activity for the course *Experimental Condensed Matter Physics* (Univ.

Sapienza).

#### Peer-Reviewed Publications

- [1] C Fasolato, M De Luca, D Djomani, L Vincent, C Renard, G Di Iorio, V Paillard, M Amato, R Rurali, and I Zardo. Crystalline, phononic and electronic properties of heterostructured polytypic Ge nanowires by Raman spectroscopy. *Nano letters*, 2018.
- [2] C Ferrante, A Virga, L Benfatto, M Martinati, Domenico De Fazio, U Sassi, C Fasolato, AK Ott, P Postorino, D Yoon, G Cerullo, F Mauri, AC Ferrari, and T Scopigno. Raman spectroscopy of graphene under ultrafast laser excitation. *Nature communications*, 9(1):308, 2018.
- [3] V Piergrossi, C Fasolato, F Capitani, G Monteleone, P Postorino, and P Gislon. Application of Raman spectroscopy in chemical investigation of impregnated activated carbon spent in hydrogen sulfide removal process. *International Journal of Environmental Science and Technology*, pages 1–12, 2018.
- [4] L Carlini, C Fasolato, P Postorino, I Fratoddi, I Venditti, G Testa, and C Battocchio. Comparison between silver and gold nanoparticles stabilized with

negatively charged hydrophilic thiols: SR-XPS and SERS as probes for structural differences and similarities. *Colloids and Surfaces A: Physicochemical and Engineering Aspects*, 532:183–188, 2017.

- [5] I Serafini, L Lombardi, C Fasolato, M Sergi, F Di Ottavio, F Sciubba, C Montesano, M Guiso, R Costanza, L Nucci, R Curini, P Postorino, M Bruno, and A Bianco. A new multi analytical approach for the identification of synthetic and natural dyes mixtures. the case of orcein-mauveine mixture in a historical dress of a Sicilian noblewoman of nineteenth century. *Natural product research*, pages 1–12, 2017.
- [6] C Fasolato, F Sacchetti, P Tozzi, and C Petrillo. Temperature dependence of the surface plasmon resonance in small electron gas fragments, self consistent field approximation. *Solid State Communications*, 260:30–33, 2017.
- [7] A Mariani, M Campetella, C Fasolato, M Daniele, F Capitani, L Bencivenni, P Postorino, S Lupi, R Caminiti, and L Gontrani. A joint experimental and computational study on ethylammonium nitrate-ethylene glycol 1: 1 mixture. Structural, kinetic, dynamic and spectroscopic properties. *Journal of Molecular Liquids*, 226:2–8, 2017.
- [8] F Domenici, C Fasolato, Edoardo Mazzi, L De Angelis, F Brasili, F Mura, P Postorino, and F Bordi. Engineering microscale two-dimensional gold nanoparticle cluster arrays for advanced Raman sensing: An AFM study. *Colloids and surfaces A: Physicochemical and engineering aspects*, 498:168–175, 2016.
- [9] C Fasolato, S Giantulli, I Silvestri, F Mazzarda, Y Toumia, F Ripanti, F Mura, F Luongo, F Costantini, F Bordi, P Postorino, and F Domenici. Folate-based single cell screening using surface enhanced Raman microimaging. *Nanoscale*, 8(39):17304–17313, 2016.
- [10] F Capitani, C Fasolato, S Mangialardo, S Signorelli, L Gontrani, and P Postorino. Heterogeneity of propyl-ammonium nitrate solid phases obtained under high pressure. *Journal of Physics and Chemistry of Solids*, 84:13–16, 2015.
- [11] HIT Hauge, MA Verheijen, S Conesa-Boj, T Etzelstorfer, M Watzinger, D Kriegner, I Zardo, C Fasolato, F Capitani, P Postorino, A Kolling, S. and Li, S Assali, J Stangl, and EPAM Bakkers. Hexagonal silicon realized. *Nano letters*, 15(9):5855–5860, 2015.
- [12] F Brasili, E Mazzi, L De Angelis, P Postorino, F Bordi, C Fasolato, F Domenici, and F Mura. Gold nanoparticle cluster arrays for advanced optical sensing: an AFM study. In *Nanotechnology (IEEE-NANO)*, 2015 IEEE 15th International Conference on, pages 1023–1028. IEEE, 2015.
- [13] C Fasolato, F Domenici, F Brasili, F Mura, S Sennato, L De Angelis, E Mazzi, F Bordi, and P Postorino. Self-assembled nanoparticle aggregates: organizing disorder for high performance surface-enhanced spectroscopy. In *AIP Conference Proceedings*, volume 1667, page 020012. AIP Publishing, 2015.

[14] C Fasolato, F Domenici, S Sennato, F Mura, L De Angelis, F Luongo, F Costantini, F Bordi, and P Postorino. Dimensional scale effects on surface enhanced raman scattering efficiency of self-assembled silver nanoparticle clusters. *Applied Physics Letters*, 105(7):073105, 2014.